



**Supercapacitor electrode materials based on  
nanostructured conducting polymers and  
metal oxides**

**Oko Unathi Gcilitshana**

**A thesis submitted in fulfillment of the requirements for the  
degree of Doctor Philosophiae in Chemical Science, in the  
Department of Chemistry, Faculty of Science, University of the  
Western Cape**

**Supervisor: Dr. S. Ji**

**November 2013**

**KEYWORDS**

**Supercapacitor electrode materials based on nanostructured conducting polymers and metal oxides**

Oko Unathi Gcilitshana

Supercapacitors

1-Dimensional Electrode Materials

Conducting Polymers

Manganese Oxide Nanorods

Ruthenium Oxide

Bio-molecules Assisted Approach

Aqueous Electropolymerization

Low Temperature Solid State Reaction

Hydrothermal Method

Adams Method

Electrode Material Morphology


Charge and Discharge Cycling

## DECLARATION

I declare that *Supercapacitor electrode materials based on nanostructured conducting polymers and metal oxides* is my own work, and that it has not been submitted for any degree or examination in any other university, and that all sources I have used or quoted have been indicated and acknowledged by complete references.

Oko Unathi Gcilitshana

November 2013

Signed:  .....

## ACKNOWLEDGEMENTS

My heartfelt gratitude goes first to the Almighty God, who has been the foundation of this study, without whom this work would have been a futile exercise.

I am grateful to Dr. Ji Shan, my supervisor, for his confidence in me, patience and guidance.

I am also indebted to Prof. Linkov for this great opportunity he afforded me, HySA Systems and the NRF for financial support.

Many thanks also go to Dr Ge for working with me and allowing me to do part of my work with his group at Xiamen University and the wonderful students under his supervision for making my work much easier.

I would also like to acknowledge Subelia Botha in the Physics Department of UWC, for her excellent work with the TEM analysis. and Dr Remy Bucher at iThemba Labs, for his excellent work with the XRD analysis. Not forgetting Ms Miranda Waldron and Miss Suzana Vasic and team at UCT for their excellent work in the SEM and BET analysis.

Special thanks to all my colleagues and staff members at the SAIAMC for all their help during this study.

I want to express my deepest gratitude to my family, especially my brothers Mzontsundu Gcilitshana and Mandilakhe Gcilitshana, whose support has been invaluable to me. I am grateful for your unceasing love, understanding and patience.

Finally, I would like to thank my fiancé Bernard Arrey for his constant and endless love, support, understanding, patience and encouragement.

**LIST OF ABBREVIATIONS**

AC	Activated carbon
BET	Brunauer-Emmett-Teller
CAG	Carbon aerogels
CB	Carbon black
CNF	Carbon nanofibres
CNT	Carbon nanotubes
CP	Conducting polymers
CV	Cyclic Voltammetry
DL	Double Layer
EC	Electrochemical Capacitors
EDLC	Electrochemical Double Layer Capacitor
EIS	Electrochemical Impedance Spectroscopy
FTIR	Fourier Transform Infra-red
HEC	Hybrid electrochemical capacitor
Hydro	Hydrothermal
1D	One dimensional
LiClO <sub>4</sub>	Lithium perchlorate
LTSS	Low temperature solid state
MnO <sub>2</sub>	Manganese oxide
MnO <sub>2</sub> /AC	Manganese oxide on activated carbon
MnO <sub>2</sub> /C	Manganese oxide on carbon
MnO <sub>2</sub> /CNT	Manganese oxide on carbon nanotubes

## LIST OF ABBREVIATIONS

MWNT	Multi walled carbon nanotubes
NMP	N-Methyl pyrrolidone
PANI	Polyaniline
PEDOT	Poly-3,4-ethylenedioxythiophene
PPy	Polypyrrole
PSD	Pore size distribution
PT	Polythiophene
PVDF	Poly-1,1-difluoroethene
RuO <sub>2</sub>	Ruthenium oxide
RuO <sub>2</sub> /AC	Ruthenium oxide on activated carbon
RuO <sub>2</sub> /CNT	Ruthenium oxide on carbon nanotubes
SC	Specific capacitance
SEM	Scanning electron microscope
SSA	Specific surface area
SWNT	Single walled carbon nanotubes
TEM	Transmission electron microscope
TSNa	Toulene-4-sulphonic acid sodium salt
XRD	Xray diffraction

## SYNOPSIS

### **Supercapacitor electrode materials based on nanostructured conducting polymers and metal oxides**

PhD Thesis, Department of Chemistry, Faculty of Science, University of the Western  
Cape

Supercapacitors are charge-storage devices. Compared to batteries, they have higher power density, more excellent reversibility and longer cycle life. Therefore, supercapacitors have played an increasingly important role in the fields of power source especially in automotive applications, such as electric and hybrid electric vehicles. The higher power density of supercapacitors offers improved vehicle acceleration and the ability to recover more energy from regenerative braking, since they can be charged and discharged at high current. Generally, the key for supercapacitors to achieve high specific power depends on the inherent properties and the surface areas of their electrode materials. Therefore, current research in the field of supercapacitors has been carried out with increased emphasis on the development of new electrode materials.

Optimal novel synthesis of electrode materials for supercapacitor application in hybrid vehicles was accomplished with polypyrrole nanowires, manganese oxide and its carbon composites, ruthenium oxide and its carbon composites being the products.

A set of structural and chemical parameters influencing the performance of synthesized electrode materials were identified. Parameters included crystallinity, particle

size, particle size distribution, surface area, electrochemical activity. A large range of analytical tools were employed in characterizing the electrode materials of interest.

High accuracy and precision in the quantitative and qualitative structural characterization of electrode materials collected by x-ray diffractometry, transmission electron microscopy, scanning electron microscopy and Fourier transform infra-red spectroscopy was demonstrated.

N<sub>2</sub>-physisorption produced surface area and pore size distribution data of high quality.

Cyclic voltammetry, charge and discharge cycling, electron impedance spectroscopy were employed in the electrochemical characterization of the synthesized electrode materials and both qualitative and quantitative information obtained.

The techniques were able to discriminate between various synthesized electrode materials and identify the highly electroactive materials. Preparation variables could be critically evaluated for the synthesis of electrode materials. The techniques were deemed to be applicable in discriminating high and low activity electrode materials based on their structural and chemical properties.



**RESEARCH OUTPUTS**

**2010 Hysa Student Seminar: Oral presentation**

Supercapacitor electrode materials based on nanostructured conducting polymers

**2011 Hysa Student Seminar: Oral presentation**

Fabrication of electrode materials for Supercapacitors

**2011 International Battery Association Meeting, Cape Town: Poster presentation**

Fabrication of electrode materials for effective use in Supercapacitors

**Electrochemical synthesis of polypyrrole nanowires in the presence of gelatin:**

Article: Synthetic Metals 161 (2011) 166–172

**2012 Hysa Student Seminar: Oral presentation**

1D Conducting polymers for use as electrode materials for Supercapacitors.

## TABLE OF CONTENTS

KEYWORDS .....	i
DECLARATION .....	ii
ACKNOWLEDGEMENTS .....	iii
LIST OF ABBREVIATIONS .....	iv
SYNOPSIS .....	vi
REASEARCH OUTPUTS .....	viii
TABLE OF CONTENTS .....	ix
LIST OF FIGURES .....	xvii
LIST OF TABLES .....	xxiv
<b>CHAPTER 1: INTRODUCTION</b> .....	<b>1</b>
<b>1.1. BACKGROUND</b> .....	<b>1</b>
<b>1.2. OBJECTIVES</b> .....	<b>4</b>
<b>1.1 . SCOPE OF RESEARCH</b> .....	<b>5</b>
<b>1.2 RESEARCH STRUCTURE</b> .....	<b>6</b>
<b>CHAPTER 2: LITERATURE REVIEW</b> .....	<b>10</b>

<b>2.1. SUPERCAPACITORS</b> .....	10
<b>2.1.1. Introduction</b> .....	10
<b>2.1.2. Electrical energy storage mechanisms of Supercapacitors</b> .....	14
2.1.2.1. Electrochemical Double Layer Supercapacitor .....	14
2.1.2.2. Psuedocapacitor .....	16
2.1.2.3. Hybrid Electrochemical Supercapacitor .....	19
<b>2.2. ELECTRODE MATERIALS FOR SUPERCAPACITORS</b> .....	20
<b>2.2.1. Electrochemical Double Layer Supercapacitor</b> .....	20
2.2.1.1. Carbon Black .....	22
2.2.1.2. Graphitic Carbon .....	24
2.2.1.3. Activated Carbon .....	26
2.2.1.3.1. <i>Thermal Activation</i> .....	27
2.2.1.3.2. <i>Chemical Activation</i> .....	27
2.2.1.4. Carbon Aerogels .....	28
2.2.1.5. Carbon Nanotubes .....	28
<b>2.2.2. Psuedocapacitor</b> .....	32
2.2.2.1. Metal Oxides .....	32
2.2.2.1.1. <i>Manganese Oxide</i> .....	33
2.2.2.1.2. <i>Ruthenium Oxide</i> .....	34
2.2.2.2. Conducting Polymers .....	35
2.2.2.2.1. <i>Polyaniline (PANI)</i> .....	37
2.2.2.2.2. <i>Polythiophene (PT)</i> .....	40
2.2.2.2.3. <i>Poly-3,4-ethylenedioxythiophene (PEDOT)</i> .....	42

TABLE OF CONTENTS	PAGES
2.2.2.2.4. Polypyrrole (Ppy).....	44
<b>2.2.3. Hybrid Supercapacitor</b> .....	<b>47</b>
2.2.3.1. Symmetric Hybrids.....	47
2.2.3.2. Assymmetric Hybrids.....	47
2.2.3.3. Battery Type Hybrids.....	48
<b>2.3 SYNTHESIS OF THE ELECTRODE MATERIALS</b> .....	<b>48</b>
<b>2.3.1. Carbon Based Materials</b> .....	<b>48</b>
<b>2.3.2. Transition Metals Oxides</b> .....	<b>51</b>
2.3.2.1 Ruthenium oxide.....	51
2.3.2.2 Manganese oxide.....	53
2.3.2.2.1 Chemical synthesis.....	53
2.3.2.2.2 Electrochemical synthesis.....	54
2.3.2.2.3 Sol-gel method.....	55
<b>2.3.3. Conducting Polymers</b> .....	<b>56</b>
2.3.3.1. Soft Template Method.....	56
2.3.3.2. Template-Free Method.....	59
2.3.3.3. Hard Template Method.....	60
2.3.3.3.1. Anodic Alumina Oxide membrane.....	61
2.3.3.3.2. Track etched membrane.....	65
2.3.3.3.3. Biomolecules -assisted approach.....	66
<b>2.4. ELECTROLYTES FOR SUPERCAPACITORS</b> .....	<b>67</b>
<b>2.4.1. Aqueous Electrolytes</b> .....	<b>67</b>

TABLE OF CONTENTS	PAGES
<b>2.5 MOTIVATION TO THE STUDY</b> .....	68
<b>CHAPTER 3: METHODOLOGY</b> .....	70
<b>3.1. CHEMICALS AND MATERIALS</b> .....	70
<b>3.2. SYNTHESIS OF POLYPYRROLE NANOWIRES</b> .....	71
3.2.1. Passivation of an Electropolymerization substrate and purification of the Monomer .....	71
3.2.2. Electrochemical Polymerization of Polypyrrole .....	72
3.2.2.1. Bio-templating Synthesis Technique for Polypyrrole Nano wires... .....	73
3.2.2.2. Electropolymerization by doping method of polypyrrole nanowires .....	74
<b>3.3. SYNTHESIS OF MANGANESE OXIDE ELECTRODE MATERIALS</b> .....	77
3.3.1. Low Temperature Solid State Reaction .....	78
3.3.2. Hydrothermal Method .....	79
<b>3.4. SYNTHESIS OF RUTHENIUM OXIDE</b> .....	82
<b>3.5. ELECTRODE PREPARATION</b> .....	85
<b>3.6. MORPHOLOGICAL AND STRUCTURAL ANALYSIS</b> .....	88
3.6.1. Scanning Electron Microscopy .....	88
3.6.2. Transmission Electron Microscopy .....	89
3.6.3. X-Ray Diffractometry .....	90
3.6.4. Surface Area and Porosity Determination by N <sub>2</sub> Physisorption .....	92
3.6.5. Fourier Transform Infrared Spectroscopy .....	93

<b>3.7 ELECTROCHEMICAL CHARACTERISATION TECHNIQUES .....</b>	<b>94</b>
3.7.1. Cyclic Voltammetry (CV) Analysis.....	94
3.7.2. Charge/Discharge Testing.....	95
3.7.3. Impedance Spectroscopy.....	95
 <b>CHAPTER 4: SYNTHESIS AND CHARACTERIZATION OF 1D CONDUCTING POLYMERS AS ELECTRODE MATERIALS FOR SUPERCAPACITORS .....</b>	 <b>97</b>
 <b>4.1. INTRODUCTION.....</b>	 <b>97</b>
 <b>4.2 ELECTROCHEMICAL POLYMERIZATION OF CONDUCTING POLYPYRROLE NANOWIRES.....</b>	 <b>99</b>
 <b>4.3. PHYSICAL CHARACTERIZATION OF CONDUCTING POLYPYRROLE NANOWIRES.....</b>	 <b>100</b>
4.3.1. Surface Morphology study for Polypyrrole nanowires.....	100
4.3.2. Functional group analysis of the synthesized Polypyrrole nanowires .....	103
4.3.3. X-ray diffraction pattern of the synthesized Polypyrrole nanowires using aqueous electropolymerization method.....	106
 <b>4.4. ELECTROCHEMICAL CHARACTERIZATION OF CONDUCTING POLYPYRROLE NANOWIRES .....</b>	 <b>107</b>
4.4.1. Cyclic Voltammetry.....	107
4.4.2 Charge and discharge cycling.....	108
4.4.3. Electrochemical Impedance Spectroscopy (EIS) analysis.....	111

<b>4.5 CONCLUSION</b> .....	112
<b>CHAPTER 5: SYNTHESIS OF SINGLE-CRYSTAL MANGANESE NANORODS USING LOW TEMPERATURE SOLID STATE REACTION AND HYDROTHERMAL METHOD</b> .....	114
<b>5.1. INTRODUCTION</b> .....	114
<b>5.2. PHYSICAL CHARACTERIZATION OF SINGLE-CRYSTAL MANGANESE OXIDE NANORODS</b> .....	115
5.2.1. Particle size and particle size distribution study of both LTSSR and Hydrothermal method synthesized MnO <sub>2</sub> electrode materials and their carbon composites.....	116
5.2.2. Particle size and crystallinity study of LTSSR and Hydrothermal method synthesized MnO <sub>2</sub> electrode materials.....	120
5.2.3. BET surface area of both LTSSR method and Hydrothermal method synthesized MnO <sub>2</sub> electrode materials;.....	122
<b>5.3. ELECTRO-CHEMICAL CHARACTERIZATION OF SINGLE-CRYSTAL MANGANESE OXIDE NANORODS</b> .....	125
5.3.1 Cyclic Voltammetry analysis.....	125
5.3.2. Charge and Discharge Cycling.....	129
5.3.3. Potassium hydroxide versus sodium sulphate electrolyte.....	136
<b>5.4. CONCLUSION</b> .....	137
<b>CHAPTER 6: EVALUATION OF SINGLE-CRYSTAL MANGANESE OXIDE CABORN COMPOSITES SYNTHESIZED USING LOW TEMPERATURE SOLID STATE REACTION AND HYDROTHERMAL METHOD</b> .....	138
<b>6.1. INTRODUCTION</b> .....	138

<b>6.2. PHYSICAL CHARACTERIZATION OF MANGANESE OXIDE NANORODS CARBON COMPOSITES</b> .....	141
6.2.1. Particle size and particle size distribution study of the synthesized MnO <sub>2</sub> carbon composites.....	141
6.2.2. Particle size and crystallinity study of the synthesized MnO <sub>2</sub> carbon composites.....	146
6.2.3. BET surface area of the Synthesized MnO <sub>2</sub> carbon composites....	150
<b>6.3. ELECTRO-CHEMICAL CHARACTERIZATION OF SINGLE-CRYSTAL MANGANESE OXIDE NANORODS CARBON COMPOSITES</b> .....	154
6.3.1. Cyclic voltammetry.....	154
6.3.2. Charge and Discharge Cycling.....	160
<b>6.4. CONCLUSION</b> .....	169
<b>CHAPTER 7: SYNTHESIS AND CHARACTERIZATION OF A POLY CRYSTALLINE RUTHENIUM OXIDE AND ITS CARBON COMPOSITES AS ELECTRODE MATERIALS</b> .....	171
<b>7.1. INTRODUCTION</b> .....	170
<b>7.2. PHYSICAL CHARACTERIZATION OF RUTHENIUM OXIDE AND ITS CARBON COMPOSITES</b> .....	174
7.2.1. Particle size distribution and composition study of the synthesized RuO <sub>2</sub> electrode materials and its carbon composites.....	171
7.2.2 Particle size and crystallinity study of Ruthenium Oxide and its carbon composite.....	174
7.2.3. BET surface area of the Synthesized MnO <sub>2</sub> carbon composites....	176



<b>7.3 ELECTRO-CHEMICAL CHARACTERIZATION OF RUTHENIUM OXIDE AND ITS CARBON COMPOSITES</b> .....	179
7.3.1. Cyclic Voltammetry.....	179
7.3.2 Charge and discharge cycling.....	182
<b>7.4. CONCLUSION</b> .....	186
<b>REFERENCES</b> .....	188
<b>APPENDICES</b> .....	211

## LIST OF FIGURES

### Chapter 2

Figure 2.1: Schematic operating system of a Lithium-ion battery.....	11
Figure 2.2: Schematic operating system of an Electrochemical- Double Layer Capacitor.....	12
Figure 2.3: Ragone plots for an array of energy storage and energy conversion devices .....	13
Figure 2.4: Schematic of an Electrical Double Layer .....	15
Figure 2.5: Schematic presentation of a Pseudocapacitor.....	17
Figure 2.6: Schematic presentation of a Hybrid Capacitor.....	19
Figure 2.7: Image for Carbon black .....	22
Figure 2.8: The stacking of graphene sheets results in a layered structure.....	24
Figure 2.9: Image for Activated Carbon .....	26
Figure 2.10: Experimental setup of arc discharge method for carbon nanotube production .....	29
Figure 2.11: Computer generated image of a multi walled carbon nanotube.....	30
Figure 2.12: Structure of single walled carbon nanotubes (SWNTs) with (a) armchair, (b) zigzag, and (c) chiral chirality.....	31
Figure 2.13: Application fields for Conducting Polymer Nanomaterials .....	36
Figure 2.14: Schematic presentation of the polymerization of aniline.....	38
Figure 2.15: Schematic presentation of the polymerization of thiophene.....	40
Figure 2.16: Schematic presentations for the polymerization of ethylenedioxythiophene.....	42
Figure 2.17: Schematic presentation of the polymerization of pyrrole.....	44

LIST OF FIGURES	PAGES
Figure 2.18: Possible chemical structures in PPy chains .....	45
Figure 2.19: Schematic illustrations of (a) oil-in-water and (b) water-in-oil micelles.....	57
Figure 2.20: Schematic illustration for the surfactant templating of (a) PPy nanosphere, (b) nanorod, and (c) layered assemblies.....	58
Figure 2.21: Schematic illustrating the use of an Al <sub>2</sub> O <sub>3</sub> membrane as a template in the synthesis of 1-D PEDOT nanostructure .....	62
Figure 2.22: Schematic presentation for Vapour Deposition Polymerization method ..	64
Figure 2.23: Simplified schematic representation of the synthetic strategy for the formation of PPy nanowires.....	66

### **Chapter 3**

Figure 3.1: A schematic illustration of an aqueous electropolymerization approach.....	75
Figure 3.2: A schematic illustration of a Low Temperature Solid State Reaction.....	79
Figure 3.3: A schematic illustration of a Hydrothermal Method.....	81
Figure 3.4: A schematic illustration of Adam's Method.....	84
Figure 3.5: Photograph of the coin cell used for electrochemical cycling testing.....	86
Figure 3.6: Schematic presentation for the electrode preparation.....	87

### **Chapter 4**

Figure 4.2.1_Potentiostatic curve for the electropolymerization of polypyrrole nanowires on a nickel foil in the presence of (a) Gelatine and (b) TSNa .....	99
Figure 4.3.1 (a), (b) SEM and (d) TEM micrograph of PPy superlong nanowires synthesized on the nickel electrode in the presence of gelatine, (c) SEM micrograph of cauliflower-like PPy synthesized in the absence of gelatin .....	101

Figure 4.3.1: (e), (f) SEM and (g), (h) TEM images of PPy nanowires synthesized on a nickel electrode in the presence of TSNa.....	102
Figure 4.3.2: FTIR spectrum of polypyrrole nanowires synthesized in the presence of gelatin.....	104
Figure 4.3.3: FTIR spectrum of polypyrrole nanowires synthesized in the presence of TSNa.....	105
Figure 4.3.4: XRD pattern for the synthesized polypyrrole nanowires synthesized in the presence of TSNa.....	106
Figure 4.4.1: Cyclic voltammograms for polypyrrole nanowires synthesized in the presence of TSNa.....	108
Figure 4.4.2: Discharge cycles of polypyrrole nanowires synthesized in the presence of TSNa.....	109
Figure 4.4.3: Discharge capacities and capacitances of polypyrrole nanowires synthesized in the presence of TSNa.....	110
Figure 4.4.4: Nyquist plot of the polypyrrole nanowires in the presence of TSNa.....	111

## Chapter 5

Figure 5.2.1: Micrographs of low temperature solid state reaction synthesized MnO <sub>2</sub> (3hrs), TEM (a), (c) and SEM (e), for (5hrs), TEM (b), (d) and SEM (f).....	117
Figure 5.2.1: Micrographs of hydrothermal method synthesized MnO <sub>2</sub> 3hrs, TEM (g), (i) and SEM (k), for (5hrs), TEM (h), (j) and SEM (l).....	118
Figure 5.2.2.1: XRD patterns of LTSSR method and hydrothermal method (3hrs and 5hrs) synthesized MnO <sub>2</sub> .....	120

Figure 5.2.3.1: The nitrogen adsorption isotherms of MnO <sub>2</sub> nanorods synthesized by LTSSR (3hrs and 5hrs) and hydrothermal method (3hrs and 5hrs) at 77K.....	124
Figure 5.2.3.2: Barrett-Joyner and Halenda (BJH) pore size distribution plots of MnO <sub>2</sub> nanorods synthesized by LTSSR (3hrs and 5hrs) and hydrothermal method (3hrs and 5hrs) at 77K.....	124
Figure 5.3.1: Cyclic voltammograms of (a) MnO <sub>2</sub> LTSSR (3hrs), (b) MnO <sub>2</sub> LTSSR (5hrs), (c) MnO <sub>2</sub> HYDRO (3hrs) and (d) MnO <sub>2</sub> HYDRO (5hrs) in a 1M Na <sub>2</sub> SO <sub>4</sub> electrolyte.....	126
Figure 5.3.2: Cyclic voltammograms of (a) MnO <sub>2</sub> LTSSR (3hrs), (b) MnO <sub>2</sub> LTSSR (5hrs), (c) MnO <sub>2</sub> HYDRO (3hrs) and (d) MnO <sub>2</sub> HYDRO (5hrs) in a 6M KOH electrolyte.....	127
Figure 5.3.3: Discharge cycles of (a) MnO <sub>2</sub> LTSSR (3hrs), (b) MnO <sub>2</sub> Hydro (3hrs), (c) MnO <sub>2</sub> LTSSR (5hrs) and (d) MnO <sub>2</sub> Hydro (5hrs) using Na <sub>2</sub> SO <sub>4</sub> electrolyte.....	130
Figure 5.3.4: The discharge capacities (a) and (b) discharge capacitances vs. cycle number for the MnO <sub>2</sub> electrode materials in sodium sulphate electrolyte.....	132
Figure 5.3.5: Discharge cycles of (a) MnO <sub>2</sub> LTSSR (3hrs), (b) MnO <sub>2</sub> Hydro (3hrs), (c) MnO <sub>2</sub> LTSSR (5hrs) and (d) MnO <sub>2</sub> Hydro (5hrs) using KOH electrolyte.....	133
Figure 5.3.6: The discharge capacity (a) and (b) discharge capacitance vs. cycle number for the MnO <sub>2</sub> electrode materials in potassium hydroxide electrolyte.....	135

## Chapter 6

Figure 6.1: Micrographs of Carbon Black, TEM (a) and SEM (b), Activated Carbon TEM (c) and SEM (d), Carbon Nanotubes TEM(e) and SEM (f).....	140
Figure 6.2.1: Micrographs of MnO <sub>2</sub> /C LTSSR 3hrs, TEM (a) and SEM (b), MnO <sub>2</sub> /AC LTSSR 3hrs, TEM (c) and SEM (d), MnO <sub>2</sub> /CNT LTSSR 3hrs, TEM (e) and SEM (f)....	142

Figure 6.2.1: Micrographs of MnO <sub>2</sub> /C LTSSR 5hrs, TEM (g) and SEM (h), MnO <sub>2</sub> /AC LTSSR 5hrs, TEM (i) and SEM (j), MnO <sub>2</sub> /CNT LTSSR 5hrs, TEM (k) and SEM (l)...	143
Figure 6.2.1: Micrographs of MnO <sub>2</sub> /C HYDRO 3hrs, TEM (m) and SEM (n), MnO <sub>2</sub> /AC HYDRO 3hrs, TEM (o) and SEM (p), MnO <sub>2</sub> /CNT HYDRO 3hrs, TEM (q) and SEM (r)	144
Figure 6.2.1: Micrographs of MnO <sub>2</sub> /C HYDRO 5hrs, TEM(s) and SEM (t), MnO <sub>2</sub> /AC HYDRO 5hrs, TEM (u) and SEM (v), MnO <sub>2</sub> /CNT HYDRO 5hrs, TEM (w) and SEM(x)	145
Figure 6.2.2.1: XRD patterns of LTSSR (3hrs and 5hrs) method and Hydrothermal method (3hrs and 5hrs) synthesized MnO <sub>2</sub> /AC electrode materials	147
Figure 6.2.2.2: XRD patterns of LTSSR (3hrs and 5hrs) method and Hydrothermal method (3hrs and 5hrs) synthesized MnO <sub>2</sub> /C electrode materials	147
Figure 6.2.2.3: XRD patterns of LTSSR (3hrs and 5hrs) method and Hydrothermal method (3hrs and 5hrs) synthesized MnO <sub>2</sub> /CNT electrode materials	148
Figure 6.2.3.1: The nitrogen adsorption isotherms of carbon support materials at 77K	150
Figure 6.2.3.2: Barrett-Joyner and Halenda (BJH) pore size distribution plots carbon support materials at 77K	151
Figure 6.2.3.3: Barrett-Joyner and Halenda (BJH) pore size distribution plot of MnO <sub>2</sub> Carbon composites prepared using LTSSR and Hydrothermal method for 3hrs	153
Figure 6.2.3.4: Barrett-Joyner and Halenda (BJH) pore size distribution plot of MnO <sub>2</sub> Carbon composites prepared using LTSSR and Hydrothermal method for 5hrs	154
Figure 6.3.1: Cyclic voltammograms of MnO <sub>2</sub> /AC LTSS 3hrs (a), 5hrs (b) and MnO <sub>2</sub> HYDRO/AC 3hrs (c), 5hrs (d), respectively	155

Figure 6.3.2: Cyclic voltammograms of MnO <sub>2</sub> /C LTSSR 3hrs (a), 5hrs (b) and MnO <sub>2</sub> HYDRO/C 3hrs (c), 5hrs (d), respectively.....	156
Figure 6.3.3: Cyclic voltammograms of MnO <sub>2</sub> /CNT LTSSR 3hrs (a), 5hrs (b) and MnO <sub>2</sub> HYDRO/CNT 3hrs (c), 5hrs (d), respectively .....	157
Figure 6.3.4: Discharge cycles of (a) MnO <sub>2</sub> /C LTSSR (3hrs) (b) (5hrs) and MnO <sub>2</sub> /C HYDRO (c) (3hrs), (d) (5hrs), respectively.....	161
Figure 6.3.5: The discharge capacity (a) and (b) discharge capacitance vs. cycle number for the MnO <sub>2</sub> /C electrode materials.....	161
Figure 6.3.6: Discharge cycles of MnO <sub>2</sub> /AC LTSSR (a) (3hrs), (b) (5hrs) and MnO <sub>2</sub> /AC HYDRO (c) (3hrs), (d) (5hrs), respectively.....	164
Figure 6.3.7: The discharge capacity (a) and (b) discharge capacitance vs. cycle number for the MnO <sub>2</sub> /AC electrode materials.....	164
Figure 6.3.8: Discharge cycles of MnO <sub>2</sub> /CNT LTSSR (a) (3hrs), (b) (5hrs) and MnO <sub>2</sub> /CNT HYDRO (c) (3hrs), (d) (5hrs), respectively.....	167
Figure 6.3.9: The discharge capacity (a) and (b) discharge capacitance vs. cycle number for the MnO <sub>2</sub> /CNT electrode materials.....	167

## Chapter 7

Figure 7.2.1: (a) crystallograph (b) and (c) TEM and SEM micrographs of Adam's method synthesized RuO <sub>2</sub> , respectively.....	172
Figure 7.2.1: TEM (d), (e) and SEM (f), (g) micrographs of Adam's method synthesized RuO <sub>2</sub> /Ac and RuO <sub>2</sub> /C, respectively.....	173

Figure 7.2.1: TEM (h) and SEM (i) micrographs of Adam's method synthesized RuO <sub>2</sub> /CNT.....	174
Figure 7.2.2: XRD patterns of as-prepared RuO <sub>2</sub> , RuO <sub>2</sub> /AC, RuO <sub>2</sub> /C and RuO <sub>2</sub> /CNT ...	175
Figure 7.2.3: The nitrogen adsorption isotherms of RuO <sub>2</sub> and its carbon composites at 77K .....	178
Figure 7.2.4: Barrett-Joyner and Halenda (BJH) pore size distribution plot of RuO <sub>2</sub> and its carbon composites.....	178
Figure 7.3.1: Cyclic voltammograms of RuO <sub>2</sub> (a), (b) and RuO <sub>2</sub> /AC (c), (d).....	180
Figure 7.3.2: Cyclic voltammograms of RuO <sub>2</sub> /C (a), (b) and RuO <sub>2</sub> /CNT (c), (d).....	181
Figure 7.3.3: Discharge cycles of RuO <sub>2</sub> (a), RuO <sub>2</sub> /AC (b), RuO <sub>2</sub> /C (c) and RuO <sub>2</sub> /CNT, (d) .....	183
Figure 7.3.4: The <b>(a)</b> discharge capacity and <b>(b)</b> discharge capacitance vs. cycle number for the RuO <sub>2</sub> and its carbon composites.....	185



## Chapter 2

Table 2.1: Comparison of EDCL and Pseudocapacitance .....	18
-----------------------------------------------------------	----

## Chapter 3

Table 3.1: List of used chemicals and materials .....	70
Table 3.2: Materials used for the Passivation of the Electropolymerization substrate.....	72
Table 3.3: Conditions for the Electrochemical Polymerization process.....	77
Table 3.4: Materials and parameters used in the Low Temperature Solid State Reaction..	79
Table 3.5: Materials and parameters used in the Hydrothermal Method .....	81
Table 3.6: Materials and parameters used in the Adam's Method .....	85
Table 3.7: Cell Materials Specifications .....	88
Table 3.8: The Operating Parameters of the FEI Nova Nano FEG SEM 230 .....	89
Table 3.9: TEM Operating Parameters.....	90
Table 3.10: XRD Operating Parameters.....	92
Table 3.11: BET Operating Parameters.....	93
Table 3.12: Cyclic Voltammetry Parameters .....	95

## Chapter 4

Table 4.4.1: Capacity and capacitance values of polypyrrole nanowires (TSNa).....	109
-----------------------------------------------------------------------------------	-----

## Chapter 5

Table 5.2.2.1: Particle size (D) and Inter-planar spacing (d) in Hydrothermal and LTSSR prepared MnO <sub>2</sub> and its carbon composites.....	121
Table 5.2.3.1: Surface Area and Porosity Data for both the Hydrothermally and LTSS prepared MnO <sub>2</sub> and its carbon composites.....	122

Table 5.3.1: Cyclic voltammetry capacitance values in 1M Na<sub>2</sub>SO<sub>4</sub> ..... 129

Table 5.3.2: Cyclic voltammetry capacitance values in 6M KOH ..... 129

**Chapter 6**

Table 6.2.2.1: Particle size (D) and Inter-planar spacing (d) in Hydrothermal and LTSSR prepared MnO<sub>2</sub> carbon composites..... 149

Table 6.2.3.1: Surface Area and Porosity Data for carbon support materials..... 151

Table 6.2.3.2: Surface Area and Porosity Data for both hydrothermally and LTSS materials..... 152

Table 6.3.1: Cyclic voltammetry capacitance values of MnO<sub>2</sub>/AC in 6M KOH..... 159

Table 6.3.2: Cyclic voltammetry capacitance values of MnO<sub>2</sub>/C in 6M KOH..... 159

Table 6.3.3: Cyclic voltammetry capacitance values of MnO<sub>2</sub>/CNT in 6M KOH..... 159

**Chapter 7**

Table 7.2.1: Particle size and inter-planar spacing of RuO<sub>2</sub> electrode material and its carbon composites..... 176

Table 7.2.2: Surface Area and Porosity Data for RuO<sub>2</sub> and its carbon composites..... 177

Table 7.3.1: Cyclic voltammetry capacitance values of RuO<sub>2</sub> and its carbon composites ..... 182

# CHAPTER 1

## INTRODUCTION

### 1.1. BACKGROUND

As the concern grows over fossil fuel usage, in terms of global warming and resource depletion, there will be a progressive swing to renewable energy. This will necessitate the development of improved methods for storing electricity when it is available and retrieving when needed. With the increasing need for high-powered energy storage devices, supercapacitors have been attracting continuous interest because of their large capacity and high rate capability, which would satisfy the energy and power demand in many electric systems and devices, such as hybrid electric vehicles, computers and mobile electric devices for electrical vehicles and mobile electronic devices [1–3].

Energy storage systems can be divided into two main categories: Batteries and Electrochemical Capacitors (ECs). Batteries store the energy in the form of chemical reactants whereas electrochemical capacitors store energy directly as charge. Due to that fundamental difference between the systems, they exhibit different energy and power outputs, charge and discharge cyclability.

Batteries can generally store significantly more energy per unit mass than ECs because they use Faradaic processes. Faradaic processes involve the transfer of charge across the interfaces between the battery electrodes and electrolyte solutions which lead to redox reactions of species at the interfaces. These redox reactions change the molecular or crystalline structure of the electrode materials when the battery is charged. This often

affects their stability, so generally batteries must be replaced after several thousand charge and discharge cycles.

On the other hand, the use of ECs in hybrid vehicles has been of interest because of the fact that they can be charged and discharged up to millions of times without showing major changes in the electrode properties during operation. Their charge-storing processes are much faster than the Faradaic processes employed in the batteries, so although ECs have lower energy densities than batteries, they have higher power density. This makes them even more attractive in the use of hybrid car vehicles because this higher power density of supercapacitors offers improved vehicle acceleration and the ability to recover more energy from regenerative braking, since they can be charged and discharged at high current. Another factor that makes the ECs more attractive is that they can be charged and discharged in seconds whereas high-performance rechargeable batteries require at least tens of minutes to charge and hours to discharge.

With a growing demand for power sources, supercapacitors, often called Electrical Double-Layer Capacitors (EDLCs), pseudocapacitances, ultracapacitors, power capacitors, have attracted worldwide research interest because of their potential applications as energy storage devices in many fields. Such a surge in interest is attributable to the fact that they combine the advantages of the high power of dielectric capacitors and the high specific energy of rechargeable batteries [4–6]. The electrode material as an important part of supercapacitor has also drawn considerable attention, especially the advanced nanomaterials, in which the ion diffusion path is dramatically shortened, leading to the high rate capability and large capacity [7–9].

Various carbon-based materials such as activated carbons (ACs) [10,11], carbon aerogels (CAGs) [12,13], graphites [6,15,16], CNTs [27,28,34], carbon nanofibers (CNFs) [29,30] and nano-sized carbon [31–33] have been actively investigated for use as the electrode materials for ECs because of their accessibility, easy processability, relatively low cost, non-toxicity, high chemical stability, and wide temperature range. Based on these materials, different methodologies have been applied to increase their Specific Surface Area (SSA) or tailoring Pore Size Distribution (PSD). This has resulted in considerable improvement of energy, power, and operation parameters of ECs.

According to the storage mechanism of EDLCs, the SSA of carbon-based materials plays an important role. It is supposed that the larger the SSA, the higher the specific capacitance. However, the major problem of high SSA carbon is that not all the BET surface area is electrochemically accessible when in contact with an electrolyte [22], that is, the gravimetric capacitance of various carbon materials does not increase linearly with the SSA.

Transition metal oxides are considered to be the best candidate materials for EC because of their high specific capacitance coupled with very low resistance resulting in a high specific power, which makes them very appealing in commercial applications [23,24]. Among the transition metal oxides,  $\text{RuO}_2$  is the most promising electrode material due to its high specific capacitance, long cycle life, high conductivity, and good electrochemical reversibility, as well as its high rate capability [25]. But the lack of abundance and cost of the precious metal ruthenium (Ru) are major disadvantages for commercial production of  $\text{RuO}_2$ .

Most attention had focused on hydrous manganese oxide as a candidate for pseudocapacitor, due to the low cost of raw materials and the fact that manganese is more environmentally friendly than any other transition metal oxide systems. However, Yang et.al [26], argues that its high rate performance is not good.

At present, many researchers have focused on the synthesis method and capacitive characterization of nanomaterials. In particular, one-dimensional (1D) nanostructured conducting polymers are recognized to be promising electrode materials for supercapacitors in view of their distinctive characteristics of conducting pathways, surface interactions, nanoscale dimensions, good thermal and chemical stability, and high electrical conductivity in the doped state.

This study focuses on the development of 1D nanostructured Polypyrrole conducting polymers and comparing their electrochemical behavior with the Manganese Oxide and Ruthenium Oxide electrode materials. All of the materials mentioned were synthesized and studied.

## **1.2 OBJECTIVES**

The main research areas of the investigation were;

- Investigation of the synthesis of Conducting Polypyrrole and examination of the physical and electrochemical properties influencing its electro-activity.
- Examination of the synthesis of  $\text{MnO}_2$  and analysis of the physical and electrochemical properties influencing its electro-activity.
- Exploration of the synthesis and comparison of carbon composite  $\text{MnO}_2$  and examination of the physical and electrochemical properties influencing its electro-activity.

- Investigation of the synthesis of RuO<sub>2</sub> with its carbon composites and analysis of the physical and electrochemical properties influencing its electro-activity.

### 1.3 SCOPE OF THE INVESTIGATION

In this study the following research areas were investigated;

- Synthesis of conducting polypyrrole nanowires using two methods: Biomolecules assisted approach, this method involves using gelatin as a structure directing agent and aqueous electropolymerization method involves the use of a Toulene-4-Sulphonic acid Sodium Salt (TsNa) as a dopant.
- Physical characterization of the conducting polypyrrole nanowires,
- Electrochemical characterization of the conducting polypyrrole nanowires,
- Synthesis of manganese oxide nanorods using two methods: Low temperature solid state reaction and in the synthetic method of solid state reaction, MnCl<sub>2</sub>.4H<sub>2</sub>O was used as the metal salts which when reacted with KMnO<sub>4</sub> offer the possibility of preparing nano sized products and in the hydrothermal method the crystal growth is anisotropic, it is prone to grow slowly toward one-dimensional direction under the hydrothermal conditions such as high pressure and temperature,
- Physical characterization of manganese oxide electrode materials,
- Electrochemical characterization of manganese oxide electrode materials,
- Synthesis of manganese oxide carbon composites and compare their properties using Low Temperature solid state reaction and hydrothermal method ,
- Physical characterization of manganese carbon composites,
- Electrochemical characterization of manganese carbon composites,
- Synthesis of ruthenium oxide and its carbon composites using Adams method, RuCl<sub>3</sub>.H<sub>2</sub>O has been used as a precursor

- Physical characterization of ruthenium oxide electrode material and its carbon composites,
- Electrochemical characterization of ruthenium oxide electrode material and its carbon composites.

## **1.4 RESEARCH STRUCTURE**

### **Chapter 2: Literature review**

The literature review looks into the various types of supercapacitors, taking a more in- depth look at electrode materials for these energy storage devices. Furthermore, the chapter explores the developments made on supercapacitors and their electrode materials. The various electrode materials commonly used for supercapacitors, the methods used in the synthesis of these materials, as well as the electrolytes used in these devices are discussed in detail. . The literature review then focuses on discussing the support materials.

### **Chapter 3: Methodology**

Chapter 3 describes the synthesis techniques utilized for the electrode materials under review. All the synthesis procedures employed in this investigation are fully outlined in this chapter. Emphasis is also placed on the physical and electrochemical characterization techniques employed in this study. The starting precursor materials, their sources and specifications are described in this chapter. In addition, the specifications of the equipment utilized for analysis and synthesis of the assorted electrode materials are all explored in this chapter.



#### **Chapter 4: Synthesis and characterization of polypyrrole as electrode materials for supercapacitors**

Chapter 4 gives in-depth look into the synthesis of Polypyrrole, for possible use as an electrode material for supercapacitor anode application. Two methods were employed for the synthesis of the polypyrrole electrode materials and the products compared and reviewed. The morphology and the surface study of the synthesized materials were accomplished by scanning electron microscopy, transmission electron microscopy, Fourier transform spectroscopy and X-ray diffraction. Electrochemical characterization of the polypyrrole electrode material was studied via cyclic voltammetry and electrochemical impedance spectroscopy. Finally, the charge/discharge cycling behavior of the conducting polypyrrole anode material was studied and the capacitance of the material determined.

#### **Chapter 5: Synthesis of single-crystal manganese oxide nanorods using low temperature solid state reaction and hydrothermal method**

Chapter 5 looks into the synthesis of single crystal manganese oxide nanorods for application in supercapacitors. Two methods were employed for the synthesis of manganese oxide electrode materials. In this chapter, synthesized products of both methods are studied and compared to understand the effect of changing parameters on the morphology and the activity of the synthesized material. The morphology and the surface study of the synthesized materials were accomplished by scanning electron microscopy, transmission electron microscopy, Brunauer-Emmett-Teller surface area analysis and X-ray diffraction. Electrochemical characterizations of the manganese oxide electrode material were studied with cyclic voltammetry and electrochemical-impedance

spectroscopy. The charge/discharge cycling behavior of the manganese oxide electrode material studied and their capacitance determined.

**Chapter 6: Comparison of single-crystal manganese oxide nanorods carbon composite electrode materials nanorods synthesized using low temperature solid state reaction and hydrothermal method**

Chapter 6 covers the synthesis of manganese oxide carbon composites. The influence of the carbon sources on the electrochemical performance of the carbon materials supported manganese oxide electrode material and their structure were intensively studied. The carbon sources investigated were carbon black, activated carbon and carbon nanotubes. The morphology and the surface study of the synthesized materials were accomplished by scanning electron microscopy, transmission electron microscopy, Brunauer-Emmett-Teller surface area analysis and X-ray diffraction. Electrochemical characterizations of the manganese oxide electrode material were studied via cyclic voltammetry and electrochemical-impedance spectroscopy. Finally, the charge/discharge cycling behavior of the manganese oxide carbon composite electrode materials were studied and their capacities determined.

**Chapter 7: Synthesis and characterization of poly crystalline ruthenium oxide and its carbon composites as electrode materials**

Chapter 7 looks into the synthesis of a poly crystalline ruthenium oxide for application in supercapacitors and the influence of the carbon source on the electrode material. The morphology and the surface study of the synthesized materials were accomplished by scanning electron microscopy, transmission electron microscopy, Brunauer-Emmett-Teller surface area analysis and X-ray diffraction. Electrochemical

characterizations of the ruthenium oxide electrode material were executed using cyclic voltammetry and electrochemical-impedance spectroscopy. The charge/discharge cycling behavior of the ruthenium oxide electrode material and its carbon composites studied and their capacitance determined

## CHAPTER 2

### LITERATURE REVIEW

#### 2.1 SUPERCAPACITORS

##### 2.1.1 Introduction

Electrochemical capacitors (ECs) which are a range of classifications, have attracted worldwide research interest because of their potential applications as energy storage devices in many fields [35,36]. Energy storage devices are classified according to energy and power density. Power density is related to the strength (wattage) of a given current and voltage combination, while energy density is related to the duration of time that wattage can be applied. Batteries and electrochemical capacitors are classified as energy storage devices. However, they differ in their energy storing mechanisms. Batteries store energy in the form of chemical reactants, whereas ECs store energy directly as charge. Consequently, they exhibit different energy and power outputs, charge and discharge cyclability and reaction scales [37].

Both the ECs and batteries require two electrodes, the cathode and the anode, an electrolyte and a conducting charge path in order to operate. ECs also have an additional component, the separator that electrically isolates the two electrodes. Today, commercially available rechargeable batteries include Lithium-ion, Nickel-metal-hydride and Nickel-cadmium devices [38]. To demonstrate the differences between batteries and ECs in terms of charge and discharge processes and components used in these devices, figures (2.1) and (2.2) of a Lithium-ion battery and an EC are given below.

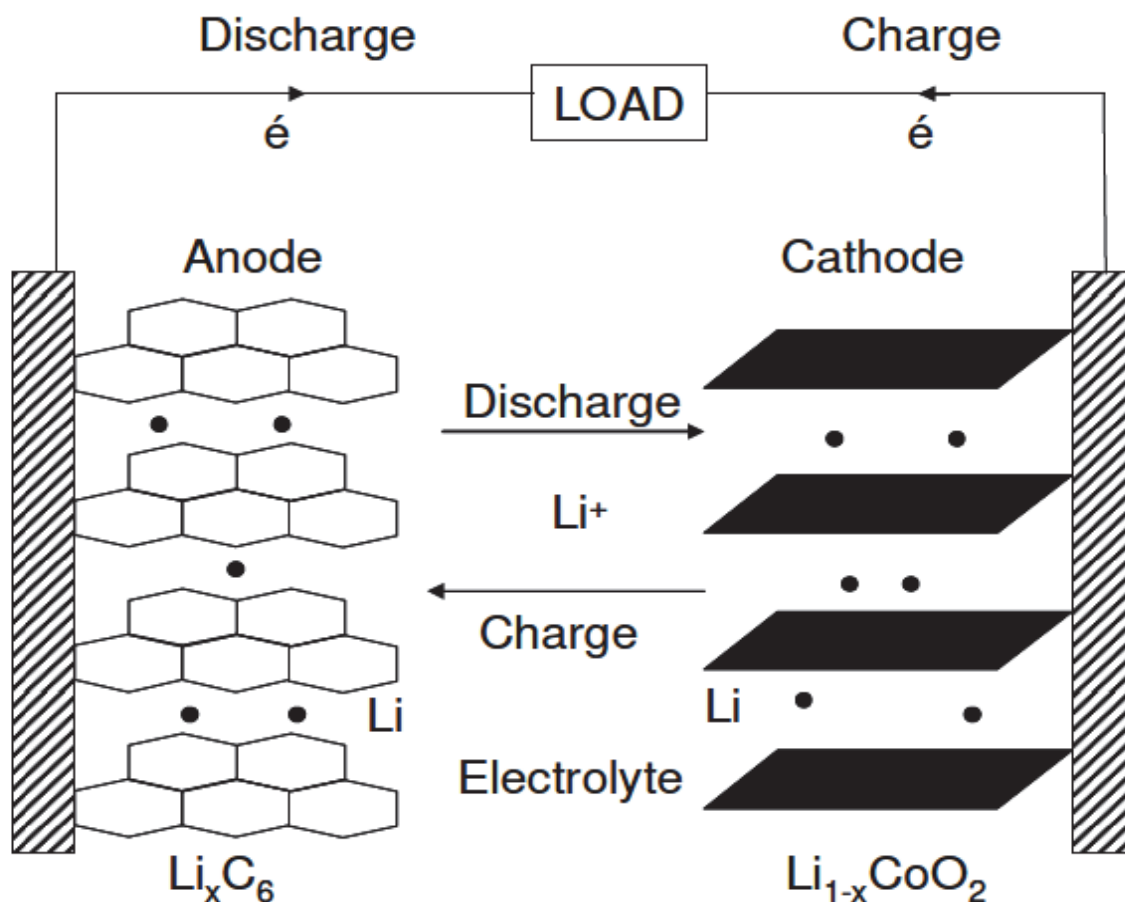


**Figure 2.1:** Schematic operating system of a Lithium-ion battery [39].

According to [39], lithium-ion batteries consist of a positive electrode (cathode), a negative electrode (anode) and an electrolyte containing dissociated salts separated by a micro-porous membrane (separator). The charge discharge process of lithium-ion batteries, involve a reversible insertion/extraction of lithium ions into/from a host matrix, the electrode material also called the lithium insertion compound. During the charging process, lithium ions extracted from the cathode host, go through the electrolyte and intercalate into the anode host. The electrons which are liberated from the cathode go through the external circuit and are accepted by the anode. The reverse process occurs during discharging.

Figure (2.2) below depicts a schematic operating system of an Electrochemical Double Layer Capacitor (EDLC).

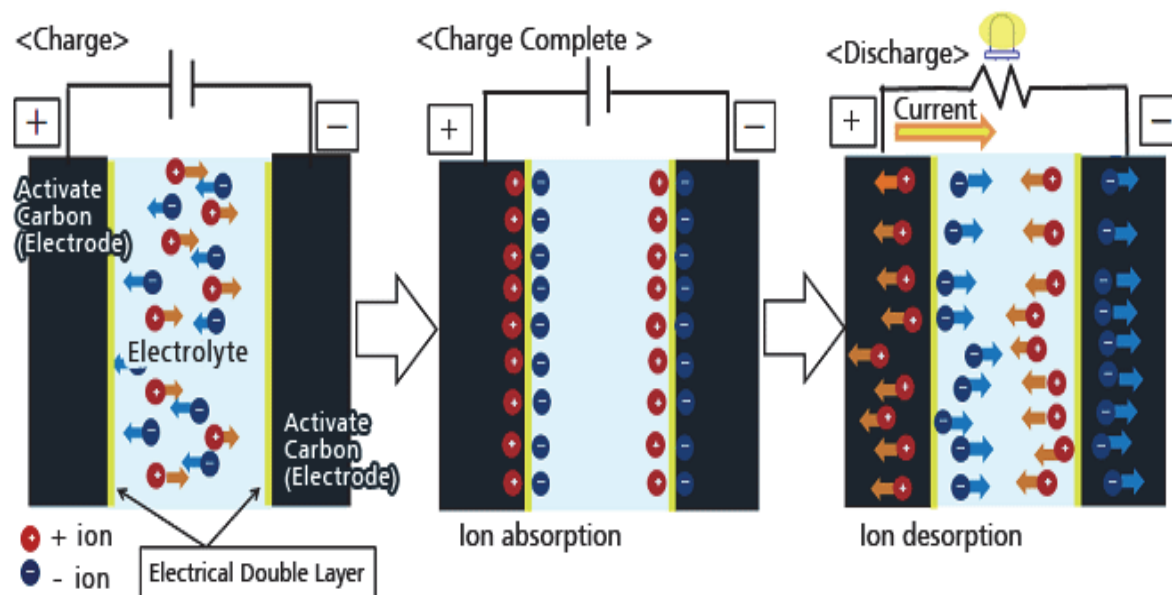


**Figure 2.2:** Schematic operating system of an electrochemical- double layer capacitor[41].

An Electrical Double-Layer Capacitor (EDLC) contains no conventional dielectric. Instead, an electrolyte (solid or liquid) is filled between two electrodes (see figure (2.2) above). In an EDLC, an electrical condition called “electrical double layer,” which is formed between the electrodes and electrolyte, works as the dielectric. In an EDLC, the solvated ions of the electrolyte are attracted to the oppositely charged electrodes when the capacitor is charged. It is noteworthy that on discharging the capacitor the reverse occurs.

The charge-storage mechanism of these capacitors is predominately due to double-layer (DL) charging effects. But in general, additional contributions of pseudocapacitance may also be part of the observed capacitance due to the functional groups present on the electrode surface [41].

Figure (2.3) below shows plots for an array of energy storage and energy conversion devices.

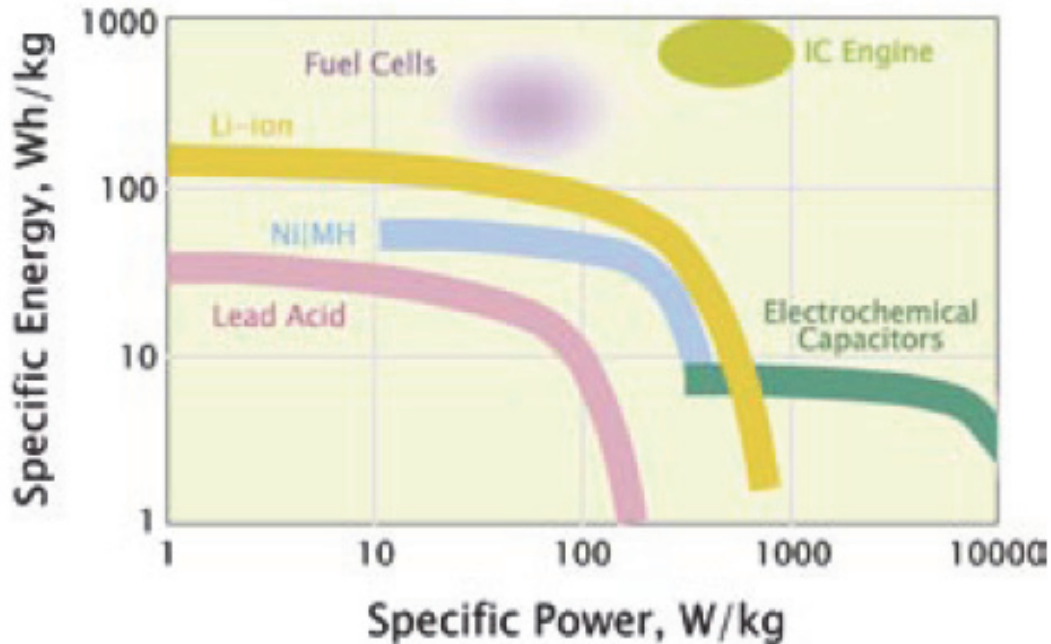


**Figure 2.3:** Ragone plots for an array of energy storage and energy conversion devices [42].

However, the higher power density, excellent reversibility (90–95% or higher), and long cycle life ( $>10^5$ ) [43] found in ECs has strongly attracted them most attention for consideration for use in a electric vehicles and electric hybrid vehicles [44, 45, 27] because of their ability to give the necessary power for the vehicle, during the vehicle's stopping or startup. The goal is to store that energy as efficiently as possible, so that it can be used in accelerating the vehicle at its next move [25].

### **2.1.2 Electrical energy storage mechanisms of supercapacitors**

Electrochemical Capacitors or supercapacitors are often classified according to the material used as the dielectric. Depending on the charge-storage mechanisms, capacitors can be classified into two types: EDLC and Pseudocapacitor, the descriptions of which are given in the following section.

#### ***2.1.2.1 Electrochemical double layer supercapacitor***

The first patent describing the concept of an electrochemical capacitor was filed in 1957 by Becker [46], who used carbon with a high specific surface area coated on a metallic current collector in a sulphuric acid solution. In 1971, NEC (Japan) developed aqueous-electrolyte capacitors under the energy company SOHIO's license for power saving units in electronics, and this application can be considered as the starting point for electrochemical capacitor use in commercial devices[14]. New applications in mobile electronics, transportation (cars, trucks, trams, trains and buses), renewable energy production and aerospace systems [47] encouraged further research.

The electrode material which is used for the construction of these supercapacitors is mainly carbon based materials [48]. Various carbon based materials used in EDLCs are activated carbons (ACs), carbon aerogels (CAGs), graphites, carbon nanotubes (CNTs), carbon nanofibers (CNFs) and nano-sized carbon [43].

EDLCs store the electric charge directly across the Double Layer (DL) of the electrode [49] and because there is no charge transfer across the interface, this is a true capacitance effect. The schematic presentation of the electrical DL is shown in figure (2.4) below.



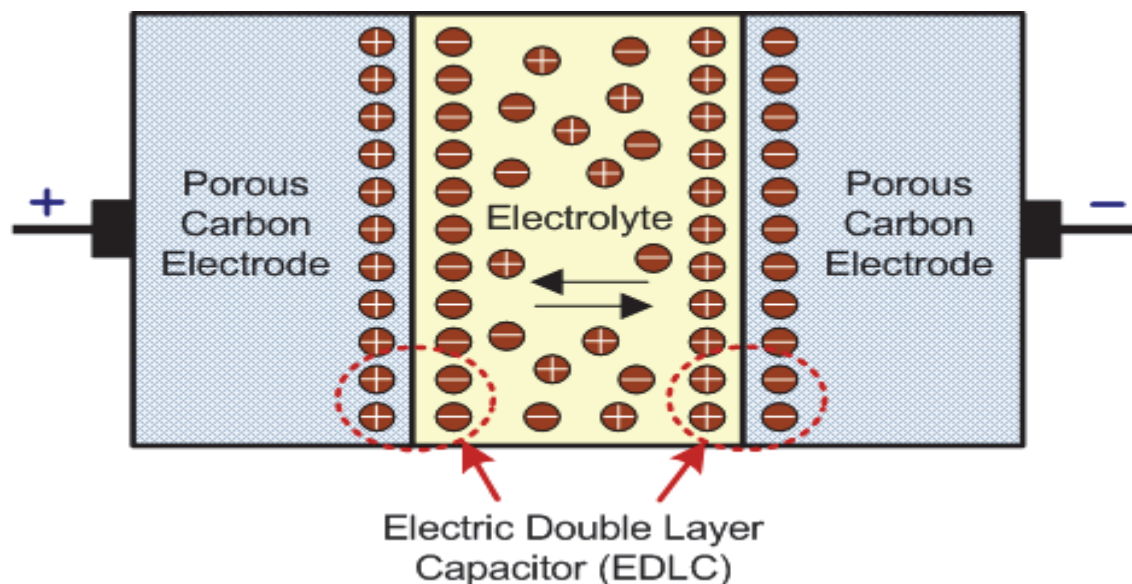


**Figure 2.4:** Schematic of an electrical double layer. [40]

The mechanism of surface charge generation can be enumerated as: surface dissociation, ion adsorption from solution, and crystal lattice defect. The capacitance arises from an electrochemical DL directly analogous to a parallel plate capacitor. As an excess or deficiency of charge builds up on the electrode surface, ions of the opposite charge build up in the electrolyte near the electrode/ electrolyte interface in order to provide electroneutrality. The thickness of the DL depends on the concentration of the electrolyte and the size of ions, which is in the order of 5–10Å for concentrated electrolytes. The DL capacitance is about 10–20 mF/cm<sup>2</sup> for a smooth electrode in concentrated electrolyte solution and can be estimated according to the following equation:

$$C = \epsilon_o \epsilon_r \left( \frac{A}{d} \right)$$

2.1

The value of relative dielectric constant  $\epsilon_r$  is assumed as 10 for the water in the DL [46], the  $d$  is the thickness of the DL, and  $A$  is the surface area. The corresponding electric field in the electrochemical DL is as high as  $10^6$  V/cm.

In addition, this surface storage mechanism allows very fast energy uptake and delivery, and better power performance. The absence of Faradaic reactions also eliminates the swelling in the active material that batteries show during charge and discharge cycles. Finally, the solvent of the electrolyte is not involved in the charge storage mechanism, unlike in Li-ion batteries where it contributes to the solid–electrolyte interphase when graphite anodes or high-potential cathodes are used. This does not limit the choice of solvents, and electrolytes with high power performances at low temperatures (down to  $-40$  °C) that can be designed for EDLCs.

However, as a consequence of the electrostatic surface charging mechanism, these devices (EDLCs) suffer from a limited energy density. This explains why today's EDLC research is largely focused on increasing their energy performance and widening the temperature limits into the range where batteries cannot operate [46].

### ***2.1.2.2 Pseudocapacitor***

Fast, reversible redox reactions at the surface of active materials used by other ECs define what is called the pseudo-capacitive behavior. Metal oxides, such as  $\text{RuO}_2$ ,  $\text{Fe}_3\text{O}_4$  or  $\text{MnO}_2$  [50, 51], as well as electronically conducting polymers [52], have been extensively studied in the past decades for this purpose. When metal oxides, metal oxide and carbon composite, conducting polymer and carbon composite are used as electrodes for the construction of EDLCs, the charge storage mechanism includes both double layer capacitance and pseudocapacitance which result in higher capacitance output and these

EDLCs are termed as supercapacitors (SCs) [148]. The specific pseudo-capacitance exceeds that of carbon materials using double layer charge storage, justifying interest in these systems. Figure (2.5), below shows the schematic presentation of a pseudocapacitor. (Ruthenium oxide ( $RuO_2$ ) and Manganese Oxide ( $MnO_2$ ) given in the diagram are examples of electrode materials which can be on either electrodes when both metal oxides are used in the supercapacitor.)

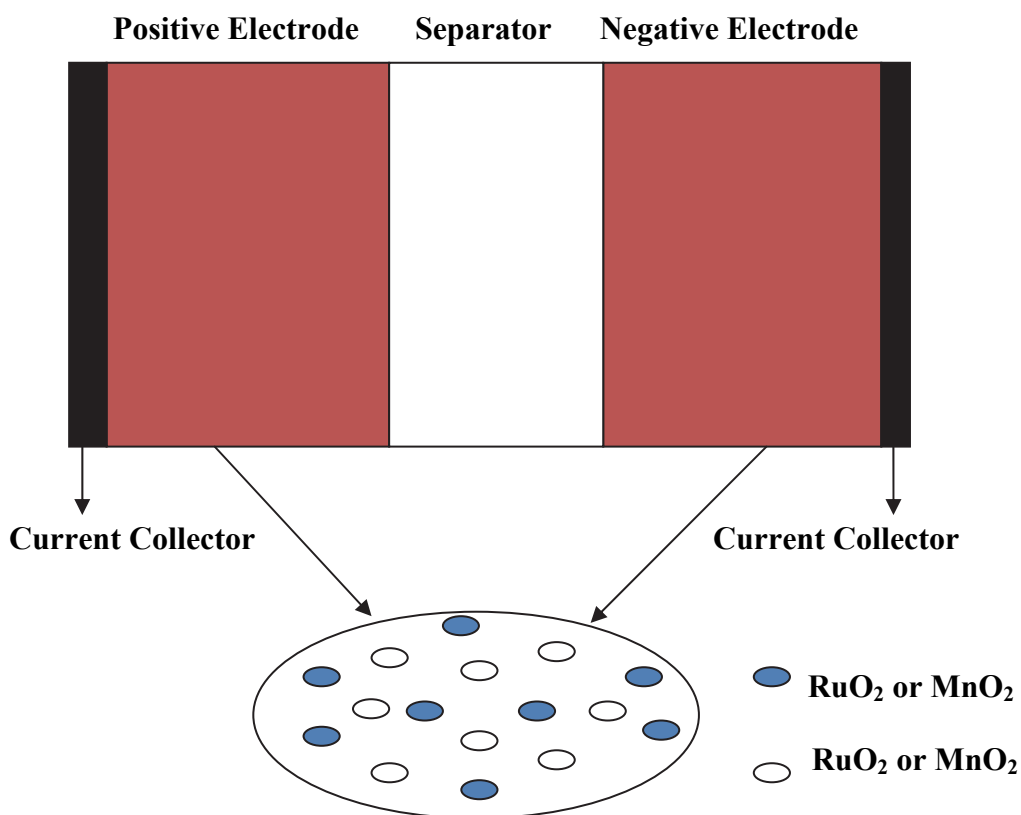


**Figure 2.5:** Schematic presentation of a pseudocapacitor [60].

Pseudocapacitance arises on electrodes when the application of a potential induces Faradaic current from reactions such as electrosorption or from the oxidation–reduction of electroactive materials (e.g.,  $RuO_2$ ,  $IrO_2$ , and  $Co_3O_4$ ) [54–57]. Electrosorption occurs when the chemisorption of an electron-donating anion such as  $Cl^-$ ,  $B^-$ ,  $I^-$ , or  $CNS^-$  takes

place in a process such as:  $M + A \leftrightarrow MA^{(1-\delta)-} + \delta e^-$ . Such an electrosorption reaction of  $A^-$  anions at the surface of an electrode, and the quantity  $\delta e^-$  are related to the so-called electrosorption valence [57].

Secondly, by an exchange of charge across the DL, rather than a static separation of charge across a finite distance, resulting in oxidation–reduction reactions (indicated as:  $O_{ad} + ne^- \rightarrow R_{ed}$ ). The charge,  $ne^-$ , exchanged in this reaction, and the energy storage is indirect and analogous to that of a battery. It is well known that the two different storage mechanisms of EDLC and pseudocapacitance have existed for the super-capacitor system. Generally, one of the storage mechanisms occupies the leading position; the other is relatively weak. The comparison of EDLC and pseudocapacitance is presented in table (2.1).

**Table 2.1:** Comparison of EDCL and pseudocapacitance.

<b>EDLC</b>	<b>Pseudocapacitance</b>
1. Non-Faradaic	Involves Faradaic process(es)
2. 20–50 $\mu\text{F}/\text{cm}^2$	2000–50 $\mu\text{F}/\text{cm}^2$ for single-state process; 200–500 $\mu\text{F}/\text{cm}^2$ for multi-state, overlapping processes
3. C fairly constant with potential, except through the potential of zero charge	C fairly constant with potential for $\text{RuO}_2$ ; for single-state process, exhibits marked maximum
4. Highly reversible charging/discharging	Can exhibit several maxima for overlapping, multi-state processes, as for H at Pt; Quite reversible but has intrinsic electrode-kinetic rate limitation determined by $R_f$
5. Has restricted voltage range (contrast non-electrochemical electrostatic capacitor)	Has restricted voltage range
6. Exhibits mirror-image voltammograms	6. Exhibits mirror-image voltammograms

### 2.1.2.3 Hybrid electrochemical capacitor

Hybrid electrochemical capacitors (HECs) have an asymmetrical configuration composed of a DL carbon material and a pseudocapacitance material which has attracted significant attention [11, 58]. Research has focused on three types of hybrid capacitors, distinguished by their electrode configuration: composite, asymmetric and battery type, respectively. A schematic presentation of a battery type hybrid capacitor is given in figure (2.6) (*AC (Activated carbon) a capacitive carbon electrode and a lithium-insertion electrodes  $\text{LiMnO}_2$  (Lithium manganese dioxide)*).

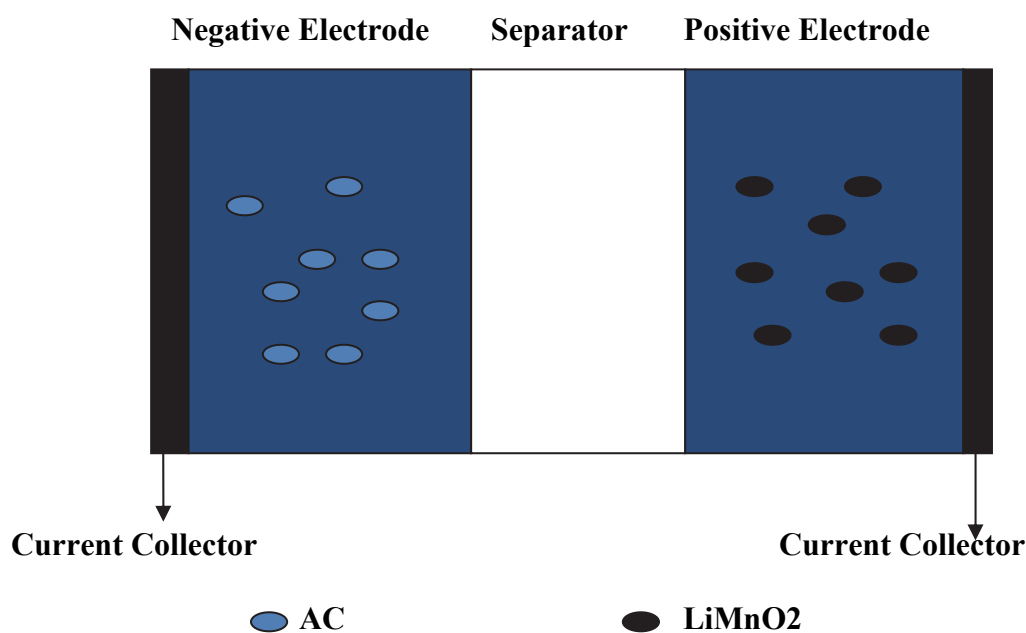


**Figure 2.6:** Schematic presentation of a hybrid capacitor [61].

An appropriate electrode combination can even increase the cell voltage, further contributing to improvement in energy and power densities [59]. Most of the hybrid electrochemical capacitors developed to date have used pseudocapacitive materials as the cathode. The charge accumulated in pseudocapacitance electrodes through Faradaic electrochemical process not only increase the specific capacitance of the capacitor, but

also extends the working voltage. In an advanced HEC, the potential range at the cathode is extended to the whole potential window of activated carbon (AC), specifically from 1.5 to 4.5 V vs.  $\text{Li/Li}^+$ , which is wider potential range than the conventional EC, where the potential ranges from 0.8 to 2.7 V vs.  $\text{Li/Li}^+$ . The energy density of an EC is equal to  $CV^2/2$ , where  $C$  is capacitance and  $V$  is the working voltage window. Therefore, the energy density of these devices can be significantly higher than for EDLCs. HECs can also be assembled using two non similar mixed metal oxides or doped conducting polymer materials [10].

## **2.2 ELECTRODE MATERIALS FOR SUPERCAPACITORS**

### **2.2.1 Electrochemical double layer supercapacitor**

The electrode material which is used for the construction of these supercapacitors is mainly carbon based materials [48]. The type of carbon determines the current and voltage characteristics and also potential side reactions. Various carbons have been specially synthesized in laboratories by the pyrolysis of various precursors.

Carbon has four crystalline (ordered) allotropes: diamond ( $\text{sp}^3$  bonding), graphite ( $\text{sp}^2$ ), carbyne ( $\text{sp}^1$ ) and fullerenes (distorted  $\text{sp}^2$ ). While two carbon allotropes are naturally found on earth as minerals, namely, natural graphite and diamond, the other forms of carbon are synthetic. Carbon is considered unusual in the number of its allotropic structures and the diversity of structural forms, as well as in its broad range of physical properties [62, 63].

Due to the wide range of carbon materials, and in order to avoid confusion, the term carbon is typically used to describe the element rather than its form. To describe a carbon-based material, it is best coupled with a qualifier such as carbon black, activated

carbon, vitreous carbon and others [64].

The majority of commercial carbons used today can be conveniently described as engineered carbons derived from carbon rich organic precursors by heat treatment in inert atmospheres (a process referred to as carbonization). According to McEnaney *et al.* [62], these are manufactured carbons that have an amorphous structure with a more or less disordered microstructure based on that of graphite. Amorphous carbons can be considered as sections of hexagonal carbon layers with very little order parallel to the layers. The ultimate properties of these carbons are dependent on a number of critical factors, e.g., the carbon precursor, its dominant aggregation state during carbonization (i.e., gas, liquid or solid), processing conditions, and the structural and textural features of the products [65].

Between the extremes of amorphous carbon and graphite, a wide variety of carbon materials can be prepared and their properties tailored, to some extent, for specific applications. The attraction of carbon as a supercapacitor electrode material arises from a unique combination of chemical and physical properties, namely:

- high conductivity,
- high surface-area range ( $\sim 1$  to  $>2000\text{m}^2\text{ g}^{-1}$ ),
- good corrosion resistance,
- high temperature stability,
- controlled pore structure,
- processability and compatibility in composite materials, and
- relatively low cost.

In general terms, the first two of these properties are critical to the construction of supercapacitor electrodes. The properties of carbon allow both conductivity and surface area to be manipulated and optimized and such activities continue to be the subject of a considerable amount of research. It is useful to consider in more detail other aspects of carbon, e.g., its structural diversity and chemical behavior, so as to establish a better understanding of the role of carbon materials in supercapacitors.

### ***2.2.1.1 Carbon Black***



**Figure 2.7:** Image for Carbon black [66].

Carbon black (figure (2.7)) is widely used as support materials for electrode materials in supercapacitors and fuel cells. They are a group of materials characterized by having near spherical carbon particles of colloidal size, which are produced by the partial combustion or thermal decomposition of hydrocarbons (usually gases, oils, or distillates) in the gas phase [67,68].



During production, the colloidal carbon particles coalesce into chemically fused aggregates and agglomerates with varying morphologies. Their fundamental properties vary with feedstock and manufacturing conditions, and they are usually classified according to their method of preparation or intended application. The key properties of carbon blacks are considered to be fineness (primary particle size), structure (aggregate size/shape), porosity, and surface chemistry.

Carbon blacks are routinely used as conductive fillers in many types of battery and supercapacitor electrodes [68-71]. Highly conductive carbon blacks are characterized by a high structure (i.e., aggregates with a highly branched, open structure), high porosity, small particle size, and a chemically clean (oxygen free) surface. The conductivity of carbon blacks is typically in the range  $10^{-1}$  to  $10^2$  ( $\Omega\text{cm}^{-1}$ ) [65] and is influenced by the relative ability of electrons to jump the gap between closely-spaced aggregates (electron tunneling) and by graphitic conduction via touching aggregates.

The loading of carbon black is of critical importance because, at low loadings, the average inter-aggregate gap is too large for the carbon black to influence the conductivity of the composite. As the loading is increased, a percolation threshold (i.e. critical loading) is reached whereby the conductivity increases rapidly up to a limiting value. High porosity or finer carbon blacks have more particles per unit weight and, therefore, reduce the average gap width between aggregates due to their greater number [65, 67]. The surface-area (BET) of carbon blacks covers a wide range i.e., from  $<10$  to greater than  $1500\text{m}^2\text{g}^{-1}$  [72, 73] and their porosity varies from mild surface pitting to the actual hollowing out of particles. Additional porosity is also created by the intra- and inter-aggregate voids that are formed between the small, fused, primary carbon particles. The surface area of carbon

blacks is generally considered to be more accessible than other forms of high surface-area carbon [73].

Supercapacitor electrodes have been produced from high surface-area carbon blacks (containing a binder) with specific capacitances of up to  $250 \text{ F g}^{-1}$ ; corresponding to double-layer capacitances in the range of  $10\text{--}16 \mu\text{F cm}^{-2}$  [73,75]. On the other hand, the low compacted density of high surface-area blacks and the high level of binder are often required to produce mechanically stable electrodes, typically results in electrodes with low electrical conductivities and volumetric capacitance.

### 2.2.1.2 Graphitic carbon

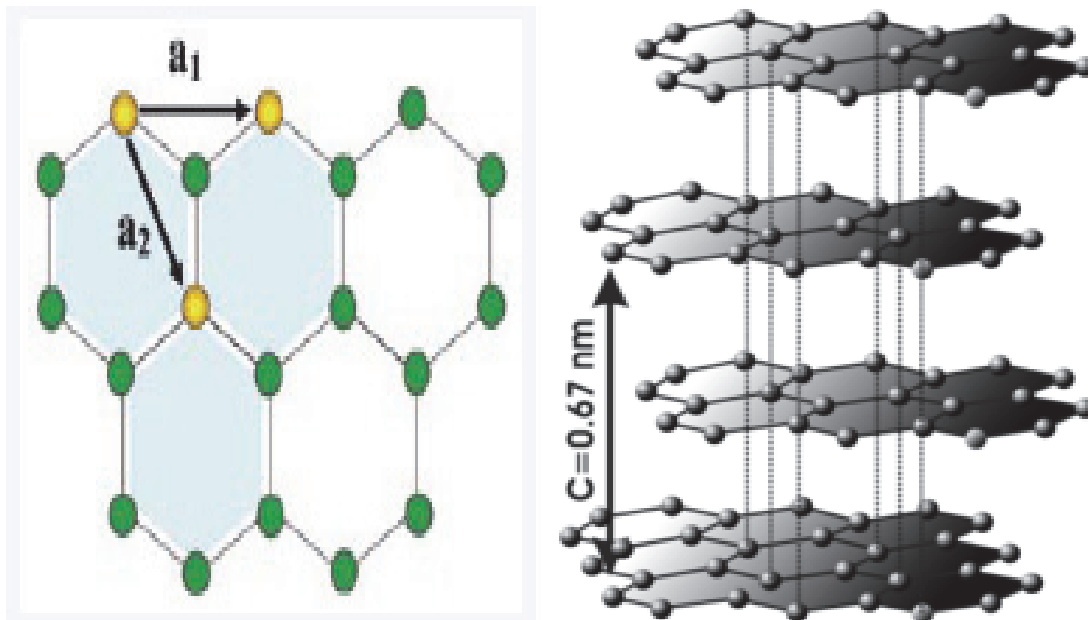


**Figure 2.8:** The stacking of graphene sheets results in a layered structure [75].

All varieties of substances consist of the element carbon, in the allotropic form of *graphite* irrespective of the presence of structural defects. The use of the term graphitic carbon is justified if three-dimensional hexagonal crystalline long-range order can be

detected in the material by diffraction methods, independent of the volume fraction and the homogeneity of distribution of such crystalline domains. Otherwise, the term *non-graphitic carbon* should be used [75].

Graphite consists of sheets of carbon atoms. In these sheets, the carbon atoms are arranged in a hexagonal, or honey comb, pattern (see figure 2.7, left.) Each carbon atom is strongly bonded to its three neighboring carbon atoms. These hexagonal sheets then appear to stack upon each other to create the overall structure of graphite (see figure 2.7, right). The bonding between the sheets is much weaker than the bonding between the atoms in the planes. The actual structure and surface of practical carbonaceous materials deviate from the ideal structure and surface. Even highly ordered graphites commonly have a high number of structural defects, such as dislocations, steps, point defects or cracks [76]. Graphitic carbon materials are the current materials of choice for the negative electrode in commercial lithium-ion batteries.

Among these graphitic carbons, highly graphitized materials are particularly attractive due to their high, reversible specific charge of up to 372 mAh/g, good cycling stability, and high electronic conductivity. Usually, graphite is not a capacitor material because of its small ability of adsorption, however, it can absorb anions in non-aqueous solutions if activated carbon is used as the counter electrode. The formation of an efficient passivation film of the graphite particle surface during the first electrochemical reduction is essential for the proper functioning of these electrode materials. The storage capacity of graphite is further increased by means of adjusting the comparative weight ratio of the activated carbon electrode. Recently, Yoshio *et al.* reported that graphite can be used as a suitable positive electrode material for high-energy electrochemical capacitors [10,15,45].

### 2.2.1.3 Activated carbon

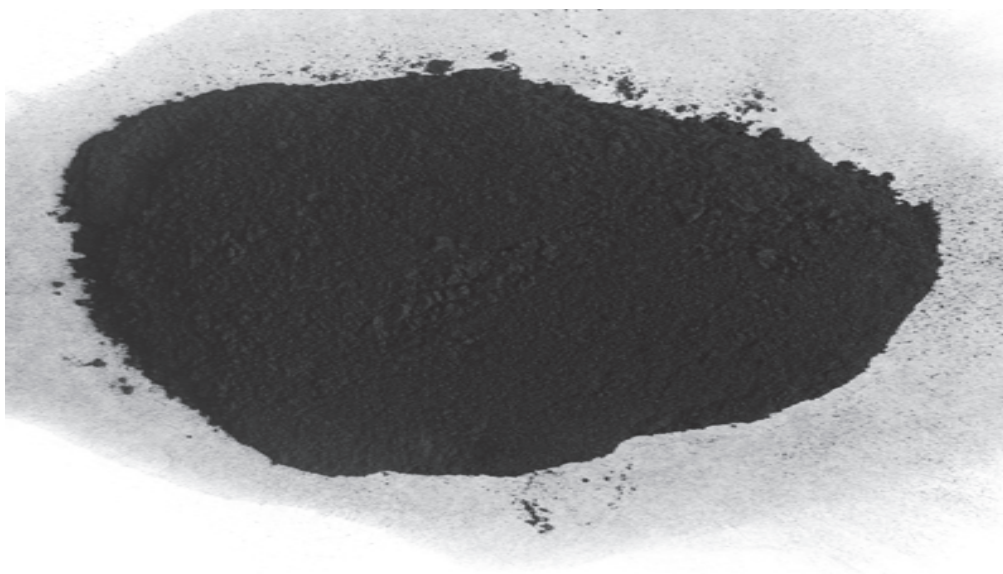


**Figure 2.9:** Image for activated carbon.

One of the great attractions of using carbon as an electrode material is that it can be readily converted into a form that has very high specific surface-area. Generally speaking, the process employed to increase surface-area (and porosity) from a carbonized organic precursor (char) is referred to as activation and the resulting broad group of materials is referred to as activated carbons (figure (2.9)).

Chars usually have a relatively low porosity and their structure consists of elementary crystallites with a large number of interstices between them. The interstices tend to be filled with disorganized carbon residues (tars) that block the pore entrances. Activation opens these pores and can also create additional porosity.

Varying the carbon precursor and activation conditions (particularly temperature, time and gaseous environment) allows some control over the resulting porosity, pore-size distribution, and the nature of the internal surfaces. Processes for the activation of carbons

can be placed into two general categories: thermal activation and chemical activation [77, 78].

#### *2.2.1.3.1 Thermal activation*

Thermal activation, sometimes referred to as physical activation, entails the modification of a carbon char by controlled gasification, and is usually carried out at temperatures between 700 and 1100°C in the presence of suitable oxidizing gases such as steam, carbon dioxide, air, or mixtures of these gases. During gasification, the oxidizing atmosphere greatly increases the pore volume and surface-area of the material through a controlled carbon burn-off and the elimination of volatile pyrolysis products. The level of burn-off is, perhaps, the most important factor governing the quality of the activated carbon and is controlled by the temperature and duration of activation. A high degree of activation is achieved by increased burn-off, but the additional activity is accompanied by a decrease in carbon strength, a lower density, reduced yield and pore widening.

#### *2.2.1.3.2 Chemical activation*

Chemical activation is usually carried out at slightly lower temperatures (~400–700°C) and involves the dehydrating action of certain agents such as phosphoric acid, zinc chloride and potassium hydroxide. Post-activation washing of the carbon is usually required to remove residual reactants as well as any inorganic residue (sometimes referred to as ash) that originates from the carbon precursor or is introduced during activation. Exceptionally high surface-area materials (>2500m<sup>2</sup>/g) have been prepared with potassium hydroxide activation techniques [79].

#### **2.2.1.4 Carbon aerogels**

Another form of carbon is carbon aerogels which are highly porous materials prepared by the pyrolysis of organic aerogels. They are usually synthesized by the polycondensation of resorcinol and formaldehyde, via a sol-gel process, and subsequent pyrolysis [80, 81]. By varying the conditions of the sol-gel process, the macroscopic properties of aerogels (density, pore size and form (shape/size)) can be controlled. The aerogel solid matrix is composed of interconnected colloidal like carbon particles or polymeric chains. After pyrolysis, the resulting carbon aerogels are more electrically conductive than most activated carbons [82, 83] and are preferred as they tend to have the highest porosity, high surface area ( $400\text{--}1000\text{m}^2\text{ g}^{-1}$ ), uniform pore sizes (largely between 2 and 50 nm) and high density. They can also be produced as monoliths, composites, thin films, powders or micro-spheres.

Electrochemical studies on carbon aerogels have reported that capacitance is more strongly correlated with mesopore surface-area than with the total BET surface-area [84, 85]. These studies showed that carbon aerogels with pore diameters in the range  $\sim 3\text{--}13$  nm exhibited stable capacitive behavior and the highest capacitances.

#### **2.2.1.5 Carbon nanotubes**

Krätshmer-Huffman reported on a Nature paper about soot they produced using an arc-evaporation technique [308]. This report triggered a fascination from Iijima to embark on a detailed TEM study of the soot which then led to the discovery of carbon nanotubes. Ten years earlier, he had studied soot formed in an arc-evaporation apparatus (Figure 2.10), similar to the one used by Krätshmer and Huffman.

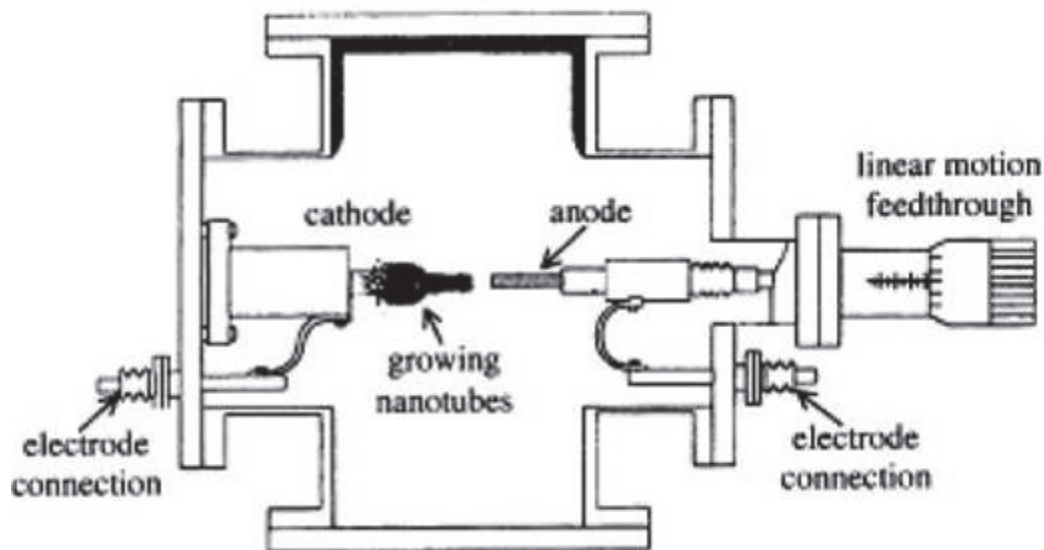


**Figure 2.10:** Experimental setup of arc discharge method for carbon nanotube production [39].

Iijima found a variety of novel carbon architectures including tightly curved, closed nanoparticles and extended tube-like structures [86, 87]. Initial high resolution TEM studies were disappointing because the soot appeared to be amorphous. Eventually, he gave up sifting through the wall soot arc evaporation vessel and turned his attention to the hard cylindrical deposit which formed on the graphite cathode after arc-evaporation.

Here, Iijima's efforts were finally rewarded because instead of an amorphous mass, the cathodic soot contained a whole range of novel graphitic structures; the most striking were long hollow fibres, finer and more perfect than any previously seen. His beautiful images of carbon nanotubes were first shown at a meeting in Richmond, Virginia in October 1991 and published in *Nature* a month later [87]. This discovery prompted the fullerene scientist all over the world to look again at the used graphitic cathodes, previously discarded as junk. These types of carbon nanotubes are multi-walled carbon nanotubes (MWNT), see figure (2.11).

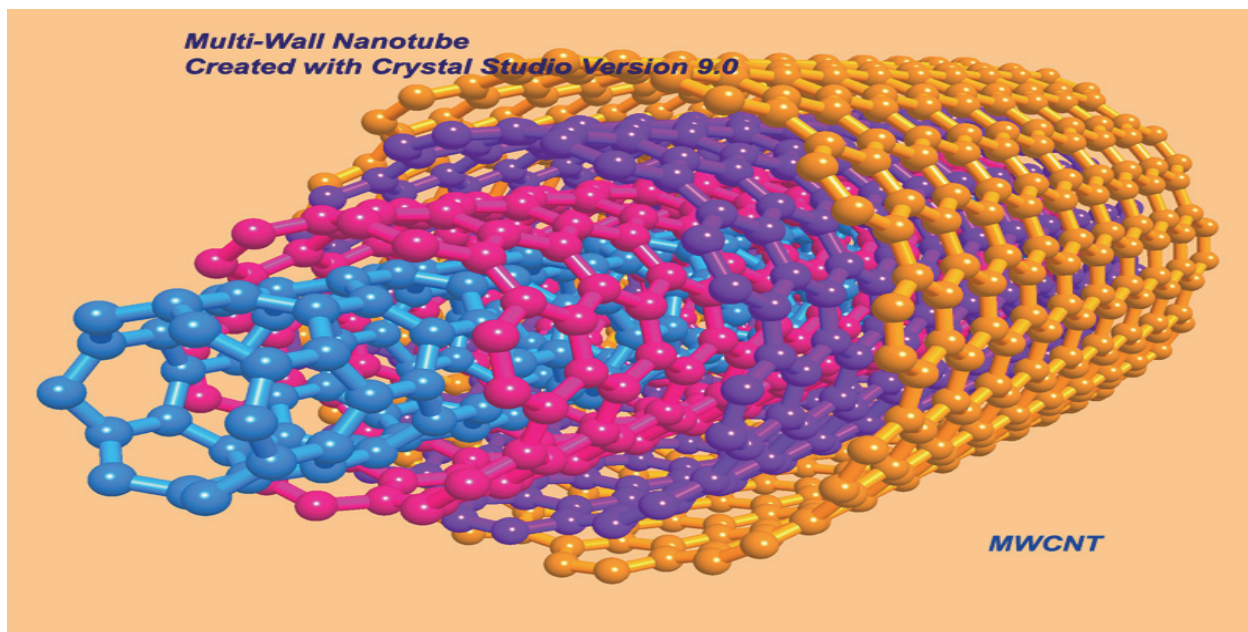


**Figure 2.11:** Computer generated image of a multi-walled carbon nanotube [98].

In 1993, nearly at the same time, Bethune et al. [89] and Iijima et al. [90] reported that single-walled nanotubes (SWNT) had been produced using Co metal catalysts in an arc discharge system, see figure (2.12).



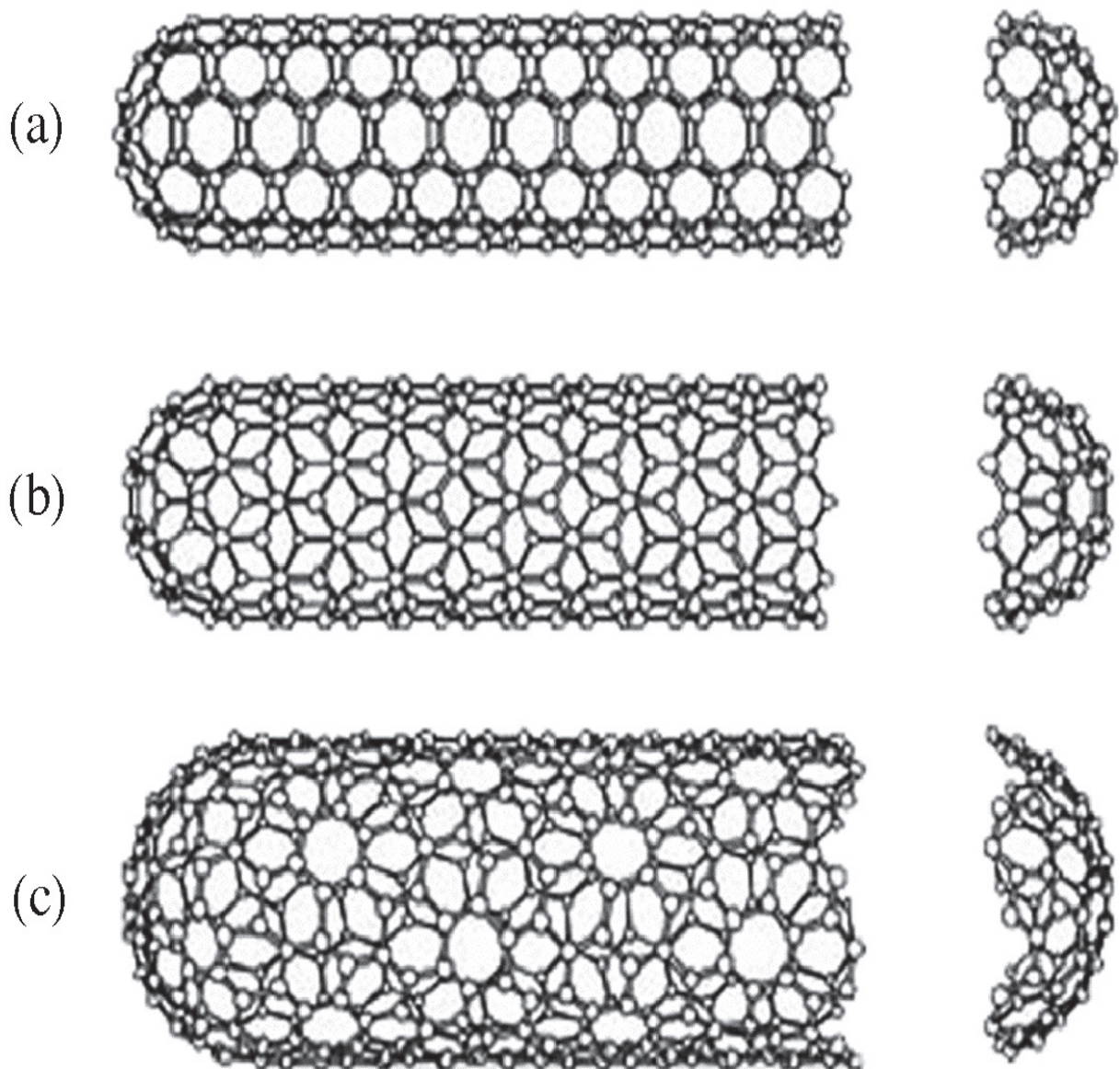


**Figure 2.12:** Structure of single-walled carbon nanotubes (SWNTs) with (a) armchair, (b) zigzag, and (c) chiral chirality [99].

There is considerable interest in the application of carbon nanotubes (CNTs) as electrode materials for supercapacitors and other energy-storage devices [90–93] due to:

- Unique combination of low electrical resistivity and high porous structure which is attributed to the nanoscale tubular morphology of these materials. The

mesoporous surface-area of CNTs is predominantly associated with the exterior of the tubes; the voids arise from the entangled nanotubes and, in some cases, from the presence of an accessible central canal.

- High capacitance of approximately  $130\text{Fg}^{-1}$  can be achieved for both Single-Walled (SWNT) and Multi-Walled Nanotubes (MWNT), which is highly dependent on their morphology and purity [94].
- High surface area which ranges from  $\sim 120$  to  $400\text{m}^2\text{g}^{-1}$  [95, 96]. Niu *et al.* [95] produced catalytically-grown MWNTs with a diameter of 8 nm and a BET surface-area of  $\sim 250\text{m}^2\text{g}^{-1}$  and after treatment of the product with nitric acid, the surface area was increased to  $430\text{m}^2\text{g}^{-1}$ .
- High power density of  $>8\text{kWkg}^{-1}$  has been reported [97].

### 2.2.2 Psuedocapacitor

The electrode material which is used for the construction of these supercapacitors is mainly metal oxides and conducting polymers [48].

#### 2.2.2.1 Metal oxides

Transition metal oxides represent a type of attractive material with high specific capacitance, wide operational potential window and stability through charge-discharge cycling. Most importantly, transition metals possess several oxidation states and are reasonably conductive. In this review, we will pay attention to two metal oxides that have gained much interest as supercapacitor electrode materials.

##### 2.2.2.1.1. Manganese oxide and

##### 2.2.2.1.2. Ruthenium oxide

### 2.2.2.1.1. Manganese oxide

Manganese oxides ( $\text{MnO}_2$ ) are a class of environmentally friendly materials compared with other metal oxides, only harmful by excessive inhalation or imbibing [168]. Throughout the years,  $\text{MnO}_2$  in various forms has been widely studied as the electrode materials in various energy storage systems, such as alkaline batteries, lithium ion batteries and supercapacitors.  $\text{MnO}_2$ , an important substance used widely as cathodic materials, catalysts and magnetic materials [199], is a non stoichiometric compound and has many crystalline forms such as  $\alpha$ -,  $\beta$ -,  $\gamma$ - and  $\delta$ - type [200]. Various 1D  $\text{MnO}_2$  nanomaterials, such as  $\alpha$ - $\text{MnO}_2$  nanorods/nanowires,  $\beta$ - $\text{MnO}_2$  nanorods/nanotubes,  $\gamma$ - $\text{MnO}_2$  nanowires/nanotubes and  $\delta$ - $\text{MnO}_2$  nanofibres have been successfully prepared by oxidation of  $\text{Mn}^{2+}$  or reduction of  $\text{KMnO}_4$  [201]. Manganese oxide can be present in various oxidation states and phases. The most often studied phases are  $\text{MnO}_2$  with an oxidation state of  $4^+$ ,  $\text{Mn}_2\text{O}_3$  with an oxidation state of  $3^+$ , or a mixture of the two phases [201].

Recently, increasing interest has been focused on the fabrication of 1D  $\text{MnO}_2$  nanostructures and single-crystal  $\text{MnO}_2$  nanowires of  $\alpha$ ,  $\beta$  and  $\gamma$ -type have also been conveniently prepared by simple hydrothermal treatment of commercial  $\gamma$ - $\text{MnO}_2$  particles in water or ammonia solution [202]. This interest arises from the state of the art of the engineering of  $\text{MnO}_2$  into composite or specific miniature nanostructure with improved electrochemical performance. Furthermore, 1D  $\text{MnO}_2$  nanomaterials show improved electrochemical properties than their bulk counterparts, which can be adopted as promising electrode materials in Zn- $\text{MnO}_2$  batteries, Li- $\text{MnO}_2$  cells and electrochemical capacitors, etc [199,203].

These mesoporous materials exhibit a high surface area, narrow pore size distribution, large pore volume, and high thermal stability, which allow them to be applied as catalysts, molecular sieves, host materials, and battery materials. The high-surface area and large-sized one-dimensional  $\text{MnO}_2$  nanostructures is one of the most promising materials as active electrode material in pseudocapacitors, as its pseudo-capacitance arises from the III/IV oxidation state change at the surface of  $\text{MnO}_2$  nanostructures. The oxidation–reduction reaction can be accelerated on the high-surface and large-sized nanostructures [205].

#### 2.2.2.1.2. Ruthenium oxide

Among the many transition metal oxides, such as ruthenium oxide, nickel oxide and iridium oxide, that have been used as an electrode materials for supercapacitors, the most success has been achieved using ruthenium oxide due to its advantages of a wide potential window of highly reversible redox reactions [182], remarkably high specific capacitance [206, 207], and a very long cycle life and metallic type conductivity. Galizzioli *et al.* [208] first recognized that the current response of thermally prepared anhydrous ruthenium oxide film was similar to that of an ideal capacitor. In recent years, [209] the use of hydrous ruthenium oxide as an electrode material was investigated.

Ruthenium oxide in both crystalline and amorphous forms is of crucial importance for theoretical as well as practical purposes, due to the unique combination of characteristics, such as metallic conductivity, high chemical and thermal stability, catalytic activities, electrochemical redox properties, and field emitting behavior. Due to such properties,  $\text{RuO}_2$  finds great promise in various applications, for example, in electronic

applications, integrated circuit development, thick or thin film resistors, ferroelectric films and a buffer layer for the high-temperature superconducting thin films.

In catalysis,  $\text{RuO}_2$  is the active component in dimensionally stable anodes for chlorine generation in the chlor-alkali industry, oxygen or hydrogen evolution in water electrolysis,  $\text{CO}_2$  reduction in photocatalysis, and CO oxidation in sensors [210]. The well-known application of  $\text{RuO}_2$  is as an electrode in energy storage electrochemical supercapacitors [53].

#### ***2.2.2.2 Conducting Polymers***

Among the synthetic polymers, conducting polymers have attracted considerable attention as important polymer materials since the initial discovery of polyacetylene in the late 1970s [101–103].

Inherently Conducting Polymers (ICPs) have the conjugated double-bonded backbone that provides the electronic conductivity after doping with suitable dopants. In general, ICPs are semiconductors with versatile properties and various applications. These peculiar characteristics have an impact on the discovery of vast conducting polymers by means of different synthetic methods. Numerous research papers have been published concerning a variety of the synthesis, physical and chemical properties and application of conducting polymers [104–107] and are shown in figure (2.13).

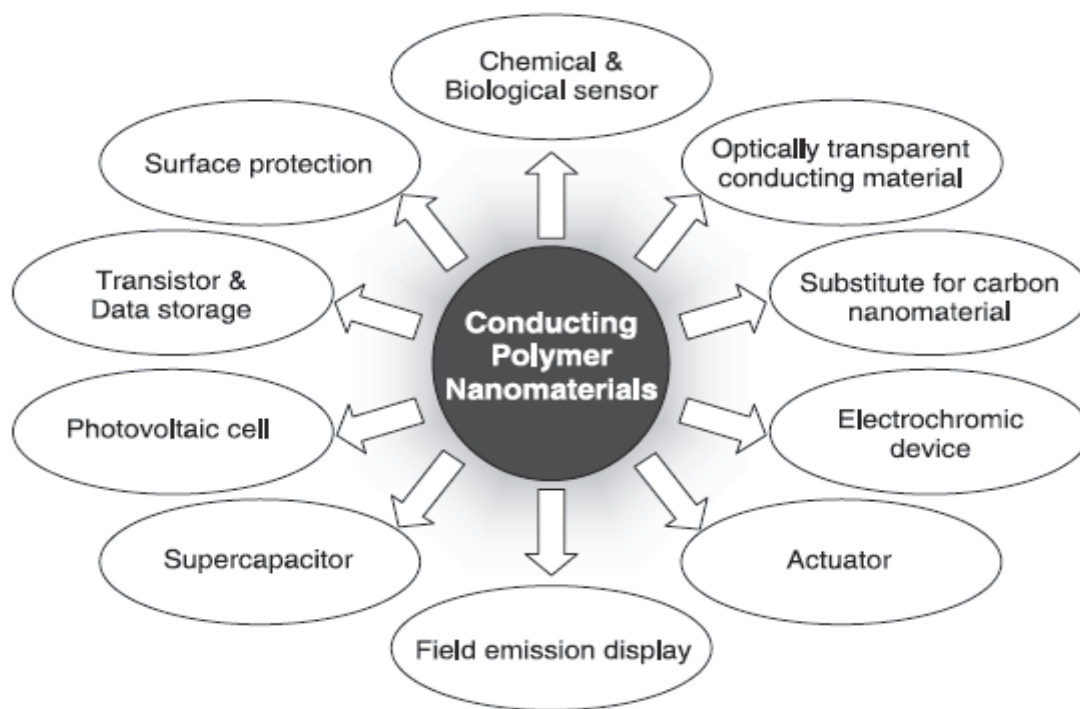


**Figure 2.13:** Application fields for conducting polymer nanomaterials.

On the other hand, this study focused on the recent achievements of the synthesis and application of CPs as electrode materials for supercapacitors. Various carbon materials have been considered for supercapacitor electrodes and a great attention now is also focused on conducting polymers. This can be attributed to the fact that carbon materials only possess double-layer capacitance, while metal oxides and conducting polymer also possess Faradaic capacitance. Generally, the Faradaic capacitance is 10 to 100 times higher than double-layer capacitance [108].

Conducting polymers (CPs) represent a very interesting family of synthetic metals due to a high doping level and a fast electrochemical switching. The possible application of CPs in electrochemical capacitors is dictated by their significant capacitance values [109, 110]. As opposed to activated carbons where only the surface is used for charge accumulation, in CPs, the total mass and volume is involved in charge storage.

Among the electrically CPs, great attention has been given to Polyaniline (PANI), Polythiophene (PT), Poly-(3,4-ethylenedioxythiophene) (PEDOT) and Polypyrrole (PPy).

#### *2.2.2.2.1 Polyaniline (PANI)*

As one of the most important conducting polymers, PANI is probably the oldest known synthetic organic polymer [111]. However, the detailed study on its structures and properties only began in the 1980s [112, 113]. Now it is generally accepted that PANI is a mixed oxidation state polymer composed of reduced benzenoid units and oxidized quinoid units [114].

Chemical polymerization of aniline has been carried out in an acidic solution [115–118]. This acidic condition provides the solubilization of the monomers as well as the formation of emeraldine salt as a conducting PANI. Figure (2.14), is a schematic presentation of the electropolymerization of aniline.

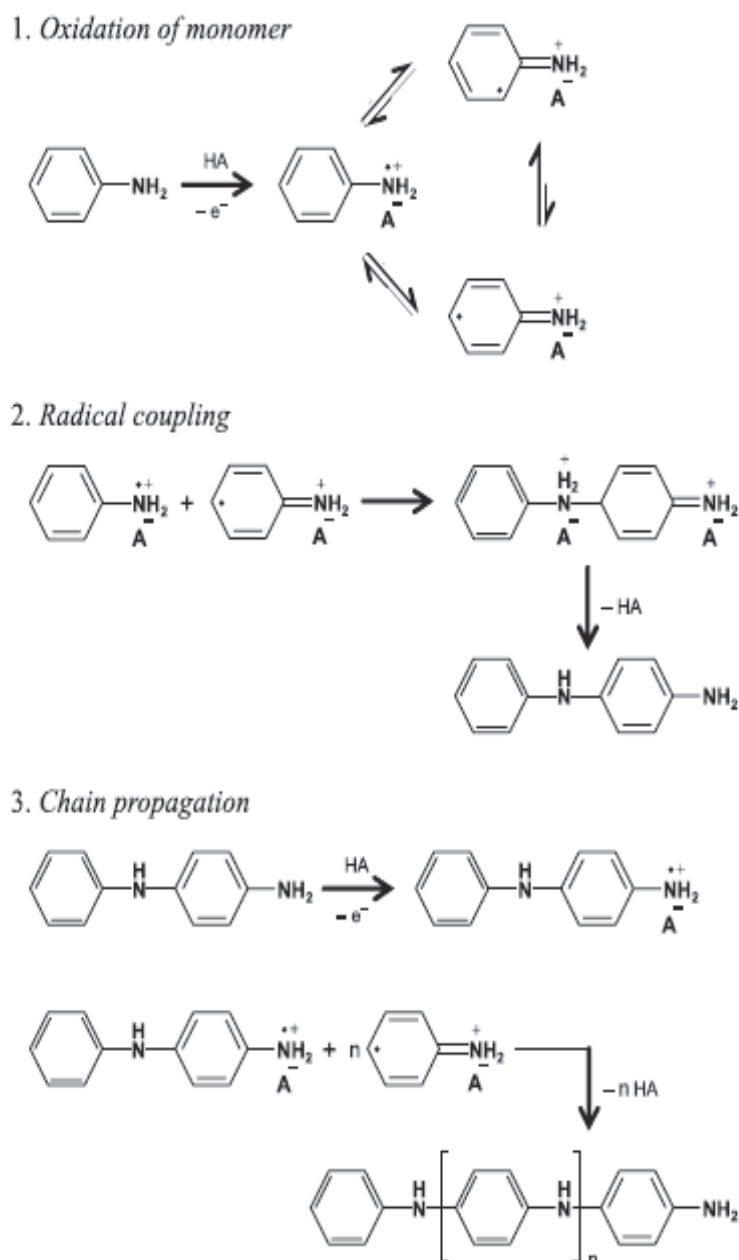


**Figure 2.14:** Schematic presentation of the polymerization of aniline [119].

Aniline monomer forms the anilinium ion in acidic medium and chemical polymerization results in the formation of protonated, partially oxidized form of PANI. The initial step involves formation of the aniline radical cation.

The next step is followed by the coupling of *N*- and *para*-radical cations with consecutive re-aromatization of the dication of *p*-amino-diphenylamine (PADPA). The



oxidation process of the diradical dication makes the fully oxidized pernigraniline salt form of PANI due to the high oxidizing power of the oxidant such as ammonium persulfate (APS)  $((\text{NH}_4)_2\text{S}_2\text{O}_8)$ . Whereas head-to-tail coupling is predominant, some coupling in the *ortho*-position also occurs, leading to conjugation defects in the final product. After consuming all the oxidant, the unreacted aniline monomer reduces the pernigraniline to produce the green emeraldine salt as the resultant polymer. From the viewpoint of color change in solution, the formation of PADPA reflects pink, and the formation of protonated pernigraniline becomes deep green. Green emeraldine salt precipitates after reduction of pernigraniline in the final step.

In the termination step, green emeraldine salt forms as a conductive PANI form and it can be converted to emeraldine base with an alkaline solution or an excess of water. The emeraldine base can be transformed to two non-conductive PANI such as the completely oxidized pernigraniline ( $m = 0$ ) and reduced leucoemeraldine ( $m = 1$ ) depending on oxidation states. Imine sites of the emeraldine base are easily protonated in acid condition, which results in the formation of green emeraldine salt as a conducting PANI [18]. The conductivity of PANI was affected by the degree of protonation and oxidation. In addition, the structural and conformational factors derived from polymerization condition also affect the conductivity of PANI.

The processability of PANI is relatively poor because it is infusible and insoluble in common solvents. PANI conducting polymer can be synthesized in different forms, namely, nanoparticle, core shell nanomaterial, hollow nanosphere, nanofiber and nanorod, nanotube and thin film and nanopattern.

## 2.2.2.2.2 Polythiophene (PT)

Polythiophene (PT) is an important conducting polymer that constructs environmentally and thermally stable materials. It has been applied as electrical supercapacitors, polymer light emitting diodes, batteries, electromagnetic shielding materials, and transistors [121, 122]. Figure 2.15 depicts the polymerization of thiophene.

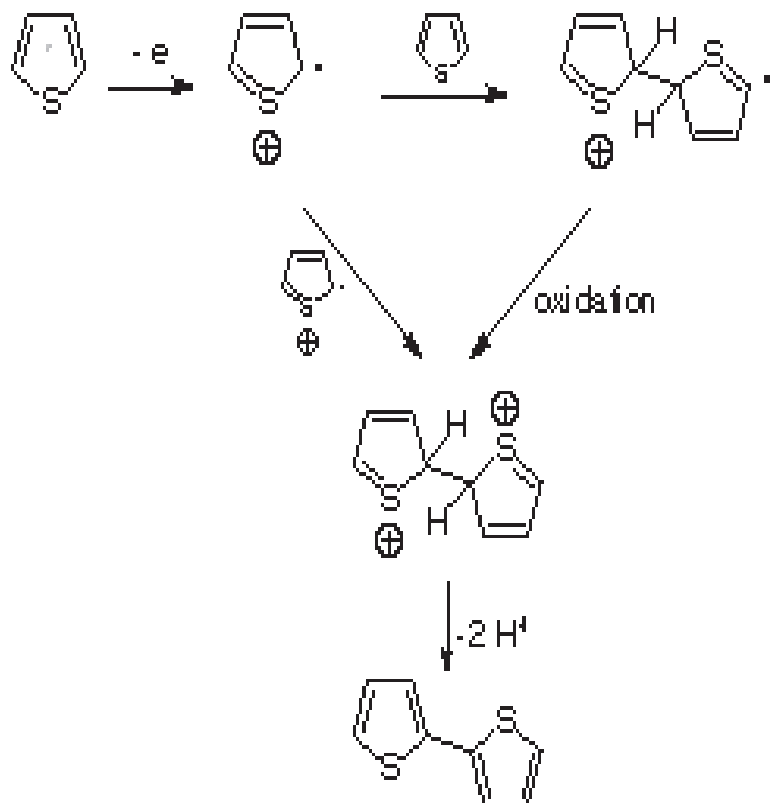


**Figure 2.15:** Schematic presentation of the polymerization of thiophene [120].

In PT, the rings coupled in the 2 and 5 positions allow the conjugation of the  $\pi$ -orbitals along the polymer chain. The large band gap of neutral PT provides a relatively low electrical conductivity of about  $10^{-8} \text{ S cm}^{-1}$ . The enhanced electrical conductivity has been achieved by oxidizing (or doping) PT. Consequently, the oxidation of PT affords a drastic change in the electronic band structure as new mid-gap states are created and resonance structure is formed.

The first chemical preparations of PT were reported in 1980 by two scientists, Yamamoto and Dudek whereby they synthesized PT by a metal-catalyzed polycondensation polymerization of 2,5-dibromothiophene [123, 124]. Several PT derivatives and substituted PTs have been developed and exploited in the diverse aforementioned applications. Owing to the recent push toward conducting polymer nanomaterials, the creative design and development of new PT nanomaterials have provided novel and fascinating materials and led to enhanced performance in certain devices. Therefore, the synthesis of PT nanomaterials has become a critical research subject. This leads to the intriguing prospect that chemical and physical properties of PT nanomaterials can be selectively tuned through specific polymerization and assembly.

PT conducting polymer can be synthesized in different forms, namely, nanoparticle, hollow nanosphere, nanofiber and nanowire, nanotube, thin film, nanocomposite and nanohybrid.

However, in contrast with studies on PPy and PANI, limited information has been available concerning the fabrication of the PT nanostructure due to the relatively low reactivity of the monomer.

## 2.2.2.2.3 Poly-3,4-ethylenedioxythiophene (PEDOT)

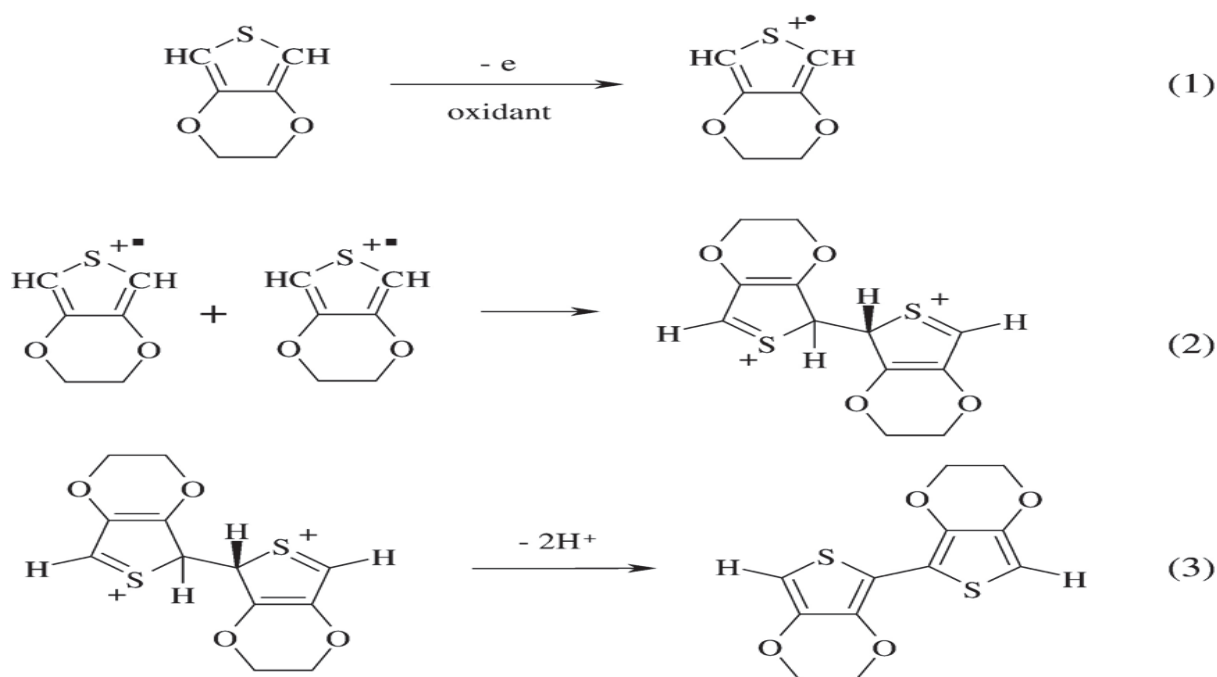


**Figure 2.16:** Schematic presentations for the polymerization of ethylenedioxythiophene [125].

PEDOT was developed as one of the PT derivatives by the Bayer AG research laboratories in Germany during the 1980s [126, 127]. It was prepared using standard oxidative or electrochemical polymerization methods. Figure (2.16), is a schematic presentation of the polymerization of ethylenedioxythiophene. Initially, PEDOT was found to be an insoluble polymer, yet exhibited some very interesting properties such as high conductivity (ca.  $300 \text{ S cm}^{-1}$ ), transparency in oxidized thin film, and excellent stability in an oxidized state. The solubility problem was subsequently overcome by a water-soluble polyelectrolyte such as PSS and this polyelectrolyte was used as the charge-balancing dopant during polymerization to form a PEDOT/PSS solution.

The combination of PEDOT and PSS electrolyte resulted in a water-soluble conducting polymer with good film forming properties: conductivity (ca.  $10 \text{ S cm}^{-1}$ ), high visible light transmittance, and excellent stability. Thin film of PEDOT/ PSS can be annealed in air at  $100^\circ\text{C}$  for over 1000 h and show only a minimal change in conductivity.

A great interest was recently focused on poly (3,4-ethylenedioxythiophene) (PEDOT), which is characterized by a good thermal and chemical stability, fast electrochemical switching and a high electrical conductivity in the p-doped state (easily up to  $550 \text{ S cm}^{-1}$ ) [128].

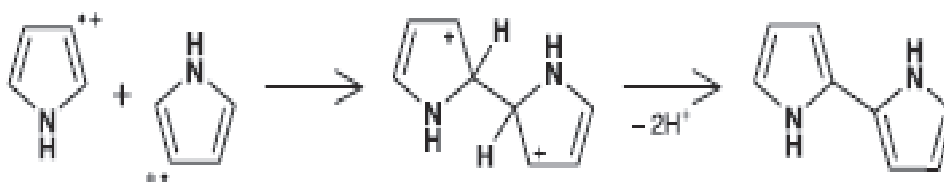
What was the most attractive, as a promising electrode material of supercapacitors, PEDOT had wider potential window. However, PEDOT, due to its relatively high molar mass, presented a moderate value of theoretical specific capacitance ( $210 \text{ F/g}$ ) compared to PPy's ( $620 \text{ F/g}$ ) [129].

## 2.2.2.2.4 Polypyrrole (Ppy)

## 1. Oxidation of monomer



## 2. Radical coupling



## 3. Chain propagation

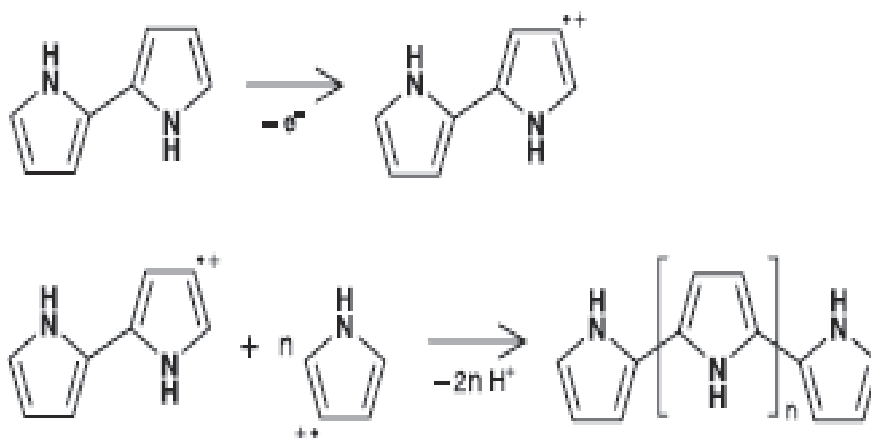


**Figure 2.17:** Schematic presentation of the polymerization of pyrrole [129].

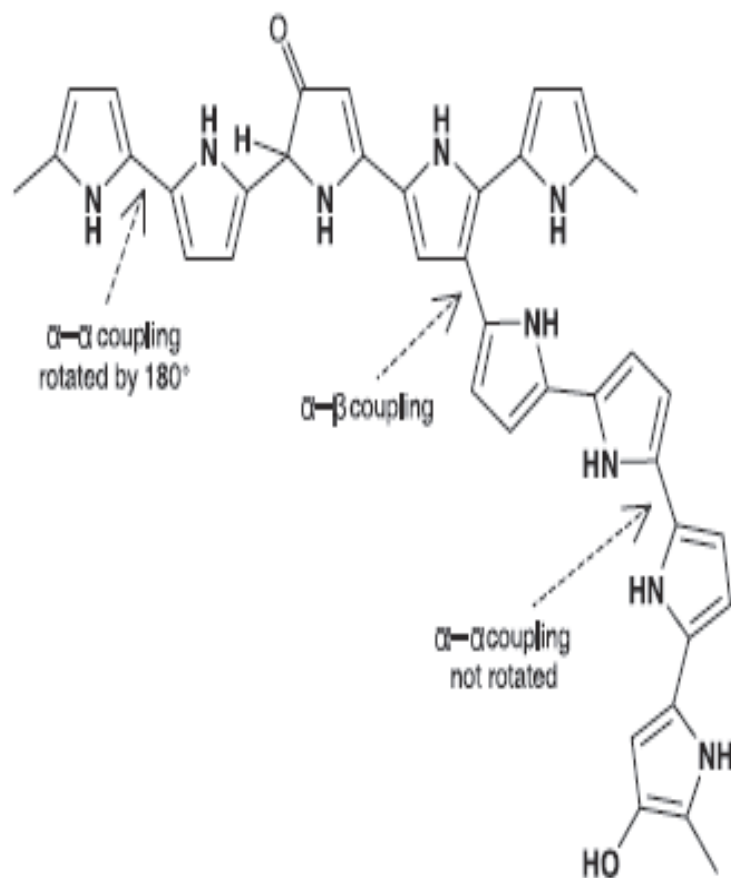


**Figure 2.18:** Possible chemical structures in PPy chains [129].

Figure (2.17) describes a typical mechanism for chemical oxidation polymerization of pyrrole. In the initiation step, radical cations ( $C_4NH_5^+$ ) are generated by the oxidation of pyrrole monomer.

A radical-radical coupling occurs between two radical cations, and forms a dimer with deprotonation, leading to a bipyrrrole. The bipyrrrole is reoxidized and couples with other radical cations. This process is repeated consecutively during the propagation step. The termination takes place due to the nucleophilic attack of water molecules or impurities in the polymer chains.

Figure (2.18) represents the possible chemical structure of PPy molecules during chemical oxidation polymerization. In the case of monomer-monomer coupling reaction, protons in the  $\alpha$ -position are more readily eliminated than those in the  $\beta$ -position. The  $\alpha$ - $\alpha$  coupling makes a major contribution to coupling reaction and leads to a linear PPy and this coupling of alternating pyrrole units provides a high degree of conjugation. On the other hand,  $\alpha$ - $\beta$  coupling occurs to the same extent and forms a cross linked PPy chain, breaking the linearity and planarity of PPy chains, owing to these is the insolubility of PPy in common solvents [130].

PPy has four different electronic band structures with changing oxidation levels and in the neutral state, it shows a large  $\pi - \pi^*$  band gap of 3.2 eV. This band gap proves to be too big to render this conducting polymer to be highly conductive. Therefore, the conducting polymer needs to undergo some transformation to bring it to its conductive state.

The process of transforming a polymer to its conductive form via chemical oxidation or reduction is called doping. The extent of enhancement of electric conductivity of a polymer primarily depends on the chemical reactivity of the dopant with the polymer. The same dopant cannot be effective for different polymers. The nature of dopant plays an important role in the stability of conducting polymers. Conductivity of polymers depends directly on the doping level. The doping level increases with exposure time of the polymer to the dopant vapor. Sometimes a sharp rise in conductivity is observed for a very small increment of the dopant level [131]. This sharp increase may be due to the rapid increase in mobility of the charge carriers, which in turn is due to interchain interaction.



Doping results in rearrangements of the polymer chains and consequently new ordered structures are formed. The dopant concentration may be as high as 50% [132]. Also, incorporation of the dopant molecules in the quasi one-dimensional polymer systems considerably disturbs the chain order leading to the reorganization of the polymer [133]. Therefore, the ultimate conductivity in polymeric semiconductors depends on many factors, viz., nature and concentration of dopants, homogeneity of doping, carrier mobility, crystallinity and morphology of polymers.

### **2.2.3 Hybrid supercapacitor**

Hybrid supercapacitors are classified into three categories, which are discussed below:

#### ***2.2.3.1 Symmetric hybrids***

Symmetric hybrid capacitor uses the same electrode material for both positive and negative electrodes. Symmetric hybrid capacitors include various combinations of positive and negative electrode materials such as carbon/metal oxide or carbon/conducting polymer. The carbon-based materials facilitate a capacitive double-layer of charge and also provide a high-surface-area backbone that increases the contact between the deposited pseudocapacitive materials and electrolyte.

#### ***2.2.3.2 Asymmetric hybrids***

The term “asymmetric hybrid capacitor” means a capacitor using different materials with different operating potentials as positive and negative electrode materials, which can increase the overall cell potential, resulting in higher energy and power densities [134]. Asymmetric hybrid capacitors include various combinations of positive and negative electrode materials such as conducting polymer/metal oxide [135, 136], metal oxide/carbon [134, 137–139] and conducting polymer/carbon material [140–142]. In

particular, the coupling of an activated carbon negative electrode with a conducting polymer positive electrode has received a great deal of attention [309].

### **2.2.3.3 Battery type hybrids**

Battery type hybrid capacitor is a new highly reliable energy storage device which is a combination of an EDLC and a battery e.g. C and Li-ion, sometimes referred to as a capattery or capacitor battery.

In a supercapacitor, two symmetric capacitors are connected in series and the total capacitance is halved.

$$1/C_{\text{total}} = 1/C + 1/C$$

$$C_{\text{total}} = C/2$$

But in a battery hybrid supercapacitor, one of the electrodes is replaced by a battery electrode. So we can get the total capacitance of the single capacitor electrode with an added advantage of the battery electrode.

## **2.3 SYNTHESIS OF THE ELECTRODE MATERIALS**

### **2.3.1 Carbon based materials**

Nano-sized carbon [19–21] have been actively investigated for use as the electrode materials of ECs because of their accessibility, easy processability, relatively low cost, non-toxicity, high chemical stability, and wide temperature range. Based on these materials, different methodologies have been applied to increase their SSA or tailoring Pore Size Distribution (PSD). This has resulted in considerable improvement of energy, power, and operation parameters of ECs.

According to the storage mechanism of EDLCs, the Specific Surface Area (SSA) of carbon-based materials plays an important role. It is supposed that the larger the SSA,

the higher the specific capacitance. However, the major problem of high SSA carbon is that not all the BET surface area is electrochemically accessible when in contact with electrolyte [22], that is, the gravimetric capacitance of various carbon materials does not increase linearly with the SSA.

Wang *et al.* [196] constructed asymmetric capacitors composed of AC electrodes with different PSDs. Results show that the negative electrode governs the characteristics of the capacitor, capacitance and rate performance. In order to obtain a high capacitance with a relatively slow charge–discharge, microporous carbon with a high SSA is effective, but in order to obtain a high rate performance, the negative electrode carbon should contain a large amount of mesopores.

It is more difficult to adsorb large dissolved solute ions in micropores (<2 nm wide) than in mesopores (2–50 nm wide), and that is more difficult with a higher rate of charge–discharge. However, Chmiola *et al.* [197] generated pores with average sizes from 0.6 to 2.25 nm and studied double-layer capacitance, in which demonstration of charge storage in pores smaller than the size of solvated electrolyte ions will lead to enhanced understanding of ionic transport in porous media. The results challenged the long-held axiom that pores smaller than the size of solvated electrolyte ions are incapable of contributing to charge storage.

Recently, Zhao *et al.* [198] synthesized ordered meso/macroporous carbon monoliths using SiO<sub>2</sub> opal and Pluronic F127 as templates by a facile method. The sample has a high SSA (1585.72m<sup>2</sup>/g) and a very large pore volume (3.98 cm<sup>3</sup>/g), and the specific capacity is about 130 F/g at a constant current density of 10 mA/cm<sup>2</sup>, which is larger than that of commercially available AC (19 F/g), carbon black (CB) (10 F/g), and CAG (23/g).

This high value is probably attributed to the novel structure of the sample, which could make full use of the inner surface of the materials.

The authors' research indicated that AC is the most extensively examined capacitor material, and the specific capacitance of AC can vary over a wide range (100–220 F/g) depending on how it is processed and the electrolyte used in the EC. Techniques adopted to achieve these features include;

- use of carbon foam and paste electrodes,
- pyrolysis of carbon based polymers,
- heat-treatment in the presence of additives,
- surface treatment, and so on.

The specific capacitance of the electrode materials can also vary significantly with current density. Hence in evaluating materials for ECs, the most direct method is to form thin electrodes from the material and perform constant current tests.

Continued research on carbon/carbon capacitors can be expected to improve their performance. These improvements will result from the utilization of carbons with higher specific capacitance and to reduce the inactive weight of the current collector and the material used to bond the carbon to the substrate with minimum contact resistance. Increasing the ECs voltage, at least 3V, is also a direct route to increasing the energy density.

The carbon materials have the following advantages: rich in resources, lower cost, higher specific surface area and so on. As result, they are considered as one of the industrialization prospect electrode material. The specific surface area and pore size distribution are the most important factors which affect the ECs performance of carbon

materials. The future research direction of this material is to obtain higher specific surface area, rational pore distribution, smaller internal resistance and surface modification of carbon materials.

### **2.3.2 Transition metals oxides**

#### ***2.3.2.1 Ruthenium oxide***

Transition metal oxides are considered to be the best candidate materials for EC due to their high specific capacitance coupled with very low resistance resulting in a high specific power, which makes them very appealing in commercial applications [178, 179]. To mention a few, ruthenium oxide, manganese oxide, nickel oxide and iron oxide are among the metal oxides under review for supercapacitor electrode materials. In this review, we will focus on ruthenium oxide and manganese oxide.

Among the transition metal oxides,  $\text{RuO}_2$  is the most promising electroactive material due to its high specific capacitance, low resistivity, high chemical stability, thermodynamic stability, long cycle life, high conductivity, and good electrochemical reversibility, as well as its high rate capability [180, 25].

But the lack of abundance and cost of the precious metal (Ru) are major disadvantages for commercial production of  $\text{RuO}_2$ . In efforts to overcome this disadvantage, synthesis of high surface area  $\text{RuO}_2$  has been attempted by sol-gel, sputtering, and precipitation methods [14, 23, 181].

Amorphous ruthenium oxide synthesized by sol-gel method showed a capacitance of over 720 F/g, which is considerably larger than that of activated carbon based electrochemical double layer capacitors [182]. However, low porosity which causes depletion of the electrolyte adsorbed on the electrode as well as rapid decrease of power

density observed at high charge and discharge rates made this material inadequate for commercial application [70].

Sato *et al.* [183] loaded amorphous  $\text{RuO}_2 \cdot x\text{H}_2\text{O}$  on the various activated carbons by sol-gel process. The results of this study indicated that the large particles made from sol-gel method blocked the mesopores in activated carbon which lowered the double layer capacitance coming from carbon.

Miller and Dunn [184, 185] deposited nanosize  $\text{RuO}_2$  particles on the carbon aerogel by chemical vapor impregnation. The high annealing temperature of approximately 300 °C used in this work initiated a crystalline transition of  $\text{RuO}_2$  and resulted in a specific capacitance of 330 F/g that is much lower than the specific capacitance obtained using the sol-gel process.

Kim *et al.* [186] synthesized nanostructured composite materials with different  $\text{RuO}_2$  loadings on carbon by colloidal method. They found the annealing temperature to be critical in optimizing the electrochemical performance of this material. The specific capacitance of  $\text{RuO}_2$ /carbon composite electrode (40 wt % Ru) was calculated to be 407 F/g and the specific capacitance of  $\text{RuO}_2 \cdot x\text{H}_2\text{O}$  was estimated to be approximately 863 F/g subtracting the contribution of double layer capacitance resulting from the carbon composite.

In this study,  $\text{RuO}_2$  was synthesized using a simple Adams method and its electrochemical activity studied (See Chapter 7).

### 2.3.2.2 Manganese oxide

Manganese dioxide is a promising active material in ECs because of its natural abundance, environmental compatibility, low cost, and high theoretical specific capacitance (SC) of 1,370 F/g expected for a redox process involving one electron per manganese atom [168–188].

#### 2.3.2.2.1 Chemical synthesis

Common chemical approaches to  $\text{MnO}_2$  include reducing  $\text{Mn}^{7+}$  to  $\text{Mn}^{4+}$  in solution with low pH by agents like ethanol in acetonitrile and oxidising  $\text{Mn}^{2+}$  to  $\text{MnO}_2$  by agents like  $\text{BrO}_3^-$  and  $\text{S}_2\text{O}_8^{2-}$  [168]. By altering the pH, various products such as  $\text{Mn}_3\text{O}_4$ ,  $\beta$ - $\text{MnOOH}$  and  $\gamma$ - $\text{MnOOH}$  can also be obtained [189].

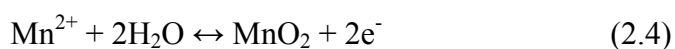
S. Pang *et al.* [190] discovered another useful and effective approach to synthesize  $\alpha$ - $\text{MnO}_2$ , that is, using  $\text{Mn}^{2+}$  to reduce  $\text{MnO}_4^-$ , e.g. adding  $\text{MnSO}_4$  into  $\text{KMnO}_4$  solution or mixing  $\text{KMnO}_4$  with manganese (II) acetate solutions in water. Such reactions are generalized in equation (2.3) below [168].



It is worth mentioning that  $\text{MnO}_4^-$  can be reduced by carbon and forms a uniform coating  $\text{MnO}_2$  onto, e.g. the surface of a graphite electrode through one step reaction in an acidic solution [191], as in equation (2.4). This inspiring discovery suggested a simple route in synthesizing various  $\text{MnO}_2$ /Carbon composites, including carbon nanotubes (CNTs), activated carbon materials and exfoliated graphite plates.

### 2.3.2.2.2 *Electrochemical synthesis*

A prominent advantage of synthesizing MnO<sub>2</sub> through electrochemical deposition is that the product will be in form of a homogenous thin film on a conducting substrate, i.e. graphite, stainless steel, titanium foil, etc., without using any binder. This can largely improve the situation of a resistive electrode caused by the aggregation of manganese oxide powders. The reaction of electrochemical deposition is represented in the equation below [168].



Successful electrochemical depositions have been carried out with various precursors, including manganese acetate, manganese sulphate, manganese chloride, etc. Manganese acetate was claimed to be a superior precursor among all due to its high deposition rate at much lower potentials and the existence of acetates having offered a more controllable reduction in the deposition material. However, the capacitance performance is independent of precursors as the mean oxidation state of Mn is not significantly affected by changing anions of manganese precursors. Different electrodeposition conditions, galvanostatic, potentiostatic and potentiodynamic were compared and the potentiodynamic deposition was claimed to be able to produce superior MnO<sub>2</sub> with optimum capacitive behavior [192, 193].

The deposition conditions and the deposition potential have been proven to have profound influence on the oxidation state of the manganese, the nanostructures, BET surface area and eventually electrochemical performance of the product. On average, the specific capacitance of the MnO<sub>2</sub> synthesized from electrochemical deposition is slightly above 200F/g, with the thickness of the film is of several tens of nanometer. However,



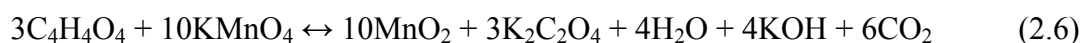
the figure could drop drastically as the thickness increases, as noted by J. Broughton *et al.* [194].

J. Broughton *et al.* [194] made another interesting finding that electrochemical oxidation can be an effective method to convert non-capacitive manganese metallic compound and crystalline oxide  $Mn_3O_4$  into capacitive  $MnO_2$ . The transformed  $MnO_2$  was confirmed to be the layer structured birnessite. High capacitance of 600-700F/g was reported for 20 nm thin films with a low current density of  $160 \mu A cm^{-2}$ . A high scan rate of 500 mV/s was achieved, resulting in a capacitance of 170F/g. An obvious advantage of this discovery is that it separated the coating process from the activation process, thus convenient techniques like sputtering and electrostatic spray can be employed to produce homogenous thin film at large quantity with low cost. However, for thin films synthesized in this manner, the thickness, corresponding to the electrolyte accessibility, remained a limiting factor for the capacitance and the maximum achievable capacitance reaches was 50F/g.

#### **2.3.2.2.3 Sol-gel method**

Sol-gel route is based on the hydrolysis and condensation of manganese ions. It was developed with the aim of producing colloidal sols containing nanoparticles which can be deposited as very thin porous films on a substrate via dipping or spinning procedure [195]. It has been discovered that homogenous and highly porous  $MnO_2$  powders can be synthesized through this route.

J. Xu *et al.* [195] reduced  $Mn^{7+}$  into amorphous  $MnO_2$  by fumaric acid as represented in equation (2.6) below.



Drying of the  $\text{MnO}_2$  gel at room temperature can produce densified xerogel of  $\text{MnO}_2$ . However, xerogel has exhibited less satisfying capacitive behavior compared with porous hydrous  $\text{MnO}_2$  films and underwent severe capacity loss of 50% after eight charge-discharge cycles.

It is also reported that a stable colloidal  $\text{MnO}_2$ , with a high concentration of  $\text{MnO}_2$ , can be prepared by reduction of tetra alkyl ammonium (methyl, ethyl, propyl and butyl) permanganate salts in aqueous solutions with 2-butanol and ethanol. This sol-gel derived tetrapro-pylammonium  $\text{MnO}_2$  thin film on nickel substrates exhibited good electrochemical behavior [162].

### **2.3.3 Conducting polymers**

Conducting polymers can be synthesized using three methods:

#### *2.3.3.1. Soft template method*

#### *2.3.3.2. Hard template method*

#### *2.3.3.3. Template-free method*

##### **2.3.3.1 Soft Template method**

The Soft template synthesis, also named self-assembly method, employs micelles formed by surfactants to confine the polymerization of conducting polymers into low dimensional nanomaterials. There are several soft templates such as surfactant, liquid crystalline polymer, cyclodextrin, and functionalized polymer [143, 144, 145–151].

Among them, surfactants, which imply cationic, anionic and non-ionic amphiphiles, are mostly used for the formation of micelle as a nanoreactor [152–153]. Microemulsions are macroscopically homogeneous mixtures of oil, water and surfactant, which on the microscopic level consist of individual domains of oil and water separated

by a monolayer of amphiphile [154]. Micelle formations in microemulsion are represented in figure (2.19) below.

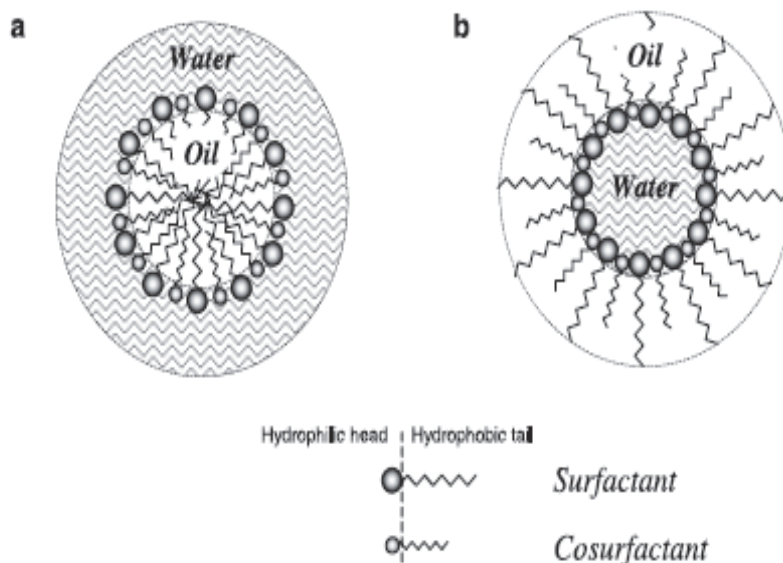


**Figure 2.19:** Schematic illustrations of (a) oil-in-water and (b) water-in-oil micelles[154].

Microemulsions act as an attractive media for polymerization reactions. Microemulsion polymerization is a novel fabrication technique which allows the preparation of ultrafine latex particles within the size range from 10 nm to 100 nm and with narrow size distribution. However, the formulation of microemulsions is subject to severe constraints due to high emulsifier level (over 10wt%) needed for achieving their thermodynamic stability [155, 156]. Besides sphere and layer morphologies, a wide range of morphological spectra could be obtained by carefully controlling the synthetic conditions. The surfactant templates for sphere, rod, and layer nanomaterials are schematically represented in figure (2.20).

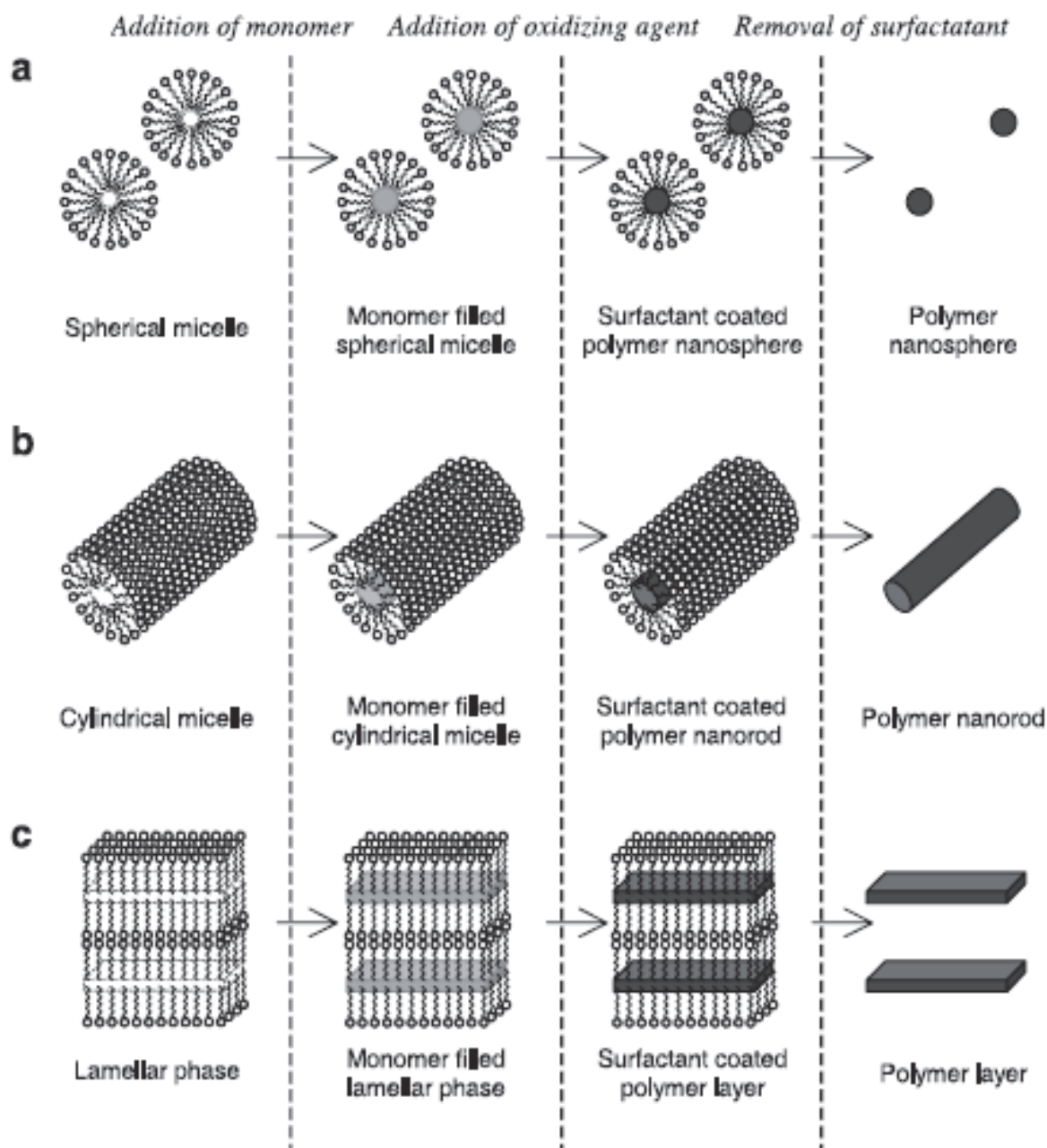


**Figure 2.20:** Schematic illustration for the surfactant templating of (a) PPy nanosphere, (b) nanorod, and (c) layered assemblies [156].

However, it is difficult to control the micelle formation during microemulsion polymerization. In general, polymerization process is kinetically and thermodynamically

unstable because of Ostwald ripening, the growth by collision between monomer droplets and monomer consumption during polymerization [157, 158].

### 2.3.3.2. *Template-free method*

Compared with hard and soft template methods, these methodologies provide a facile and practical route to produce pure, uniform, and high quality nanofibers. Template free methods encompass various methods such as electrochemical synthesis, chemical polymerization, aqueous/organic interfacial polymerization, radiolytic synthesis, and dispersion polymerization.

Xu *et al.* [167] synthesized Poly (3,4-ethylenedioxythiophene)/polypyrrole composite electrodes by electropolymerization of 3,4-ethylenedioxythiophene (EDOT) on the surface of polypyrrole (PPy) modified tantalum electrodes. Pure PPy or PEDOT electrodes were galvanostatically prepared on tantalum electrodes in a solution containing 0.3M Py or EDOT and 0.1M PTSNa. PEDOT/PPy composite electrodes were obtained by galvanostatical electropolymerization of EDOT on the PPy-modified electrodes.

Girija *et al.* [168] potentiodynamically deposited polyaniline on a nickel substrate in the presence of *p*-toluene sulfonic acid. An electrolyte solution of 0.05M aniline and 0.5M PTS was used for electropolymerisation. Deposition of PANI was carried out potentiodynamically by subjecting the working electrode to potential cycling between  $-0.2$  and  $1.2\text{V}$  at a scan rate of  $300\text{mVs}^{-1}$  for 50 cycles.

The application of ultrasonic irradiation in preparing conducting polymer as active material for supercapacitor was studied by Li *et al.* [169]. Symmetric supercapacitor was fabricated from poly(3,4-ethylenedioxythiophene) (PEDOT) with 1 M H<sub>2</sub>SO<sub>4</sub> as supporting electrolyte. The PEDOT was prepared by chemical oxidization in aqueous

media, where  $\text{FeCl}_3$  was oxidant and *p*-toluenesulfonic acid as dopant. Ultrasonic irradiation was introduced to enhance both chemical yield and specific capacitance of the material.

Conducting polypyrrole (PPy) films doped with *p*-toluenesulfonate  $\text{TOS}^-$ ,  $\text{ClO}_4^-$ , and  $\text{Cl}^-$  were electrochemically prepared by Wang *et al.* [170]. Pyrrole monomer was distilled and the concentrations of 0.1 mol to 0.6 mol·L were introduced into the electrolyte. The supporting salts ( $\text{TOSNa}$ ,  $\text{LiClO}_4$ , and  $\text{KCl}$ , respectively) were also 0.1–0.6 mol·L<sup>-1</sup>, while the pH was adjusted to 1–9 by using  $\text{TOSH}$ ,  $\text{HClO}_4$ , and  $\text{HCl}$ , correspondingly. The solvent was deionized water. The temperature of electrolytes was controlled between 0–25 °C. The polymerization current density was 0.5–10 mA·cm<sup>-2</sup>, and the polymerization charge was 2 mAh (7.2 C). The work electrodes (10 mm×10 mm) were cut from tantalum slices, burnished by metal sand papers, washed with acetone in ultrasonic.

### 2.3.3.3. *Hard template method*

In template synthesis of nanostructures, the chemical stability and mechanical properties of the template as well as the diameter, uniformity and the density of the pores are important characteristics to consider. There are a number of different templates that have been used for 1-D nanostructure synthesis; these include anodic alumina, nano-channel glass, ion track-etched polymers and mica films. The frequently used templates for nanowire synthesis are Anodic Alumina oxide and track-etched membranes.

Almost any solid matter can in principle be synthesized within nanoporous templates, provided a suitable chemical pathway can be developed [159, 160]. The limits to which materials can be used in template synthesis are defined by the chemistry required

to synthesize the material. There are, however, some concerns that need to be addressed when developing new template synthetic methods;

- the viscosity of the precursor solutions used to prepare the material,
- the rate of the deposition reaction (if proceeding too fast may result in pore blockage at the membrane surface before tubule/fibre growth can occur within the pores), and
- (the stability of the host membrane with respect to the reaction conditions [161]).

The commonly used templates for the synthesis of conducting polymers are AAO membrane, and track-etched PC membrane, whose pore size ranges from 10 nm to 100  $\mu\text{m}$ .

#### *2.3.3.3.1 Anodic alumina oxide membrane*

Porous anodic alumina templates are produced by anodizing pure Al films in various acids [161]. The membranes are commercially available in fixed sizes with specific pore diameters, and also prepared in the laboratory using electrochemical means.

In general, the polymerization of a conducting monomer is performed at the nanochannel, used as a nanoreactor. Hard templates are removed after polymerization in order to fabricate 1-D conducting polymer nanomaterials. When the pore is filled with appropriate material, it generates a self-assembled nanofiber. During the polymerization process, the conducting polymer preferentially nucleates and grows on the pore walls of the membranes. A high level of control could be exerted on the geometric characteristics of the PEDOT structures through a variation in synthetic conditions.

Resultant polymer tubular structures are tuned by polymerization time. On the one hand, short polymerization time provides the thin wall of conducting polymer nanotube, and on the other hand, long polymerization time produces thick walls.

Han *et al.* [162], reported that 1-dimensional (1-D) PEDOT nanostructures in the form of tubes, rods, thimbles, and belts had been successfully synthesized through the use of a hard template - AAO membrane. The preparation of the PEDOT 1-D structures was performed inside the membrane pores. Below is a schematic presentation illustrating the use of an  $\text{Al}_2\text{O}_3$  membrane as a template in the synthesis of 1-D PEDOT nanostructures.

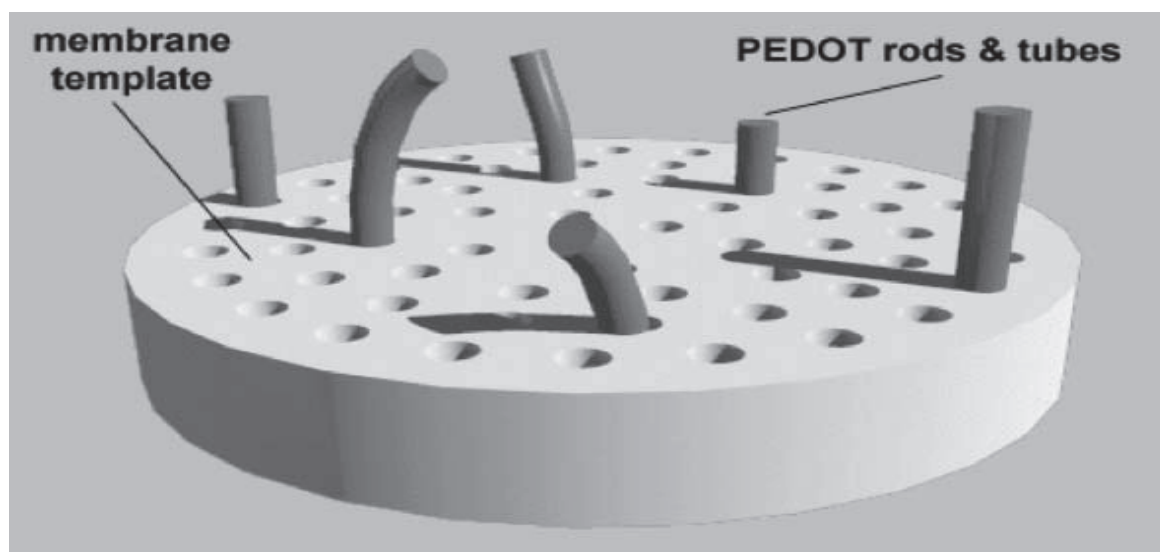


**Figure 2.21:** Schematic presentation illustrating the use of an  $\text{Al}_2\text{O}_3$  membrane as a template in the synthesis of 1-D PEDOT nanostructures [162].

However, Han *et al.* [162] expressed some challenges which were encountered while using this method namely;

- lack of an interaction between the PEDOT and AAO,
- poor solubility of the 3,4-ethylenedioxythiophene (EDOT) monomer in water, and,
- difficulty in controlling the reaction rate.



In trying to overcome these drawbacks, he stated that, the AAO membrane was first filled with EDOT monomer under negative pressure, and then the EDOT-filled AAO membrane was quickly transferred to an aqueous oxidant solution to initiate the polymerization. Due to the extremely low solubility of EDOT in the reaction solution, the monomer was retained in the pore of the AAO.

In addition, the solvophobic properties of the PEDOT polymer led to its preferential growth on the pore wall. After polymerization, the nanostructured PEDOT was separated from the AAO membrane by dissolving the AAO in a 20 vol.% hydrofluoric acid (HF) aqueous solution and washing the residue with an excess of HF, deionized water, methanol, and then again with deionized water.

Jang *et al.* produced PPy nanotube and carbon nanotube (CNT) using vapor deposition polymerization (VDP) mediated AAO membrane method [163]. An experimental scheme of this method is represented by figure (2.22).

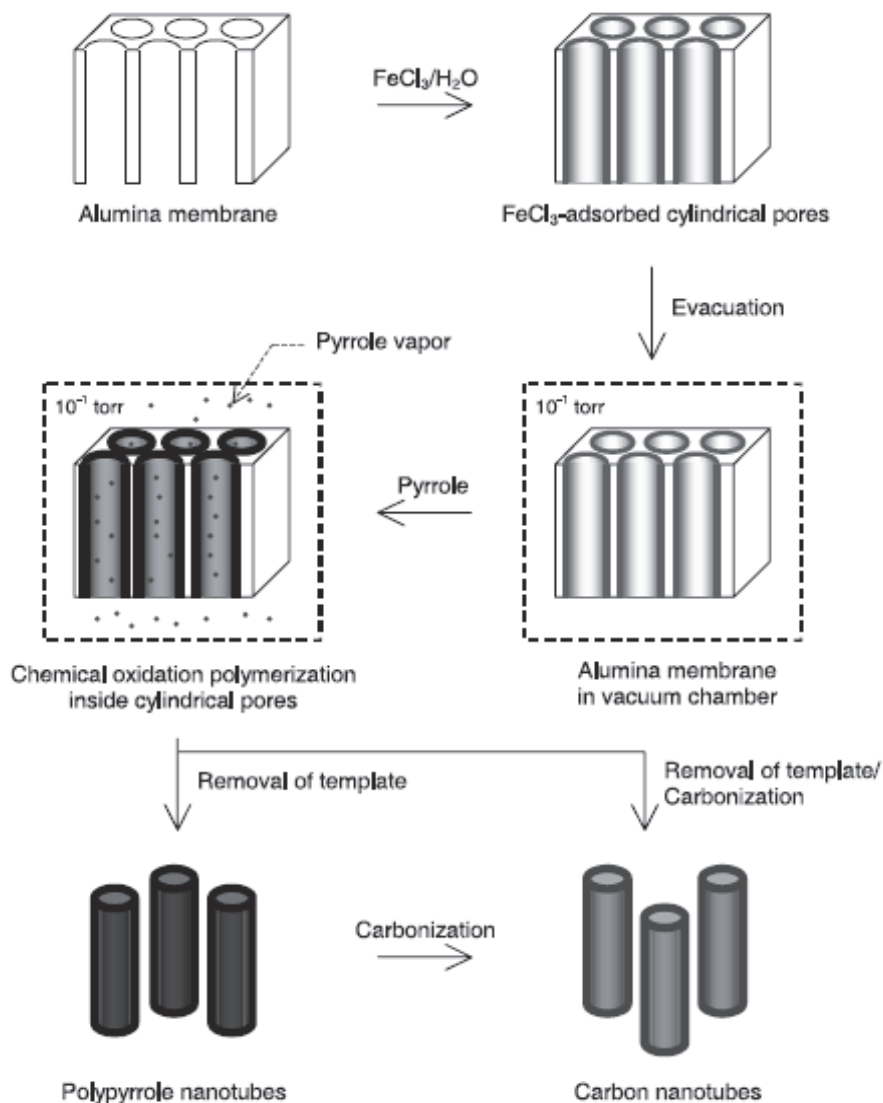


**Figure 2.22:** Schematic presentation for Vapour Deposition Polymerization (VDP) method [133].

Although the VDP process is experimentally convenient, the nature of polymerization has not been fully explored. Additionally, in this configuration, it is difficult to distinguish the polymers that have been formed in the gas phase with subsequent deposition onto the surface, from those polymerized by monomers adsorbed on the surface.

#### 2.3.3.3.2 Track etched membrane

These are produced by the bombardment (irradiation) of a membrane target with high energy heavy ions, followed by chemical etching. The number of pores per square unit, i.e., the pore density, depends on the intensity and duration of the irradiation, whereas the diameter of the resulting pores depends mainly on the intensity of the etching process.

Champagne and Legras [164] reported the electrochemical synthesis of the polypyrrole inside the pores of a polycarbonate particle track etched membrane. They deposited a rather thick layer ( $\pm 500$  nm) of gold on one side of the template membrane using a vacuum coating. This metal film was used as an anode to electrochemically synthesize the polymer within the pores of the membrane.

Martin and Piraux *et al.* [165, 166] proposed to explain this phenomenon as the electrostatic attraction between the growing polycationic polymer and anionic sites along the pore walls of the polycarbonate membrane. Champagne and Legras agreed with them and also stated that the formation may also be the result from a limited diffusion of the monomer and the electrolyte inside the pores. Furthermore, they explained that at the beginning of the electropolymerization process, the monomer contained in the pores was rapidly consumed. As the growing of the chain along the pore walls was very fast, the first tubules emerged rapidly from the surface and progressively covered the opening of the pores. When the pores were completely corked with polypyrrole, the diffusion of the reagents was stopped and consequently it was no more possible to thicken the tubules walls.

### 2.3.3.3.3 Biomolecules -assisted approach

Using biomolecules as morphology-directing agents is a new route to obtain 1D nanostructures of conducting polymers. Within the past few years, biomolecules have rapidly become promising templates for the synthesis of 1D nanostructures. By selecting suitable biomolecules, novel nanostructures of certain inorganic materials have been produced, such as DNA-assisted synthesis of Au,[171] Ag [172] particle nanowires, amino-acid controlled growth of tellurium nanotubes and nanowires,[173] protein-templated synthesis of bismuth nanowires,[174] polypeptide based synthesis of snowflake-like structures of bismuth sulfide nanorods,[175] and virus-guided synthesis of magnetic and semiconductor nanowires [176].

Very recently, organic conducting polymer 1D nanostructures including polypyrrole (PPy) nanowires and polyaniline nanofibers have been prepared in the presence of biomolecules, heparin and sodium alginate, respectively.[176] Shi *et al.* [177] synthesized Ppy nanowires using starch molecule as a structural directing agent.

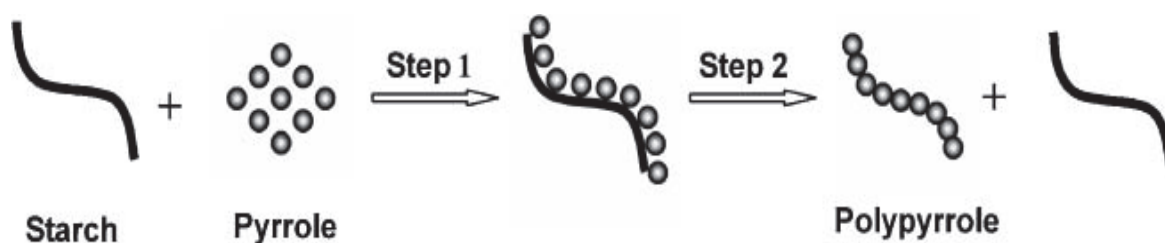


**Figure 2.23:** Simplified schematic representation of the synthetic strategy for the formation of PPy nanowires [177].

The biomolecules assisted method proved to be a simple and straight forward approach. Here, the chain-shaped structure of starch played a template-like role whereby the pyrrole monomer was adsorbed onto the starch molecules through the hydrogen bonds formed between the pyrrole molecules and the –OH groups of starch. Another fact that

makes this approach to be more attractive than the previously mentioned is the fact that the removal of the starch molecules adsorbed was done only by rinsing the products with water.

The important requirements for the template applications of biomolecules are what motivated the pursuit of our study whereby in our case gelatine was used as a structural directing biomolecule for the polypyrrole synthesis. These requirements being that they should:

- possess the ability to guide the oriented growth of organic or inorganic substances,
- be thermally and chemically stable,
- be easy to obtain,
- be cheap and if possible,
- be environmentally friendly.

## **2.4 ELECTROLYTES FOR SUPERCAPACITORS**

The electrolyte is typically one or more solvents containing one or more dissolved ionic species. In many cases, the physical and electrochemical properties of the electrolyte are a key factor in determining the internal resistance of the supercapacitor and the power properties.

### **2.4.1 Aqueous electrolytes**

Aqueous electrolyte solutions have been often applied as electrolytes for supercapacitors because of these properties

- high conductivity,
- low resistance inside the capacitor,
- easily wetting with the surface of electrode,

- and cost effectiveness.

In general, the aqueous electrolyte solutions include acidic (e.g.  $\text{H}_2\text{SO}_4$ ), neutral ( $\text{Na}_2\text{SO}_4$ ) and basic solution (e.g.  $\text{KOH}$ ). Due to these remarkable properties,  $\text{H}_2\text{SO}_4$ ,  $\text{Na}_2\text{SO}_4$  and  $\text{KOH}$  electrolytes were used in this study.

## **2.5 MOTIVATION TO THE STUDY**

In recent years, as the movement for environmental protection is increasingly dominant and the rapidly increasing price of oil is an undeniable reality, the automobile industry has been looking to introduce electric vehicles (EV), hybrid electric vehicles (HEV) and fuel cell vehicles (FCV), in place of conventional internal combustion vehicles (ICV) as early as possible. In this regard, development of advanced energy storage technologies for application in transportation has become one of the top priorities due to its role as a critical technology for practical use of EV, HEV and FCV.

EV, HEV and FCV are regarded as promising candidate to replace the ICV and would revolutionize the future transportation sector. EV, HEV and FCV have several advantages, such as low emissions, high fuel efficiency, good vehicle performance and low maintenance, over ICV. In the past decade, intensive effort has been put into the R&D of EV, HEV and FCV technologies and significant progress in technologies has increased the prospects for EV, HEV and FCV application in transportation.

The one of many barriers for EV, HEV and FCV commercialization in automobile industry is the high cost of energy storage unit used in these vehicles. In the case of hybrid vehicle system, the high cost can be reduced by integrating new energy storage system into these vehicles. In this system, the power peak for acceleration and hill-climbing of the vehicle is provided by an energy storage system. The supercapacitor is a critical

component for energy storage systems. The higher power density of supercapacitors offers improved vehicle acceleration and the ability to recover more energy from regenerative braking, since they can be charged/discharged at high current. Generally, the key for supercapacitors to achieve high specific power depends on the inherent properties and the surface areas of their electrode materials.

Consequently, the preparation and characterization of the high-surface-area nanomaterials such as nanowires and nanotubes have been being carried out extensively in the past few years. Among these nanostructures, one-dimensional (1D) conducting polymer nanomaterials have attracted much attention because of their low cost, ease of synthesis, relatively high conductivities and nano-scale dimensions.

We therefore propose in this project to synthesize and characterize nano-scale:

- One dimensional conducting polypyrrole polymer will be synthesized electrochemically by a fast and environmentally friendly biomolecules-assisted method and aqueous electropolymerization.
- One dimensional manganese oxide will be synthesized by an easy low temperature solid state reaction and hydrothermal method.
- Polycrystalline ruthenium oxide will be synthesized using Adam's method for comparison with the synthesized  $\text{MnO}_2$  nanorods.

## CHAPTER 3

### METHODOLOGY

#### 3.1. CHEMICALS AND MATERIALS

The chemical materials used in this study are listed in table (3.1) below.

**Table 3.1:** List of used chemicals and materials.

Chemical or Material	Molecular Formula	Specifications	Supplier
Manganese Chloride	$\text{MnCl}_2 \cdot 2\text{H}_2\text{O}$	96.0%	Merck
Potassium Permanganate	$\text{KMnO}_4$	99.0%	Merck
Manganese Sulphate	$\text{MnSO}_4 \cdot 4\text{H}_2\text{O}$	98.5%	Merck
Ammonium Sulphate	$\text{NH}_4\text{SO}_4$	99.0%	Merck
Ammonium Persulphate	$(\text{NH}_4)_2\text{S}_2\text{O}_8$	98.0%	Alfa Aesar
Sodium Sulphate	$\text{NaSO}_4$	99.0%	Alfa Aesar
Potassium Hydroxide	$\text{KOH}$	85% AR	Kimix
Ruthenium Chloride	$\text{RuCl}_3 \cdot \text{H}_2\text{O}$	99.98%	Sigma Aldrich
Sodium Nitrate	$\text{NaNO}_3$	99.0%	Sigma Aldrich
Isopropanol	$\text{C}_3\text{H}_8\text{O}$	99.5%	Alfa Aesar
Pyrrrole	–	–	Alfa Aesar
Toulene-4-Sulphonic acid Sodium Salt	$\text{C}_7\text{H}_7\text{NaSO}_3$	–	Sinopharm Chemical Reagent Co. Ltd. (China)
Gelatin	–	–	Alfa Aesar
Lithium Perchlorate	$\text{LiClO}_4$	–	Alfa Aesar
Disodium Hydrogen Phosphate	$\text{Na}_2\text{HPO}_4$	96%	Alfa Aesar
Sodium dihydrogen Phosphate	$\text{NaH}_2\text{PO}_4$	99.0%	Alfa Aesar
Carbon Black, Acetylene, 100 % compressed	AC	99.9+ %	Sigma Aldrich



Carbon Nanotubes	CNT	MWCNT(diam. 5-20nm) length: 10 micrometer	Carbon nano-material technology Co. Ltd. (Korea)
Carbon Black	C	99.9+ %	Sigma Aldrich
Nickel Foil	Ni	99.5% (metal basis)	Alfa Aesar
Silicon Carbide Paper	-	1200 grit	Sinopharm Chemical Reagent Co. Ltd. (China)
Acetone	C <sub>3</sub> H <sub>6</sub> O	-	Kimix
Ethanol	C <sub>2</sub> H <sub>6</sub> O	99.0 % AR	Kimix

## 3.2 SYNTHESIS OF POLYPYRROLE NANOWIRES

### 3.2.1 Passivation of an electropolymerization substrate and purification of the monomer

It is known that electrochemical deposition of conductive polymers onto substrate surfaces is usually accompanied by the passivation of substrate electrode (particularly for active metals). The passive film generated causes a stronger connection of the electroactive film to the electrode surface, as it contains more suitable sites for the deposition of the electroactive material.

The nickel foil used as the substrate was polished with 1200 grit silicon carbide paper and ultrasonicated for 5 minutes in Acetone, another 5 minutes in Ethanol and then finally with ultra pure water and dried, before use.

Prior to polymerization, pyrrole, which was used as a monomer was purified by distillation in the atmosphere of nitrogen gas and stored in the refrigerator until use.

**Table 3.2:** Materials used for the passivation of the electropolymerization substrate.

<b>Electropolymerization Substrate</b>	Nickel foil
<b>Passivating material</b>	1200 grit Silicon Carbide paper Acetone Ethanol
<b>Monomer</b>	Pyrrrole
<b>Flushing gas</b>	(N <sub>2</sub> )Nitrogen gas (UHP) obtained from Afrox

### 3.2.2 Electrochemical polymerization of the polypyrrole nanowires

Compared with chemical oxidation polymerization, electrochemical polymerization is performed at an electrode (conductive substrate) using the positive potential [211–215]. Whereas the powder forms are obtained by chemical polymerization, the electrochemical method leads to films deposited on the anode. When a positive potential is applied at the electrode, a pyrrole monomer such as a heterocyclic compound is oxidized to form a delocalized radical cation, which includes the possible resonance forms. Radical-radical coupling reaction produces the dimerization of the monomer radicals at the  $\alpha$ -position. Removal of 2H<sup>+</sup> ions consequently forms the neutral dimer. The next step is chain propagation which includes the oxidation of the neutral dimer to form the dimer radical. The resultant radical can react with other monomer or dimer and this radical coupling and the electrochemical oxidation processes repeat in order to extend the polymer chain. The final step involves the termination of chain growth and the resultant PPy film is formed on the anodic electrode.

Three techniques are generally used for polypyrrole synthesis, electrochemical polymerization [216], chemical polymerization in solution [217] and chemical vapour deposition [218]. Electrochemical polymerization was chosen for this study because the

structure, thickness, conductivity and electrochemical properties of a resulting polypyrrole film can be controlled by film growing parameters (formation potentials and current densities) formation charges, temperature, solvents and supporting electrolytes [219,220].

Also, with electrochemical polymerization method, polypyrrole can be easily formed as a strong adherent to various substrates, as a film possessing good mechanical properties and environmental stability.

Two methods were employed for the synthesis of polypyrrole nanowires;

3.2.2.1. Bio-templating method

3.2.2.2 Dopant electropolymerization method

### **3.2.2.1 Bio-templating synthesis technique for polypyrrole nano-wires**

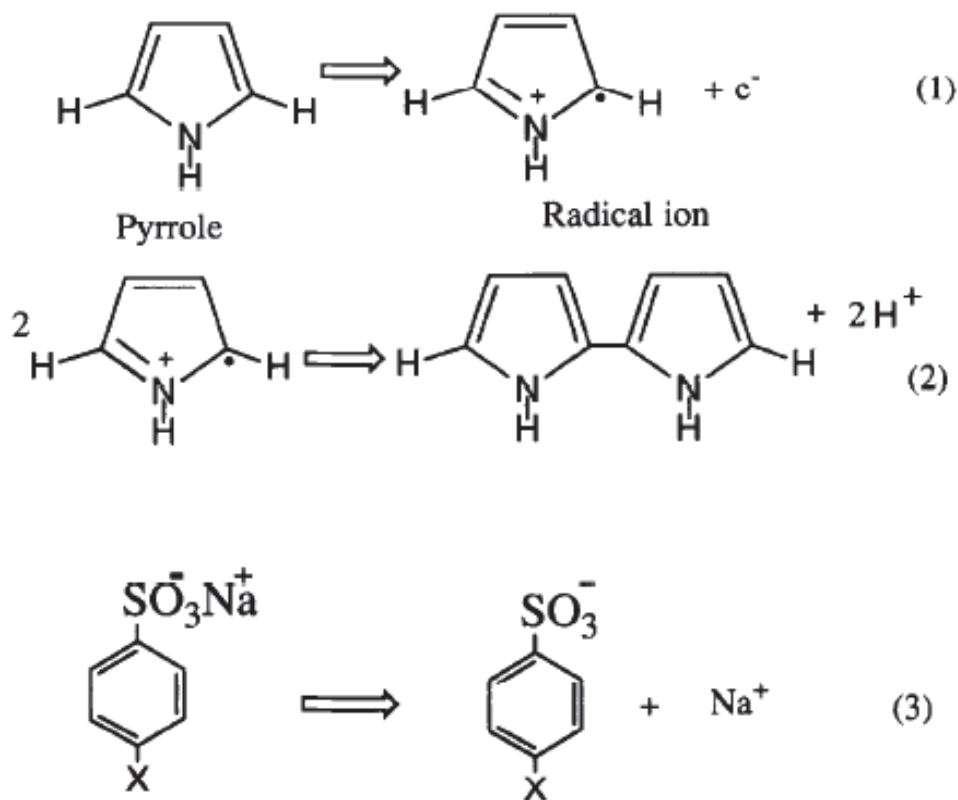
Biomolecules are very intriguing building blocks for nanotechnology from the material science point of view because they naturally exist in the nanometer size range. There is, therefore, increasing interest in the potential applications of biomolecules in the fields of nanoscale science [221–223]. An important aspect involves the use of one-dimensional (1D) biomolecules as templates for the fabrication of various 1D non-biological nanostructures [224–226].

Biomolecules-assisted approach is a simple, cheap, rapid, mild and environmentally benign method to produce uniform nano-scale conducting polymers without the need to remove the templates as well as to recycle the surfactants.

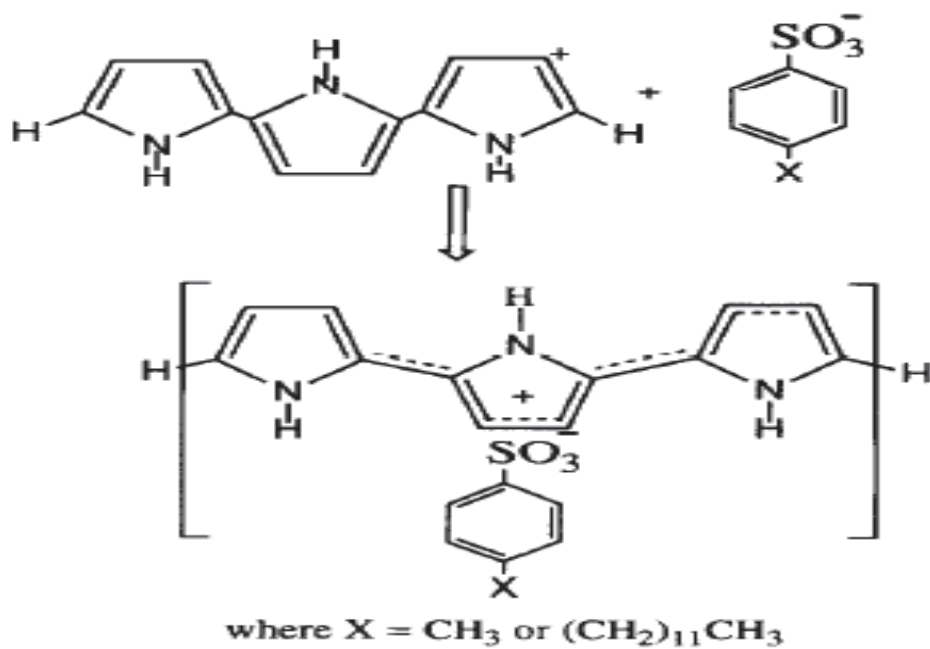
Gelatine, a rod-shaped protein with repeating glycine–proline–proline and glycine–proline–hydroxyproline sequences in the polypeptide linkages, was used as a biotemplate for the synthesis of polypyrrole nanowires. Figure (2.23) in Chapter 2, gives an illustration of the process involved in the Biomolecules-assisted approach.

### 3.2.2.2 Electropolymerization by doping method of polypyrrole nanowires

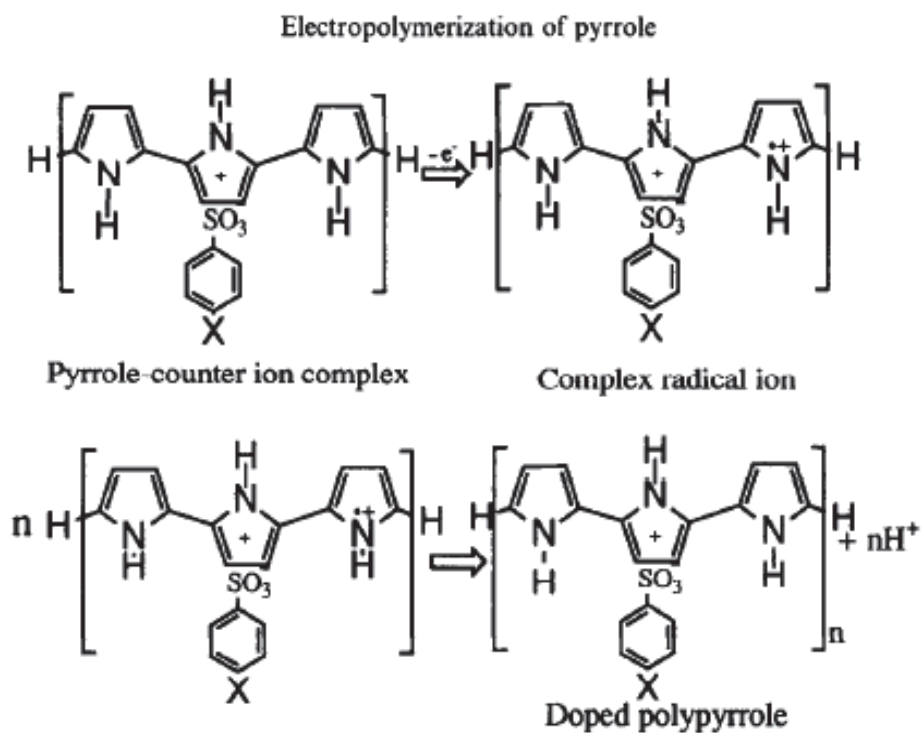
Compared with hard templates, the utilization of the soft templates avoids the further template-removal step and these soft templates act not only as structure-directing agents but also, in most of the cases, as dopants during the nanostructure formation. It was noted that the incorporation of molecules or molecular assemblies into the conducting polymer may afford some new properties to the final products, and thus making the methods very attractive for the synthesis of functional nanomaterials of conducting polymers. Below is a schematic presentation of the method used.



Scheme 1. Initiation of aqueous polymerization of pyrrole.



Scheme 2. Complexation reaction.



Scheme 3. Formation of doped polypyrrole.

**Figure 3.1:** A schematic illustration of an aqueous electropolymerization approach [228].

PPy nanowires for both methods were synthesized via a typical electrochemical polymerization which was performed at room temperature in a one-compartment cell using an LK2005A electrochemical workstation. The electrolyte solution used was 0.2M phosphate buffer Solution containing 0.07M LiClO<sub>4</sub>, 0.2 wt% gelatine and 0.14M pyrrole and 0.2M phosphate buffer solution containing 0.85M TSNa and 0.14M pyrrole for bio-templating method and aqueous electropolymerization method, respectively.

The working electrode was the Nickel foil, and reference electrode used was a saturated calomel electrode and the counter electrode was platinum gauze. The working electrode and the counter electrode were placed 1 cm apart. The potential applied on the bio-templating method was 0.75V for 200s and for the aqueous electropolymerization method, the potential was 0.78V for 600s, first layer and 0.80V for 800s, second layer.

After the electropolymerization of the nanowires, the working electrodes were removed from the solution, rinsed with ultra pure water and dried at room temperature. Table 3.3 displays materials and parameters of the method used.

**Table 3.3** Conditions for the electrochemical polymerization process.

	<b>Biomolecules Assisted Method</b>	<b>Doping Method</b>
<b>Working Electrode</b>	Nickel Foil	Nickel Foil
<b>Reference Electrode</b>	SCE	SCE
<b>Counter Electrode</b>	Platinum wire mesh	Platinum wire mesh
<b>Electrolyte</b>	0.2 M PBS, (pH = 6.98) containing 0.07M LiClO <sub>4</sub> , 0.2 wt% Gelatine and 0.14M pyrrole	0.2 M PBS, (pH = 6.98) containing 0.85M TSNa and 0.14M pyrrole
<b>Method</b>	Potentiostatic	Potentiostatic
<b>Potential</b>	0.75V	0.80V for 1 <sup>st</sup> layer 0.78V for 2 <sup>nd</sup> layer
<b>Time</b>	300s	600s 1 <sup>st</sup> layer 800s 2 <sup>nd</sup> layer
<b>Degassing gas</b>	Nitrogen gas (N <sub>2</sub> )	Nitrogen gas (N <sub>2</sub> )

### 3.3. SYNTHESIS OF MANGANESE OXIDE ELECTRODE MATERIALS

During the synthesis of the manganese oxide electrode materials, two methods were employed:

#### 3.3.1 Low temperature solid state reaction

#### 3.3.2 Hydrothermal method

### 3.3.1 Low temperature solid state reaction

It is generally accepted that the necessary condition for the occurrence of solid state reaction at room temperature is that one of the reactants should have crystalline waters or a low melting point on the one hand, whilst on the other hand sufficient grinding is also required to provide the reactant molecules with more contact opportunities. When salts with crystalline waters are reacted with other reactants, the crystalline waters are considered to be released from the structure of its molecules forming a layer of liquid film over particles, which in fact constructed a micro-aqueous-environment for the reactant molecules. It is believed that this reaction offers the possibility to prepare nano-sized products. In the synthetic method of solid state reaction,  $\text{MnCl}_2 \cdot 4\text{H}_2\text{O}$  is welcome as the form of metal salts.

Q. Li *et al.* [229] attempted selecting Mn salts without crystalline waters such as  $\text{MnSO}_4$  or  $\text{MnCO}_3$  as reactants, but neither of the salts reacted with solid  $\text{KMnO}_4$  even at higher heating temperatures ( $100^\circ\text{C}$ ). This confirmed that crystalline water played an important role in the solid phase reaction at room or low heating temperature.

In this study, equal parts of  $\text{MnCl}_2 \cdot 2\text{H}_2\text{O}$  and  $\text{KMnO}_4$  were ground together for an hour using a mortar and a pestle. During the process of grinding, the strong odor of HCl could be detected, and the color of the mixture gradually changed from violet to black. The product was then transferred in a glass vial and placed in a water bath at  $70^\circ\text{C}$  for three and five hours. The product was then taken out of the water bath cooled, washed with ultra pure water and dried in an oven at  $120^\circ\text{C}$  for 5-10 hours. For supported materials carbon materials were added together with the raw materials to give an 80  $\text{MnO}_2$ : 20 carbonaceous material ratios. The resulting  $\text{MnO}_2$  material was then physically and electrochemically characterized and the results are reported in Chapter 5. Below is a schematic presentation of the method used.



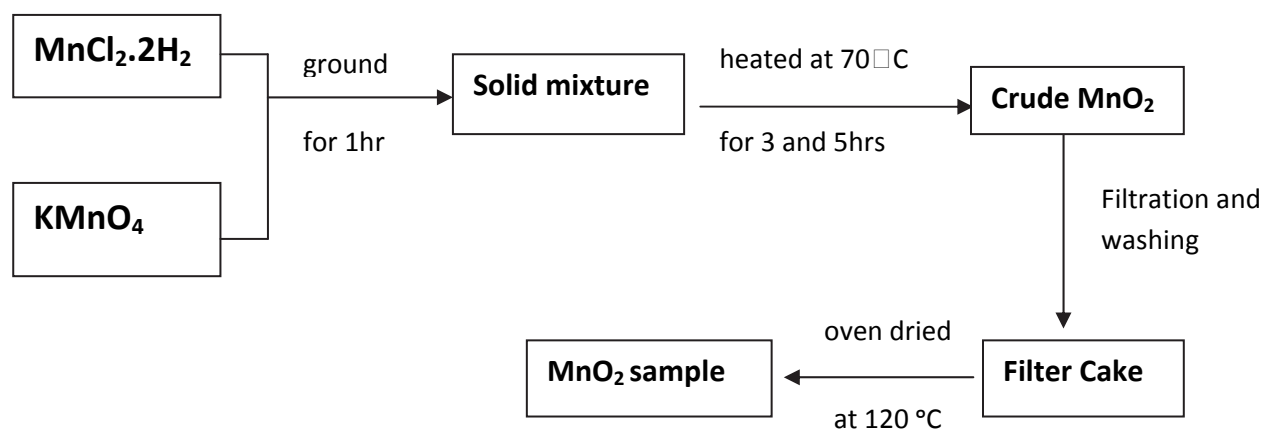


**Figure 3.2:** A schematic illustration of a low temperature solid state reaction.

**Table 3.4:** Materials and parameters used in the low temperature solid state reaction.

<b>Materials used</b>	MnCl <sub>2</sub> .2H <sub>2</sub> O, KMnO <sub>4</sub> , AC, CNT
<b>Heating Apparatus</b>	Water Bath at 70°C
<b>Mixing Apparatus</b>	Agate Mortar and Pestle
<b>Rinsing Apparatus</b>	Vacuum Filtration
<b>Drying Apparatus</b>	Oven at 120 °C

### 3.3.2 Hydrothermal method

Electrochemical properties of MnO<sub>2</sub> depend strongly on the crystalline structure and morphology of the oxide. It has been well known that the manganese dioxides exist in various polymorphic forms concluding  $\alpha$ -,  $\beta$ -,  $\gamma$ - and  $\delta$ - MnO<sub>2</sub>, which are different in the spatial arrangement of basic octahedral [MnO<sub>6</sub>] units. Among all of these manganese dioxides,  $\alpha$  - MnO<sub>2</sub> have now received special attention as electrode materials for supercapacitors, since the large 2x2 tunnels existing in the crystalline lattice of  $\alpha$  -MnO<sub>2</sub> are believed to facilitate the accommodation and transportation of electrolyte ions.

Hydrothermal method is a simple and feasible method to prepare one-dimensional nanomaterials. As the crystal growth is anisotropic, it is prone to grow slowly toward one-dimensional direction under the hydrothermal conditions such as high pressure and temperature. Materials with 1-D nano structure not only have sufficiently high surface area and short distance from surface to interior core, but also have smallest dimension, which will provide more effective electrical transport continuity and minimize electrolyte-ion diffusion path. Based on this consideration, there has been increasing interest recently in the fabrication of one-dimensional nano-MnO<sub>2</sub>, such as MnO<sub>2</sub> nanowires [230-233] and nanorods [233-236].

For example, X. Wang, *et al.* [231, 234] have reported the synthesis of 1-D  $\alpha$ -MnO<sub>2</sub> single-crystal nanowires and nanorods in a hydrothermal method through the oxidation of MnSO<sub>4</sub> by (NH<sub>4</sub>)<sub>2</sub>S<sub>2</sub>O<sub>8</sub> or KMnO<sub>4</sub>, respectively. Q. Li, *et al.* [230] have synthesized well-aligned  $\alpha$ -MnO<sub>2</sub> nanowires by electrochemical step-edge decoration. Also,  $\alpha$ -MnO<sub>2</sub> nanorods with uniform diameter were obtained by M. Sugantha *et al.* through a sol-gel synthetic route [235].

In this study, the electrode materials were synthesized using the hydrothermal method whereby the predetermined amounts of salts were dissolved in ultra pure water to give a concentration of 0.08M MnSO<sub>4</sub>.4H<sub>2</sub>O, 1.16M NH<sub>4</sub>SO<sub>4</sub> and 0.08M (NH<sub>4</sub>)<sub>2</sub>S<sub>2</sub>O<sub>8</sub> solution. The solution was then transferred to an autoclave and placed in a preheated oven at 120°C for three and five hours. This resulted in a dark brown crude MnO<sub>2</sub> precipitate which was then washed with ultra pure water and dried in an oven at 120°C for 10 hours. The resulting MnO<sub>2</sub> material was then physically and electrochemically characterized and the results are reported in Chapter 5. For supported materials carbon materials were added together with the raw materials to

give an 80 MnO<sub>2</sub>: 20 carbonaceous material ratios. Below is a schematic presentation of the method used and a table with materials and parameters of the method used.

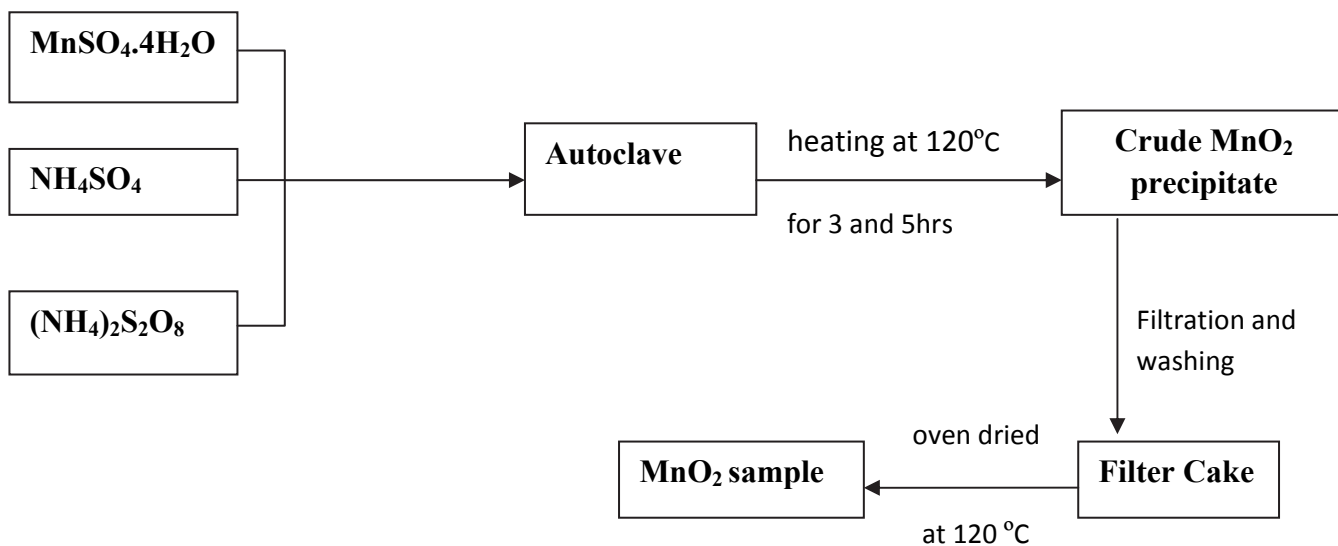


**Figure 3.3:** A schematic illustration of a hydrothermal method.

**Table 3.5:** Materials and parameters used in the hydrothermal method.

<b>Materials used</b>	MnSO <sub>4</sub> .4H <sub>2</sub> O NH <sub>4</sub> SO <sub>4</sub> (NH <sub>4</sub> ) <sub>2</sub> S <sub>2</sub> O <sub>8</sub> Activated Carbon Carbon Nanotubes
<b>Heating Apparatus</b>	Autoclave at 120°C
<b>Rinsing Apparatus</b>	Vacuum Filtration
<b>Drying Apparatus</b>	Oven at 120 °C

### 3.4 SYNTHESIS OF RUTHENIUM OXIDE

In this section, Adams method was employed for the synthesis of ruthenium oxide electrode material.

*“When I returned from war service in the spring of 1919, several of the problems I assigned my students involved catalytic reduction. For this purpose we were using as a catalyst platinum black made by the generally accepted best method known at the time. The students had much trouble with the catalyst they obtained in that frequently it proved to be inactive even though prepared by the same detailed procedure which resulted occasionally in an active product. I therefore initiated a research to find conditions for preparing this catalyst with uniform activity.” - Roger Adams*

In trying to solve the problem they had, Adams and his group of students converted the spent catalyst to chlorplatinic acid and it was contaminated with some organic materials. Boiling aqua regia dissolved the platinum but the solution remained black from the presence of some unknown substance that was not oxidized. To remove this it seemed wise to employ oxidation at a higher temperature than that involved with boiling aqua regia, so fusion with solid sodium nitrate was selected for the purpose. Removal of the aqua regia by evaporation and then fusion of the residue with sodium nitrate gave voluminous fumes of nitric dioxide and after a bit a brown precipitate appeared which proved to be platinum dioxide. A test of this product as a catalyst resulted in its immediate reduction to a platinum black with potent activity.

They put more effort in trying to find conditions for preparing a catalyst of satisfactory and uniform activity. In 1922 in the Journal of American Society, V. Voorhees with Adams as a joint author [258] set out not only the method of preparation of platinum oxide catalyst, but also the details of the presumed mechanism of its operation. The presence of oxygen in platinum

black had already been postulated as necessary to its activity as a catalyst in hydrogenation reactions and Adams and Voorhees concluded that the oxides of platinum, if prepared in a finely divided state, would be as effective catalysts as any that could be prepared, and would be distinctly more active than the best platinum black since the maximum amount of oxygen in the latter as platinum oxides was only around 20 per cent.

After these efforts and trying to improve the method at hand, a number of papers including Adams as the joint author emerged. In England, Johnson Matthey collaborated with May & Baker Limited, ammonium chlorplatinite was substituted for chlorplatinic acid, the sodium nitrate was first fused alone, and the final melt was poured directly into water so that the excess sodium nitrate and other salts dissolved immediately, leaving the platinum oxide behind, so avoiding the tedious digestion of the melt and reducing the time required for preparation. This method has since been the subject of further modifications in terms of the temperatures employed and of the ratio of sodium nitrate to ammonium chlorplatinite, but basically it still serves as one reliable means of production, and large quantities of Adams' catalyst have been prepared in this way over the years. Recently in 1960, Dr. Shigeo Nishimura, of the University of Tokyo put forth an interesting development where he prepared an Adams-type catalyst using rhodium oxide and platinum oxide. Notably, in the past 40 years, other types of hydrogenation catalysts have been developed and a great-if incomplete wealth of understanding of their behavior has been built up [259]. In this study, the synthesis of the ruthenium oxide electrode material was inspired by the Adams method whereby a pre-determined amount of the catalyst precursor was dissolved in 10mL of Isopropanol until a metal concentration of  $3.5 \times 10^{-2}$  M was achieved and magnetically stirred for 1 and a half hour. 5g of the finely ground  $\text{NaNO}_3$  was added to the mixture and stirred for a further 30 minutes. This mixture was then placed in a

pre-heated oven at 80°C until all the Isopropanol had evaporated. The dried precursor or salt mixture was then reacted in a pre-heated furnace at 280°C. The obtained metal oxide was then cooled and washed with UP water until all unreacted salt was removed. The final step was to dry the metal oxide in an oven at 100°C. Below is a schematic presentation of the method used and a table with materials and parameters used in the method. The molar ratio of the materials were (Ru 0.00035: NaNO<sub>3</sub> 0.059: Isopropanol 0.166 and the support material 0.007mol).

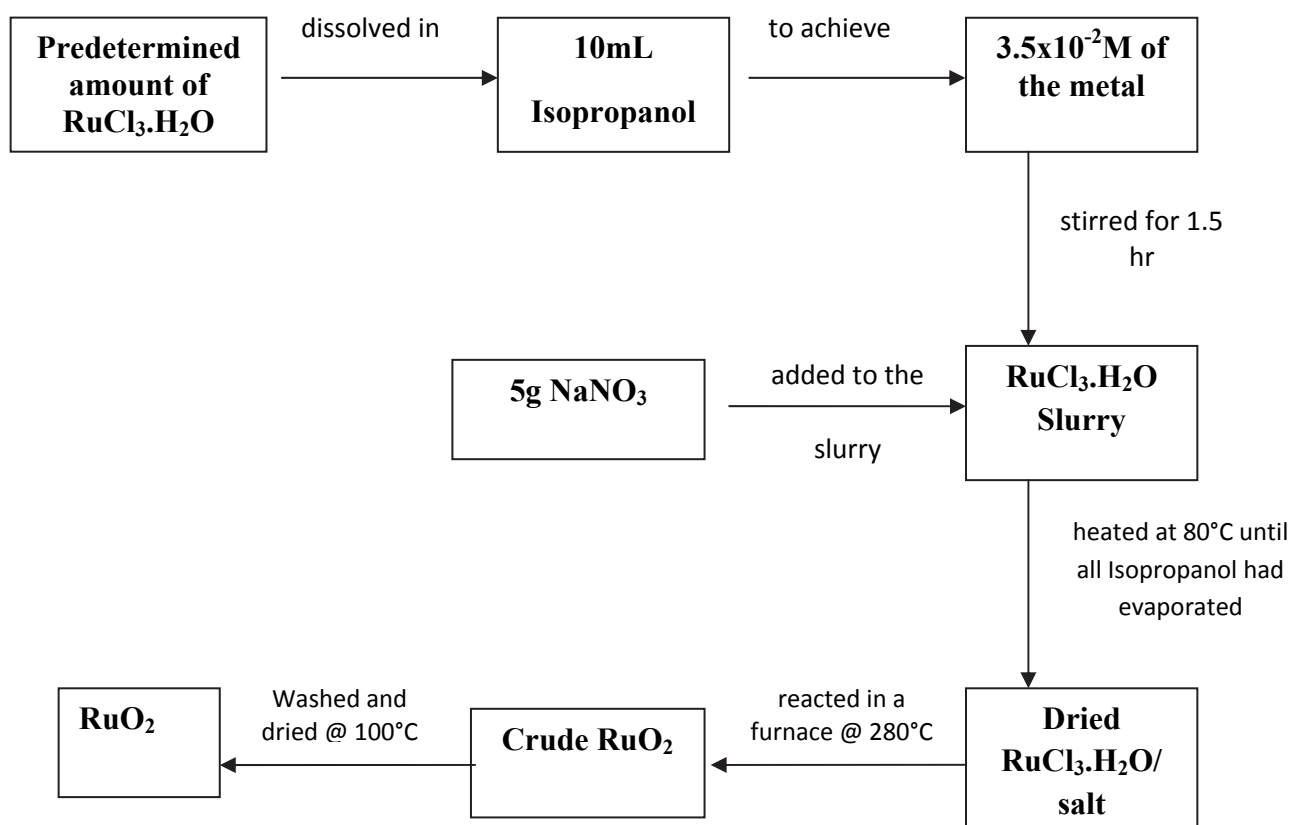


**Figure 3.4:** A schematic illustration of Adam's Method.

**Table 3.6:** Materials and parameters used in the Adams Method.

<b>Materials used</b>	RuCl <sub>3</sub> .H <sub>2</sub> O Isopropanol NaNO <sub>3</sub>
<b>Solvent Evaporation</b>	Oven at 80°C
<b>Rinsing Apparatus</b>	Vacuum Filtration
<b>Drying Apparatus</b>	Oven at 100°C

### 3.5 ELECTRODE PREPARATION

For all the electrode material powders, electrodes were prepared using the procedure follows;

- (1) 80wt% Active material
- (2) 10wt% Carbon Black
- (3) 10wt% PVDF
- (4) N-Methyl Pyrrolidone (NMP) solvent

Slurry of ingredients (1) to (3) in NMP was prepared in a marble mortar and pestle. Carbon paper was used as the current collector. The electrode material was then deposited on the carbon paper using a small paint brush. Thereafter, the samples were dried under vacuum oven at 120 °C overnight. After drying, the electrode was rolled flat and punched into 10 mm diameter circles, which were used as electrodes for the electrochemical testing. The electrochemical cycling performances of the synthesized electrode materials electrodes were tested with button cells (see figure (3.5)).



**Figure 3.5.:** Photograph of the coin cell used for electrochemical cycling testing.

The button cell consists of a stainless steel and copper discs with the same diameter as the working electrodes, but 10 times more than the electrode in thickness. The two electrodes and the separator were soaked in the electrolyte solution first before being assembled in the button cell. The copper side was negatively charged whereas the stainless steel side was positively charged to give a galvanostatic charge/discharge curves using 6M KOH and 1M  $\text{Na}_2\text{SO}_4$ . A schematic presentation of the electrode preparation is as follows:



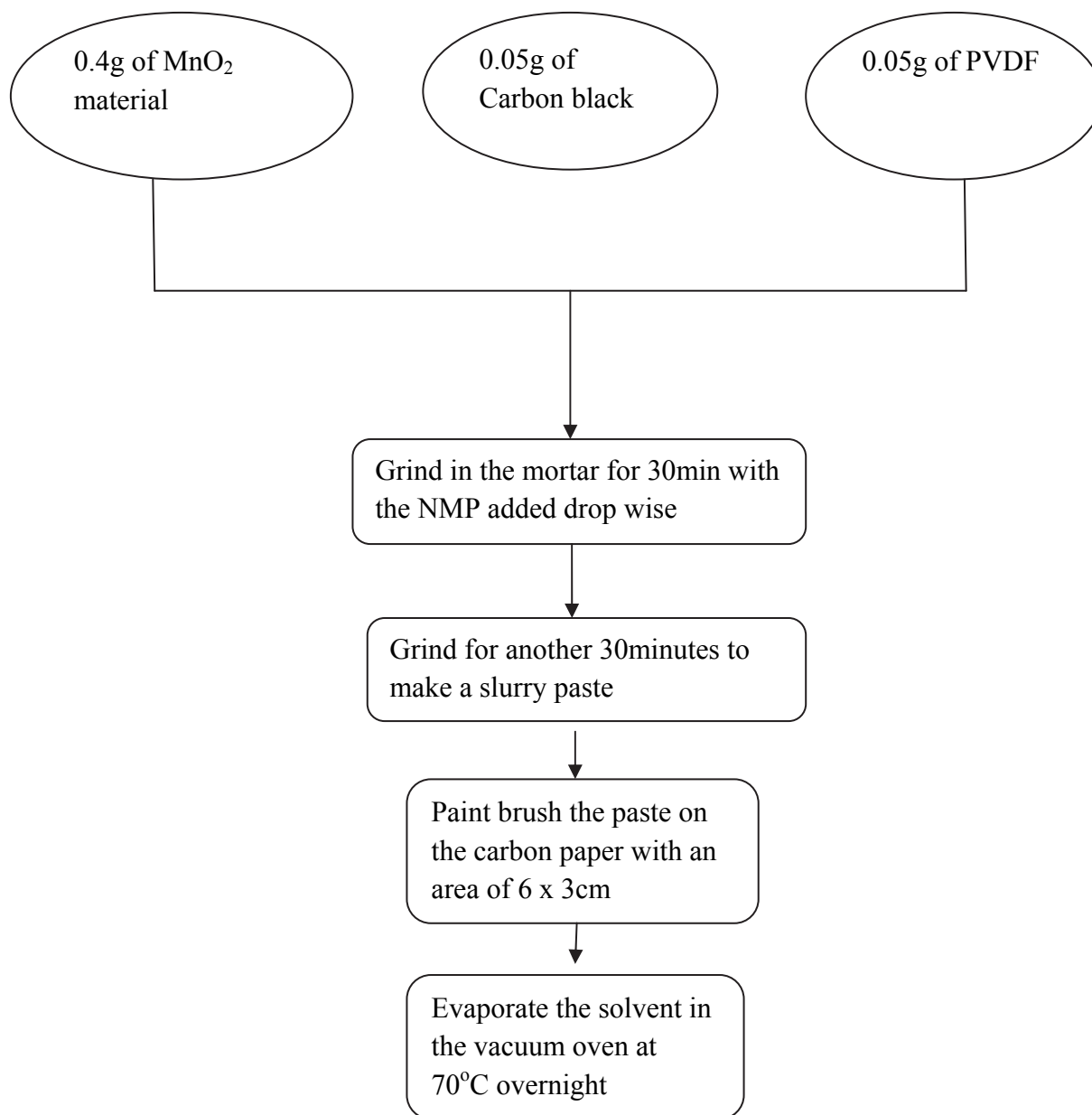


**Figure 3.6.:** Schematic presentation for the electrode preparation.

**Table 3.7:** Cell materials specifications.

<b>Electrode Area</b>	0.78 cm
<b>Electrolytic Separator Membrane</b>	Celgard® 2325
<b>Celgard® 2325 Porosity</b>	41 %
<b>Celgard® 2325 Thickness</b>	25 $\mu\text{m}$
<b>Electrolyte</b>	6M KOH and 1M Na <sub>2</sub> SO <sub>4</sub> .

### 3.6 MORPHOLOGICAL AND STRUCTURAL ANALYSIS

The morphological and structural analysis of novel electrode materials were systematically investigated by scanning electron microscope (SEM), transmission electron microscope (TEM), X-ray diffraction (XRD) and Brunauer-Emmett-Teller (BET) analysis.

#### 3.6.1 Scanning Electron Microscopy

Scanning Electron Microscopy (SEM) is more powerful as compared to using an ordinary microscope. The combination of higher magnification, larger depth of focus, greater resolution, and ease of sample observation makes the SEM one of the basic research tools. SEM is a versatile imaging technique capable of producing three-dimensional images of material surfaces. The basic operation in SEM entails the interaction of an accelerated highly mono-energetic electron beam, originating from the cathode filament, with the atoms at the sample surface. Scattered electrons are collected by a detector, modulated and amplified to produce an exact reconstruction of the sample surface and particle profile.

A prerequisite for effective viewing is that the surface of the samples should be electrically conductive. During operation, electrons are deposited onto the sample. These electrons must be conducted away to earth. Thus, conductive materials such as metals and

carbon can be placed directly into the SEM whereas non-metallic samples have to be coated with a gold metal layer to be observed.

The microscope beam energy can be varied over the range from 5 – 40 KeV, with a maximum resolution of 10 nm. The EDAX analyzer is equipped with window range, allowing light elements analysis from carbon upwards. Parameters for SEM analysis are tabulated below.

**Table 3.8:** The Operating Parameters of the FEI Nova Nano FEG SEM 230

<b>Accelerating gun filament</b>	Tungsten
<b>Filament Current</b>	28pa
<b>Accelerating voltage</b>	3kV
<b>Aperture</b>	30 $\mu$ mm
<b>Resolution</b>	3 nm

### 3.6.2 Transmission Electron Microscopy

Transmission Electron Microscopy (TEM) probes the internal structure of solids and provides access to micro-structural details. In electrode materials studies, TEM is used in the investigation of average particle size, particle shape and particle size distribution.

In TEM operation, a narrow electron beam originating from a tungsten filament is concentrated onto an ultrathin sample surface using a series of magnetic lenses. The electrons interact with sample atoms while penetrating the thin sample structure leading to the transmittance of electrons and the production of secondary electrons. Secondary electrons pass through an aperture to produce an image on a fluorescent screen. For carbon-supported metal electrocatalysts, metal particles appear as dark areas and low atomic weight carbon supports appear as light areas in the resultant micrographs due to differences in electron transmittance

with increasing atomic weight [237-247]. The obtained information is often complemented by quantitative information such as total surface area and porosity.

TEM analyses were done on the synthesized electrode materials samples. A spatula tip of the sample material was dispersed in 5 ml ethanol, followed by sonication of the suspension for 10 minutes. One drop of the suspension was dropped onto a hollow formvar film-coated copper grid, and the ethanol allowed to evaporate, before mounting the grid into the shaft of the microscope.

**Table 3.9:** TEM Operating Parameters.

<b>Microscope</b>	Tecnai G2 F20 X-Twin Mat FEG-TEM
<b>Accelerating Voltage</b>	200 kV
<b>Extraction Voltage</b>	3950 V
<b>FEG emission Current</b>	54 $\mu$ A
<b>Condenser aperture</b>	3
<b>Objective aperture</b>	2
<b>Exposure Time</b>	3 seconds

### 3.6.3 X-Ray Diffractometry

X-ray Diffractometry (XRD) is a powerful tool in the study of crystallinity and atomic structure of materials and forms an integral part in a comprehensive characterization study of electrode materials..

It is used extensively in the determination of Bravais lattice types and unit cell dimensions. The dimensions of x-ray wavelengths are in the same order as nanoparticle sizes, hence its application in this study.

XRD allows for the study of crystal anisotropy and the correlation between structural features and observed chemical properties [248].

In XRD, crystalline solids are bombarded with a collimated x-ray beam which causes crystal planes atoms, serving as diffraction gratings, to diffract x-rays in numerous angles. Each set of crystal planes ( $hkl$ ) with inter-planar spacing ( $d_{hkl}$ ) can give rise to diffraction at only one angle. The diffractions are defined from Bragg's Law ( $n\lambda = 2d \sin \theta$ ), where the intensities of diffracted x-rays are measured and plotted against corresponding Bragg angles ( $2\theta$ ) to produce a diffractogram. The intensities of diffraction peaks are proportional to the densities or abundance of the corresponding crystal facets in the material lattice. Diffractograms are unique for different materials and can therefore qualitatively be used in material identification. XRD can also be used quantitatively for the determination of average particle size by use of the Scherrer equation, given as:

$$D = 0.9\lambda / \beta \cos \theta \quad (3.1)$$

D = particle size,

0.9 = shape factor;

$\lambda$  = x-ray wavelength,

$\beta$  = peak-width at half peak height (radians);

$\theta$  = angle of reflection [249-253].

Experimental parameters for the XRD analysis are given as follows:

**Table 3.10:** XRD Operating Parameters.

<b>X-ray Diffractometer</b>	Bruker multipurpose powder diffractometer (D8 Advance)
<b>Tube</b>	Copper
<b>Detector</b>	Sodium Iodide
<b>Monochromator</b>	Graphite
<b>Generator operation</b>	40kV and 40mA
<b>Electron intensity</b>	40 kV
<b>X-ray source</b>	CuK $\alpha$ 1 ( $\lambda = 1.5406\text{\AA}$ )
<b>Scan rate</b>	0.05 $^{\circ}$ /min

### 3.6.4 Surface Area and Porosity Determination by N<sub>2</sub> Physisorption

In this investigation, the surface area and porosity of the synthesized electrode materials were investigated with high sensitivity using an accelerated surface area and porosity analyzer (Micromeritics ASAP 2010). This information was used to demonstrate how the surface area and porosity which may affect the reactivity of the materials as it increases, affects the surface area for electron transfer.

Haber [253] stated that the Brunauer-Emmett-Teller (BET) method, in gas-adsorption, was best suited for the determination of total surface area and porosity of materials. The best known theory of physisorption is undoubtedly that of Brunauer, Emmett and Teller [254] who developed the earlier Langmuir's ideas to describe multi-molecular adsorption. By introduction of some simplifying assumptions, the BET theory provides an extension of the Langmuir monolayer model. The operating parameters are listed in table (3.11).

**Table 3.11:** BET Operating Parameters.

<b>BET Analyser</b>	Micromeritics ASAP 2010
<b>Purging Gas</b>	Helium (UHP) obtained from Afrox
<b>Analysis Temperatur</b>	-196 °C

The accelerated surface area and porosity analyzer consisted of a mercury manometer; gas-tight burette, thermostat; liquid N<sub>2</sub>-cooled Dewar flask, and a high-vacuum oil pump. High pressures and cryogenic temperatures are used to increase the adsorption rate onto solid surfaces [254]. Approximately 100 mg of the sample powder was transferred and sealed in a sample tube. Calibration with a silica-alumina standard was conducted prior to analysis.

### 3.6.5 FOURIER TRANSFORM INFRARED SPECTROSCOPY

In this investigation the molecular fingerprints of the materials were characterized by Fourier-transform infrared spectroscopy (FTIR, AVATAR 360, America). IR radiation is passed through a sample. Some of the infrared radiation is absorbed by the sample and some of it is passed through (transmitted). The resulting spectrum represents the molecular absorption and transmission, creating a molecular fingerprint of the sample. Like a fingerprint no two unique molecular structures produce the same infrared spectrum.

This fingerprint representation of a sample has absorption peaks which correspond to the frequencies of vibrations between the bonds of the atoms making up the material. Because each different material is a unique combination of atoms, no two compounds produce the exact same infrared spectrum. Therefore, infrared spectroscopy can result in a positive identification (qualitative analysis) of every different kind of material. In addition, the size of the peaks in the spectrum is a direct indication of the amount of material present. With modern software

algorithms, infrared is an excellent tool for quantitative analysis. And these attributes made infrared spectroscopy attractive and useful for our investigation.

### 3.7 ELECTROCHEMICAL CHARACTERISATION TECHNIQUES

#### 3.7.1 Cyclic Voltammetry (CV) Analysis

Cyclic voltammetry (CV) was used in the study of electrode surface reactions, the behavior of electrochemically-active species, and in the investigation of the quality of electrode materials. CV provides information on the thermodynamics of redox processes and the kinetics of heterogeneous electron-transfer reactions. It plays an integral role in a comprehensive characterization of nanophase electrocatalysts. CV can be used advantageously to probe surface reactions *in-situ* under well-controlled conditions, giving insight into the catalytic mechanisms and the activity of the electrode materials [255, 256].

CV entails cycling a potential applied to an electrode immersed in a quiescent electrolyte solution, containing an analyte species, through a defined potential range and measuring the resultant current. The measured current is a result of electron flow through the electrochemical circuit and is due to diffusional mass transfer of electroactive species as migration and convection are minimized. The applied potential is swept back and forth between two designated potentials, at a constant rate, by a potentiostat. Typically, a three-electrode system consisting of a working electrode, reference electrode, and counter electrode is used. The working electrode is the electrode of interest at which potential is applied. The reference electrode experiences zero current and has a known standard potential against which all other potentials are measured. The counter electrode completes the circuit and is usually Pt wire, graphite, or glassy carbon [245]. The output signal is called a voltammogram which represents a plot of current in amperes, versus potential in volts.



In this work, it was used to study the electrochemical properties and the analyses were conducted at room temperature (25 °C). Electrochemical experimental parameters are given in table (3.12)

**Table 3.12:** Cyclic Voltammetry Parameters.

<b>Voltammetric Assembly</b>	Metrohm
<b>Potentiostat</b>	Eco-Chemie Autolab PGSTAT 30
<b>Reference Electrode</b>	Standard Calomel Electrode
<b>Counter Electrode</b>	Platinum Gauze

### 3.7.2 Charge/discharge testing

Charge/discharge tests were carried out using a Land-BTL10 fully automatic program test instrument. The system is capable of switching between charge and discharge automatically according to the cut off potentials set. For the supercapacitors electrode materials synthesized, tests were run at a voltage range of 0.1 to 1V versus. The capacitance values were calculated using the equation below:

$$C = \frac{3.6 Q}{\Delta V} \quad (3.2)$$

Where  $C$  = Capacitance in  $F$  ,  $Q$  = Capacity in mAh/g and  $\Delta V$  = Voltage difference in V

### 3.7.3 Impedance Spectroscopy

Electrochemical Impedance Spectroscopy (EIS) is a powerful method of characterizing many electrical properties of materials and their interfaces with electronically conducting electrodes. Its application to the mechanistic study of electrochemical processes has expanded rapidly over the last two decades and has proved to be a powerful experimental method for the study of surface processes. It was applied in the present work to study the discharge mechanism

of the negative electrodes (anodes) of Li-ion batteries. Impedance analysis was conducted using an Eco-Chemie AUTOLAB PGSTAT30 Frequency Response Analyzer. The entire system applies an AC excitation to an electrochemical cell and measures the response of the cell to the excitation, and digitizes and stores the resulting data for processing and display. The frequency of the AC excitation ranges from 50  $\mu$ Hz to 100 kHz.

# CHAPTER 4

## SYNTHESIS AND CHARACTERIZATION OF 1D CONDUCTING POLYMERS AS ELECTRODE MATERIALS FOR SUPERCAPACITORS

### 4.1 Introduction

Conducting polymers are unique for provision of pulsed high power. They possess high pseudo capacitance which arises from a doping process which in the simplest case involves the introduction of positive holes (or polarons) together with charge-balancing anions. Also the charge processes, pertain to the whole polymer mass and not only the surface as is the case with the double layer activated carbons and this contributes to the high capacitance. Furthermore their charge-discharge processes are generally fast and these features suggest the possibility to develop devices with low Equivalent Series Resistance (ESR) and high specific energy and power.

1D nanostructures (structures that are defined as having at least one dimension, between 1 and 100 nm) were of interest in this study due to the fact that they have fascinating properties and applications which are superior to their bulk counterparts [4-6]. Realization of making new types of nanostructures like downsizing the existing structures into the 1-100nm regime might create a large number of opportunities. An example is provided where ‘smaller’ has meant greater performance in microelectronics ever since the invention of integrated circuits: more components per chips, faster operation, lower cost and less power consumption [7]. Miniaturization may also represent a trend in a range of other technologies. A wealth of interesting and new phenomena are associated with nanometer-sized structures e.g. size-dependent excitation or emission [9] quantized or (ballistic) conductance [263], Coulomb

blockade (or single-electron tunneling, SET)[264] and metal insulator transition [265]. They are regarded as a good system to investigate the dependence of electrical or mechanical properties on dimensionality and size reduction or quantum confinement and also they are expected to play a role as both interconnects and functional units in fabricating electrochemical devices with nanoscale dimensions.

In this study 1D polypyrrole nanowires were synthesized using two methods, Biomolecules assisted method and electropolymerization by doping because, currently, the synthesis of 1D nanostructures of conducting polymers is often accomplished with the assistance of a porous membrane known as “hard template” [326,176]. Porous alumina, track-etched polycarbonate membrane, zeolite and glass membrane have been used as templates to synthesize conducting polymer nanostructures. These templates need to be removed after the polymerization in order to get nanostructures. However, the step of removing templates is inconvenient and may lead to disorder or destruction of the final products. Using sacrificial template to prepare conducting polymer nanostructures is an interesting and efficient route to solve this problem. Recently, Pan and co-workers have synthesized PANI nanotubes in the presence of nanowires or nanotubes of manganese oxide that was spontaneously removed after the reaction. These “self-assembly” or “soft template” approaches are alternative ways to obtain 1D conducting polymer nanostructures without the need for further removal of templates. These methods use nanostructured molecules or molecular assemblies, such as surfactant micelles, to control the growth of conducting polymers. However, it is very difficult to recycle the surfactants after polymerisation. Using biomolecules as morphology-directing agents is a new route to obtain 1D nanostructures of conducting polymers (176). Compared to the methods mentioned above, biomolecules-assisted approach is a simple, cheap, rapid, mild

and environmentally benign method to produce uniform nano-scale conducting polymers without the need to remove the templates as well as to recycle surfactants. In addition, porous network of 1D conducting polymer nanostructures can be electrochemically deposited directly on various electrodes such as metal oxide and carbon based electrode. As a result, 1D conducting polymer nanostructures prepared by this method may exhibit excellent electrochemical capacitance performance and thus would be good candidates for electrode materials of supercapacitors.

## 4.2 ELECTROCHEMICAL POLYMERIZATION OF CONDUCTING POLYPYRROLE NANOWIRES

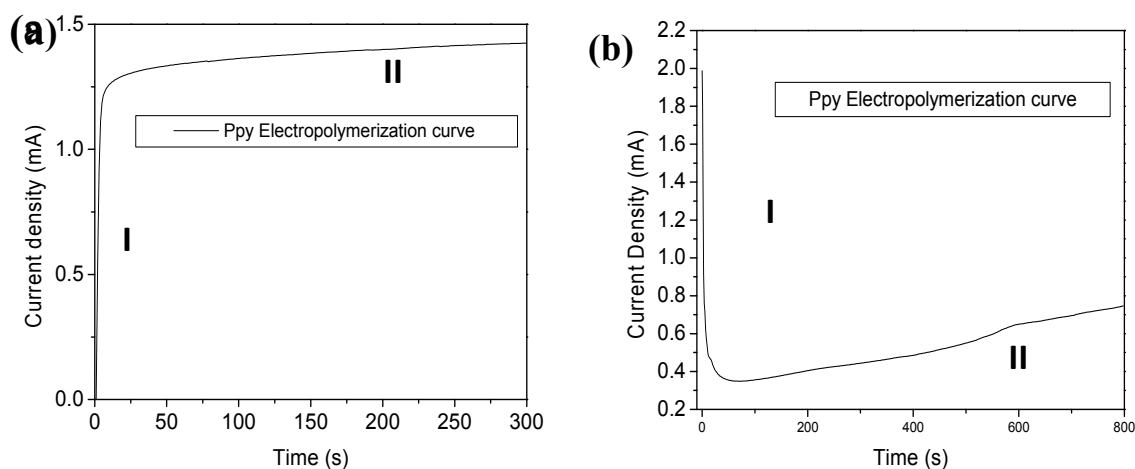


**Figure 4.2.1** Potentiostatic curve for the electropolymerization of polypyrrole nanowires on a nickel foil in the presence of (a) Gelatine and (b) TSNa.

Potentiostatic curves for the electropolymerization of polypyrrole nanowires in the presence of gelatin and TSNa are presented in figure (4.2.1). The electropolymerization of pyrrole in the presence of TSNa was initiated at  $\sim 0.35$  mA current density, which was much lower than that of pyrrole in the presence of gelatine with 0.07M LiClO<sub>4</sub> which was at

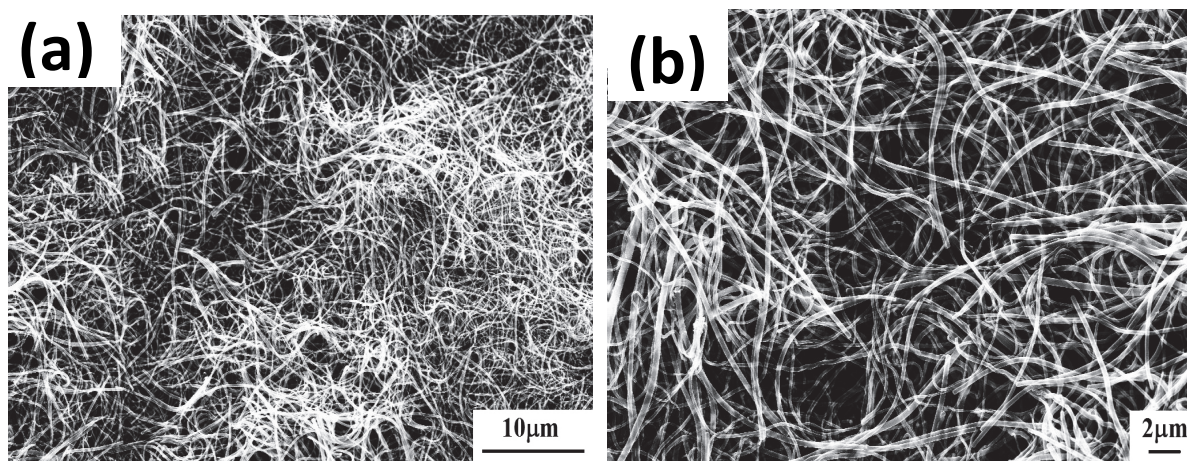
~1.6mA . This implied that the electropolymerization of pyrrole was much easier in TSNa than in LiClO<sub>4</sub>/gelatine system.

Two different phases can be distinguished for each electropolymerization curve. At phase **(I)** of **(a)** there is an initial current increase of the process; this is due to the electrical charge of the double layer and the diffusion layer. And at phase **(I)** of **(b)**, the current decreases as a result of metal ion depletion or the formation of the diffusion layer. For both curves at phases **(II)** the current remains nearly constant during the growth of the polypyrrole nanowires on the substrate.

### 4.3 PHYSICAL CHARACTERIZATION OF CONDUCTING POLYPYRROLE NANOWIRES

#### 4.3.1. Surface morphology study for polypyrrole nanowires

The morphologies of the polypyrrole nanowires synthesized were studied via scanning electron microscopy (SEM) and transmission electron microscopy (TEM) and their micrographs are presented in figure (4.3.1) and discussed.



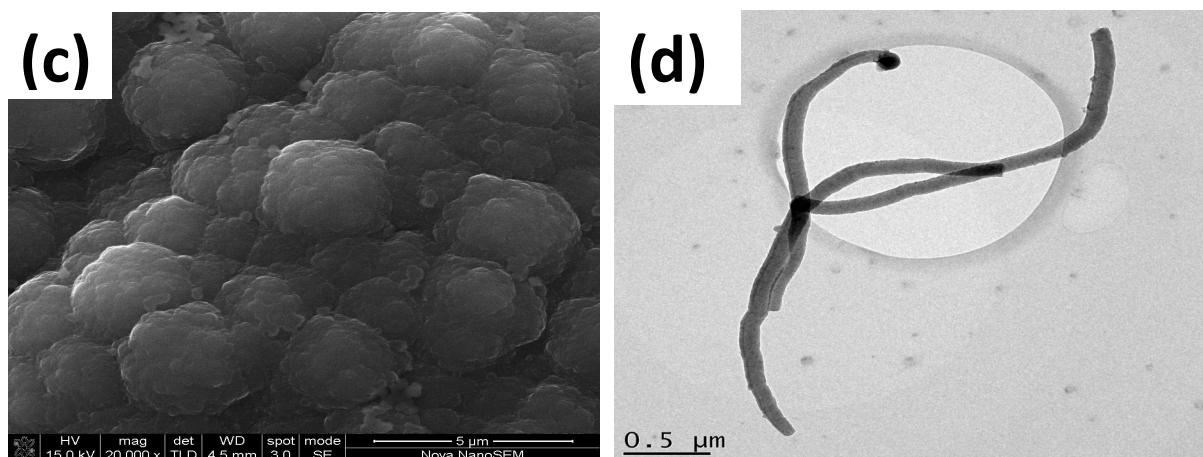


**Figure 4.3.1** (a), (b) SEM and (d) TEM micrograph of PPy superlong nanowires synthesized on the nickel electrode in the presence of gelatin, (c) SEM micrograph of cauliflower-like PPy synthesized in the absence of gelatin.

It is well known that gelatin is an amphoteric polyelectrolyte with a long chain containing various amino acids. Amino acids have  $-\text{NH}_2$  and  $-\text{COOH}$  functional groups, both of which provide the active sites for the adsorption of pyrrole monomer through hydrogen bond [274, 275]. As a result, pyrrole monomer are adsorbed onto the surfaces of the chain-shaped gelatin chain and then polymerized preferentially along this chain to form the PPy nanowires as the electrochemical reaction is initiated. Here, gelatin molecule acts as a soft template to guide the formation of the PPy nanowires. The effects of the concentrations of gelatin and pyrrole on the morphologies of the PPy nanowires were examined in order to further confirm the above-mentioned formation mechanism.

It can be seen clearly that the gelatin has a strong effect on the morphologies of the resulting PPy products. When the synthesis of the PPy was conducted without the gelatin figure 4.3.1 (c), only cauliflower-like products were obtained. On the other hand, regular, uniform and much longer wire-like PPy nanostructures can be observed with the addition of gelatin to the reaction system. The average diameter of the nanowires is about 100nm and the length is up to tens of microns, exhibiting ultra high aspect ratio. A close-up view of the

nanowires, Fig. 4.3.1(b), reveals that these nanowires are very uniform in shape with very even and smooth surface and rather flexible. It should be noted that, to the best of our knowledge, the PPy nanowires synthesized here are the longest so far synthesized by the soft template method. The TEM micrograph reveals also the smoothness and the uniformity of the surface of the nanowires and that they are solid.

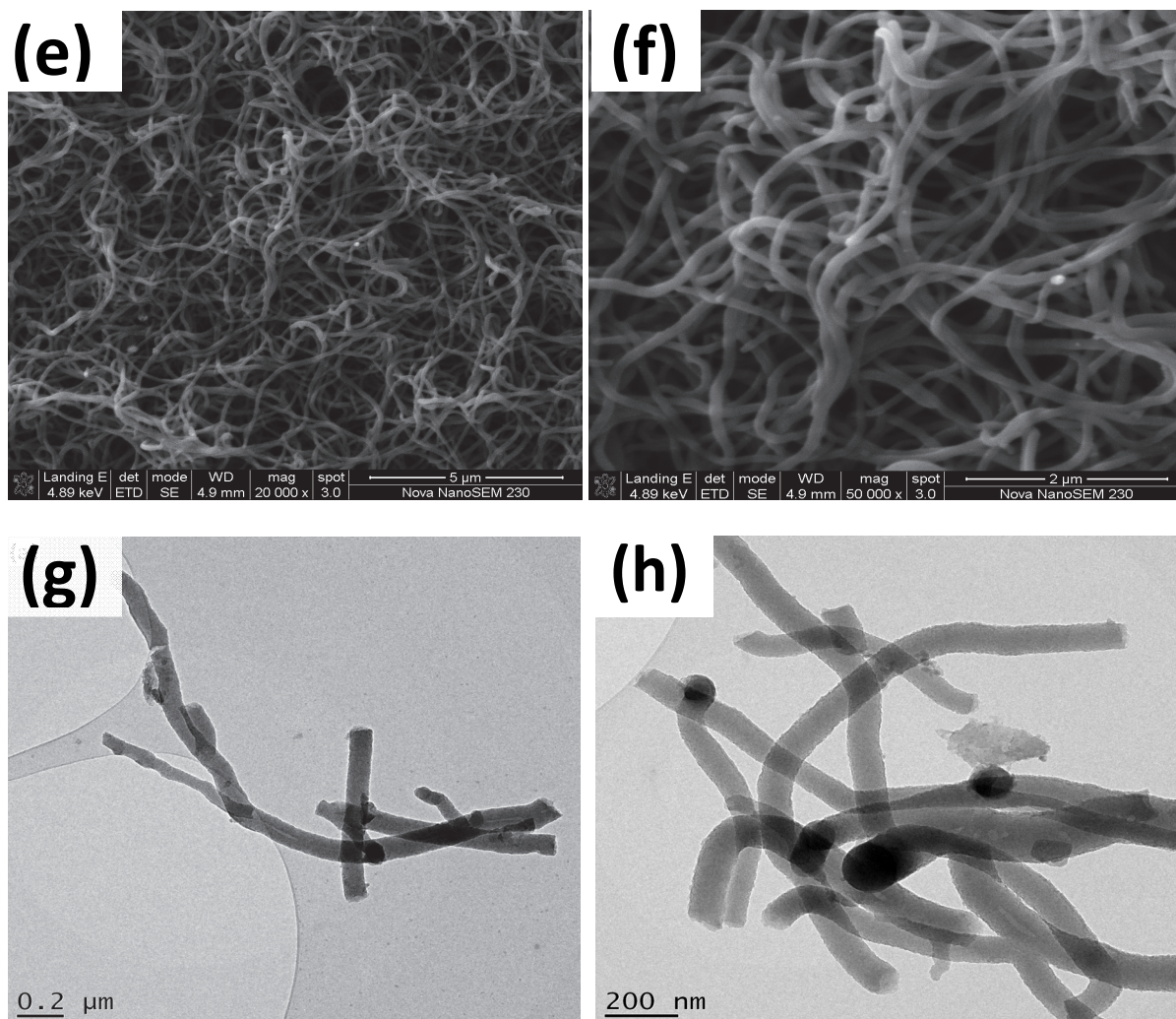


**Figure 4.3.1:** (e), (f) SEM and (g), (h) TEM images of PPy nanowires synthesized on a nickel electrode in the presence of TSNa.

It was noted that the incorporation of molecules or molecular assemblies into the conducting polymers, like dopants as is the case here, may afford some new properties to the



final products, and thus making the methods very attractive for the synthesis of functional nanomaterials of conducting polymers.

The second set of polypyrrole nanowires were also synthesized on a nickel foil but TSNa was used as a dopant. It is interesting to observe that the obtained nanowires were thicker, also long but not as the former and the average diameter of the nanowires was 200nm, which is double that of the nanowires synthesized in the presence of gelatine. The dopant method synthesized nanowires also display a uniform shape with even and smooth surface and flexibility. The TEM Micrographs also reveal the smoothness, uniformity of the surface and solidity of the nanowires.

#### **4.3.2 Functional groups analysis of the synthesized polypyrrole nanowires**

In this investigation the molecular fingerprints of the materials were characterized by Fourier-transform infrared spectroscopy (FTIR, AVATAR 360, America). IR radiation is passed through a sample. Some of the infrared radiation is absorbed by the sample and some of it is passed through (transmitted). The resulting spectrum represents the molecular absorption and transmission, creating a molecular fingerprint of the sample. Like a fingerprint no two unique molecular structures produce the same infrared spectrum.

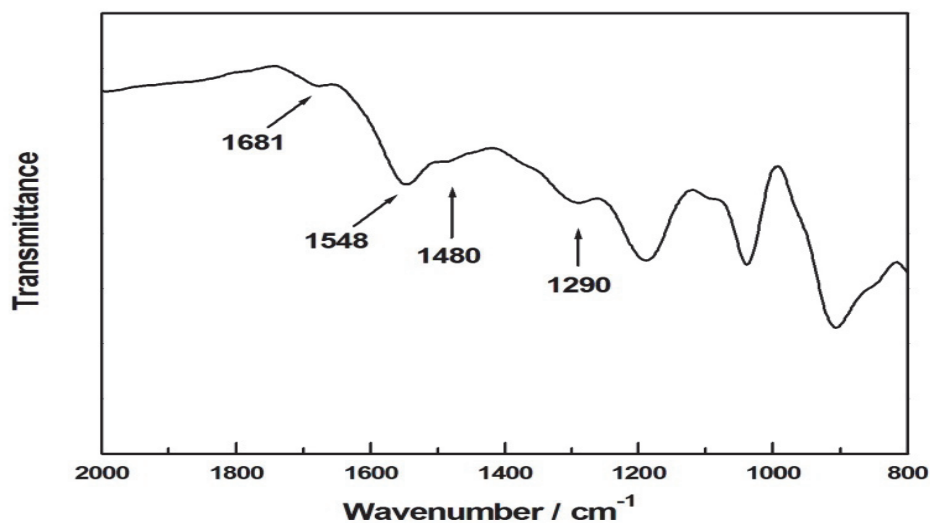


**Figure 4.3.2:** FTIR spectrum of polypyrrole nanowires synthesized in the presence of gelatin.

Figure (4.3.2) shows the typical FTIR spectrum of the superlong nanowires synthesized in the presence of gelatin. The characteristic peaks of PPy, such as asymmetric ring stretching vibration at  $1548\text{cm}^{-1}$ , symmetric ring stretching vibration at  $1480\text{cm}^{-1}$ , and the C–N stretching vibration at  $1290\text{cm}^{-1}$  were observed, thus confirming the formation of the PPy. The peak at  $1681\text{cm}^{-1}$  should be owned to the presence of the gelatin, which means that gelatin has been incorporated into the superlong nanowires as a dopant.

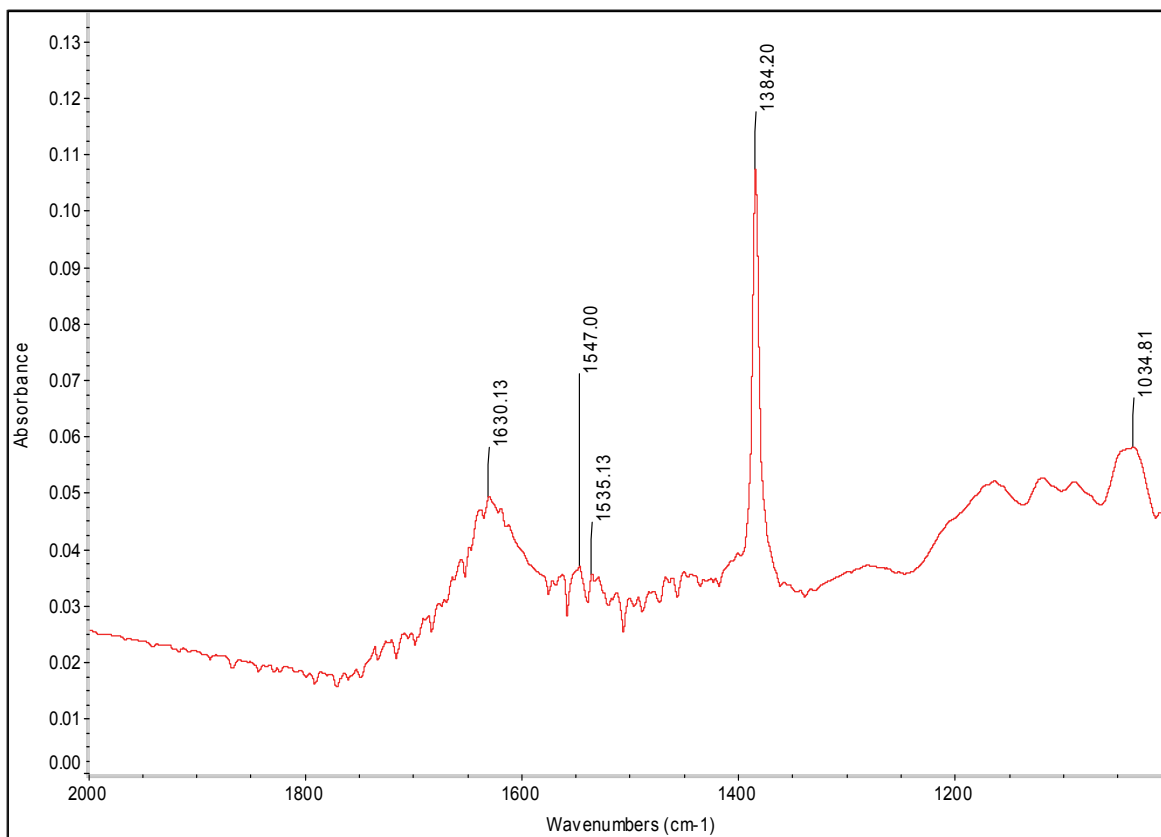


**Figure 4.3.3:** FTIR spectrum of polypyrrole nanowires synthesized in the presence of TSNa.

Figure (4.3.3) above is an FTIR spectrum of the Polypyrrole nanowires synthesized in the presence of TSNa as a dopant. According to [276, 277], the most significant feature which reflects the doping process is the appearance of the broad absorption band above  $2000\text{cm}^{-1}$ , attributed to an intra-chain (free carrier) excitations. The band  $1630.13\text{cm}^{-1}$  is due to the presence of the doping agent TSNa. The  $1552\text{cm}^{-1}$  band corresponds to the C-C stretching vibrations in the pyrrole ring. The red shift of this band to  $1547\text{cm}^{-1}$  has been observed and is known that the skeletal vibrations involving the delocalized  $\pi$ - electrons are affected by doping of the polymer. The observed shift of this band may be caused by the degree of doping of the polymer [278]. The  $1537\text{cm}^{-1}$  peak is assigned to the stretching vibration of the C=C double bond of PPy [279]. The band at  $1384.20\text{cm}^{-1}$  is due to the C-H vibrations. The C-H and N-H in plane deformation vibration band is observed around  $1074\text{cm}^{-1}$  and  $926\text{cm}^{-1}$  and with

the sample, the band is observed at  $1034.81\text{cm}^{-1}$ . The red shifts which are observed in these bands determine that the sample has higher conductivity.

### 4.3.3 X-ray diffraction pattern of the synthesized polypyrrole nanowires in the presence of TSNa

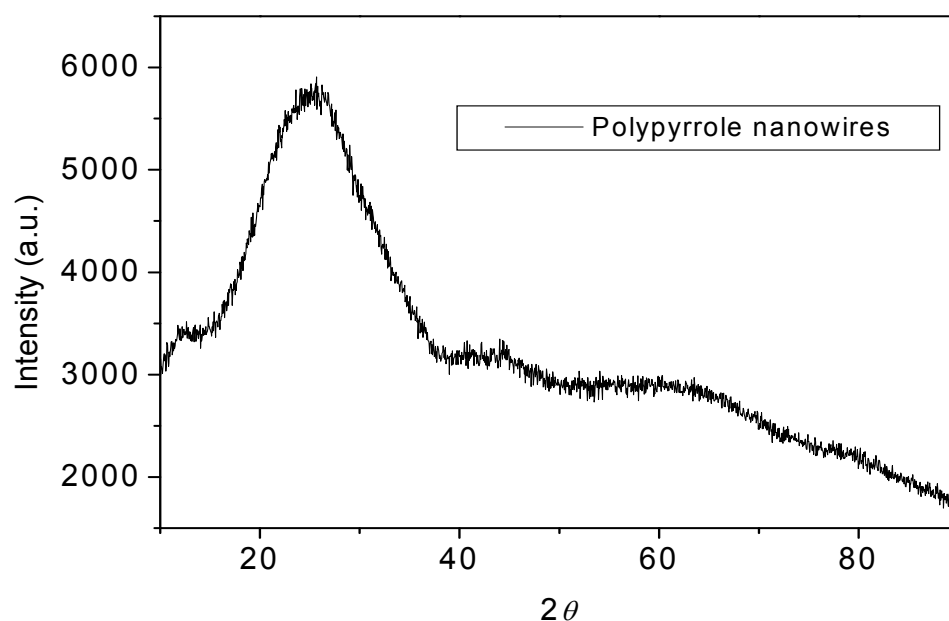


**Figure 4.3.4:** XRD pattern for the synthesized polypyrrole nanowires synthesized in the presence of TSNa

Figure (4.3.4) represents the Xrd pattern of the synthesized polypyrrole nanowires. He *et al.* [280] synthesized polypyrrole with three different morphologies, granular ( $2\theta = 18.5^\circ$  and  $d = 4.80 \text{ \AA}$ ), short nanowires ( $2\theta = 23.7^\circ$  and  $d = 3.64 \text{ \AA}$ ) and nanowire networks ( $2\theta = 22.8^\circ$  and  $d = 3.89 \text{ \AA}$ ). It was observed that the  $d$  spacing decreased in the PPy samples with the nanowires and nanowire networks morphology, in comparison with that in a common granular PPy and proposed the probability that there is a crystalline domain with condensed  $0.364 \text{ nm}$  spacing between PPy chains in the PPy sample with the nanowire morphology.

In this study, the X-ray diffraction pattern of PPy wires exhibits a broad peak at  $2\theta = 25.23^\circ$  ( $d=3.54\text{\AA}$ ) which is assigned to the scattering from PPy chain at the interplanar spacing in the PPy-TSNa [281, 282]. The results imply that the PPy chains in the PPy wires have ordered arrangement to some extent and agree with He *et al.* [280], TEM and the SEM analysis that there is a crystalline domain with condensed 0.354 nm spacing between PPy chains in the PPy sample with the nanowire morphology.

#### **4.4 ELECTROCHEMICAL CHARACTERIZATION OF CONDUCTING POLYPYRROLE NANOWIRES**

Electrochemical studies of the polypyrrole nanowires synthesized only in the presence of TSNa were carried out and are discussed in this section.

##### **4.4.1 Cyclic Voltammetry**

Cyclic Voltammetry (CV) of the polypyrrole electrode material was conducted, with nickel foil used as a working electrode, saturated calomel electrode used as the reference electrode and platinum gauze used as the counter electrode. Figure (4.4.1) shows the cyclic voltammograms of the polypyrrole electrode material. The potential range was -0.9V to 0.9V and the scan rate varied from 20, 25, 50 and 100mV/s at room temperature. The steady-state cyclic voltammogram presented broad anodic and cathodic peaks. Though the PPy/TSNa had poorly defined but distinguishable oxidation and reduction peaks, these can be observed at scan rates 50 and 100mV/s ~ -0.1 and -0.5 V, respectively.

Two features of this graph are especially remarkable. First, the box-like shape, indicating good electrochemical capacitive behavior with an almost 'square end' at the anodic reversal point, becomes more distinct right up to the highest sweep rates. Secondly, the

electrode material also performed well with a slight decrease in capacitance at higher scan rates.

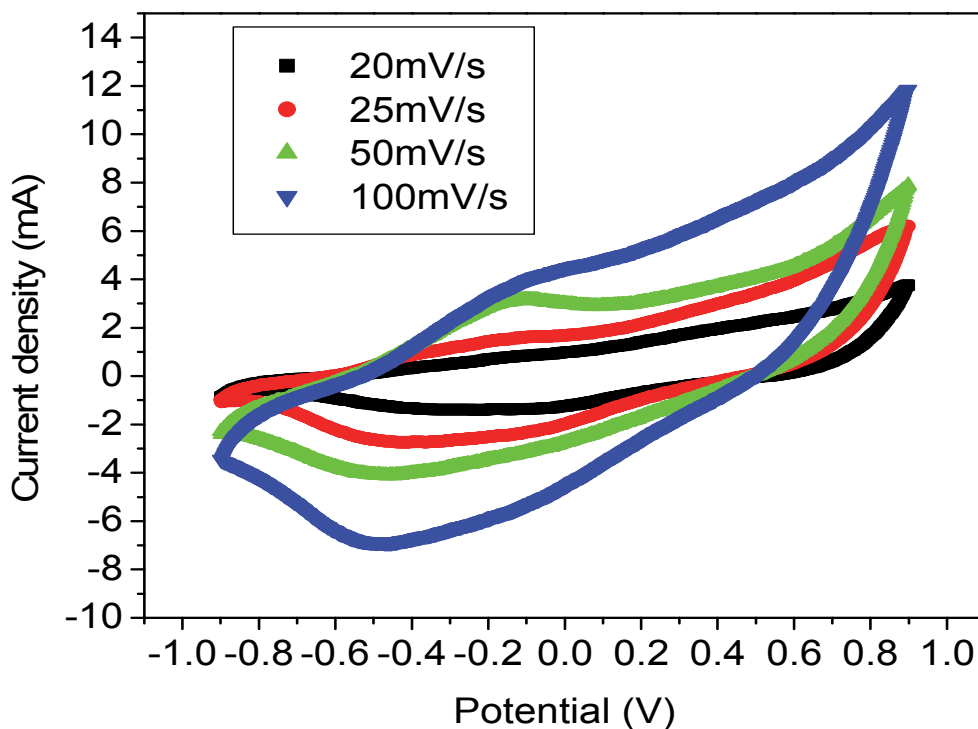


**Figure 4.4.1:** Cyclic voltammograms for polypyrrole nanowires synthesized in the presence of TSNa

Capacitance calculated from the cyclic voltammetric curves at 20, 25, 50 and 100mV/s scan rates, were determined to be 450 F/g, 496 F/g, 320 F/g and 400 F/g, respectively.

#### 4.4.2 Charge and discharge cycling

The Charge-discharge tests of the polypyrrole electrode material were done at a charge-discharge current of 60  $\mu\text{A}$  in a button cell from 0V to 1V. The charge-discharge cycles of the synthesized materials are presented in this section.

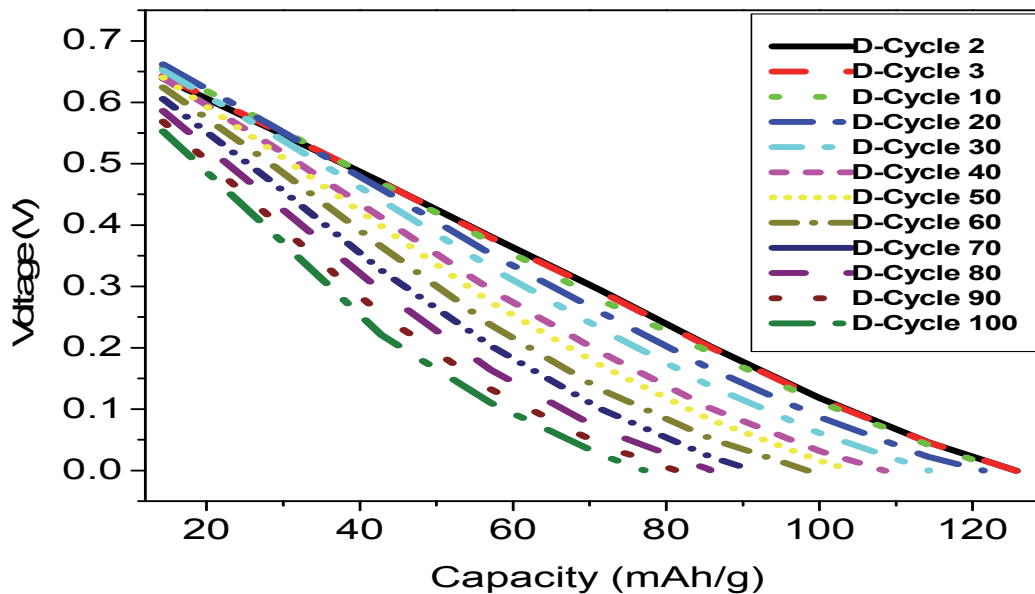
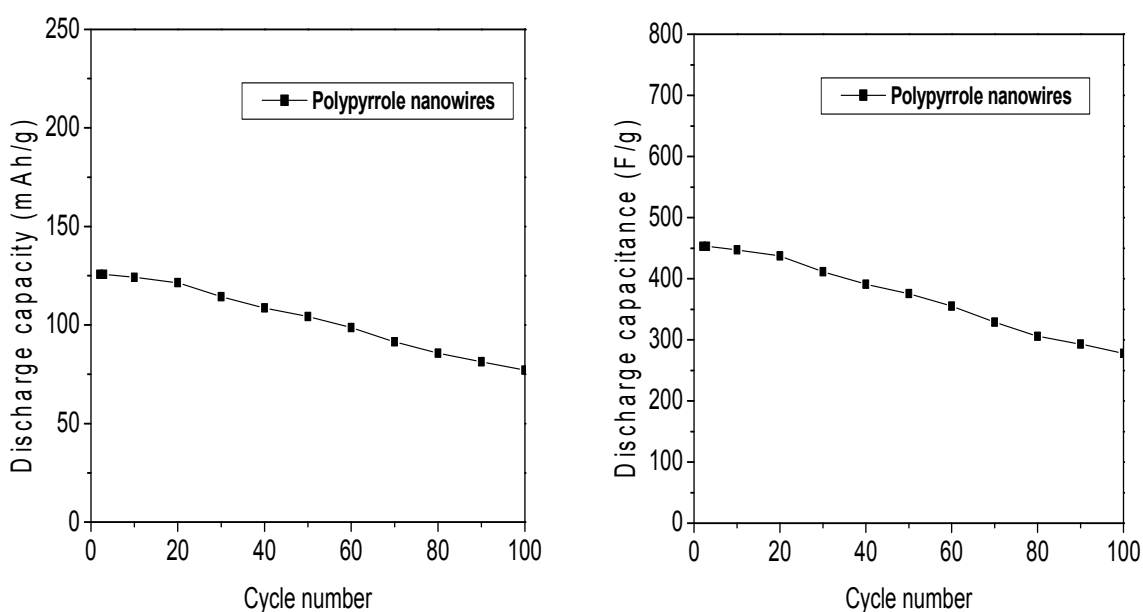


**Figure 4.4.2:** Discharge cycles of polypyrrole nanowires synthesized in the presence of TSNa

**Table 4.4.1:** Capacity and capacitance values of polypyrrole nanowires (TSNa).

Cycle Number	Charge Capacity (mAh/g)	Discharge Capacity (mAh/g)	Charge Capacitance (F)	Discharge Capacitance (F)	Efficiency %
2	172.9	125.7	622.4	453.0	72.7
3	168.6	125.7	607.0	453.0	74.6
10	157.1	124.2	566.0	447.1	79.1
20	152.9	121.4	550.4	437.0	79.4
30	140.0	114.3	504.0	411.5	81.6
40	128.6	108.6	463.0	391.0	84.4
50	125.7	104.3	453.0	375.5	83.0
60	115.7	98.6	417.0	355.0	85.2
70	108.6	91.4	391.0	329.0	84.2
80	101.4	85.7	365.0	305.5	84.5
90	97.1	81.4	350.0	293.0	84.0
100	92.9	77.1	334.4	277.6	83.0

The polypyrrole nanowires synthesized in the presence of TSNa, delivered a charge capacitance of 622.4F/g and a discharge capacitance of 453.0F/g with 72.73 % cycle efficiency, for the second cycle. For the third cycle, a charge capacitance of 607.0F/g and discharge capacitance of 453.0F/g were observed with 74.6% cycle efficiency. 334.4F/g and 277.6F/g charge and discharge capacitance for the 100<sup>th</sup> cycle, respectively, were observed. The 100<sup>th</sup> cycle discharge capacitance was 61.3% of the 2<sup>nd</sup> and 3<sup>rd</sup> cycle discharge capacitances, respectively. The discharge capacities and capacitances versus cycle number for the electrode materials are compared in figure (4.4.3).



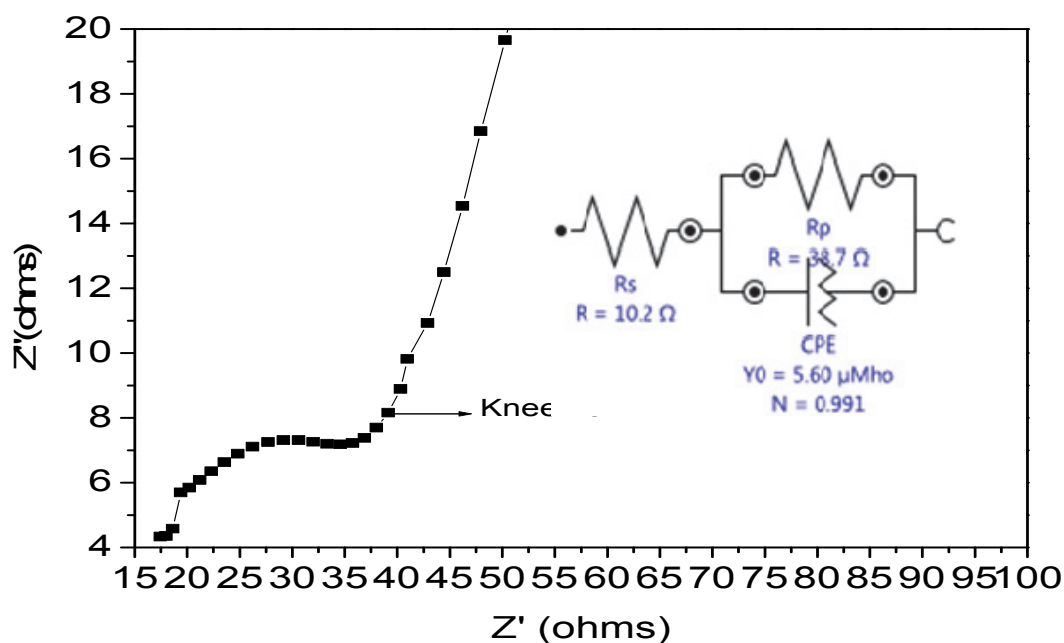
**Figure 4.4.3:** Discharge capacities and capacitances of polypyrrole nanowires synthesized in the presence of TSNa

Figure (4.4.3) shows that the polypyrrole nanowires discharge capacities and capacitances. After 100 cycles the discharge capacities and capacitances of the polypyrrole were 61.3% of the 2<sup>nd</sup> cycle with an average of ~4 % capacitance loss per cycle.



### 4.4.3 ELECTROCHEMICAL IMPEDANCE SPECTROSCOPY (EIS) ANALYSES

Electrochemical Impedance Spectroscopy (EIS) is an important analysis for a supercapacitor, since it can be used to evaluate the electrical properties that are useful for actual applications.



**Figure 4.4.4:** Nyquist plot of the polypyrrole nanowires in the presence of TSNa.

Figure (4.4.4) shows the impedance plots of polypyrrole nanostructures in 0.2M PBS recorded using a frequency range from 100 kHz to 0.1Hz at the applied voltage of 0 V versus SCE and an equivalent circuit diagram insert.

Firstly, there was a semicircle in the high frequency which is attributed to double-layer charging/discharging process [283]. The semicircle results from the parallel combination of resistance and capacitance and it was not well defined and this indicates that the charge transfer resistance is small, and our electrochemical system is kinetically fast. Thus, charges

(electrons) can be readily transferred into the highly conductive polypyrrole solid phase. This favourable charge transfer between the PPy and electrode surface is natural because the PPy was grown electrochemically in good contact with the base electrode. In addition, from the high frequency intercept of the real axis, the internal resistance ( $R_s$ ) was observed, which include the resistance of the electrolyte, the intrinsic resistance of the active material, and the contact resistance at the interface active material/current collector. Secondly, in the intermediate frequency region, the  $45^\circ$  line is the characteristic of ion diffusion into the porous structure of the electrode.

Thirdly, in the low frequency region, the linear region leans more towards imaginary axis and this indicates good capacitive behavior [283] and the slope of the plot increases and tends to become purely capacitive (vertical lines characteristic of a limiting diffusion process), which demonstrated that the electrochemical capacitance of this capacitor is higher.

The knee frequency of the PPy nanowires was determined to be 49.4Hz, the same value obtained by Peng et al.[322] and a better frequency response means a better power performance.

## 4.5 CONCLUSION

Optimal synthesis conditions for polypyrrole nanowires were established with the use of gelatin as a structure directing agent and TSNa as a dopant.

TEM and SEM micrographs confirmed the successful synthesis of polypyrrole nanowires which were solid, uniform in shape, smooth, flexible and long with an average diameter of about 100nm and the length is up to tens of microns. The molecular fingerprints of the products were in agreement with the TEM and SEM results and the absorption bands confirmed the formation of the doped polypyrrole nanowires. XRD analysis confirmed the

nanowire morphology of the synthesized products. Cyclic Voltammetry (CV) of the polypyrrole electrode material was conducted to study the electrochemical behavior of the synthesized materials. The box-like shape of the CV voltammograms indicated good electrochemical capacitive behavior of the material with 496F/g being the highest capacitance recorded for the materials. This high capacitive behavior was confirmed with the charge and discharge cycling of the material. The polypyrrole nanowires delivered a charge capacitance of 622.4F/g and a discharge capacitance of 453.0F/g with 72.7% cycle efficiency, for the second cycle. The impedance results confirmed the cyclic voltammetric and charge/discharge cycling results. This material's ease of synthesis, environmental friendliness, good capacitive behavior, high durability, low charge transfer resistance and fast kinetics proves its potential to be the suitable candidate for a use in high power density supercapacitors for hybrid vehicles.

# CHAPTER 5

## SYNTHESIS OF SINGLE-CRYSTAL MANGANESE NANORODS USING LOW TEMPERATURE SOLID STATE REACTION AND HYDROTHERMAL METHOD

### 5.1 Introduction

Manganese oxide has attracted interest in this study as a candidate for supercapacitor application for hybrid vehicles. Its attraction is due to the low cost of raw material, more environmentally friendliness than any other transition metal oxide systems, ease of synthesis using our two methods. What stands out the most is the fact that the surface area and pore distribution of the manganese oxide material can be manipulated by adjusting the reaction time and the content of reactants. Due to this ability of manipulating the conditions of synthesis a vast number of manganese oxide forms can be synthesized with impeccable properties that make them suitable candidates for supercapacitor applications.

Attention has been focused on the porous materials of transition metal oxides and manganese oxides with tunnel structures have been extensively synthesized. Manganese oxides with tunnel and layered crystal structures can constitute a large family of porous materials from ultramicropore to mesopore. Turner and Buseck [312], have proposed that tunnel and layered manganese oxide minerals can be classified into the pyrolusite- ramsdellite family with (1xn) tunnel structure, the hollandite-romanechite family with (2xn) tunnel structure, and the todorokite family with (3xn) tunnel structure, respectively. The structures all contain infinite chains of edge-shared  $\text{MnO}_6$  octahedral structural units, and the numbers 1, 2, 3, and n correspond to the number of octahedra in the unit chain width.

$\alpha\text{-MnO}_2$  in this study has attracted much attention because it has the hollandite-type

structure with space group of  $I4/m$  (No. 87). It is known that  $\alpha$ -MnO<sub>2</sub>, alone, has no stabilizing cation in its tunnel cavity, resulting in a large accessible surface area for electrolyte ion adsorption, whereas the other porous manganese oxides (e.g., romanechite and todorokite) have some large stabilizing cations in their tunnels [310]. This open tunnel oxide,  $\alpha$ -MnO<sub>2</sub>, is an attractive material for use as supercapacitors electrode material due to specific properties for various industrial applications [311], including rechargeability in terms of capacity, excellent cation-exchange and molecule adsorptive properties.

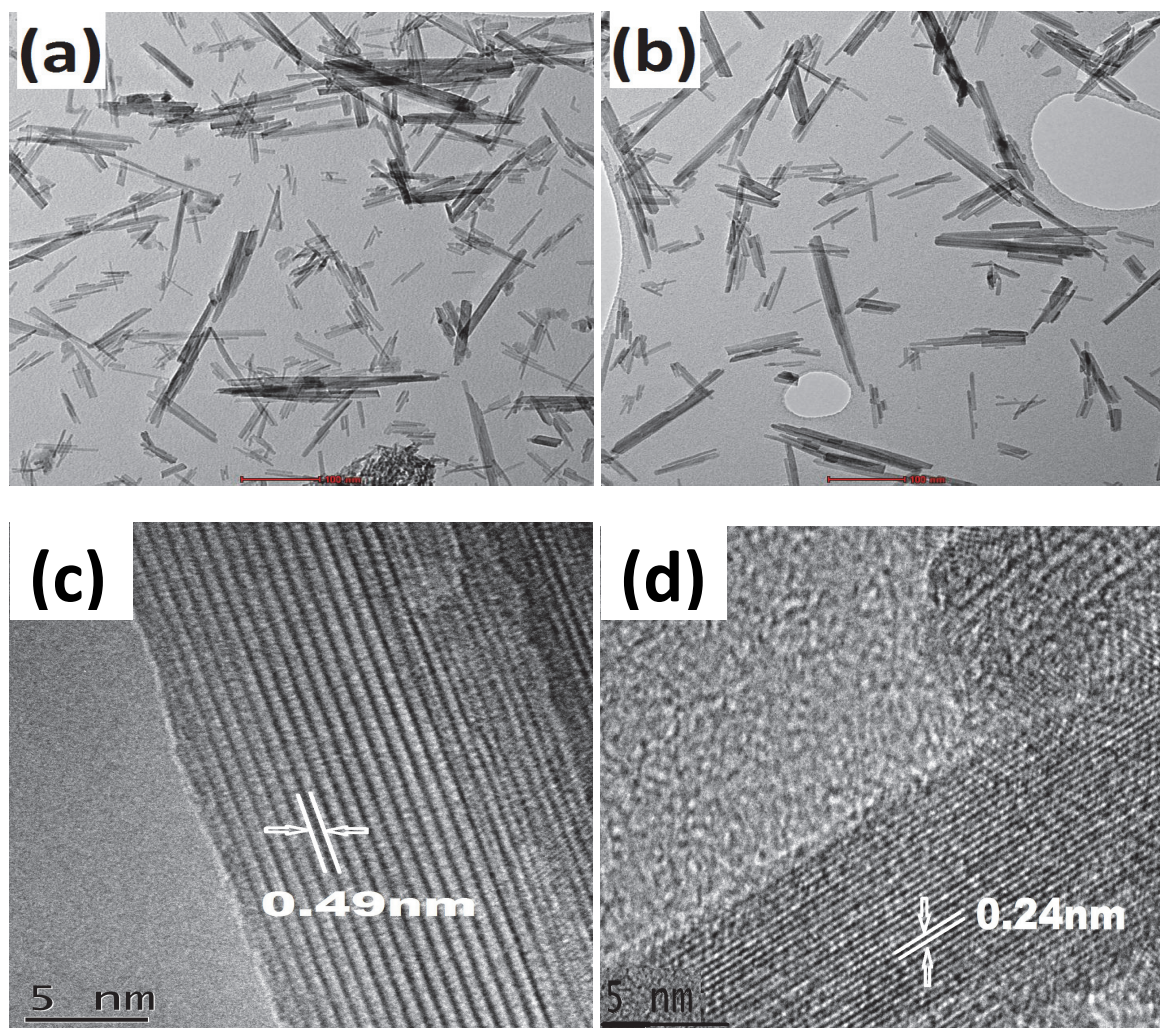
The one-dimensional (1D) nanostructures are anticipated to have potential applications in a wide range of sectors, and thus great efforts are being made to prepare 1D nanostructural crystalline manganese dioxides. Therefore in this chapter, (1D)  $\alpha$ -MnO<sub>2</sub> nanorods were synthesized using two methods: Low temperature solid state reaction and hydrothermal method. These two methods both produced manganese oxide nanorods, pure  $\alpha$ -MnO<sub>2</sub> nanorods and a mixture of  $\alpha$  and  $\beta$  MnO<sub>2</sub> nanorods. These nanorods had various characteristics which made them best candidates for use for supercapacitors in hybrid vehicles. Besides the ease of synthesis they possessed high surface area, high porosity, high capacitance and high durability.

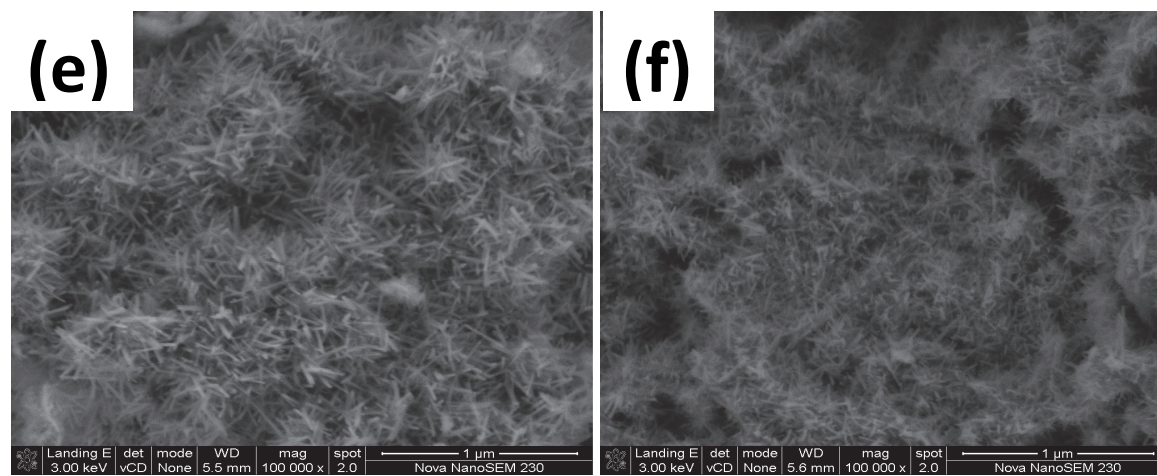
## **5.2 PHYSICAL CHARACTERIZATION OF SINGLE-CRYSTAL MANGANESE NANORODS USING LOW TEMPERATURE SOLID STATE REACTION AND HYDROTHERMAL METHOD**

In this section, the physical properties of the low temperature solid state reaction and the hydrothermal method synthesized MnO<sub>2</sub> electrode materials are presented. Physical characterization techniques, namely TEM, SEM, BET and XRD were employed for this investigation.

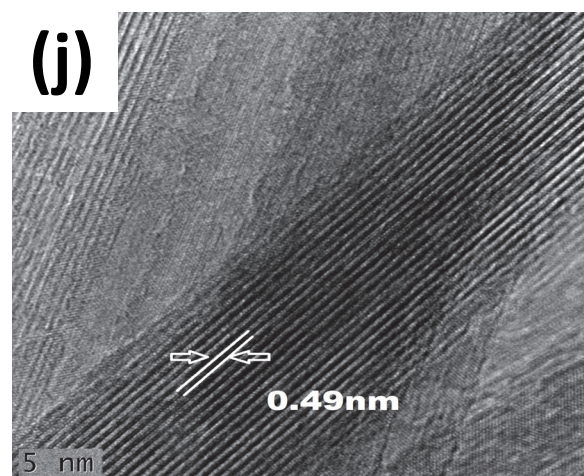
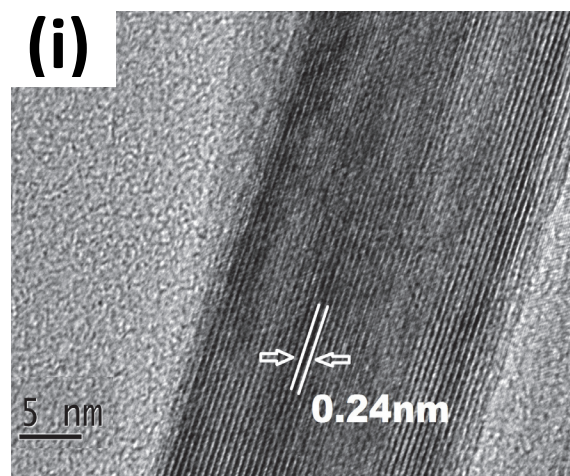
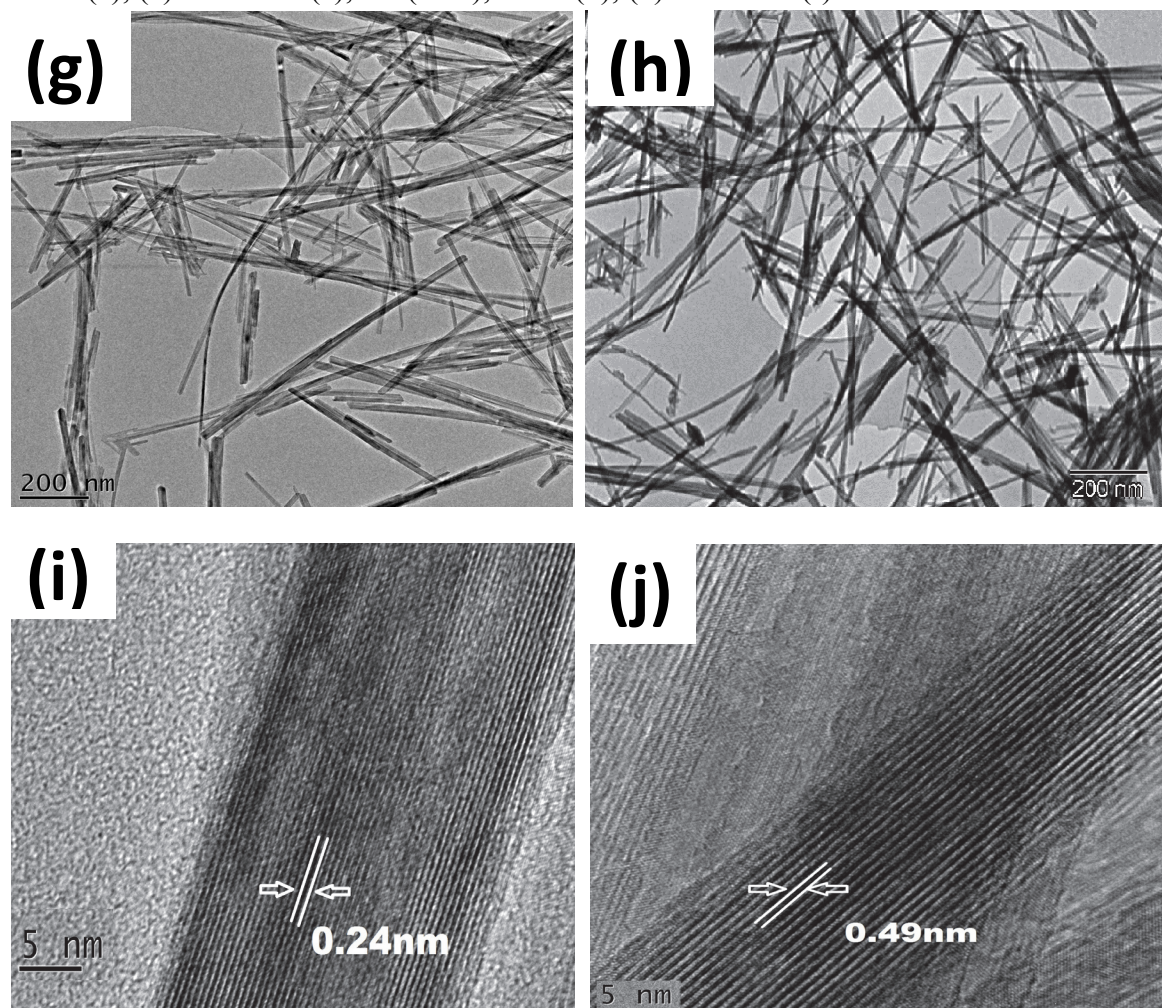
### 5.2.1. Particle size and particle size distribution study of both LTSS and Hydrothermal method synthesized MnO<sub>2</sub> electrode materials and their carbon composites.

TEM analysis was conducted on the synthesized electrode materials to investigate the morphology, metal particle size and particle size distribution using TEM. TEM-EDX was also employed to determine the composition of the synthesized products. TEM images of the synthesized MnO<sub>2</sub> electrode materials are shown in figure 5.2.1.





**Figure 5.2.1** Micrographs of low temperature solid state reaction synthesized MnO<sub>2</sub> (3hrs), TEM (a), (c) and SEM (e), for (5hrs), TEM (b), (d) and SEM (f).



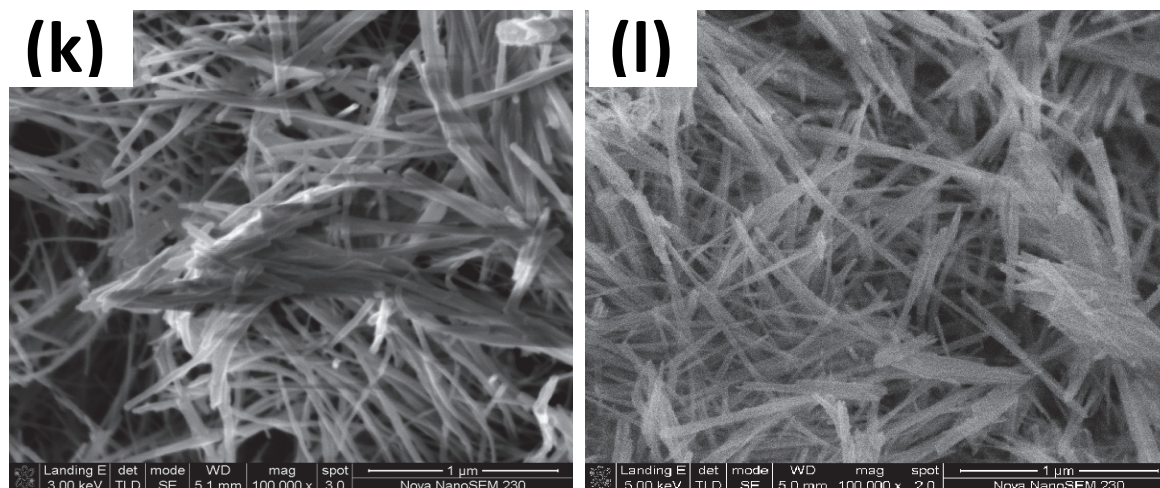


**Figure 5.2.1** Micrographs of hydrothermal method synthesized  $\text{MnO}_2$  3hrs, TEM (g), (i) and SEM (k), for (5hrs), TEM (h), (j) and SEM (l).

It is known that natural hollandite minerals are found typically as fibrous crystals {(figure 5.2.1 (a),(b), (e) and (f), LTSSR synthesized products.)} and less commonly as prismatic crystals {(figure 5.2.1 (g), (h), (k) and (l), hydrothermal synthesized products.)} [313]. Our results are consistent with this fact. SEM image of LTSS synthesized products indicate that the product can be self-organized into dendritic nanostructures with high quantities and that the nanocluster arrays are composed of uniform tetragonal prism nanorods. The TEM micrographs, (c) and (j), reveal lattice spacings of  $\sim 0.49$  nm between adjacent lattice planes, for both products, which corresponds to the (200) crystal plane in an  $\alpha\text{-MnO}_2$ . TEM micrographs, (d) and (i), reveal the lattice spacing of  $\sim 0.24$  nm, which corresponds to the (211) crystal plane of an  $\alpha\text{-MnO}_2$  phase [314]. The presence of clear lattice fringes in the TEM images confirms the single-crystal nature of the nanorods.

The SEM micrographs of the hydrothermal synthesized products reveal that the products consist of intercrossed nanorods, arranged in no particular order. The TEM micrographs reveal that the hydrothermal synthesized nanorods are more crystallized than the LTSS synthesized nanorods. And also on the basis of the TEM images, for both products, it



can be concluded that the particle size and a more ordered state of the products is dependent on the reaction dwell time. For example the higher the dwell reaction time the less agglomerates (e.g. LTSS 3hrs and 5hrs). For instance, the particle size for the LTSS synthesized nanorods with 3hrs and 5hrs dwell time is 5-12nm and 5-14nm, respectively. The particle size for the hydrothermally synthesized nanorods with 3hrs and 5hrs dwell time is about 6-16nm and 6-20nm, respectively. The length of the LTSS synthesized nanorods goes up to 200nm and that of hydrothermal synthesized nanorods goes beyond that.

The formation of these nanorods can be explained by the Ostwald ripening process. In 1900, Wilhelm Ostwald published a famous paper on the approach to equilibrium for a solution where a dense phase and a dilute phase coexist [284-286]. When the dense phase is present in the form of a distribution of compact clusters with different sizes, he argued that the Gibbs–Thomson effect [287] provides a thermodynamic driving force for large clusters to grow at the expense of small clusters. This phenomenon is called ripening or coarsening.

Here a large number of nuclei are formed in a short time, and a slow crystal aggregate follows to form a sphere with a solid core. This stage might last for several hours till an interior cavity is gradually formed via a core evacuation process due to higher surface energy [271]. A subsequent increase in the hydrothermal dwell time leads to a subsequent dissolution-recrystallization process in which the amorphous components in the agglomerates would dissolve again and grow into nanorods. The larger nanorods grow at the cost of the ones in thermodynamically stable environment and urchin structures are damaged completely into many individual nanorods.

Elemental composition study of the LTSS and hydrothermal method synthesized  $\text{MnO}_2$  electrode materials were studied using TEM EDX. The TEM-EDX revealed that indeed

the products are  $\text{MnO}_2$  and no impurities were observed from the samples.

### 5.2.2 Particle size and crystallinity study of LTSS and hydrothermal method synthesized $\text{MnO}_2$ electrode materials

The X-ray diffraction measurements were performed to examine the nature of crystallinity of the synthesized manganese oxide electrode materials. The method for synthesizing  $\text{MnO}_2$  was optimized to see if the reaction time plays a role on the physical nano-structured properties of the metal oxide.

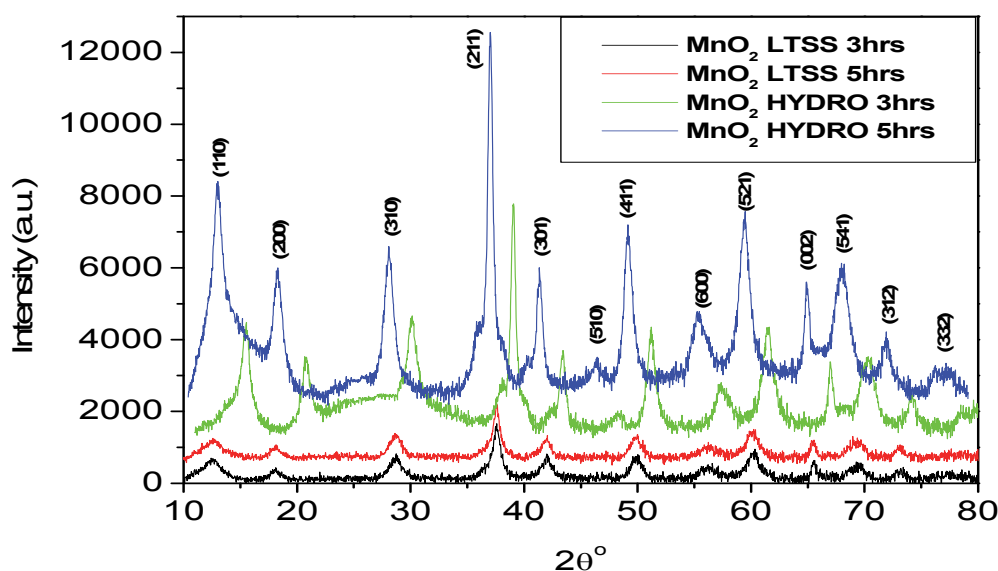


**Figure 5.2.2.1:** XRD patterns of LTSS method and hydrothermal method (3hrs and 5hrs) synthesized  $\text{MnO}_2$ .

It is well-known that the crystallinity of  $\beta$ -  $\text{MnO}_2$  is usually better than that of  $\alpha$ - $\text{MnO}_2$ . Notably, better crystallinity of the hydrothermally synthesized  $\text{MnO}_2$  has been observed both in the above figure and in the TEM micrographs presented in section 5.2.1. The diffraction peaks in figure (5.2.2.1) for the LTSS synthesized products correspond to the tetragonal  $\alpha$ - $\text{MnO}_2$  with lattice constants of  $a = 9.784 \text{ \AA}$  and  $c = 2.863 \text{ \AA}$  which are in agreement with the standard values reported by Chen *et al.* [288] and the diffraction peaks for the hydro

synthesized products can be identified as those of the mixture of  $\alpha$ -MnO<sub>2</sub> and  $\beta$ -MnO<sub>2</sub>.

There is presence of amorphous halo on the diffraction peaks indicating poor crystallization of the products, which is associated with the less reaction dwell time. No impurities were formed during the synthesis of the materials. However, there is always a possibility of co-existing potassium ion in the  $\alpha$ -MnO<sub>2</sub> matrix arising from KMnO<sub>4</sub> [266]. The amount of potassium ion may be negligible using XRD. A shift to the higher 2 $\theta$  values for the Hydro (3hrs) sample is observed because the lattice spacing tends to decrease as the particle size decreases from bulk [315]. The particle sizes were determined by the Scherrer equation (3.1). It was found that the reaction time does affect the particle size of the synthesized materials and the results are tabulated in table (5.2.2.1) below.

**Table 5.2.2.1.:** Particle size (D) and inter-planar spacing (d) in hydrothermal and LTSS prepared MnO<sub>2</sub> and its carbon composites

MnO <sub>2</sub>	Facet (211) 2 $\theta$	Facet (301) 2 $\theta$	Facet (411) 2 $\theta$	Facet (521) 2 $\theta$	d (211) (Å)	d (301) (Å)	d (411) (Å)	d (521) (Å)	D (211) (nm)	D (301) (nm)	D (411) (nm)	D (521) (nm)
MnO <sub>2</sub> (3hrs)	37.6	42.0	49.9	60.4	2.38	2.13	1.81	1.53	9.8	9.3	7.2	6.8
MnO <sub>2</sub> (5hrs)	37.6	42.0	49.9	60.2	2.38	2.13	1.81	1.53	10.8	7.7	6.1	6.2
MnO <sub>2</sub> Hydro (3hrs)	39.4	43.7	51.5	62.0	2.31	2.08	1.77	1.50	15.9	16.8	10.0	7.2
MnO <sub>2</sub> Hydro (5hrs)	37.5	41.8	49.7	59.9	2.38	2.19	1.85	1.55	19.3	14.0	10.0	8.4

Observed from table (5.2.2.1) above, is that the synthesis dwell time is directly proportional to the size the particle size of the electrode materials. The slightly bigger particle size of the LTSS 3hrs, is due to slight agglomeration (see section 5.2.1) particle This proves that indeed the synthesis or formation of these nanoparticles is due to the Ostwald Ripening process.

### 5.2.3 BET analysis LTSS method and hydrothermal method synthesized MnO<sub>2</sub> electrode materials.

The porous texture of any type of electrode material has an immediate relevance (positive or negative) on reactivity and on most of their applications. Therefore, knowledge about their porosity, pore size distribution and surface area is essential. A convenient classification of pores according to their average diameter is recommended by the International Union of Pure and Applied Chemistry (IUPAC) [316]:

- micropores, size less than 2nm,
- mesopores, size between 2nm and 50nm,
- macropores, size more than 50nm.

The surface area and porosity of the synthesized MnO<sub>2</sub> electrode materials synthesized using both methods was determined using N<sub>2</sub> physisorption. The methodology for the surface area and porosity determination via the N<sub>2</sub> physisorption technique is detailed in Chapter 3, section (3.5.4.). The results obtained for the synthesized electrode materials are tabulated in table (5.2.3.1).

**Table 5.2.3.1:** Surface area and porosity data for both the hydrothermally and LTSS prepared MnO<sub>2</sub> and its carbon composites.

Electrode Material	BET Surface Area (m <sup>2</sup> /g)	External Surface Area (m <sup>2</sup> /g)	Internal Pore area (m <sup>2</sup> /g)	Pore Volume Ads. (cm <sup>3</sup> /g)	Pore Volume Des. (cm <sup>3</sup> /g)	Av. Ads Pore Diameter (nm)	Av. Des Pore Diameter (nm)
MnO <sub>2</sub> LTSS (3hrs)	148.86	158.20	156.78	0.202	0.201	5.157	4.87
MnO <sub>2</sub> LTSS (5hrs)	138.48	144.44	143.43	0.187	0.186	5.214	4.90
MnO <sub>2</sub> (hydro 3hrs)	67.10	65.58	70.76	0.264	0.259	14.93	14.89
MnO <sub>2</sub> (hydro 5hrs)	70.75	61.37	71.71	0.259	0.258	14.55	14.15

The specific surface area of the pure  $\alpha$ -MnO<sub>2</sub>, 3hrs and 5hrs (LTSS), is 148.86m<sup>2</sup>/g and 138.48 m<sup>2</sup>/g, respectively, which is much larger than that of an  $\alpha$  and  $\beta$  mixture MnO<sub>2</sub>, 3hrs and 5hrs (hydro) which are 67.10m<sup>2</sup>/g and 70.75m<sup>2</sup>/g respectively. This difference in specific surface area probably comes from their difference in nanorod sizes.

Figure (5.2.3.1) show the N<sub>2</sub> adsorption-desorption isotherm of the synthesized MnO<sub>2</sub> nanorods. The isotherms are not a type I but a type IV adsorption, which is a characteristic of mesoporous materials [317], because the initial rise due to micropore filling at the lower  $P/P_0$  regions is not observed. The hysteresis loops for  $\alpha$ -MnO<sub>2</sub> products observed at the middle range of  $P/P_0$ , due to capillary condensation, confirm that products have mesopores. The hysteresis loops for the hydro synthesized MnO<sub>2</sub> products indicate that they have a high degree of pore-size uniformity. The BJH pore size distribution plot for the MnO<sub>2</sub> electrode materials is plotted in Figure (5.2.3.2). The pores size distribution of both  $\alpha$ -MnO<sub>2</sub> products, is mostly concentrated between 4–20nm, whereas the  $\alpha$ ,  $\beta$ -MnO<sub>2</sub> 3hrs and 5hrs, products show pore- size distribution range between 4–60nm and 4-30nm, respectively.

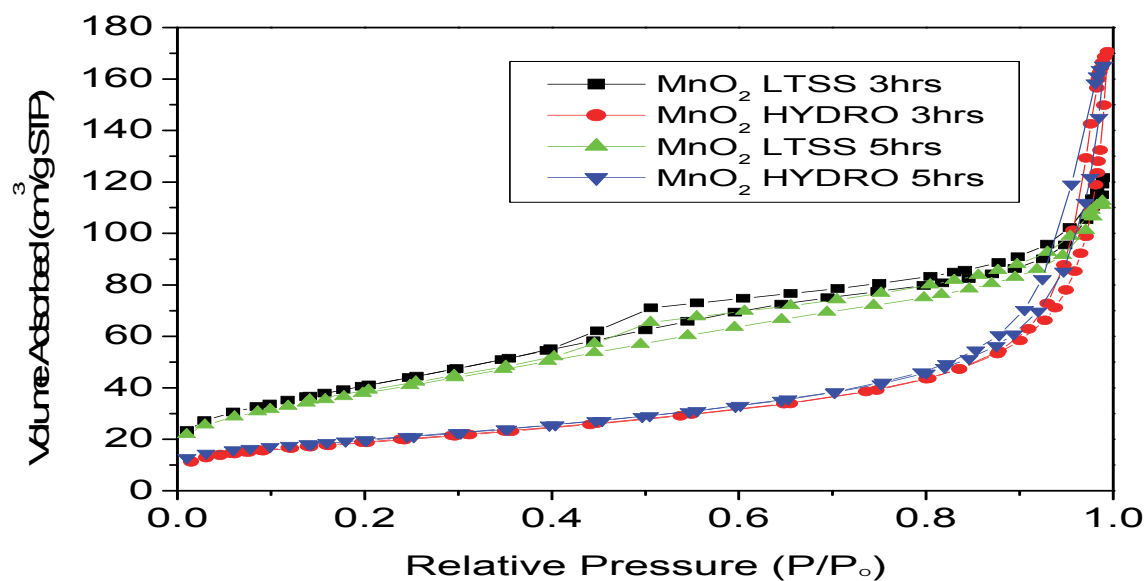


**Figure 5.2.3.1:** The nitrogen adsorption isotherms of  $\text{MnO}_2$  nanorods synthesized by LTSS (3hrs and 5hrs) and hydrothermal method (3hrs and 5hrs) at 77K.

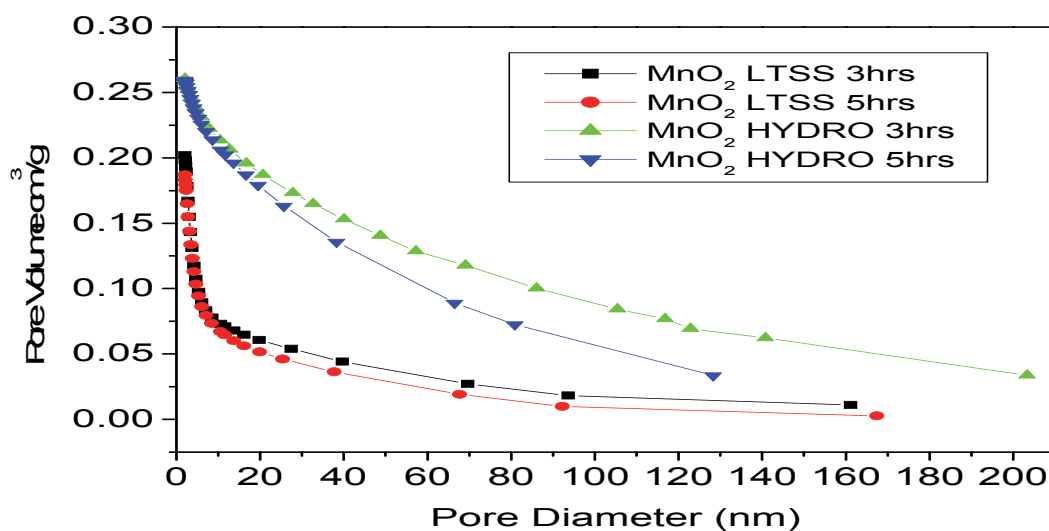


**Figure 5.2.3.2:** Barrett-Joyner and Halenda (BJH) pore size distribution plots of  $\text{MnO}_2$  nanorods synthesized by LTSS (3hrs and 5hrs) and hydrothermal method (3hrs and 5hrs) at 77K.

### 5.3. ELECTRO-CHEMICAL CHARACTERIZATION OF SINGLE-CRYSTAL MANGANESE OXIDE NANORODS

#### 5.3.1 Cyclic Voltammetry analysis

Cyclic voltammetry (CV) of the LTSS and HYDRO synthesized  $\text{MnO}_2$  electrode materials were conducted, with  $\text{MnO}_2$  on a carbon paper used as a working electrode, Ag/AgCl used as a reference electrode, platinum gauze as a counter electrode in 1M  $\text{Na}_2\text{SO}_4$  electrolyte.

Figure (5.3.1) shows cyclic voltammograms of  $\text{MnO}_2$  LTSS (3hrs),  $\text{MnO}_2$  LTSS (5hrs),  $\text{MnO}_2$  HYDRO (3hrs) and  $\text{MnO}_2$  HYDRO (5hrs), respectively, and using 1M  $\text{Na}_2\text{SO}_4$  electrolyte at 5, 10, 20, 25, 50 and 100mV/s.

The CV curves show a nearly rectangular shape and more so at lower scan rates, indicating good electrochemical capacitive behavior. There have been two mechanisms proposed to account for the charge storage in  $\text{MnO}_2$ -based capacitors. One is based on the concept of the intercalation of proton or alkali metal cations such as  $\text{Na}^+$  in the electrode during the reduction process and deintercalation on the oxidation process [190]. The other is based on the adsorption of cations in the electrolyte on the electrode [294]. In current CV tests, the redox process should be mainly accomplished by the intercalation/deintercalation of  $\text{Na}^+$  from the electrolyte into the porous  $\text{MnO}_2$  electrodes. Therefore, the increase of the scan rate will have a considerable effect on the diffusion of  $\text{Na}^+$  ions into the  $\text{MnO}_2$  matrix. That is to say, the faster scan rates will lead to the  $\text{Na}^+$  ions accessing only the outer surfaces of  $\text{MnO}_2$  electrodes instead of the interior cavities of the  $\text{MnO}_2$  matrix, which would significantly reduce the available capacitance and thereby distorting the shape of the voltammograms. No redox peaks can be seen on the CV curves at different scan rates, indicating that the charge–

discharge process of the active materials occurred at a pseudo-constant rate over the whole potential window [319].

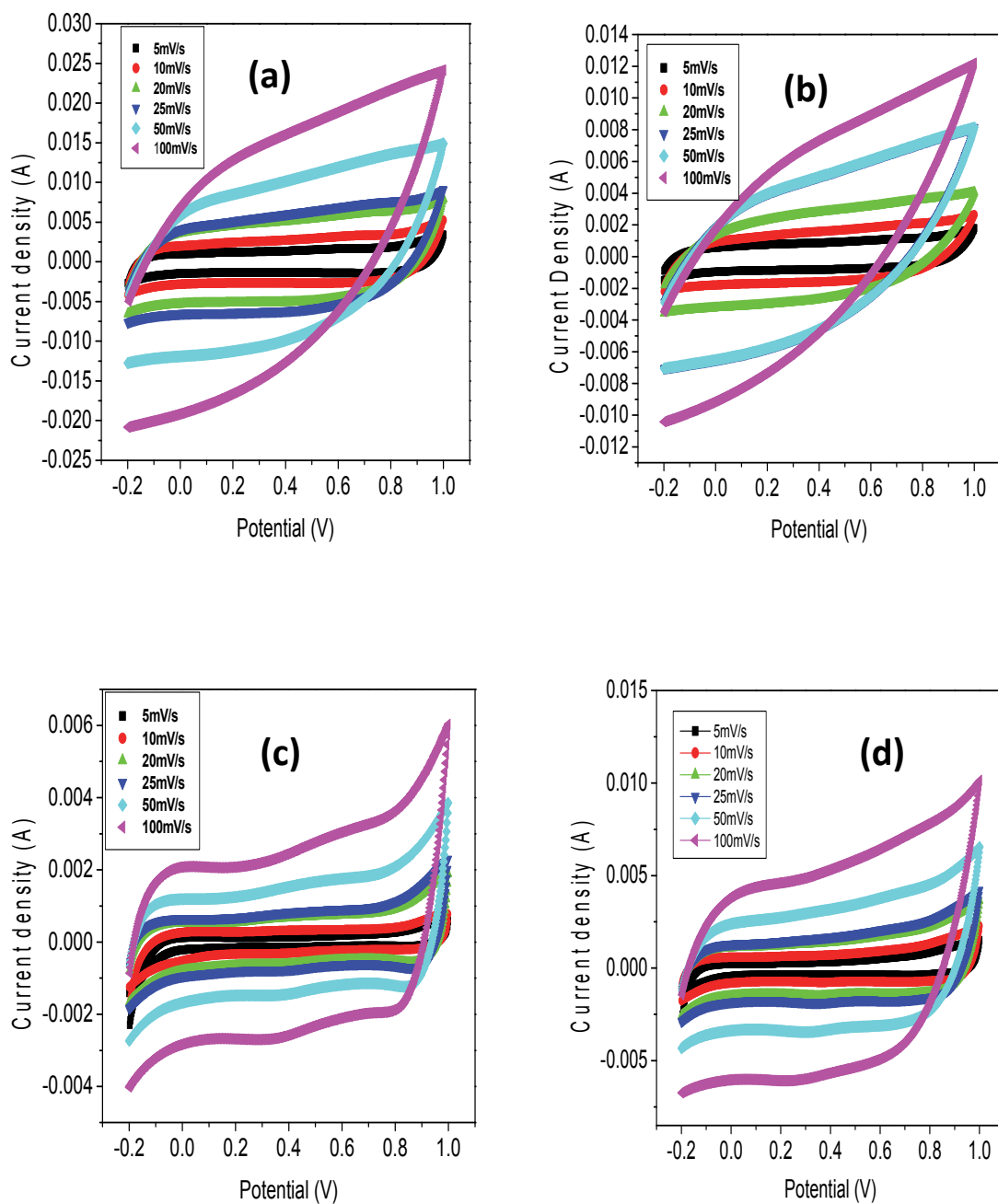


**Figure 5.3.1:** Cyclic voltammograms of (a) MnO<sub>2</sub> LTSS (3hrs), (b) MnO<sub>2</sub> LTSS (5hrs), (c) MnO<sub>2</sub> HYDRO (3hrs) and (d) MnO<sub>2</sub> HYDRO (5hrs) in a 1M Na<sub>2</sub>SO<sub>4</sub> electrolyte.



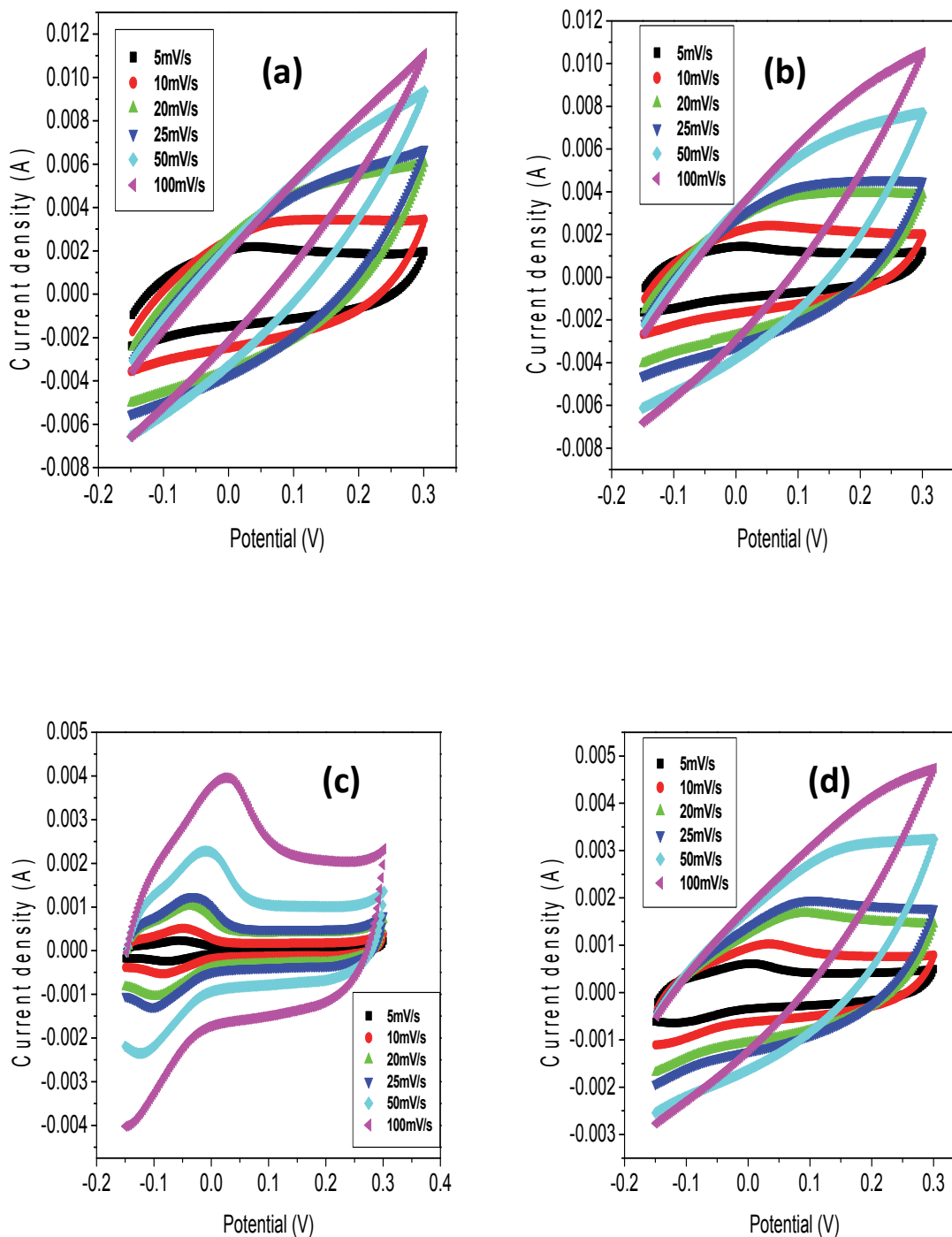


**Figure 5.3.2:** Cyclic voltammograms of (a) MnO<sub>2</sub> LTSS (3hrs), (b) MnO<sub>2</sub> LTSS (5hrs), (c) MnO<sub>2</sub> HYDRO (3hrs) and (d) MnO<sub>2</sub> HYDRO (5hrs) in a 6M KOH electrolyte.

Figure (5.3.2) shows cyclic voltammograms of MnO<sub>2</sub> LTSS (3hrs), MnO<sub>2</sub> LTSS (5hrs), MnO<sub>2</sub> HYDRO (3hrs) and MnO<sub>2</sub> HYDRO (5hrs), respectively, and using 6M KOH electrolyte at 5, 10, 20, 25, 50 and 100mV/s. CV curves for the electrodes showed the presence of redox peaks, indicating that faradic reactions took place during the charge–discharge processes. The CV curves show an increase in capacitance towards the increasing negative potentials. However, with the increasing scan rate, the deviation from semi rectangularity of the CV becomes obvious.

The LTSS synthesized MnO<sub>2</sub> (3hrs) and (5hrs) in Na<sub>2</sub>SO<sub>4</sub> and KOH electrolytes delivered the highest capacitances. MnO<sub>2</sub> LTSS 3hrs, at a scan rate of 5mV/s, delivered 380 F/g and 543F/g in Na<sub>2</sub>SO<sub>4</sub> and KOH electrolytes, respectively. And MnO<sub>2</sub> LTSS (5hrs), at the same scan rate and respective electrolytes, delivered 409F/g and 747F/g. This large capacitance is attributed to the highly mesoporous structure of the hollandite type nanostructures, which favor the ion transfer to the porous structure and having more redox reactions [321].

The MnO<sub>2</sub> HYDRO (3hrs), at a scan rate of 5mV/s in the Na<sub>2</sub>SO<sub>4</sub> electrolyte delivered the capacitance of 49F/g and 58F/g in KOH. The MnO<sub>2</sub> HYDRO (5hrs) delivered the capacitance of 104F/g in a Na<sub>2</sub>SO<sub>4</sub> and 125F/g in KOH at the same scan rate. The capacitance calculated from the CV curves is tabulated on table (5.3.1).

**Table 5.3.1:** Cyclic voltammetry capacitance values in 1M Na<sub>2</sub>SO<sub>4</sub>

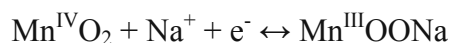
	5mV/s	10mV/s	20mV/s	25mV/s	50mV/s	100mV/s
<b>MnO<sub>2</sub>LTSS (3hrs)</b>	380F/g	288F/g	217F/g	199F/g	158F/g	130 F/g
<b>MnO<sub>2</sub>HYDRO(3hrs)</b>	49F/g	38F/g	46F/g	44F/g	38F/g	29F/g
<b>MnO<sub>2</sub>LTSS (5hrs)</b>	409F/g	307F/g	233F/g	227F/g	184F/g	138F/g
<b>MnO<sub>2</sub>HYDRO(5hrs)</b>	104F/g	96F/g	77F/g	71F/g	66F/g	50F/g

**Table 5.3.2:** Cyclic voltammetry capacitance values in 6M KOH

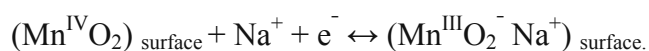
	5mV/s	10mV/s	20mV/s	25mV/s	50mV/s	100mV/s
<b>MnO<sub>2</sub>LTSS (3hrs)</b>	543 F/g	423F/g	362F/g	324F/g	229F/g	139F/g
<b>MnO<sub>2</sub>HYDRO(3hrs)</b>	58F/g	41F/g	49F/g	40 F/g	38 F/g	33 F/g
<b>MnO<sub>2</sub>LTSS (5hrs)</b>	747F/g	606F/g	505F/g	456F/g	394F/g	303F/g
<b>MnO<sub>2</sub>HYDRO(5hrs)</b>	125F/g	96F/g	74F/g	69F/g	57F/g	42F/g

### 5.3.2 Charge and discharge cycling

According to the previous reports [8, 270, 292], the redox charge storage mechanism of MnO<sub>2</sub> in neutral Na<sub>2</sub>SO<sub>4</sub> aqueous electrolyte occurs via insertion–deinsertion of sodium ions;



or by surface adsorption via,



The Charge-discharge tests of the MnO<sub>2</sub> electrode materials synthesized with low temperature solid state reaction and hydrothermal method were done at a charge-discharge current of 200 μA in a button cell using two electrolytes, 1.0 M Na<sub>2</sub>SO<sub>4</sub> and 6M KOH from

0.1V to 1V. The discharge cycles of the synthesized materials are presented in this section.

The capacitance values were calculated and are tabulated in Appendix B.

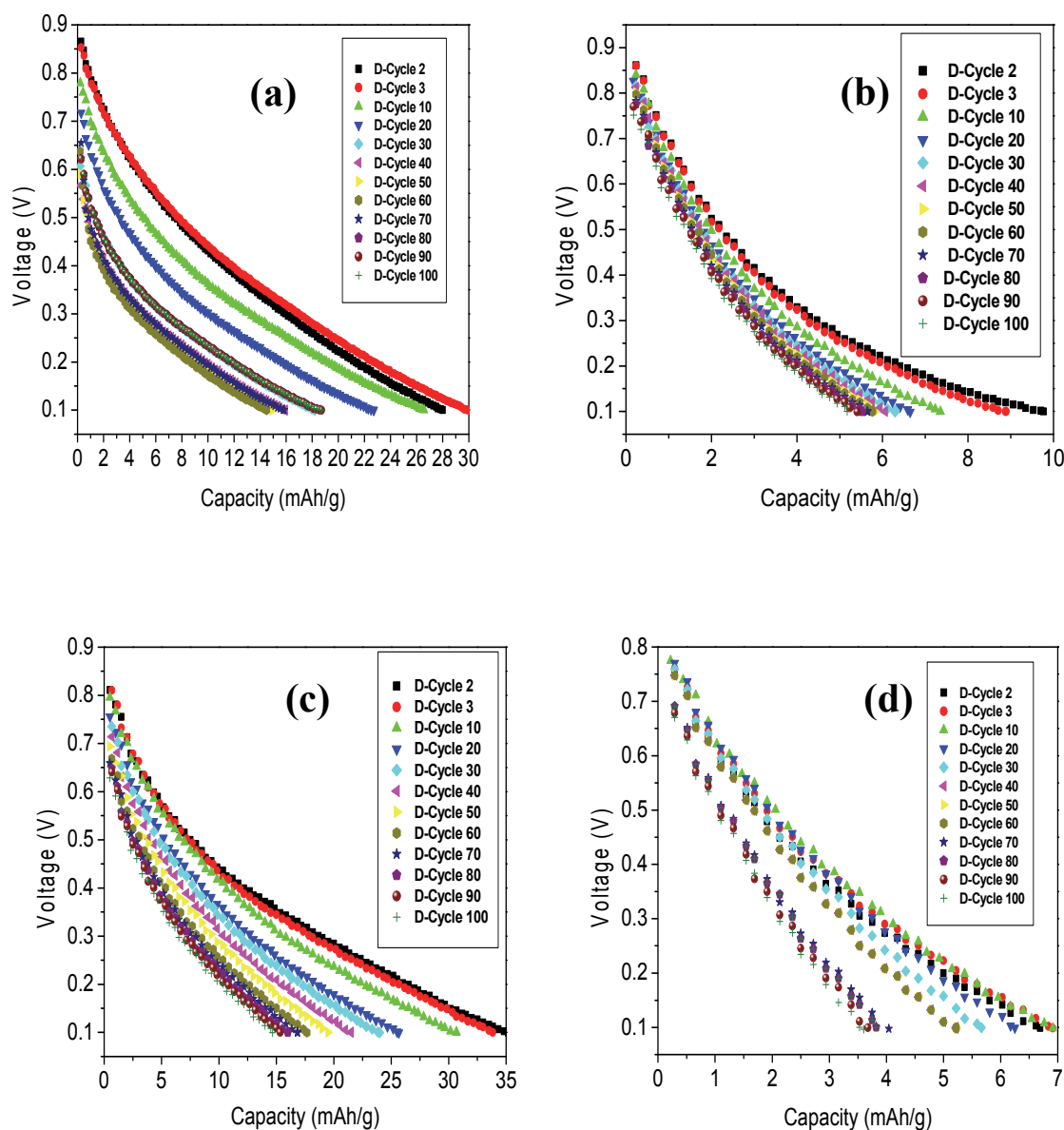


**Figure 5.3.3:** Discharge cycles of (a) MnO<sub>2</sub> LTSS (3hrs), (b) MnO<sub>2</sub> Hydro (3hrs), (c) MnO<sub>2</sub> LTSS (5hrs) and (d) MnO<sub>2</sub> Hydro (5hrs) using Na<sub>2</sub>SO<sub>4</sub> electrolyte.

Figures (5.3.3) show discharge curves for the MnO<sub>2</sub> electrode materials synthesized using the low temperature solid state reaction and hydrothermal method.

The material synthesized using the LTSS method with 3 hours dwell time with a sodium sulphate electrolyte, delivered a charge capacitance of 161.80 F/g and a discharge capacitance of 112.19F/g for the second cycle with 69.3 % cycle efficiency. For the third cycle, charge capacitance of 197.08F/g and discharge capacitance of 120.03 F/g were observed with 60.9% cycle efficiency. 83.40 F/g and 81.64 F/g charge and discharge capacitance for the 100<sup>th</sup> cycle were observed. The 100<sup>th</sup> cycle discharge capacitance was 72.8% of the 2<sup>nd</sup> and 68.0% of the 3<sup>rd</sup> cycle.

The material synthesized using the LTSS method with 5 hours dwell time delivered a charge capacitance 167.80F/g and discharge capacitance of 140.40F/g with 69.3 % cycle efficiency for the 2<sup>nd</sup> cycle. For the third cycle, a charge capacitance of 197.08 F/g and a discharge capacitance of 120.03F/g were observed. 83.40F/g and 81.64 F/g charge and discharge capacitance for the 100<sup>th</sup> cycle were observed. The discharge capacitance of the 100<sup>th</sup> cycle was 41.9% of the 2<sup>nd</sup> and 43.4% of the 3<sup>rd</sup> cycle, respectively.

The material synthesized using the HYDRO method with 3 hours dwell time delivered a charge capacitance 37.84F/g and discharge capacitance of 19.48F/g with 51.5% cycle efficiency, for the 2<sup>nd</sup> cycle. For third cycle, a charge capacitance of 25.76/g and a discharge capacitance of 17.80 F/g were observed with a cycle efficiency of 69.1%. 10.64 F/g and 10.40 F/g charge and discharge capacitance, respectively, for the 100<sup>th</sup> cycle were observed with 97.7% cycle efficiency. The discharge capacitance for the 100<sup>th</sup> cycle was 53.4.0% of the 2<sup>nd</sup> and 58.4% of the 3<sup>rd</sup> cycle, respectively.

And the material with 5hrs dwell time delivered a charge capacitance of 35.96 F/g and a discharge capacitance of 26.64 F/g with 84% cycle efficiency for the 2<sup>nd</sup> cycle. 34.32 F/g and 27.80 F/g with a cycle efficiency of 81% for the 3<sup>rd</sup> cycle and 14.56 F/g and 14.56 F/g for the

100<sup>th</sup> cycle with a 100% cycle efficiency. The discharge capacitance for the 100<sup>th</sup> cycle was 55.0% and 52.4% of the 2<sup>nd</sup> and 3<sup>rd</sup> cycle, respectively. The discharge capacities and capacitances versus cycle number for the electrode materials in sodium sulphate electrolyte are compared in figure (5.3.4).

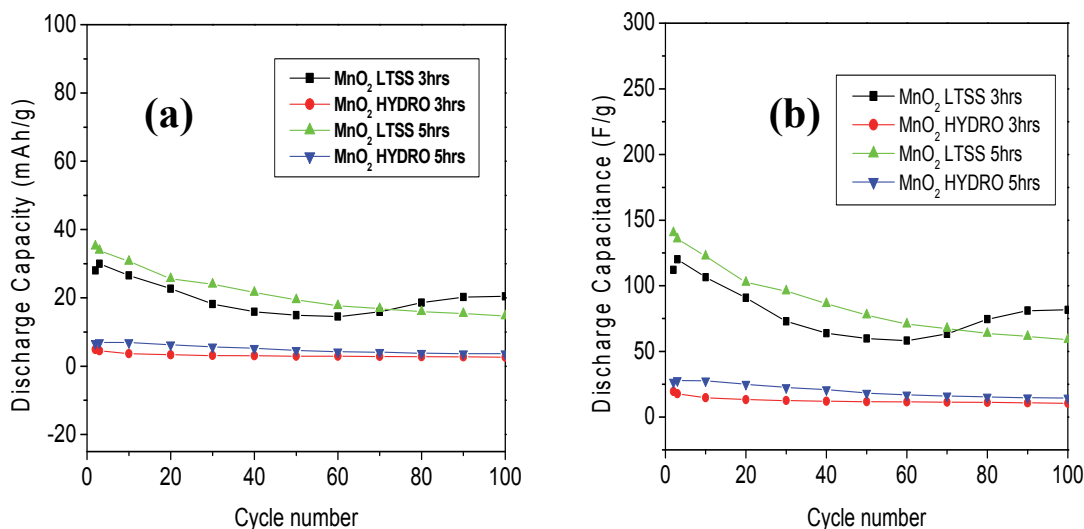


**Figure 5.3.4:** The discharge capacities (a) and (b) discharge capacitances vs. cycle number for the MnO<sub>2</sub> electrode materials in sodium sulphate electrolyte.

Figure (5.3.4) above shows that LTSS MnO<sub>2</sub> 3hrs and 5hrs proves to be better electrode materials because of their higher capacitance when compared to the HYDRO MnO<sub>2</sub> 3hrs and 5hrs. However, MnO<sub>2</sub> LTSS 3hrs shows some instability when compared to the other materials and the reason for this could be the fact that a fraction of the electrolyte ions inserted during the initial discharge cycles become locked within the crystal structure of MnO<sub>2</sub> for lattice stabilization. Also, it is observed that as the synthesis dwell time increases so does the stability of the material. MnO<sub>2</sub> electrode materials synthesized with the HYDRO method have a lower capacitance as compared to the LTSS synthesized method materials but much better stability.

The second electrolyte which was used for the charge and discharge tests was the KOH and the results are presented below.

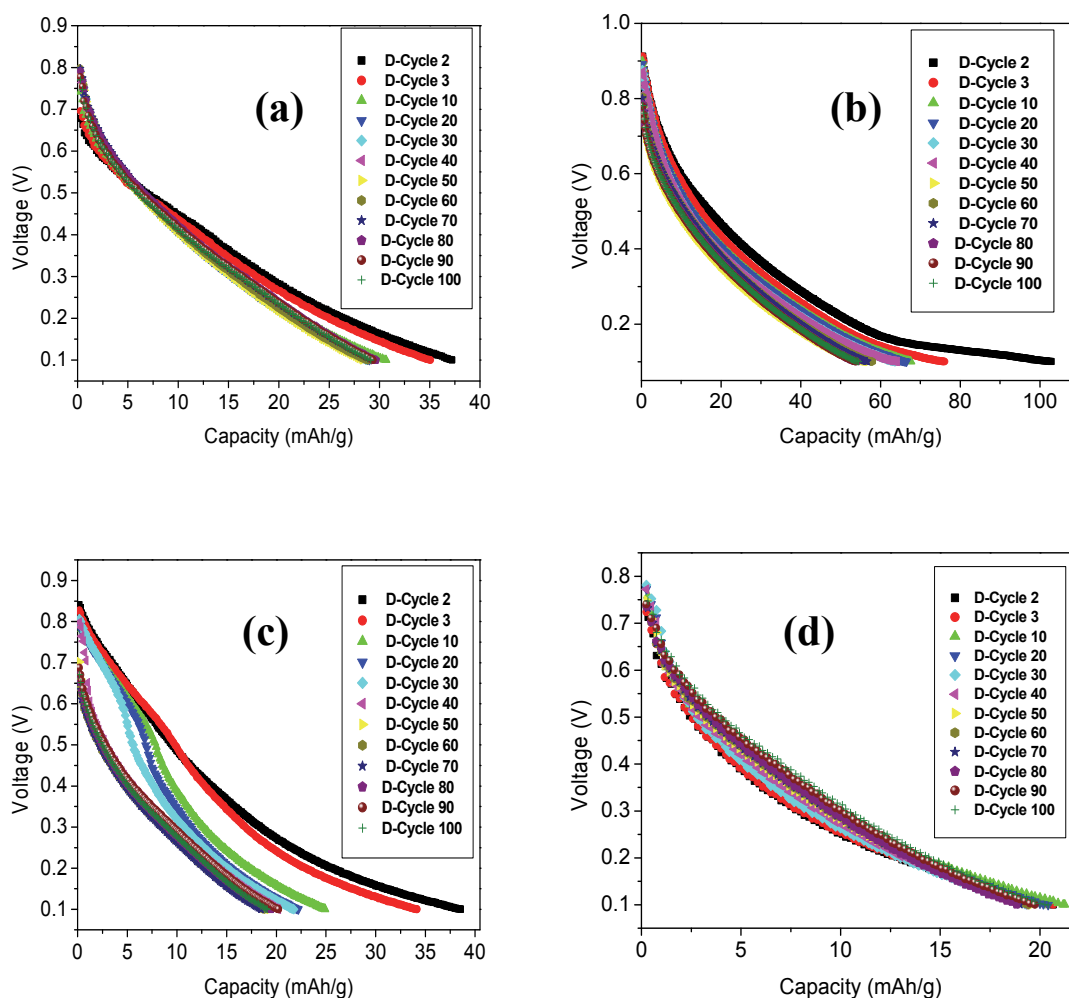


**Figure 5.3.5:** Discharge cycles of (a) MnO<sub>2</sub> LTSS (3hrs), (b) MnO<sub>2</sub> Hydro (3hrs), (c) MnO<sub>2</sub> LTSS (5hrs) and (d) MnO<sub>2</sub> Hydro (5hrs) using KOH electrolyte.

The charge/discharge cycling behaviors of the MnO<sub>2</sub> electrode materials were tested at the rate of 10C. Figures (5.3.5) show discharge curves for the MnO<sub>2</sub> electrode materials synthesized using the low temperature solid state reaction and hydrothermal method, in the potential range of 0.1 – 1 V, using potassium hydroxide as an electrolyte.

The material synthesized using the LTSS method with 3 hours dwell time delivered a charge capacitance of 433.08 F/g for the second cycle and a discharge capacitance of 148.84 F/g with 34.4 % cycle efficiency. For the third cycle, charge capacitance of 314.16 F/g and discharge capacitance of 140.84 F/g were observed with 44.6 % cycle efficiency. 159.0 F/g and 116.6 F/g charge and discharge capacitance for the 100<sup>th</sup> cycle was observed. Cycle 100<sup>th</sup> cycle was 78.3% of the 2<sup>nd</sup> and 83.3% of the 3<sup>rd</sup> cycle, respectively.

The material synthesized using the LTSS method with 5 hours dwell time delivered a charge capacitance of 456.44F/g and discharge capacitance of 411.28F/g with 90.1% cycle efficiency for the 2<sup>nd</sup> cycle. For third cycle, a charge capacitance of 313.56F/g and a discharge capacitance of 304.08F/g were observed with 97.0% cycle efficiency. 218.72F/g and 217.64F/g charge and discharge capacitance for the 100<sup>th</sup> cycle with 99.5% cycle efficiency. Charge and discharge capacitance for 100<sup>th</sup> cycle were observed to be 52.9% of the 2<sup>nd</sup> and 71.6% of the 3<sup>rd</sup> cycle.

The material synthesized using the HYDRO method with 3 hours dwell time delivered a charge capacitance 84.9F/g and discharge capacitance of 55.2F/g with 65.0% cycle efficiency, for 2<sup>nd</sup> cycle. For the third cycle, a charge capacitance of 80.7F/g and a discharge capacitance of 54.6F/g were observed with a cycle efficiency of 68.0%. 49.36F/g and 44.48F/g charge and discharge capacitance for the 100<sup>th</sup> cycle were observed with a 90.1% cycle efficiency. The 100<sup>th</sup> cycle discharge capacitance was 81.0% of the 2<sup>nd</sup> and 3<sup>rd</sup> cycle, respectively.

The material with 5hrs dwell time (HYDRO) delivered a charge capacitance of 116.72 F/g and a discharge capacitance of 82.8 F/g with 71.0% efficiency for the 2<sup>nd</sup> cycle. This capacitance is higher than 71.1 F/g, reported by Wang et al. [204]. 109.84 F/g and 82.6 F/g



with a cycle efficiency of 75.0% for the 3<sup>rd</sup> cycle. Notably, 90.2 F/g and 81.5F/g with 90.0 % cycle efficiency for 100<sup>th</sup> cycle were observed and they were 98.5% and 98.7% of the 2<sup>nd</sup> and 3<sup>rd</sup> cycle, respectively. The discharge capacities and capacitances versus cycle number for the electrode materials in potassium hydroxide electrolyte were compared in figure (5.3.6) below.

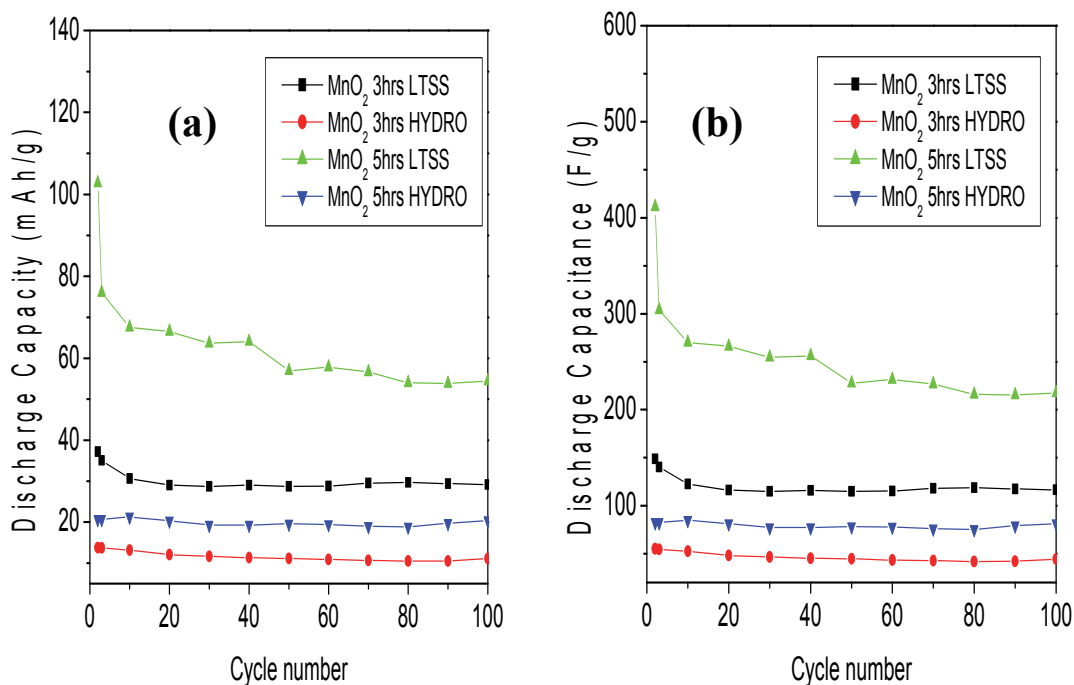


**Figure 5.3.6:** The discharge capacity (a) and (b) discharge capacitance vs. cycle number for the MnO<sub>2</sub> electrode materials in potassium hydroxide electrolyte.

According to [297-299], MnO<sub>2</sub> can also be an excellent pseudo-capacitive material with the theoretical high capacitance of 200 F/g. In the same vein, Xu *et al.* [300] reported that among the methods which are used to synthesize MnO<sub>2</sub> electrode materials, sol-gel process and electrochemical route have been considered as comparatively better methods for synthesizing MnO<sub>2</sub> electrodes of ECs, because they exhibit a relative large specific capacitance, ranging from 110 to 220 F/g. However, these preparation processes are very

complicated and difficult to control [301, 302]. In this study, the  $\text{MnO}_2$  synthesized using low temperature solid state reaction 3hrs and 5hrs, which is a simple and straight forward method, showed a capacitance of more than 400 F/g and with the hydrothermal method a 116.72 F/g capacitance was obtained which is higher than that reported by Wang et. al.[201]. It can be observed that the capacitance in both electrolytes follow this order,  $\text{MnO}_2$  LTSSR 5hrs >  $\text{MnO}_2$  LTSS 3hrs >  $\text{MnO}_2$ HYDRO 5hrs>  $\text{MnO}_2$  HYDRO 3hrs at a given current density.  $\text{MnO}_2$  LTSS 5hrs shows the highest specific capacitance at a current density of 200  $\mu\text{A/g}$ .

### 5.3.3 Potassium hydroxide versus sodium sulphate electrolyte

Table (5.3.2) show the capacitances of the synthesized products calculated from their cyclic voltammograms using KOH as an electrolyte and figure (5.3.6) shows the discharge capacities and capacitances of the electrode materials versus cycle number obtained from the charge and discharge cycles of the synthesized products. Observing from the results, the  $\text{MnO}_2$  electrode material performed better in the KOH electrolyte than in the  $\text{Na}_2\text{SO}_4$  electrolyte. The metal oxide supercapacitors are charged by chemisorption of cations of the electrolyte, proton or the alkaline ion depending on their availability. Therefore, a chosen electrolyte plays a vital role in the charging and discharging of the material. As the hydrated ionic radius of  $\text{K}^+$  (3.31 Å) is the smaller, its ionic conductivity is higher (73.48) and its mobility (7.62) faster than that of  $\text{Na}^+$ , (hydrated ionic radius: 3.58 Å, with a conductivity of (50.08) and the mobility of (5.19), its access to the inner surface of the  $\text{MnO}_2$  electrode is much easier [303]. Besides, as the charge density of the  $\text{K}^+$  ion is the smallest, its polarization for the desolvation process is the smallest. As a consequence, in  $\text{K}^+$  based electrolyte the  $\text{MnO}_2$  nanorods show the largest capacitance, [318]. Also, 6 mol/L KOH aqueous solutions is

suitable for electric double layer capacitors, because of the fast formation of electric double layers in such conditions [320].

#### **5.4 CONCLUSION**

TEM and SEM analyses confirmed the synthesis of MnO<sub>2</sub> NANORODS USING low temperature solid state reaction and hydrothermal method. LTSS method produced fibrous crystals which are typical of a Hollandite MnO<sub>2</sub>. Hydrothermal method produced MnO<sub>2</sub> with prismatic crystals. TEM revealed ~0.49nm and ~0.24nm lattice spacings from both products which correspond to (200) and (211) crystal planes of an alpha MnO<sub>2</sub>. Xray analyses results confirmed the TEM results. BET analysis showed that the products had type IV isotherms which are a characteristic of mesoporous materials. It is known that a high capacitance is attributed to highly mesoporous structure, together with with size, conductivity and mobility of the electrolyte ions. And this was confirmed by the electrochemical results. The best performance was achieved MnO<sub>2</sub> LTSS 5hrs in a 6M KOH electrolyte solution with a capacitance of 747F/g obtained with CV and a discharge capacitance of 411.3F/g obtained with charge and discharge cycling. The high surface area, high porosity, high capacitance and high durability, possessed by these materials makes them best candidates for commercial use as electrode materials for supercapacitors.

## CHAPTER 6

### EVALUATION OF SINGLE-CRYSTAL MANGANESE OXIDE CARBON COMPOSITES SYNTHESIZED USING LOW TEMPERATURE SOLID STATE REACTION AND HYDROTHERMAL METHOD

#### 6.1 Introduction

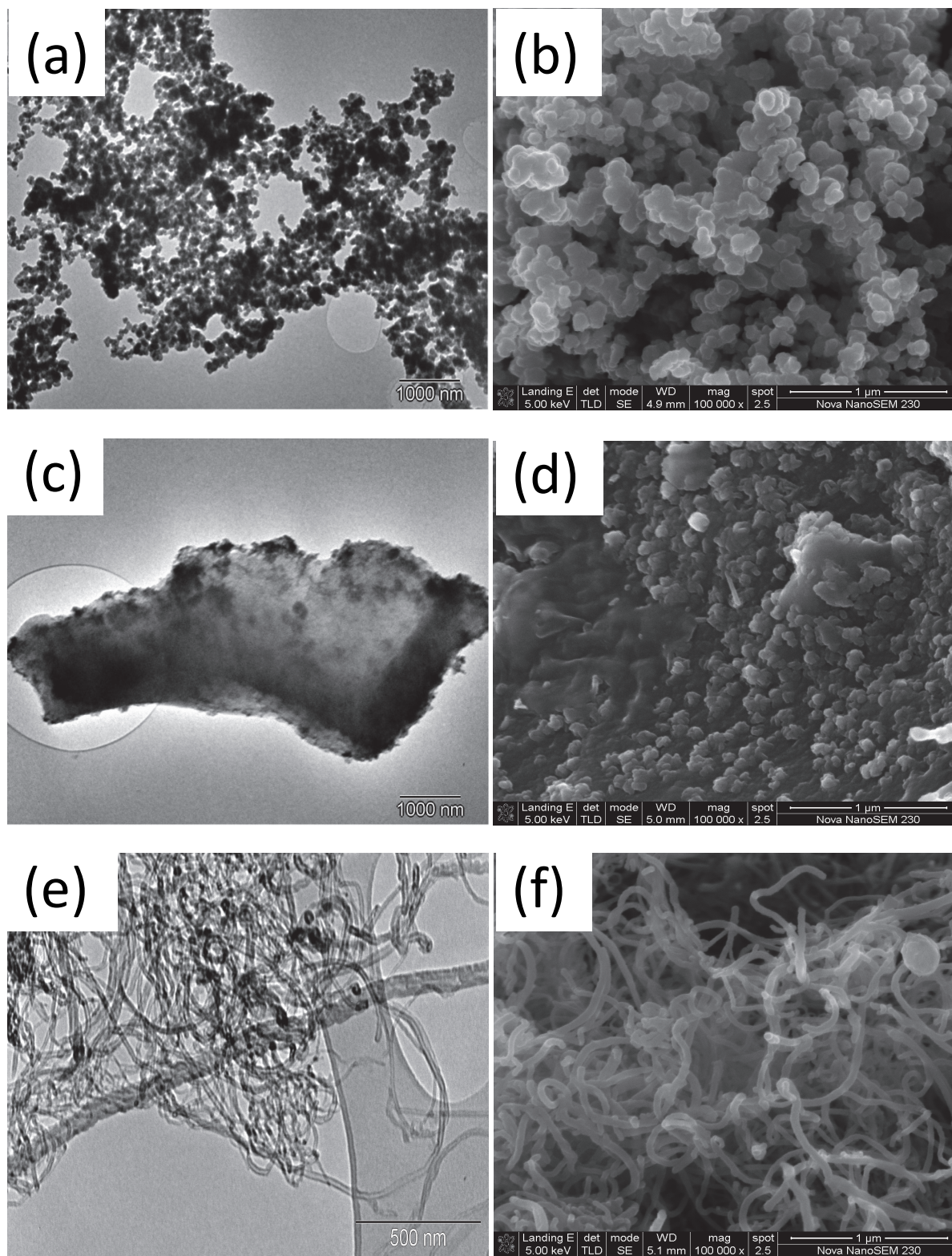
Ideally, electrochemists demand maximum electrode material activity with low catalyst loading so as to reduce material costs. The electrode material activity can be enhanced and electrode material loading lowered by increasing the surface area via high dispersion of electrode material on inert support materials, such as carbon or carbon nanotubes. The support material should be electro-conductive and stable in the presence of acidic or alkaline electrolytes, reactants, and reaction products [327]. The surface microstructure of the support may also influence the availability of active surface sites on the electrode material for reversible electrolyte accommodation. Typical support materials include activated carbon, alumina, silica, carbon black, carbon nanotubes.

Carbon blacks, such as Vulcan XC-72®, are typically used to support electrode materials and offer various advantages including: high electrical conductivity, good corrosion resistance, high thermal conductivity and low thermal expansion coefficient, mechanical stability and strength. In this study three support materials were used:

- Carbon black (figure {6.1 (a) and (b)}) and it consists of primary carbon particles which are spherical and of colloidal size. These primary particles have sizes between 12-75 nm and surface areas between 25m<sup>2</sup>/g and several hundred m<sup>2</sup>/g, depending on the grade.

- Activated carbon (figure {6.1 (c) and (d)}) Carbon material can be readily converted into a form that has very high specific surface-area. This process is employed to increase surface-area and porosity from a carbonized organic precursor (char) is referred to as activation and the resulting material is referred to as activated carbon. Chars usually have a relatively low porosity and their structure consists of elementary crystallites with a large number of interstices between them. The interstices tend to be filled with disorganized carbon residues (tars) that block the pore entrances. Activation opens these pores and can also create additional porosity
- Carbon nanotubes (figure {6.1 (e) and (f)}) can be regarded as rolled up graphite cylinders. With regard to surface properties, carbon nanotubes are not significantly different from the other classical carbon forms which are also constituted of graphitic carbon layers. However, due to their nanoscale size morphology and inner cavity which can host various species, carbon nanotubes are expected to present specific properties. The porous texture of any type of carbon has an immediate relevance (positive or negative) on reactivity and on most of their applications.

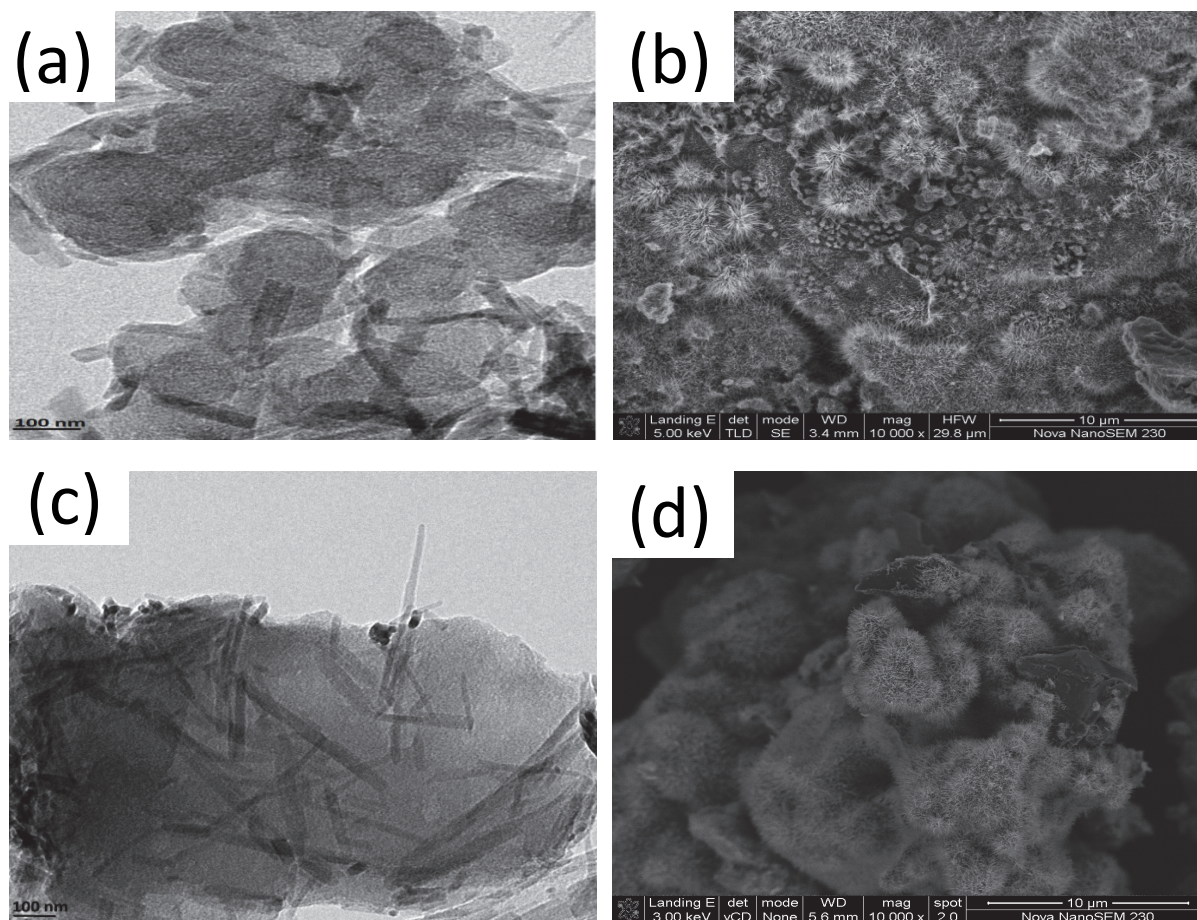
With regard to these interesting properties these materials have, they were employed in this study as support materials for the  $\text{MnO}_2$  synthesized electrode materials and their performance examined and the results are presented in this section.

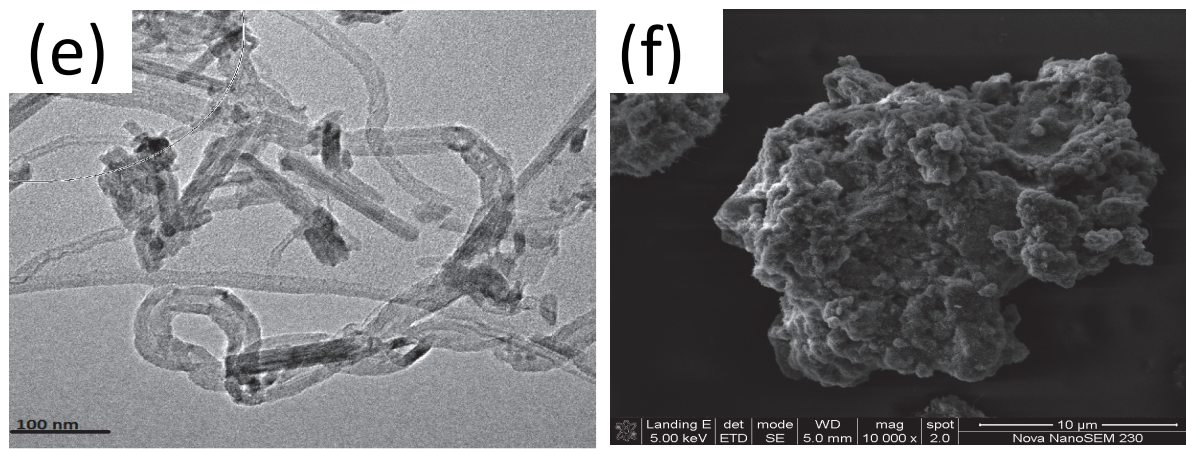


**Figure 6.1** Micrographs of Carbon Black, TEM (a) and SEM (b), Activated Carbon TEM (c) and SEM (d), Carbon Nanotubes TEM (e) and SEM (f).

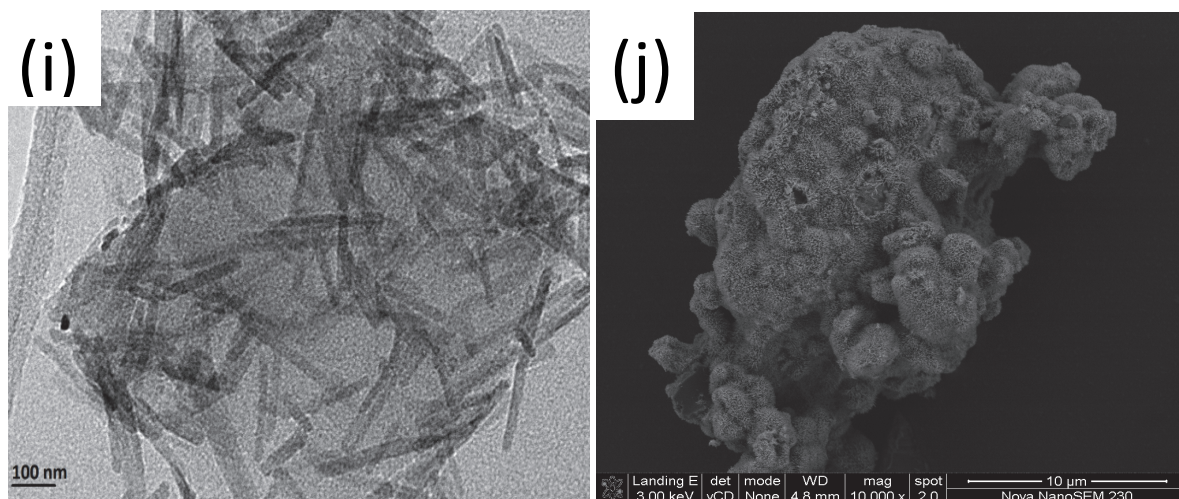
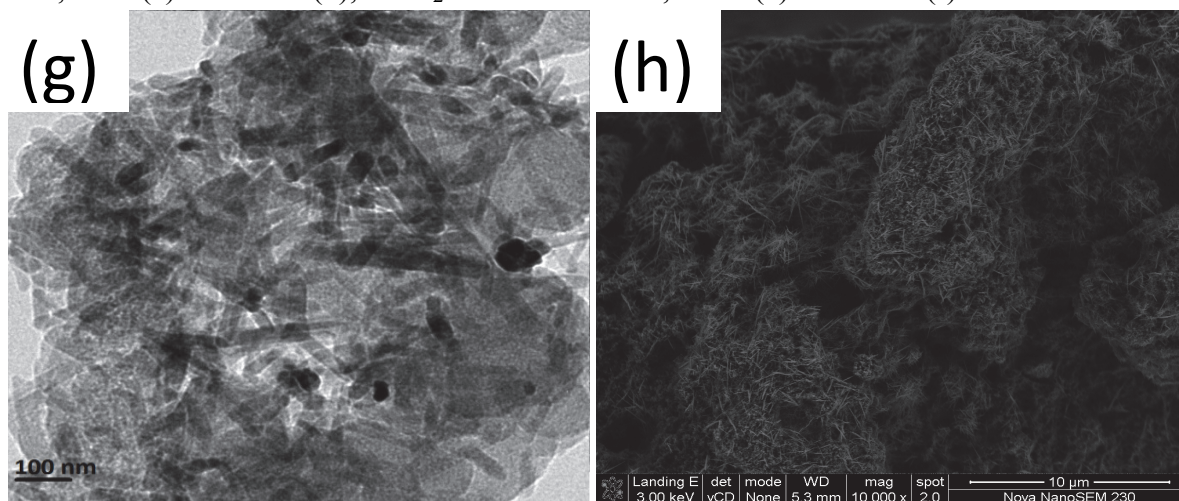
### 6.2.1. Particle size and particle size distribution study of both LTSS and Hydrothermal method synthesized $\text{MnO}_2/\text{C}$ , $\text{MnO}_2/\text{AC}$ and $\text{MnO}_2/\text{CNT}$ electrode materials

Manganese oxide carbon composites were synthesized under the same conditions as the manganese oxide materials presented in Chapter 5. As the support materials differ in morphology and particle distribution so are the final products of the supported materials. Activated carbon materials display some form of ordered arrangement as compared with the other carbonaceous materials. TEM and SEM were used to study the surface morphology of the synthesized material and the results are presented in this section.





**Figure 6.2.1.** Micrographs of MnO<sub>2</sub>/C LTSS 3hrs, TEM (a) and SEM (b), MnO<sub>2</sub>/AC LTSS 3hrs, TEM(c) and SEM (d), MnO<sub>2</sub>/CNT LTSS 3hrs, TEM (e) and SEM (f).





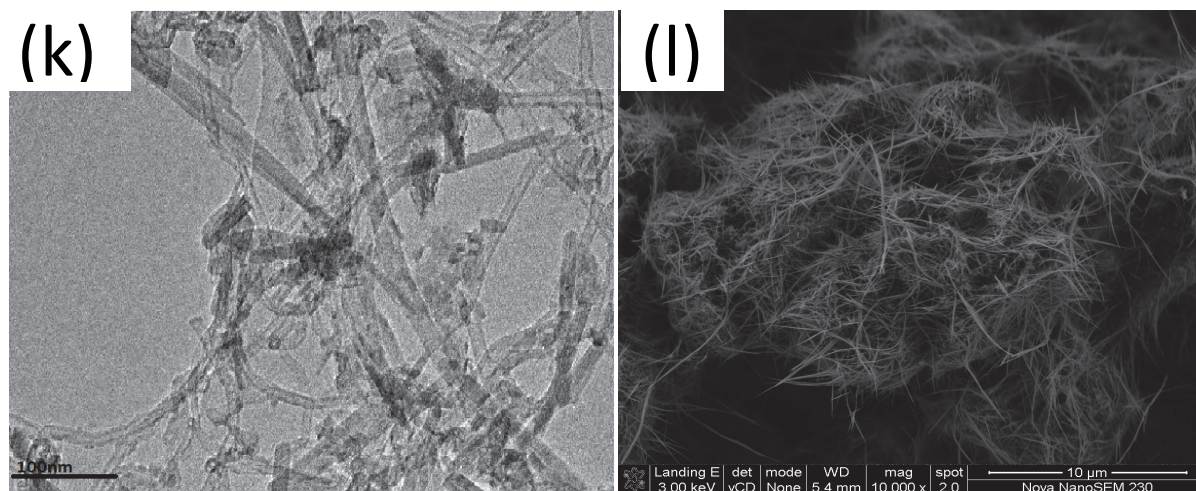


**Figure 6.2.1.** Micrographs of MnO<sub>2</sub>/C LTSS 5hrs, TEM (g) and SEM (h), MnO<sub>2</sub>/AC LTSS 5hrs, TEM (i) and SEM (j), MnO<sub>2</sub>/CNT LTSS 5hrs, TEM (k) and SEM (l).

Figure {6.2.1(a) – (l)} shows the successful synthesis of the MnO<sub>2</sub> carbon composites using LTSS reaction at 3hrs and 5hrs dwell times. The fibrous crystals, typical of a natural hollandite, can be observed on the micrographs successfully adhered onto the support materials.

SEM micrographs of the LTSS synthesized products indicate that the product are still self-organized into dendritic nanostructures on the carbon and activated carbon supports, with high quantities and that the nanocluster arrays are composed of uniform tetragonal prism nanorods. The activated carbon supported materials display a much more ordered arrangement as compared to the other supports with uniform particle size distribution. The carbon nanotubes supported materials displayed a more intertwined elongated fibrous arrangement.

TEM micrographs show high dispersion of MnO<sub>2</sub> nanorods on the carbon support materials with the MnO<sub>2</sub> nanorods adherence on the outer walls of the carbon nanotubes. Elemental composition of the LTSS reaction synthesized MnO<sub>2</sub> electrode materials were studied using TEM EDX. The TEM-EDX revealed that no impurities were observed from the samples.

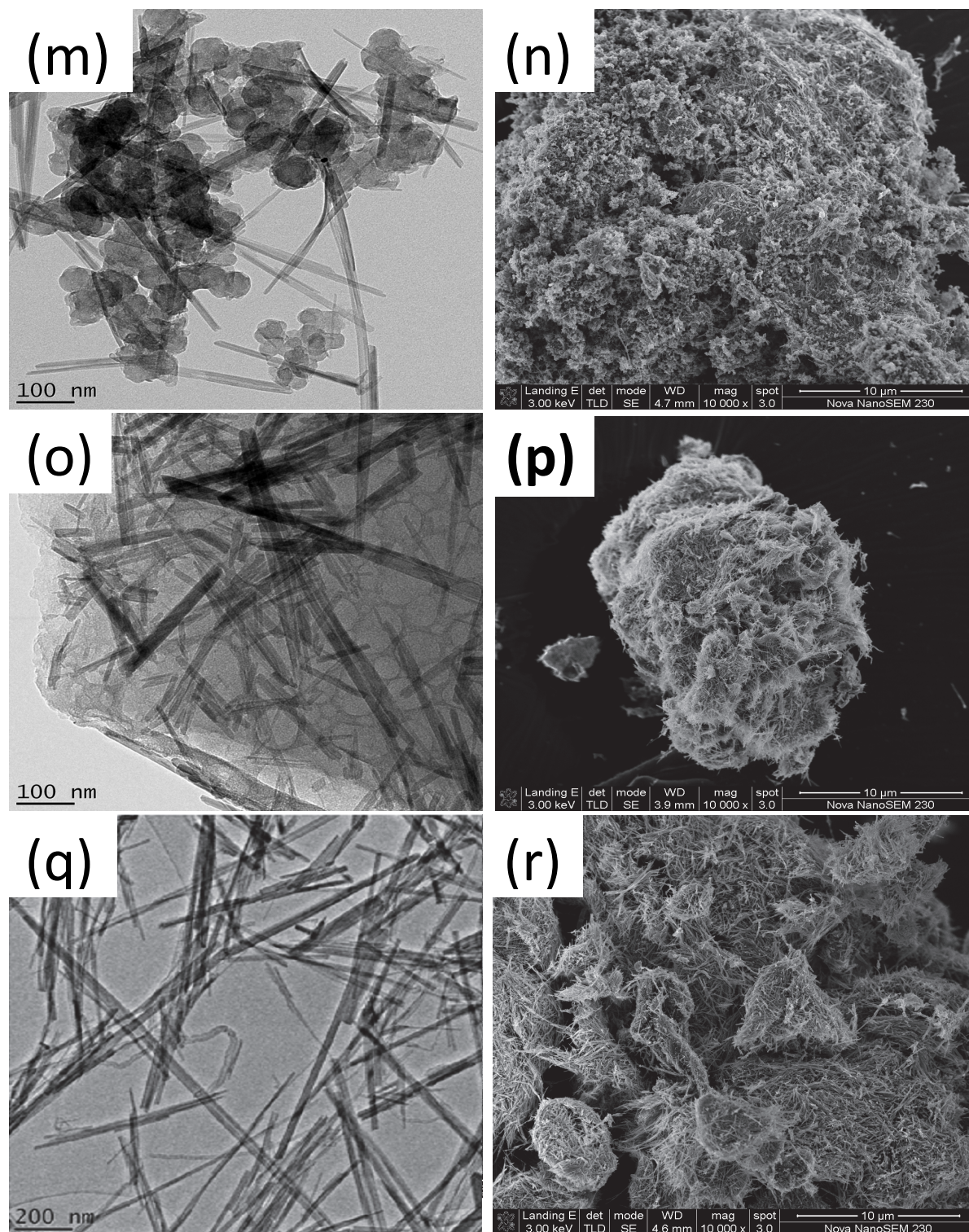


**Figure 6.2.1:** Micrographs of MnO<sub>2</sub>/C HYDRO 3hrs, TEM (m) and SEM (n), MnO<sub>2</sub>/AC HYDRO 3hrs, TEM (o) and SEM (p), MnO<sub>2</sub>/CNT HYDRO 3hrs, TEM (q) and SEM (r).

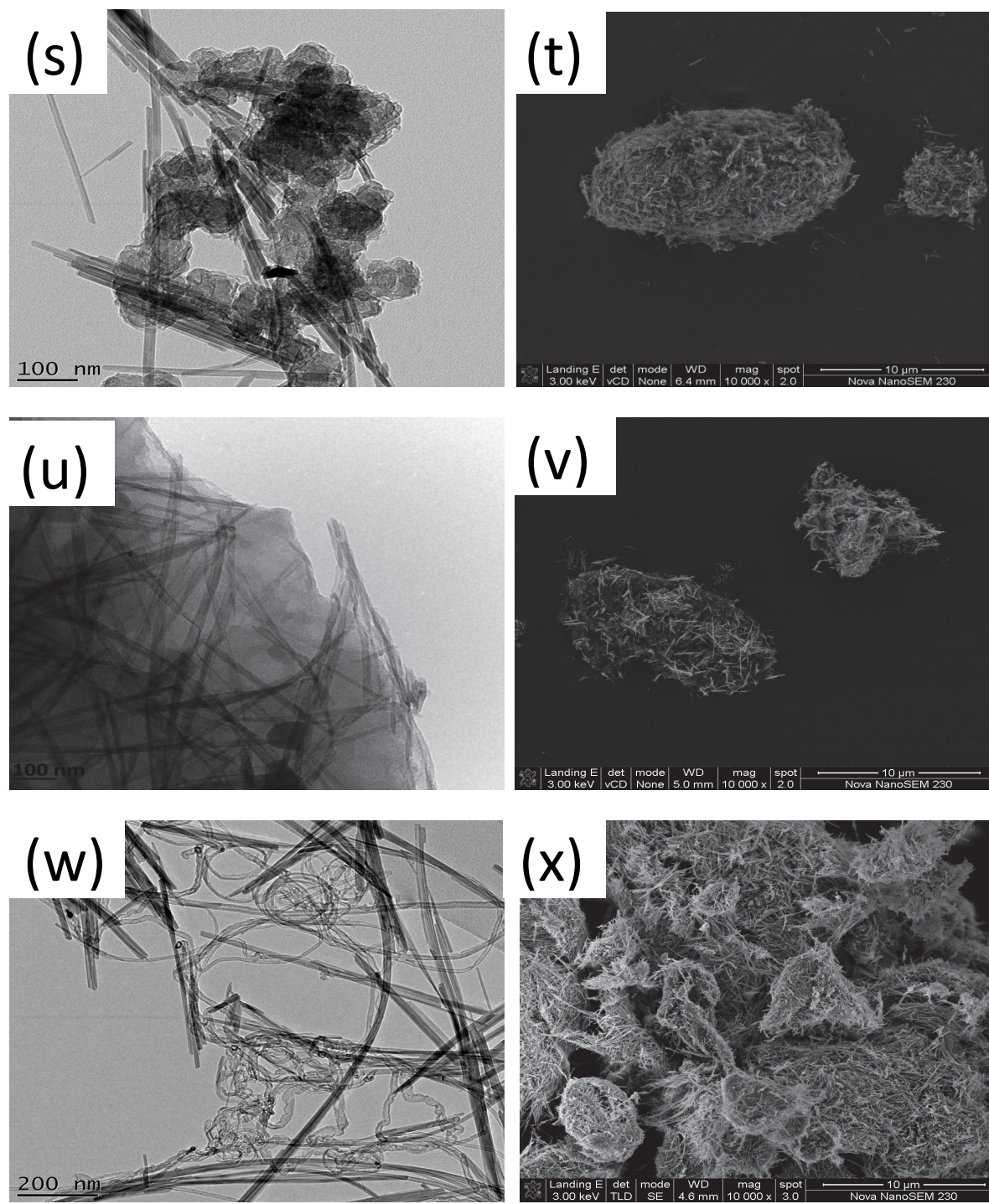


**Figure 6.2.1:** Micrographs of MnO<sub>2</sub>/C HYDRO 5hrs, TEM(s) and SEM (t), MnO<sub>2</sub>/AC HYDRO 5hrs, TEM(u) and SEM (v), MnO<sub>2</sub>/CNT HYDRO 5hrs, TEM (w) and SEM(x).

Figure {6.2.1 (m)–(x)} shows the successful synthesis of the MnO<sub>2</sub> carbon composites using hydrothermal method at 3hrs and 5hrs dwell times. The prismatic crystals, can be

observed on the micrographs successfully adhered onto the support materials.

SEM micrographs of the hydrothermal synthesized products show the intercrossed nanorods successfully adhered to the carbon supports. The carbon materials supported MnO<sub>2</sub> at (3hrs) show good particle dispersion and uniform particle size whereas with the MnO<sub>2</sub> (5hrs) the particles vary in shape and sizes.

TEM micrographs show high dispersion of MnO<sub>2</sub> nanorods on the carbon support materials and the MnO<sub>2</sub> nanorods adherence on the outer walls of the carbon nanotubes.

Elemental composition study of the hydrothermal method synthesized MnO<sub>2</sub> electrode materials were studied using TEM EDX. The TEM-EDX revealed that no impurities were observed from the samples

### **6.2.2 Particle size and crystallinity study of the synthesized MnO<sub>2</sub> carbon composites electrode materials**

Particle size and crystallinity study of the low temperature solid state reaction and hydrothermal method synthesized MnO<sub>2</sub> carbon composite electrode materials was studied with X-ray diffraction technique. Figures (6.2.2.1), (6.2.2.2) and (6.2.2.3) show XRD patterns of the obtained MnO<sub>2</sub> carbon composites electrode materials synthesized using low temperature solid state reaction and hydrothermal method.

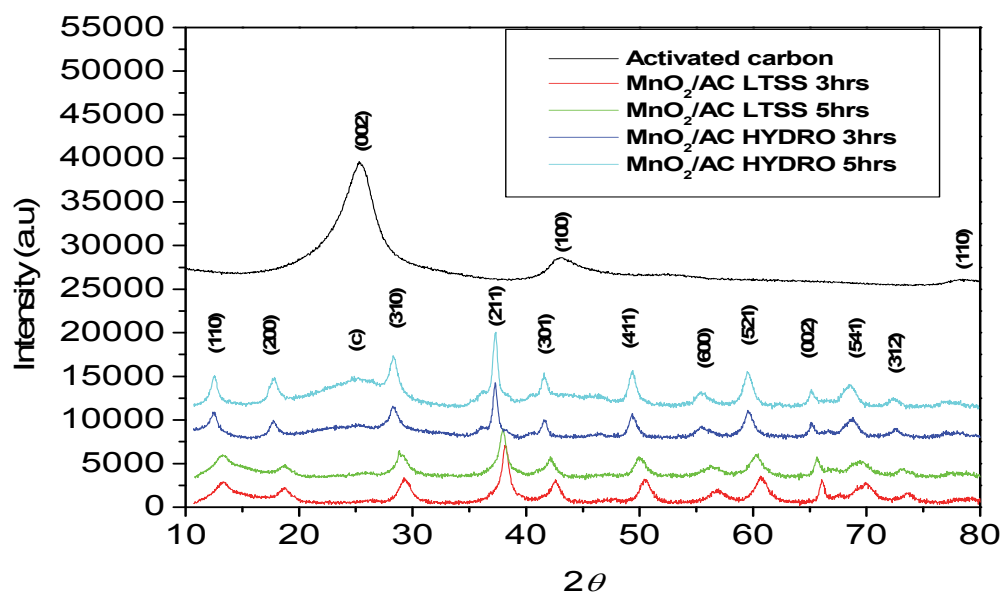


**Figure 6.2.2.1:** XRD patterns of LTSS (3hrs and 5hrs) method and Hydrothermal method (3hrs and 5hrs) synthesized MnO<sub>2</sub>/AC electrode materials.

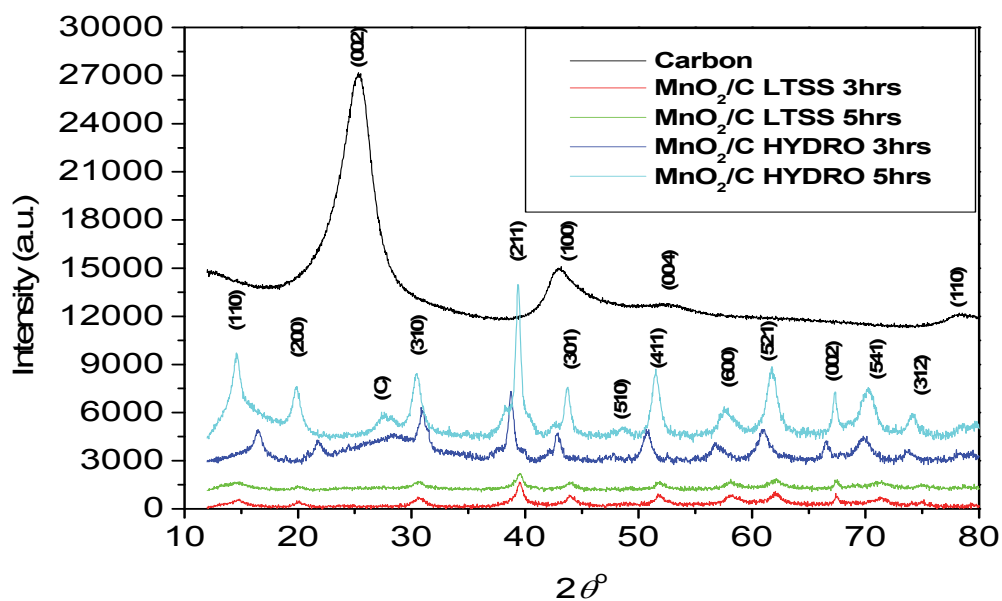


**Figure 6.2.2.2:** XRD patterns of LTSS (3hrs and 5hrs) method and Hydrothermal method (3hrs and 5hrs) synthesized MnO<sub>2</sub>/C electrode materials.

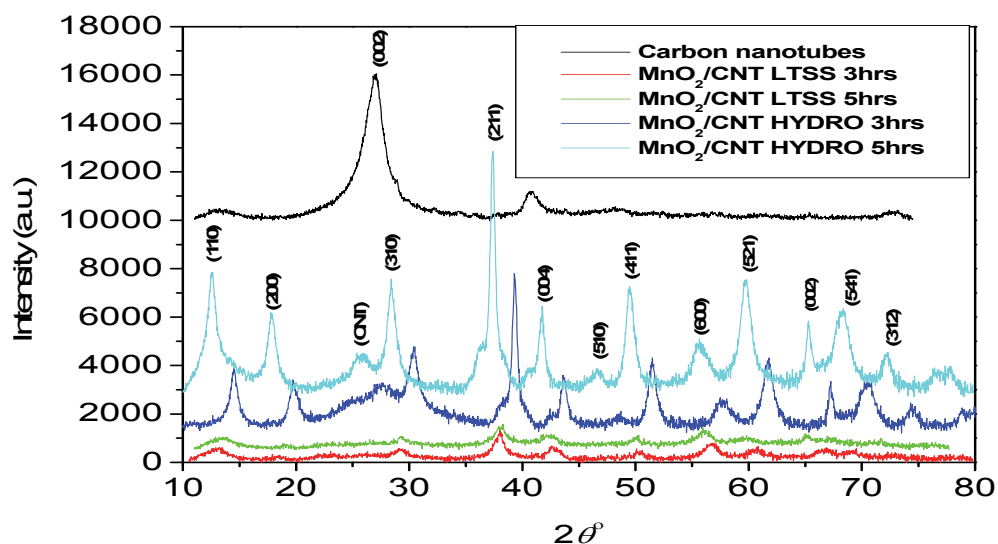


**Figure 6.2.2.3:** XRD patterns of LTSS (3hrs and 5hrs) method and Hydrothermal method (3hrs and 5hrs) synthesized  $\text{MnO}_2/\text{CNT}$  electrode materials.

According to the obtained results, the materials can be assigned to tetragonal  $\alpha$   $\text{MnO}_2$ . The diffraction peak centered at around  $27^\circ$  is attributed to the (0 0 2) plane of the hexagonal phase of the carbon support. The particle sizes were determined using the Scherrer equation (3.1) and the results are tabulated in table (6.2.2.1).

Comparing these trends with that of the unsupported materials, an increase in particle size was observed with the with  $\text{MnO}_2/\text{C}$ ,  $\text{MnO}_2/\text{AC}$  and  $\text{MnO}_2/\text{CNT}$  (3hrs and 5hrs) synthesized with LTSS method, this increase is associated with the shift to the lower 2 theta values which is as a result in the slight increase in lattice spacing. The increase or decrease in lattice spacing is as a result of the change in crystalline structure of the materials as the alloying with the support material takes place.

With the  $\text{MnO}_2/\text{C}$ ,  $\text{MnO}_2/\text{AC}$  and  $\text{MnO}_2/\text{CNT}$  (3hrs and 5hrs) synthesized with the hydro method, a different trend was observed.  $\text{MnO}_2/\text{AC}$  samples the particle size also increased with the increase in lattice spacing and a shift to the lower 2 theta values.  $\text{MnO}_2/\text{C}$

products, the shift to the lower theta values and increase in lattice spacing did not increase their particle size, instead it was decreased.

With MnO<sub>2</sub>/CNT products a shift to the lower theta values was observed without a change in their d spacing which resulted in decrease in particle size. From the trends that were observed, the lattice spacing of the supported materials proved to play an important role on the particle size distribution of the materials.

**Table 6.2.2.1:** Particle size (D) and Inter-planar spacing (d) in Hydrothermal and LTSS prepared MnO<sub>2</sub> carbon composites.

MnO <sub>2</sub>	Facet (211) 20	Facet (301) 20	Facet (411) 20	Facet( 521) 20	d (211) (Å)	d (301) (Å)	d (411) (Å)	d (521) (Å)	D (211) (nm)	D (301) (nm)	D (411) (nm)	D (521) (nm)
MnO <sub>2</sub> /C (3hrs)	37.5	41.9	49.9	60.1	2.38	2.13	1.81	1.55	12.7	10.3	6.9	7.8
MnO <sub>2</sub> /AC (3hrs)	37.5	41.9	49.9	60.0	2.38	2.13	1.81	1.55	13.7	9.8	8.8	7.9
MnO <sub>2</sub> /C (5hrs)	37.5	41.9	49.8	60.0	2.38	2.13	1.81	1.55	10.4	10.6	7.1	7.1
MnO <sub>2</sub> /Ac (5hrs)	37.5	41.9	49.8	60.2	2.38	2.13	1.81	1.55	11.0	10.0	6.4	7.2
MnO <sub>2</sub> /C Hydr (3hrs)	37.3	41.6	49.6	59.8	2.38	2.19	1.85	1.55	13.4	12.4	9.4	5.6
MnO <sub>2</sub> /AC Hydr (3hrs)	37.3	41.6	49.4	59.5	2.38	1.85	1.85	1.55	17.9	16.9	16.8	8.2
MnO <sub>2</sub> /C Hydr (5hrs)	35.5	40.0	47.7	57.9	2.53	2.25	1.89	1.58	14.9	12.7	8.9	8.5
MnO <sub>2</sub> /AC Hydr (5hrs)	35.3	39.6	47.4	57.9	2.53	2.25	1.94	1.58	15.8	16.6	9.5	7.6
MnO <sub>2</sub> /CNT (3hrs)	37.5	42.1	49.6	60.3	2.38	2.13	1.85	1.53	11.6	10.1	8.3	3.6
MnO <sub>2</sub> /CNT (5hrs)	37.5	42.2	49.9	59.9	2.38	2.13	1.85	1.58	11.6	10.1	8.3	6.5
MnO <sub>2</sub> /CNT Hydr (3hrs)	39.3	43.6	51.5	62.0	2.31	2.08	1.77	1.50	13.4	11.2	8.2	6.0
MnO <sub>2</sub> /CNT Hydr (5hrs)	37.4	41.7	49.5	59.8	2.38	2.19	1.85	1.55	13.0	12.0	8.0	6.4

### 6.2.3 BET surface area of both LTSS method and Hydrothermal method synthesized MnO<sub>2</sub> carbon composites electrode materials.

The porous texture of any type of carbon has an immediate relevance (positive or

negative) on reactivity and on most of their applications. Therefore, knowledge about their porosity, pore size distribution and surface area is essential.

BET analysis allows us to show the influence of both, the structural organization and the different treatments on the interfacial characteristics of these nanocarbons. The results obtained for the electrode materials are presented in this section.

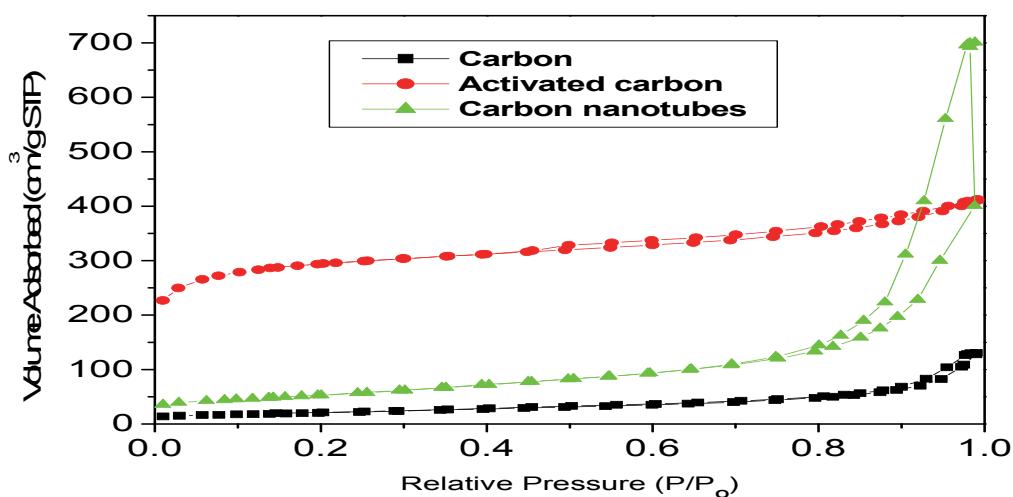


**Figure 6.2.3.1:** The nitrogen adsorption isotherms of carbon support materials at 77K.

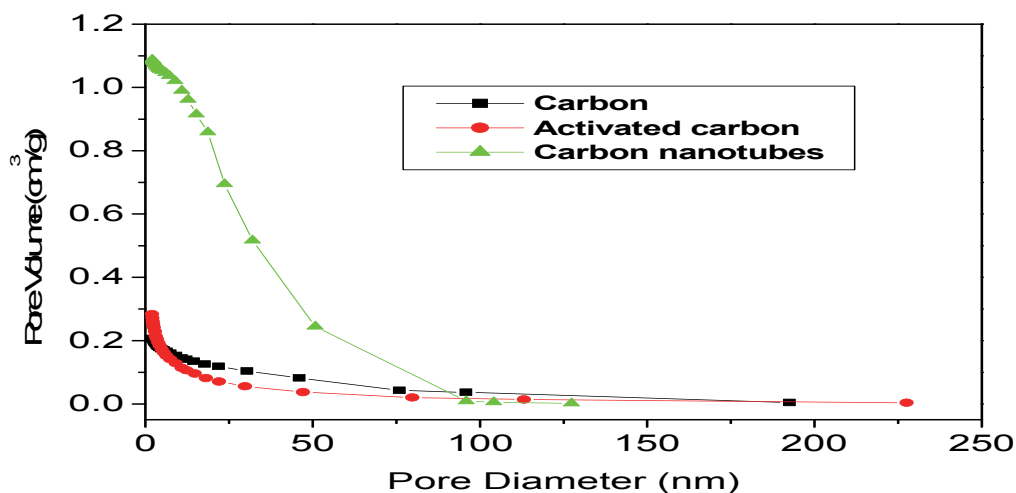


**Figure 6.2.3.2:** Barrett-Joyner and Halenda (BJH) pore size distribution plots carbon support materials at 77K.



**Table 6.2.3.1:** Surface Area and Porosity Data for carbon support materials.

Electrode Material	BET Surface Area (m <sup>2</sup> /g)	External Surface Area (m <sup>2</sup> /g)	Internal Pore area (m <sup>2</sup> /g)	Pore Volume Ads. (cm <sup>3</sup> /g)	Pore Volume Des. (cm <sup>3</sup> /g)	Av. Ads Pore Diameter (nm)	Av. Des Pore Diameter (nm)
<b>Carbon</b>	72.29	74.61	118.70	0.206	0.206	10.29	9.91
<b>Activated carbon</b>	992.26	312.39	218.39	0.284	0.295	5.20	4.84
<b>Carbon nanotubes</b>	188.78	185.72	224.31	1.091	1.090	19.42	18.20

The BET surface area of the support materials, carbon, activated carbon and carbon nanotubes was determined to be 72.29m<sup>2</sup>/g, 992.26m<sup>2</sup>/g, and 188.78m<sup>2</sup>/g, respectively. Figure (6.2. 3.1) shows the nitrogen adsorption isotherms of carbon support materials at 77K. From the isotherms shown in the figure the amount of adsorbed nitrogen is in this order, 700 cm<sup>3</sup>/g for carbon nanotubes > 400 cm<sup>3</sup>/g for activated carbon > 150 cm<sup>3</sup>/g for carbon. However, when we observe the BET surface areas of the materials, activated carbon would be expected to have the highest nitrogen adsorption as compared to carbon nanotubes but in this case the gas adsorption of activated carbon is that of a Type II isotherm whereby the gas adsorption is a contribution from the external surface area. Porous carbon sample only has a specific surface area of 72.29m<sup>2</sup>/g, due to its large pore sizes and the existence of closed pores which cannot be reached by any adsorbate in the spheres [324]. It can be noted from the above table that the greater the volume of pores of a material the higher the rate of adsorption regardless of the BET surface area.

Figure 6.2.3.2 presents the Barrett-Joyner and Halenda pore size distribution plots carbon support materials at 77K and the pores size distribution of the carbon support materials is mostly concentrated between 2–20nm, confirming that the materials are composed mainly of mesopores.

These support materials were used to support the MnO<sub>2</sub> electrode materials presented in the preceding chapter and the surface area and porosity of the supported material was studied and the results are tabulated in table (6.2.3.2)

**Table 6.2.3.2:** Surface Area and Porosity Data for both the hydrothermally and LTSS hen

Electrode Material	BET Surface Area (m <sup>2</sup> /g)	External Surface Area (m <sup>2</sup> /g)	Internal Pore Area (m <sup>2</sup> /g)	Pore Volume Ads. (cm <sup>3</sup> /g)	Pore Volume Des. (cm <sup>3</sup> /g)	Av. Ads Pore Diameter (nm)	Av. Des Pore Diameter (nm)
MnO <sub>2</sub> /C (3hrs)	103.50	103.51	118.70	0.267	0.265	9.00	8.18
MnO <sub>2</sub> /AC (3hrs)	72.89	72.06	82.42	0.219	0.219	10.65	10.54
MnO <sub>2</sub> /CNT (3hrs)	94.48	93.58	105.39	0.306	0.305	11.62	10.51
MnO <sub>2</sub> /C (5hrs)	89.72	86.60	100.79	0.374	0.373	14.86	13.46
MnO <sub>2</sub> /AC (5hrs)	55.65	54.40	69.93	0.231	0.231	13.20	12.32
MnO <sub>2</sub> /CNT (5hrs)	45.44	44.00	51.51	0.167	0.167	13.00	11.68
MnO <sub>2</sub> /C (hydro 3hrs)	49.01	44.62	52.29	0.191	0.188	14.59	14.71
MnO <sub>2</sub> /AC(hydro 3hrs)	110.28	79.98	86.72	0.197	0.207	9.01	9.26
MnO <sub>2</sub> /CNT(hydro 3hrs)	97.19	91.11	109.62	0.341	0.340	12.43	12.40
MnO <sub>2</sub> /C (hydro 5hrs)	71.10	65.84	75.84	0.213	0.214	11.26	11.13
MnO <sub>2</sub> /AC (hydro 5hrs)	94.70	91.10	102.94	0.346	0.346	13.44	13.25
MnO <sub>2</sub> /CNT(hydro 5hrs)	99.52	95.68	105.56	0.324	0.323	12.26	12.11

When comparing the trends of supported electrode materials with that of the unsupported, it was observed that for the LTSS synthesized materials the pore volumes and sizes were enhanced which is in agreement with the particle size increase determined by XRD analysis.

With the hydrothermal method synthesized supported electrode materials, XRD showed a decrease in particle size of the supported materials which is in agreement with the decrease of the pore volume and pore sizes observed with the BET analysis. Except for the pore volumes of MnO<sub>2</sub>/AC 5hrs and MnO<sub>2</sub>/CNT 3hrs and 5hrs which could be associated with the with the lattice spacing behaviour observed with XRD patterns of the materials. This

behaviour resulted in the increase in porosity which is a result of the  $\text{MnO}_2/\text{AC}$  lattice expansion [248].

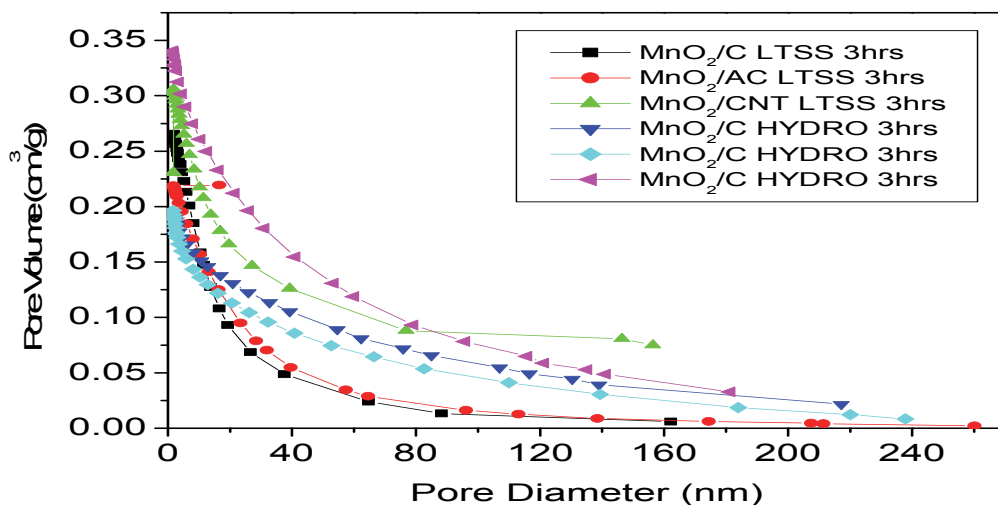


**Figure 6.2.3.3:** Barrett-Joyner and Halenda (BJH) pore size distribution plot of  $\text{MnO}_2$  Carbon composites prepared using LTSS and Hydrothermal method for 3hrs.

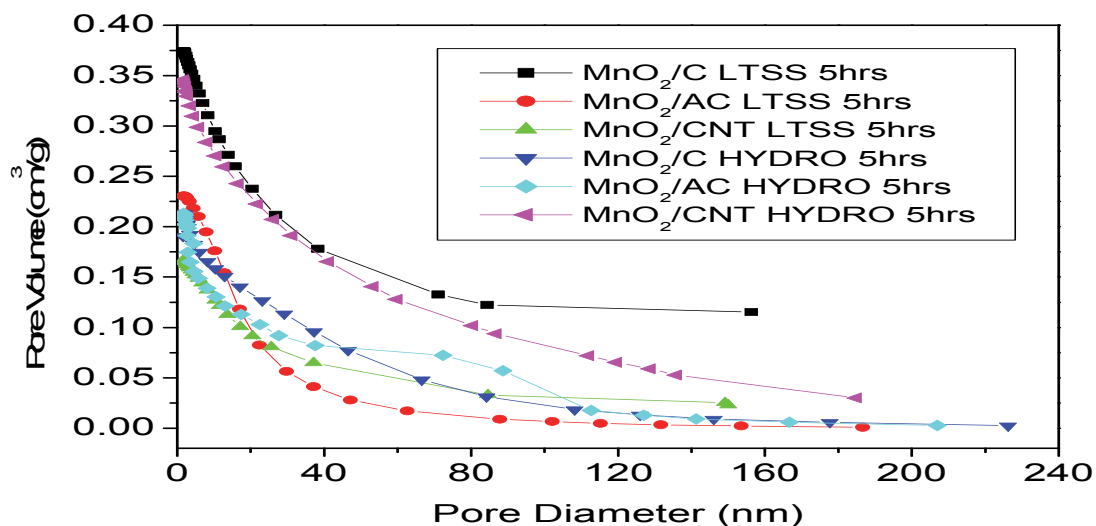


**Figure 6.2.3.4:** Barrett-Joyner and Halenda (BJH) pore size distribution plot of  $\text{MnO}_2$  Carbon composites prepared using LTSS and Hydrothermal method for 5hrs.

Figure (6.2.3.3) and figure (6.2.3.4) presents the Barrett-Joyner and Halenda pore size distribution plots of the carbon supported MnO<sub>2</sub> materials at 77K and the pores size distribution of the carbon support materials is mostly concentrated between 2–40nm, confirming that the materials are composed mainly of mesopores.

### **6.3. ELECTRO-CHEMICAL CHARACTERIZATION OF SINGLE-CRYSTAL MANGANESE OXIDE NANORODS CARBON COMPOSITES**

#### **6.3.1 Cyclic voltammetry**

Cyclic voltammetry (CV) of the LTSS and HYDRO synthesized MnO<sub>2</sub> carbon composites electrode materials were conducted, with MnO<sub>2</sub> carbon composites on a carbon paper used as a working electrode, Ag/AgCl used as a reference electrode, platinum gauze as a counter electrode in 6M KOH electrolyte.

Figure (6.3.1) shows cyclic voltammograms of MnO<sub>2</sub>/AC LTSS (3hrs), MnO<sub>2</sub>/AC LTSS (5hrs), MnO<sub>2</sub>/AC HYDRO (3hrs) and MnO<sub>2</sub>/AC HYDRO (5hrs), figure (6.3.2) shows cyclic voltammograms of MnO<sub>2</sub>/C LTSS (3hrs), MnO<sub>2</sub>/C LTSS (5hrs), MnO<sub>2</sub>/C HYDRO (3hrs) and MnO<sub>2</sub>/C HYDRO (5hrs) and figure (6.3.3) ) shows cyclic voltammograms of MnO<sub>2</sub>/CNT LTSS (3hrs), MnO<sub>2</sub>/CNT LTSS (5hrs), MnO<sub>2</sub>/CNT HYDRO (3hrs) and MnO<sub>2</sub>/CNT HYDRO (5hrs) respectively, at 5, 10, 20 and 25mV/s scan rates with 50 and 100mV/s scan rates found in Appendix A.

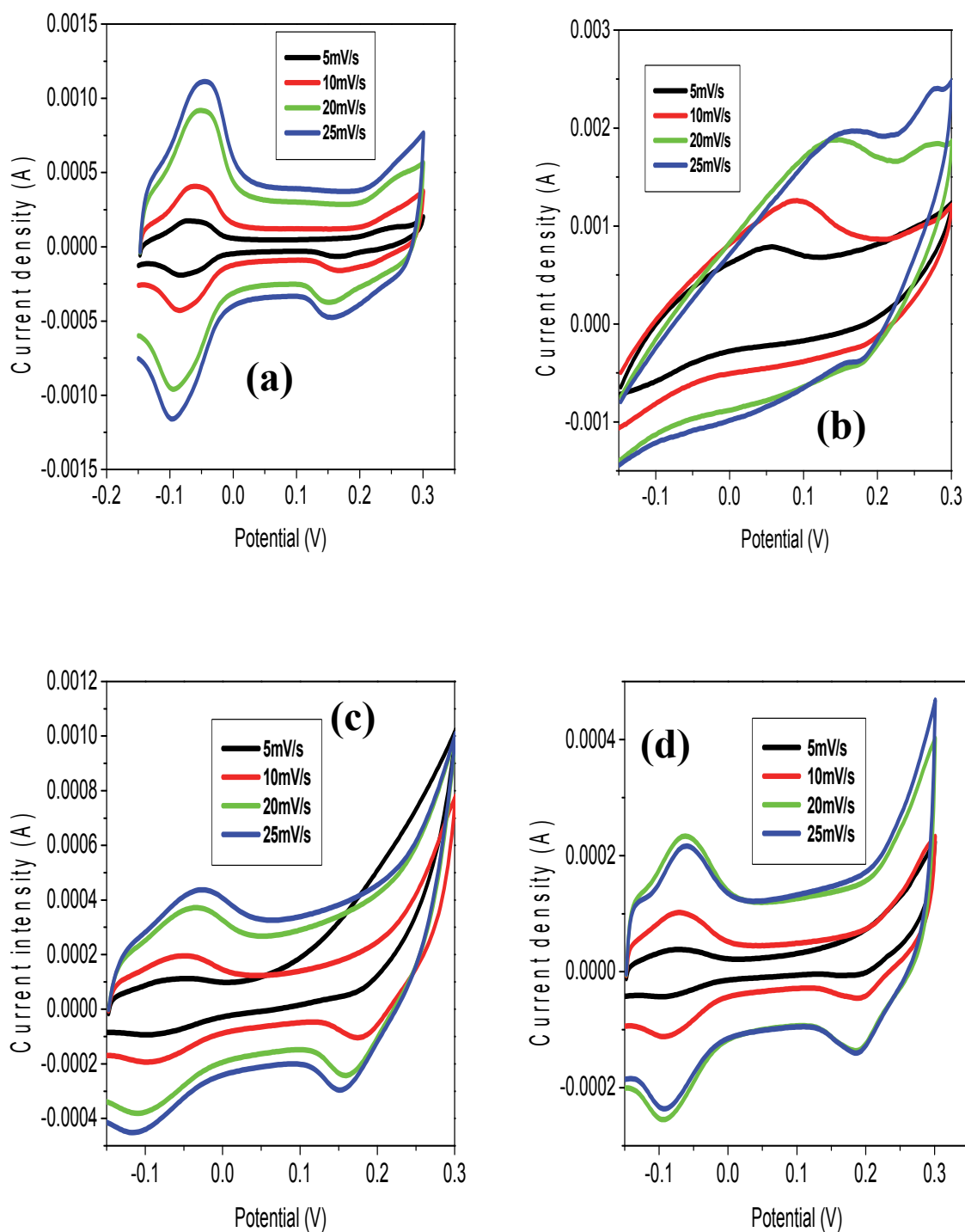


**Figure 6.3.1:** Cyclic voltammograms of MnO<sub>2</sub>/AC LTSS 3hrs (a), 5hrs (b) and MnO<sub>2</sub> HYDRO/AC 3hrs (c), 5hrs (d), respectively.

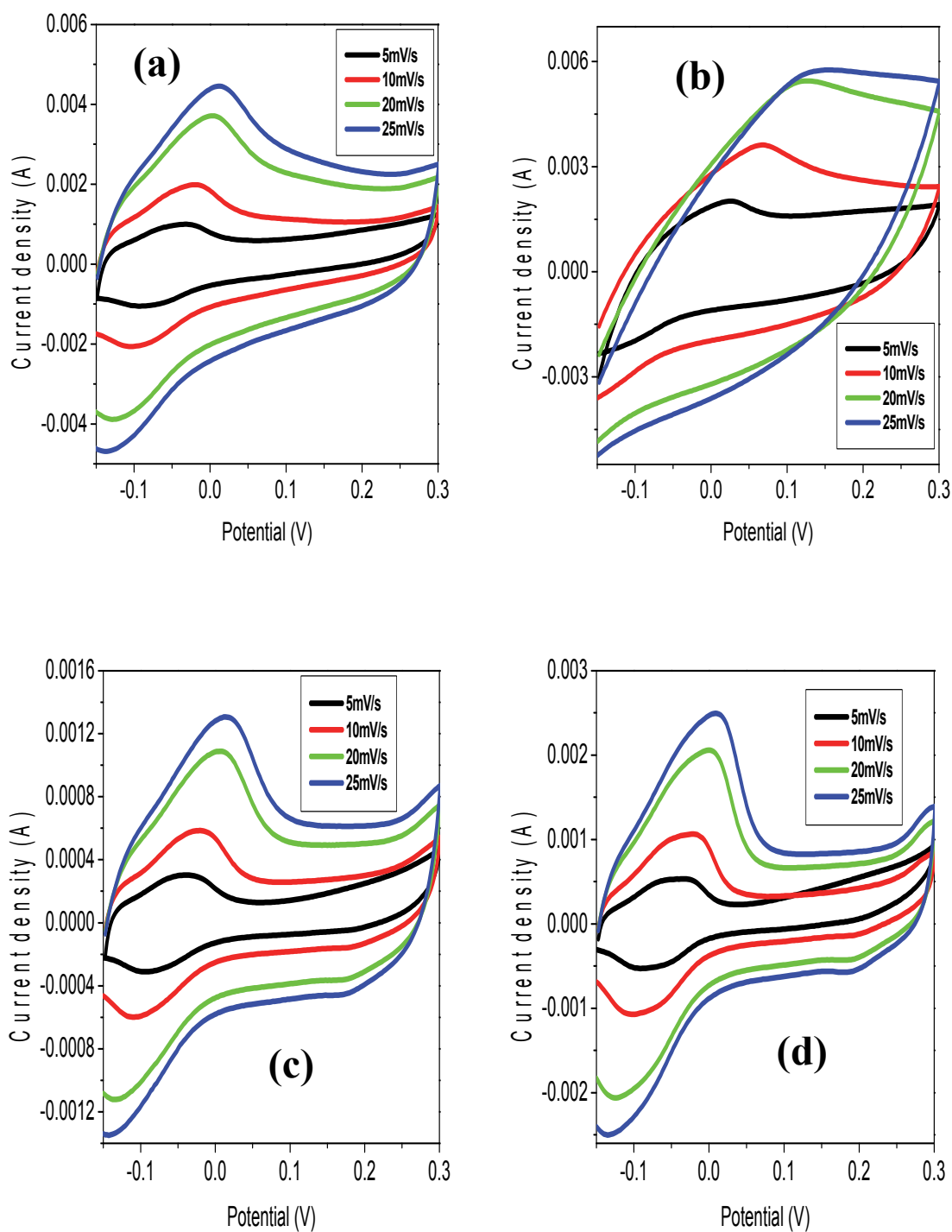


**Figure 6.3.2:** Cyclic voltammograms of MnO<sub>2</sub>/C LTSS 3hrs (a), 5hrs (b) and MnO<sub>2</sub> HYDRO/C 3hrs (c), 5hrs (d), respectively.

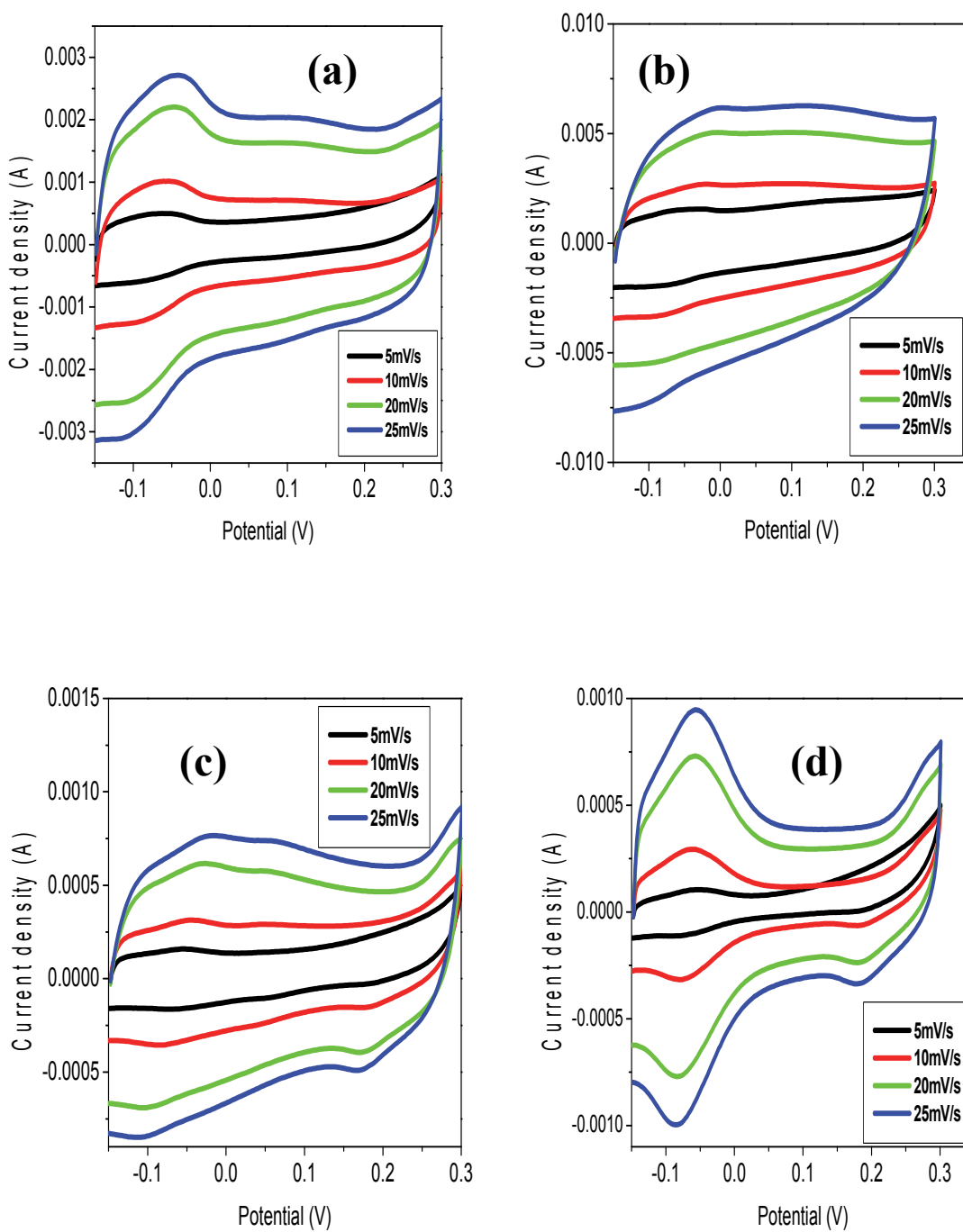


**Figure 6.3.3:** Cyclic voltammograms of MnO<sub>2</sub>/CNT LTSS 3hrs (a), 5hrs (b) and MnO<sub>2</sub> HYDRO/CNT 3hrs (c), 5hrs (d), respectively.

The CV curves are not ideally rectangular in shape but electrodes exhibit mirror image traces characteristic of a capacitor. Most curves show an increase in capacitance towards the increasing negative potentials. The recorded performance for the LTSS synthesized  $\text{MnO}_2$  (3hrs) when supported with activated carbon, carbon and carbon nanotubes was 100F/g, 263 F/g and 523F/g, respectively. And these values were obtained at the scan rate of 5mV/s. For  $\text{MnO}_2$  LTSS 5hrs, the performance in the same order of support material was recorded as 239F/g, 284F/g and 657F/g, respectively. The  $\text{MnO}_2/\text{CNT}$  nanocomposite electrode in the present study exhibits a superior supercapacitive performance with improved specific capacitance and rate capability compared to  $\text{MnO}_2/\text{CNT}$  nanocomposites in previous studies.  $\text{MnO}_2/\text{CNT}$  nanocomposite electrode prepared by Li et al. [284] was able to deliver a specific capacitance of 205 F/g at a scan rate of 2mV/s, but only 43.2F/g at a scan rate of 50mV/s.

Mats of highly entangled carbon nanotubes offer an open network of mesopores which favors the access of molecules and ions to the active surface [303] and this has been evident on the carbon nanotubes supported LTSS synthesized electrode materials. The LTSS synthesized materials performed better when carbon nanotubes were used as a support material compared to other support materials with a capacitance deficit of 3.7% for  $\text{MnO}_2/\text{CNT}$  3hrs and 12.05% capacitance deficit for  $\text{MnO}_2/\text{CNT}$  5hrs when compared to their respective unsupported materials. Hydrothermal method synthesized  $\text{MnO}_2$  carbon composites electrode materials recorded an increase in the capacitance with all the support materials, at 3hrs dwell time, an increase of 63.4% when supported with the activated carbon, 67.3% when supported with carbon and 80.8% when supported with carbon nanotubes was recorded. At 5hrs dwell time a 64.6% capacitance increase with the carbon support and a 58.4% with carbon nanotubes.



The cyclic voltammetric results confirm that, although activated carbon has a high specific surface area, it has a low electrical conductivity which tends to be a limiting factor in high power density supercapacitors [325] and in our study it displayed low capacitance values compared to the other two carbon supports. The calculated capacitance values for the MnO<sub>2</sub> supported materials are tabulated in tables (6.3.1- 6.3.3) below.

**Table 6.3.1:** Cyclic voltammetry capacitance values of MnO<sub>2</sub>/AC in 6M KOH

	<b>5mV/s</b>	<b>10mV/s</b>	<b>20mV/s</b>	<b>25mV/s</b>	<b>50mV/s</b>	<b>100mV/s</b>
<b>MnO<sub>2</sub>/AC LTSS (3hrs)</b>	100F/g	54F/g	58F/g	58F/g	55F/g	50 F/g
<b>MnO<sub>2</sub>/AC HYDRO(3hrs)</b>	134F/g	53F/g	33F/g	26F/g	14F/g	10F/g
<b>MnO<sub>2</sub>/AC LTSS (5hrs)</b>	239F/g	169F/g	125F/g	139F/g	119F/g	89F/g
<b>MnO<sub>2</sub>/AC HYDRO(5hrs)</b>	55F/g	27F/g	24F/g	22F/g	21F/g	18F/g

**Table 6.3.2:** Cyclic voltammetry capacitance values of MnO<sub>2</sub>/C in 6M KOH

	<b>5mV/s</b>	<b>10mV/s</b>	<b>20mV/s</b>	<b>25mV/s</b>	<b>50mV/s</b>	<b>100mV/s</b>
<b>MnO<sub>2</sub>/C LTSS (3hrs)</b>	263F/g	243F/g	178F/g	153F/g	118F/g	79F/g
<b>MnO<sub>2</sub>/C HYDRO(3hrs)</b>	150F/g	92F/g	90F/g	81 F/g	72 F/g	59 F/g
<b>MnO<sub>2</sub>/C LTSS (5hrs)</b>	284 F/g	227F/g	216F/g	205F/g	182F/g	142F/g
<b>MnO<sub>2</sub>/C HYDRO(5hrs)</b>	294F/g	178F/g	164F/g	156F/g	141F/g	117F/g

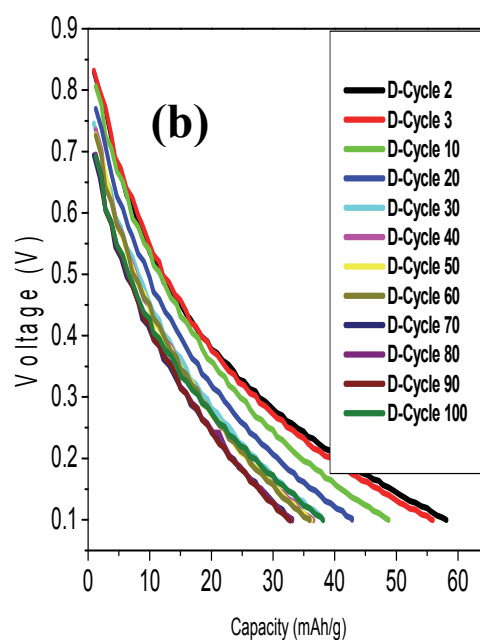
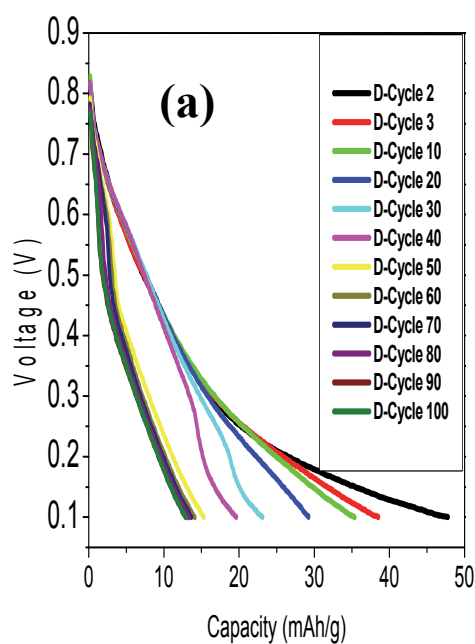
**Table 6.3.3:** Cyclic voltammetry capacitance values of MnO<sub>2</sub>/CNT in 6M KOH

	<b>5mV/s</b>	<b>10mV/s</b>	<b>20mV/s</b>	<b>25mV/s</b>	<b>50mV/s</b>	<b>100mV/s</b>
<b>MnO<sub>2</sub>/CNT LTSS (3hrs)</b>	523F/g	261F/g	250F/g	245F/g	245F/g	216 F/g
<b>MnO<sub>2</sub>/CNT HYDRO(3hrs)</b>	255F/g	150F/g	98F/g	90 F/g	80 F/g	70 F/g
<b>MnO<sub>2</sub>/CNT LTSS (5hrs)</b>	657F/g	243F/g	193F/g	286F/g	177F/g	171F/g
<b>MnO<sub>2</sub>/CNT HYDRO(5hrs)</b>	250F/g	120F/g	93F/g	95F/g	100F/g	95F/g

### 6.3.2 Charge and discharge cycling

The charge/discharge cycling behaviors of the MnO<sub>2</sub> carbon composites electrode materials were tested at the at a charge/discharge current of 200  $\mu$ A in a button cell using 6M KOH as an electrolyte from 0.1V to 1V at room temperature. Figures 6.3.4 to 6.3.8 show charge/discharge curves for the MnO<sub>2</sub> carbon composites electrode materials synthesized using the low temperature solid state reaction and hydrothermal method.

The electrodes in this section were prepared using the method stipulated in Chapter 3, section 3.5.



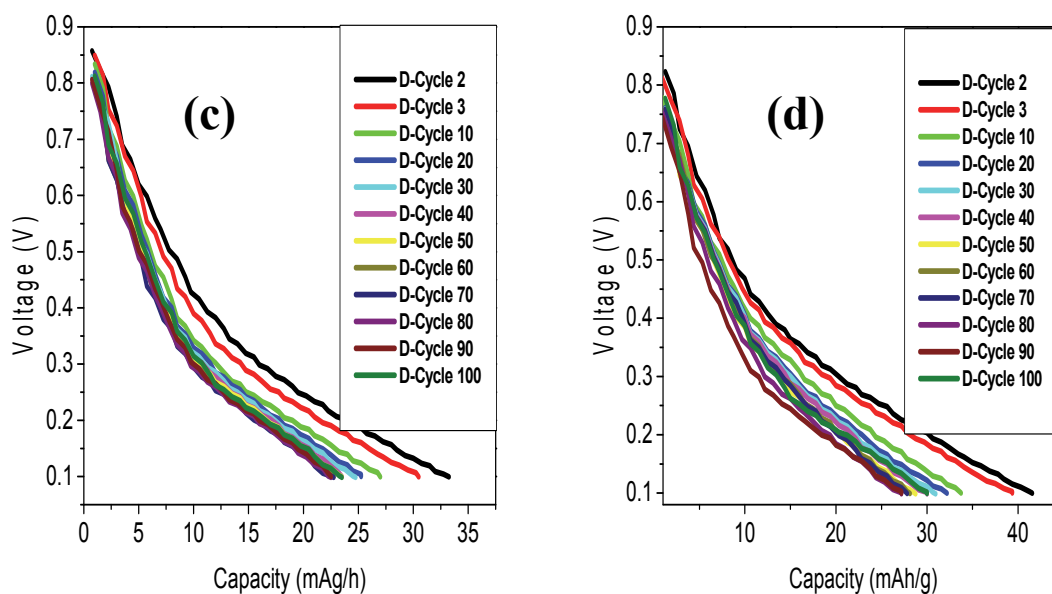


**Figure 6.3.4:** Discharge cycles of (a) MnO<sub>2</sub>/C LTSS (3hrs) (b) (5hrs) and MnO<sub>2</sub>/C HYDRO (c) (3hrs), (d) (5hrs), respectively.

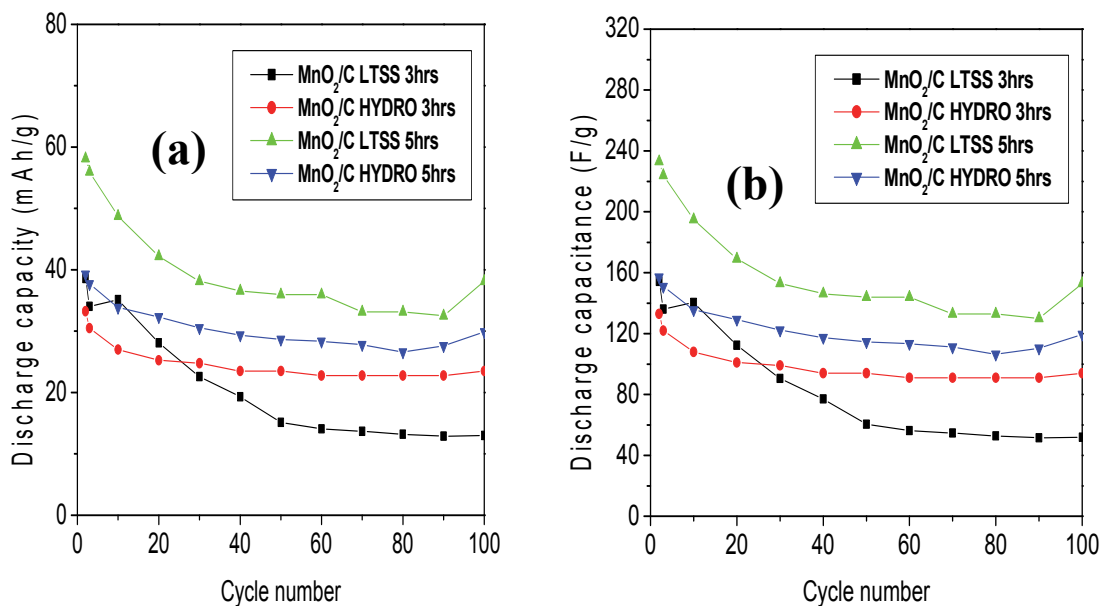


**Figure 6.3.5:** The discharge capacity (a) and (b) discharge capacitance vs. cycle number for the MnO<sub>2</sub>/C electrode materials.

In figure (6.3.4) MnO<sub>2</sub>/C LTSS 3hrs delivered a charge capacitance of 178.7F/g and a discharge capacitance of 154.2F/g for the second cycle with 86.3 % cycle efficiency. For the third cycle, charge capacitance of 161.2F/g and discharge capacitance of 136.1F/g was observed with 84.5% cycle efficiency. 55.7F/g and 51.8F/g charge and discharge capacitance for the 100<sup>th</sup> cycle were observed with 93.0% cycle efficiency. The 100<sup>th</sup> cycle discharge capacitance was 34.0% of the 2<sup>nd</sup> and 38.1% of the 3<sup>rd</sup> cycle.

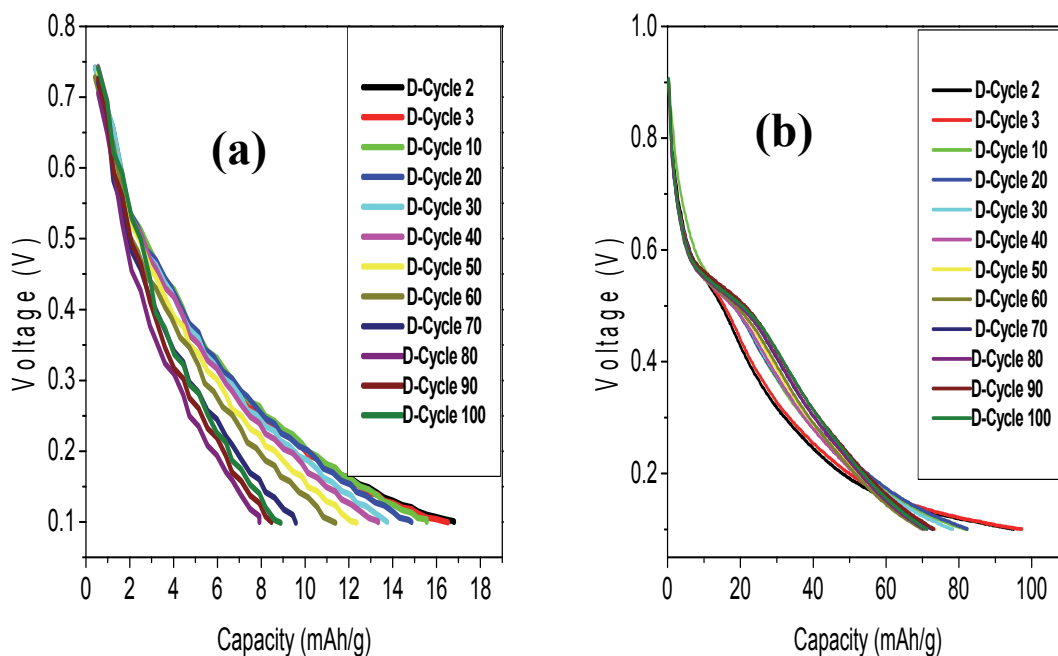
MnO<sub>2</sub>/C HYDRO 3hrs delivered a charge capacitance of 137.0F/g and a discharge capacitance of 133.0F/g for the second cycle with 97.1 % cycle efficiency. For the third cycle, charge capacitance of 134.0F/g and discharge capacitance of 122.0F/g was observed with 91.0% cycle efficiency. 107.0F/g and 94.0F/g charge and discharge capacitance for the 100<sup>th</sup> cycle was observed with 88.0% cycle efficiency. The 100<sup>th</sup> cycle discharge capacitance was 71.0% of the 2<sup>nd</sup> and 77.0% of the 3<sup>rd</sup> cycle.

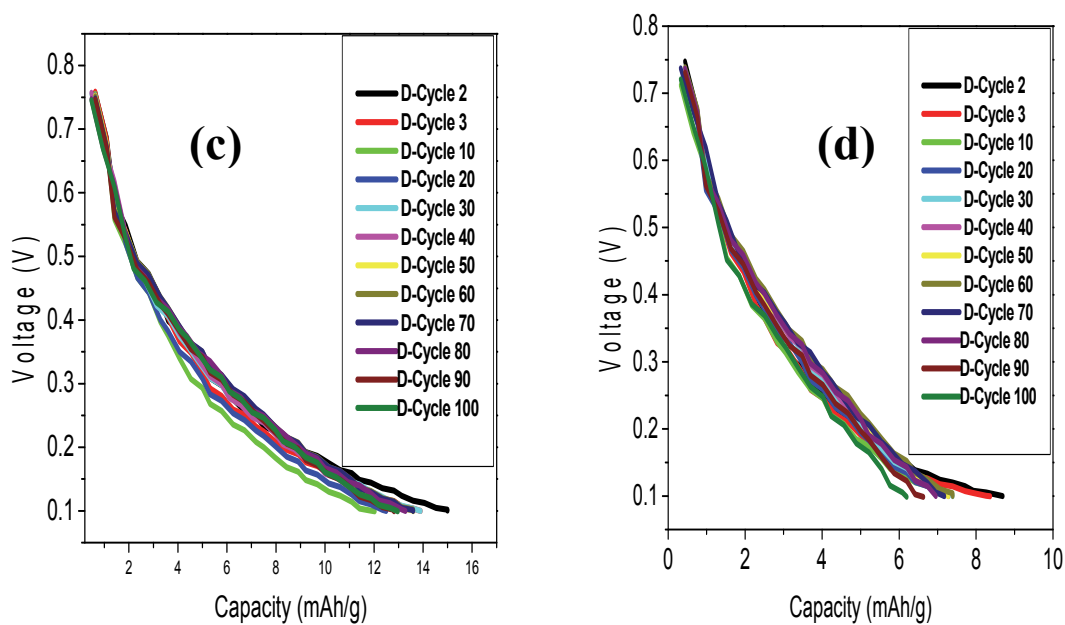
MnO<sub>2</sub>/C LTSS 5hrs delivered a charge capacitance of 241.2F/g and a discharge capacitance of 233F/g for the second cycle with 96.4 % cycle efficiency. For the third cycle, charge capacitance of 228.8F/g and discharge capacitance of 224.0F/g was observed with 97.8% cycle efficiency. 154.0F/g and 153.0F/g charge and discharge capacitance for the 100<sup>th</sup> cycle was observed with 99.2% cycle efficiency. The 100<sup>th</sup> cycle discharge capacitance was 67.0% of the 2<sup>nd</sup> and 68.3% of the 3<sup>rd</sup> cycle.

MnO<sub>2</sub>/C HYDRO 5hrs delivered a charge capacitance of 171.0F/g and a discharge capacitance of 157.0F/g for the second cycle with 92.0% cycle efficiency. For the third cycle, charge capacitance of 162.0F/g and discharge capacitance of 151.0F/g was observed with 93.1% cycle efficiency. 157.7F/g and 119.5F/g charge and discharge capacitance for the 100<sup>th</sup>

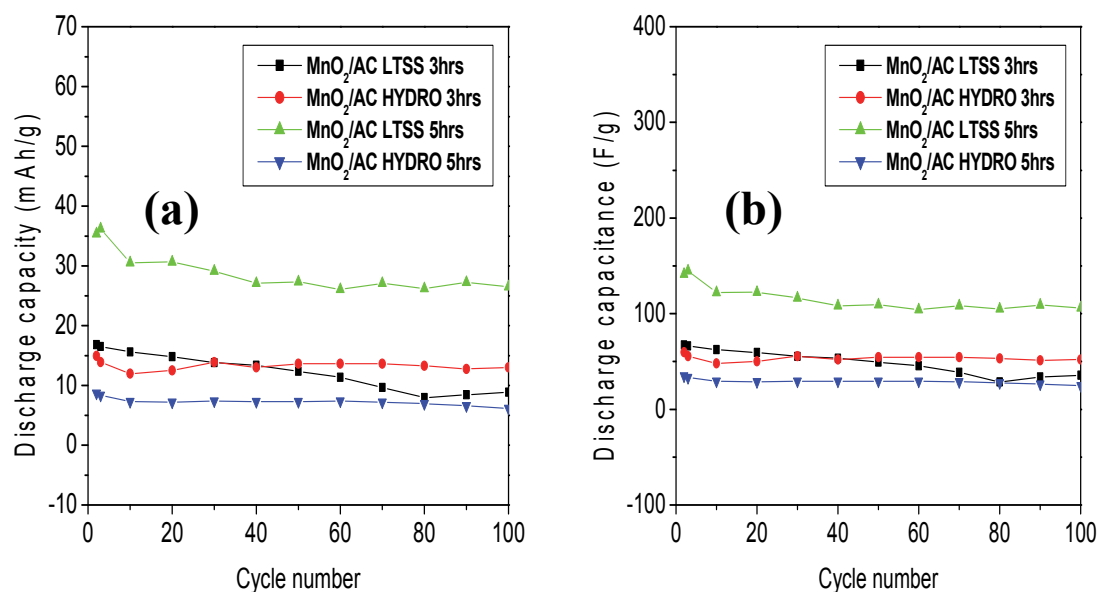
cycle was observed with 76.0% cycle efficiency. The 100<sup>th</sup> cycle discharge capacitance was 75.0% of the 2<sup>nd</sup> and 79.1.0% of the 3<sup>rd</sup> cycle.

Figure (6.3.5) shows that MnO<sub>2</sub>/C LTSS 5hrs has the highest capacitance in comparison with other materials followed by MnO<sub>2</sub>/C HYDRO 5hrs. Indicating that, longer synthesis dwell time favors the activity of these materials. Hydrothermally synthesized electrode materials display better durability with only 29% and 25% capacitance deficit after 100 cycles for MnO<sub>2</sub>/C HYDRO 3hrs and MnO<sub>2</sub>/C HYDRO 5hrs, respectively as opposed to 66% for MnO<sub>2</sub>/C LTSS 3hrs.





**Figure 6.3.6:** Discharge cycles of MnO<sub>2</sub>/AC LTSS (a) (3hrs), (b) (5hrs) and MnO<sub>2</sub>/AC HYDRO (c) (3hrs), (d) (5hrs), respectively.



**Figure 6.3.7:** The discharge capacity (a) and (b) discharge capacitance vs. cycle number for the MnO<sub>2</sub>/AC electrode materials.

In figure (6.3.6) MnO<sub>2</sub>/AC LTSS 3hrs delivered a charge capacitance of 135.88F/g and a discharge capacitance of 67.32F/g for the second cycle with 50.0% cycle efficiency. For the third cycle, charge capacitance of 120.12F/g and discharge capacitance of 66.08F/g was observed with 55.0% cycle efficiency. 60.20F/g and 35.52F/g charge and discharge capacitance for the 100<sup>th</sup> cycle were observed with 59.0% cycle efficiency. The 100<sup>th</sup> cycle discharge capacitance was 53.0% of the 2<sup>nd</sup> and 54.0% of the 3<sup>rd</sup> cycle.

MnO<sub>2</sub>/AC HYDRO 3hrs delivered a charge capacitance of 131.04F/g and a discharge capacitance of 59.74F/g for the second cycle with 46.0 % cycle efficiency. For the third cycle, charge capacitance of 110.80F/g and discharge capacitance of 55.56F/g was observed with 50.1% cycle efficiency. 77.80F/g and 52.08F/g charge and discharge capacitance for the 100<sup>th</sup> cycle was observed with 66.9% cycle efficiency. The 100<sup>th</sup> cycle discharge capacitance was 87.2% of the 2<sup>nd</sup> and 94.0% of the 3<sup>rd</sup> cycle.

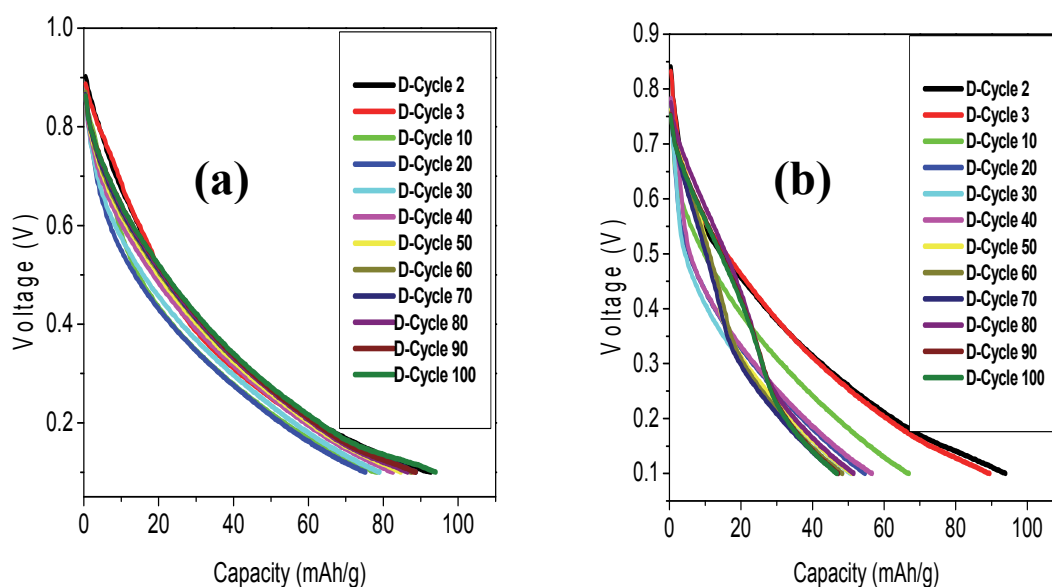
MnO<sub>2</sub>/AC LTSS 5hrs delivered a charge capacitance of 172.16F/g and a discharge capacitance of 141.40F/g for the second cycle with 82.0 % cycle efficiency. For the third cycle, charge capacitance of 200.52F/g and discharge capacitance of 144.76F/g was observed with 72.2% cycle efficiency. 160.76F/g and 106.04F/g charge and discharge capacitance for the 100<sup>th</sup> cycle was observed with 65.9% cycle efficiency. The 100<sup>th</sup> cycle discharge capacitance was 75.0% of the 2<sup>nd</sup> and 73.3% of the 3<sup>rd</sup> cycle.

MnO<sub>2</sub>/AC HYDRO 5hrs delivered a charge capacitance of 53.88F/g and a discharge capacitance of 34.80F/g for the second cycle with 65.0% cycle efficiency. For the third cycle, charge capacitance of 46.12F/g and discharge capacitance of 33.32F/g was observed with 72.2% cycle efficiency. 31.88F/g and 24.64F/g charge and discharge capacitance for the 100<sup>th</sup>

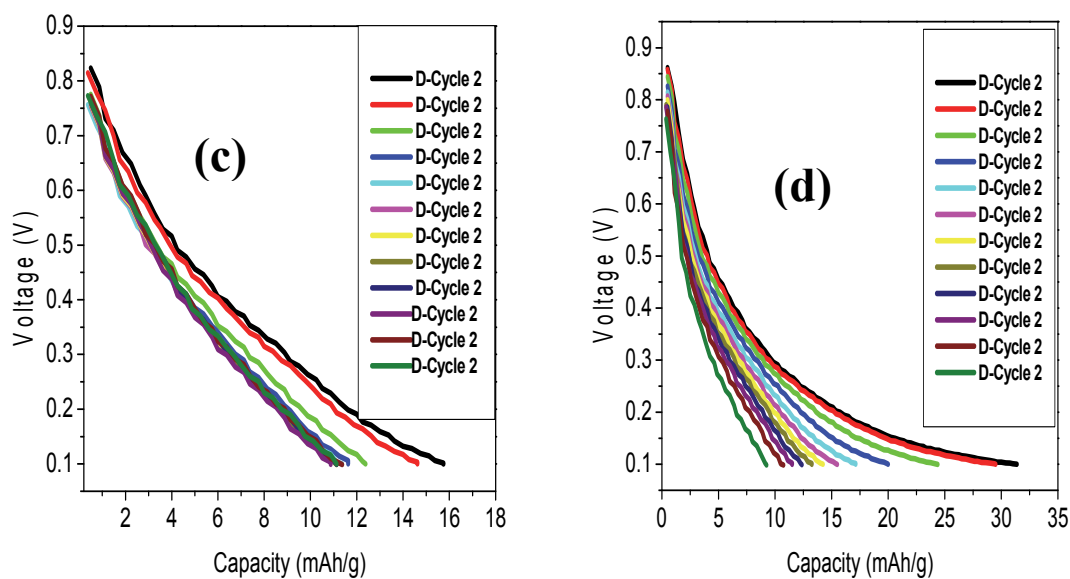
cycle was observed with 67.0% cycle efficiency. The 100<sup>th</sup> cycle discharge capacitance was 71.0% of the 2<sup>nd</sup> and 74.0% of the 3<sup>rd</sup> cycle.

Figure (6.3.7), shows that MnO<sub>2</sub>/AC LTSS 5hrs a higher capacitance than other materials. There is a very interesting phenomenon that we observed in the charge/discharge of these materials. The capacitance did not decrease but actually increased in some subsequent cycles and this process is termed electro-activation. A highly possible reason is that, because engineered or manufactures carbons have an amorphous structure with a more or less disordered microstructure based to that of graphene, the graphene sheets can move to adjust to the different electrolyte ions [62]. The long time charging and discharging may also help the ions accessing fully the graphene sheets to take full advantages of the surface area.

Hydrothermally synthesized electrode materials still displayed better durability with only 12.8% and 29.0% capacitance deficit after 100 cycles for MnO<sub>2</sub>/C HYDRO 3hrs and MnO<sub>2</sub>/C HYDRO 5hrs, respectively as opposed to 47.2% for MnO<sub>2</sub>/C LTSS 3hrs.







**Figure 6.3.8:** Discharge cycles of MnO<sub>2</sub>/CNT LTSS (a) (3hrs), (b) (5hrs) and MnO<sub>2</sub>/CNT HYDRO (c) (3hrs), (d) (5hrs), respectively.

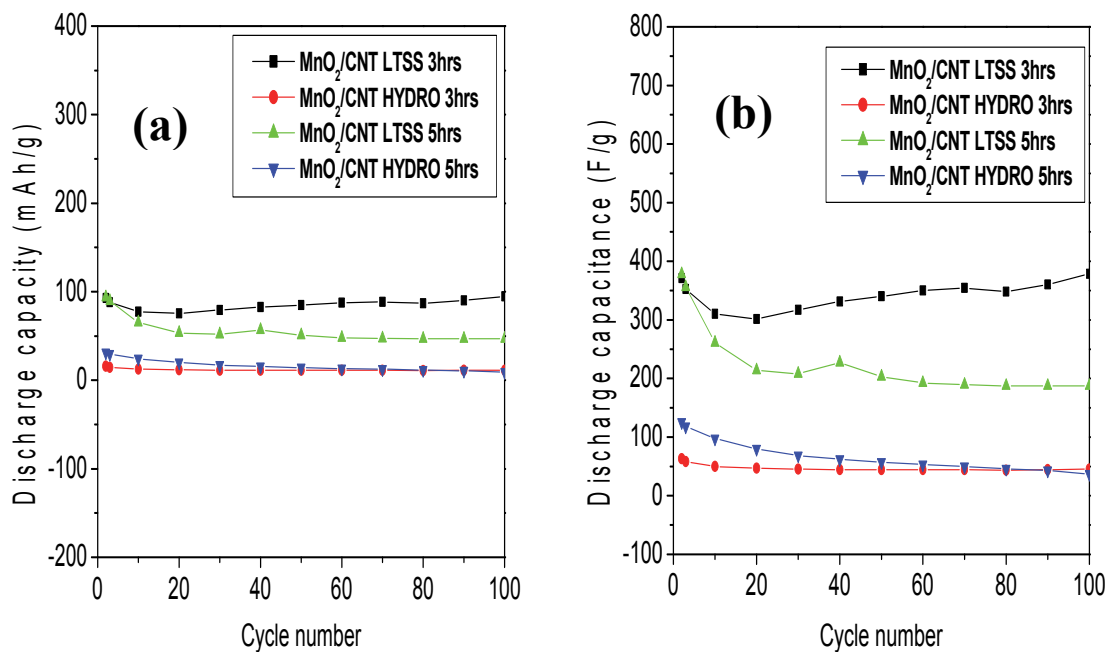


**Figure 6.3.9:** The discharge capacity (a) and (b) discharge capacitance vs. cycle number for the MnO<sub>2</sub>/CNT electrode materials.

In figure (6.3.8) MnO<sub>2</sub>/CNT LTSS 3hrs delivered a charge capacitance of 679.1F/g and a discharge capacitance of 378.0F/g for the second cycle with 55.3% cycle efficiency. For the third cycle, charge capacitance of 585.0F/g and discharge capacitance of 356.0F/g was observed with 61.2% cycle efficiency. 193.0F/g and 187.3F/g charge and discharge capacitance for the 100<sup>th</sup> cycle were observed with 97.1% cycle efficiency. The 100<sup>th</sup> cycle discharge capacitance was 50.0% of the 2<sup>nd</sup> and 53.0% of the 3<sup>rd</sup> cycle.

MnO<sub>2</sub>/CNT HYDRO 3hrs delivered a charge capacitance of 150.0F/g and a discharge capacitance of 63.04F/g for the second cycle with 42.0 % cycle efficiency. For the third cycle, charge capacitance of 121.68F/g and discharge capacitance of 58.40F/g was observed with 48.2% cycle efficiency. 57.52F/g and 45.28F/g charge and discharge capacitance for the 100<sup>th</sup> cycle was observed with 78.5% cycle efficiency. The 100<sup>th</sup> cycle discharge capacitance was 72.0% of the 2<sup>nd</sup> and 78.0% of the 3<sup>rd</sup> cycle.

MnO<sub>2</sub>/CNT LTSS 5hrs delivered a charge capacitance of 463.96F/g and a discharge capacitance of 370.88F/g for the second cycle with 80.0 % cycle efficiency. For the third cycle, charge capacitance of 415.60F/g and discharge capacitance of 352.28F/g was observed with 84.8% cycle efficiency. 423.96F/g and 370.64F/g charge and discharge capacitance for the 100<sup>th</sup> cycle was observed with 87.4% cycle efficiency. The 100<sup>th</sup> cycle discharge capacitance was 99.9% of the 2<sup>nd</sup> and 5.2% more than the 3<sup>rd</sup> cycle.

MnO<sub>2</sub>/CNT HYDRO 5hrs delivered a charge capacitance of 172.84F/g and a discharge capacitance of 125.82F/g for the second cycle with 72.5% cycle efficiency. For the third cycle, charge capacitance of 154.48F/g and discharge capacitance of 118.08F/g was observed with 76.4% cycle efficiency. 45.28F/g and 37.24F/g charge and discharge

capacitance for the 100<sup>th</sup> cycle was observed with 82.2% cycle efficiency. The 100<sup>th</sup> cycle discharge capacitance was 30.0% of the 2<sup>nd</sup> and 32.0% of the 3<sup>rd</sup> cycle.

Figure (6.3.9), shows that MnO<sub>2</sub>/CNT LTSS 3hrs has a higher capacitance than other materials and an electro-activation phenomenon is also observed for this material.

Hydrothermally synthesized electrode materials still displayed better durability with only 12.8% and 29.0% capacitance deficit after 100 cycles for MnO<sub>2</sub>/C HYDRO 3hrs and MnO<sub>2</sub>/C HYDRO 5hrs, respectively as opposed to 47.2% for MnO<sub>2</sub>/C LTSS 3hrs.

## 6.4 CONCLUSION

The electrode material activity can be enhanced by increasing the surface area via high dispersion of electrode material on inert support materials, such as carbon, activated carbon or carbon nanotubes. SEM, TEM and XRD morphology and crystallinity analyses showed the successful synthesis of manganese oxide electrode materials carbon composites. Both methods were studied at two synthesis dwell times which are 3hours and 5hours and good dispersion of nanorods on the carbon supports was obtained. The XRD analysis also showed that the MnO<sub>2</sub> electrode materials integrity was maintained as the introduction of support materials did not affect their nanorod array crystallinity. BET surface area studies showed that an increase in the surface areas of the supported materials was achieved with crystal restructuring associated with the introduction of support materials. The CV results of the supported materials showed characteristic behaviour of a capacitor. Better performance was recorded from the LTSS synthesized materials when carbon nanotubes were used as a support material with a capacitance deficit of 3.7% for MnO<sub>2</sub>/CNT 3hrs and 12.05% capacitance deficit for MnO<sub>2</sub>/CNT 5hrs when compared to their respective unsupported materials, followed by the carbon supported materials then activated carbon supported materials. Charge

and discharge cycling results confirmed the cyclic voltammetric results. The high surface area, high porosity, high capacitance and high durability, possessed by these materials makes them best candidates for commercial use as electrode materials for supercapacitors.

## CHAPTER 7

### SYNTHESIS AND CHARACTERIZATION OF A POLY CRYSTALLINE RUTHENIUM OXIDE AND ITS CARBON COMPOSITES AS ELECTRODE MATERIALS

#### 7.1 Introduction

A curious feature of transition metal oxides is their wide range of conductivity, spanning roughly fifteen to twenty orders of magnitude. The rutile structured  $\text{RuO}_2$ , which consists of a tetragonal lattice with two  $\text{RuO}_2$  molecules per unit cell and octahedral coordination with each ruthenium atom surrounded by six oxygen neighbors, is the most thermodynamically stable and has significant technological interest [323].

In this study a rutile structured  $\text{RuO}_2$  was synthesized using Adams method and its physical and electrochemical behavior studied and compared with the  $\text{MnO}_2$  nanorods electrode materials presented in previous chapters.

#### 7.2 PHYSICAL CHARACTERIZATION OF RUTHENIUM OXIDE ELECTRODE MATERIALS

##### 7.2.1. Particle size distribution and composition study of the synthesized $\text{RuO}_2$ electrode materials and its carbon composites.

Ruthenium oxide electrode material and its carbon composites were synthesized using Adam's method which involved the reduction of the  $\text{RuCl}_3 \cdot \text{H}_2\text{O}$  precursor to produce  $\text{RuO}_2$  electrode material as described in Chapter 3. The prepared  $\text{RuO}_2$  product was then modified by supporting it with activated carbon, carbon and carbon nanotubes. TEM, TEM EDX and SEM analysis were conducted on the synthesized materials to investigate their metal particle

size distribution and elemental composition. TEM micrographs of the synthesized electrode materials are shown below in figure 7.2.1.

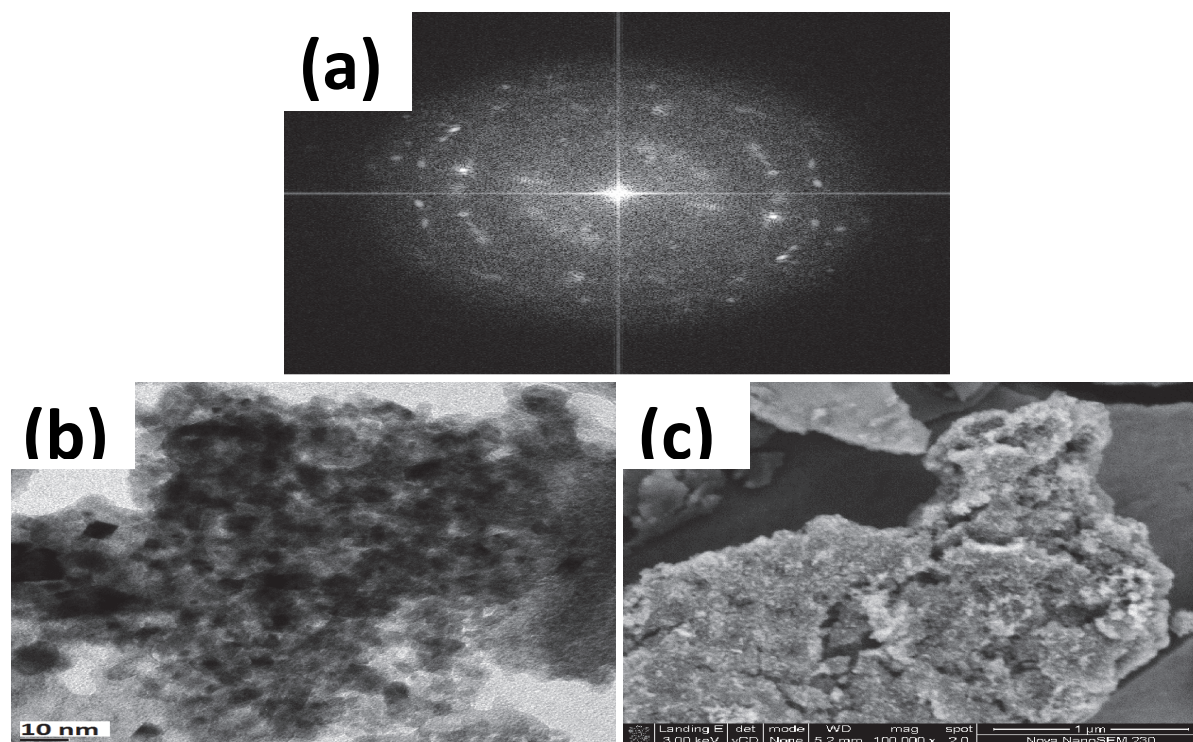
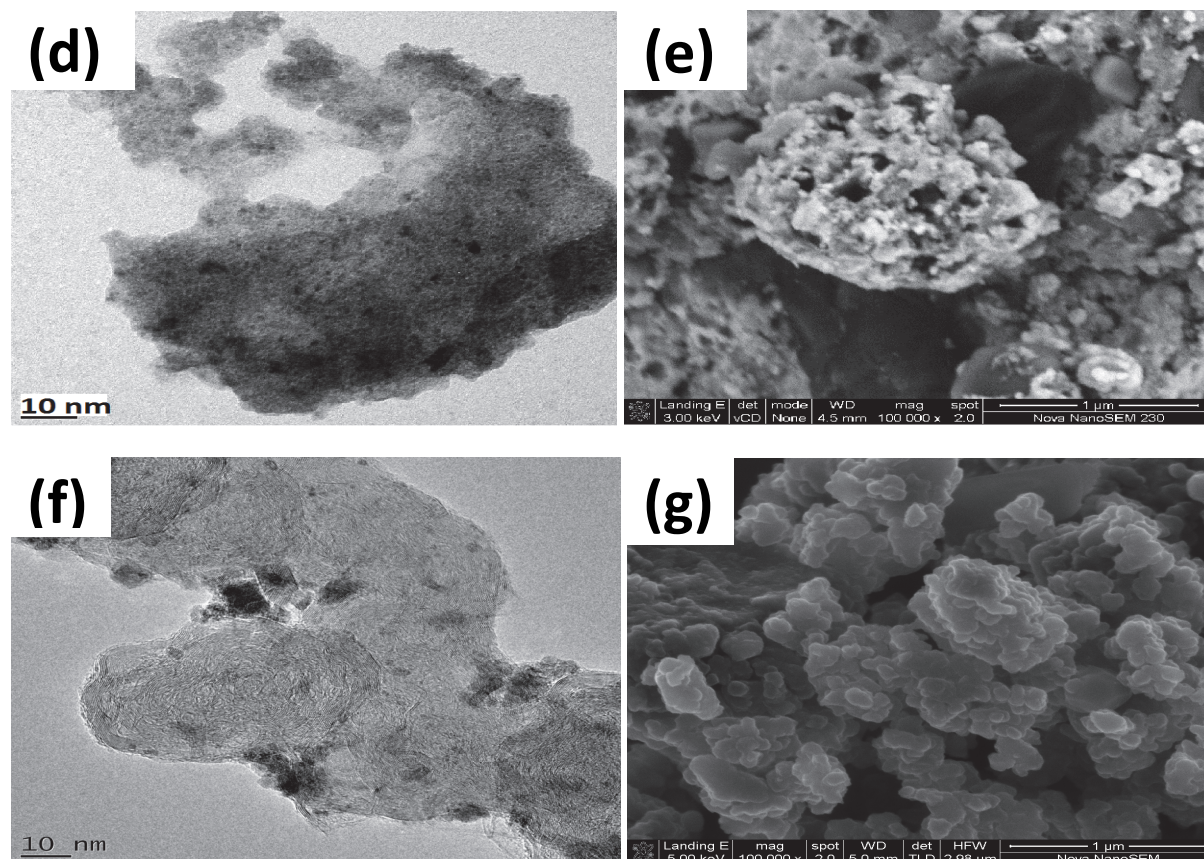


**Figure 7.2.1:** TEM, (a) crystallogram, (b) and SEM (c) micrographs of Adam's method synthesized  $\text{RuO}_2$ .

Figure (7.2.1 a) is a crystallogram of  $\text{RuO}_2$  synthesized with Adams method. The crystallogram reveals that the synthesized product is polycrystalline. This is an attractive property since pseudocapacitance is related to the degree of crystallinity and the pseudocapacitance is maximized only when the transport of electrons and protons in  $\text{RuO}_2$  structure are balanced [305]-[307].

Micrograph (b) and (c) confirms this polycrystalline nature as the particles which are observed vary in shapes and sizes. The particles are well connected to provide a porous structure that favors the anion/cation diffusion and adsorption/desorption during the

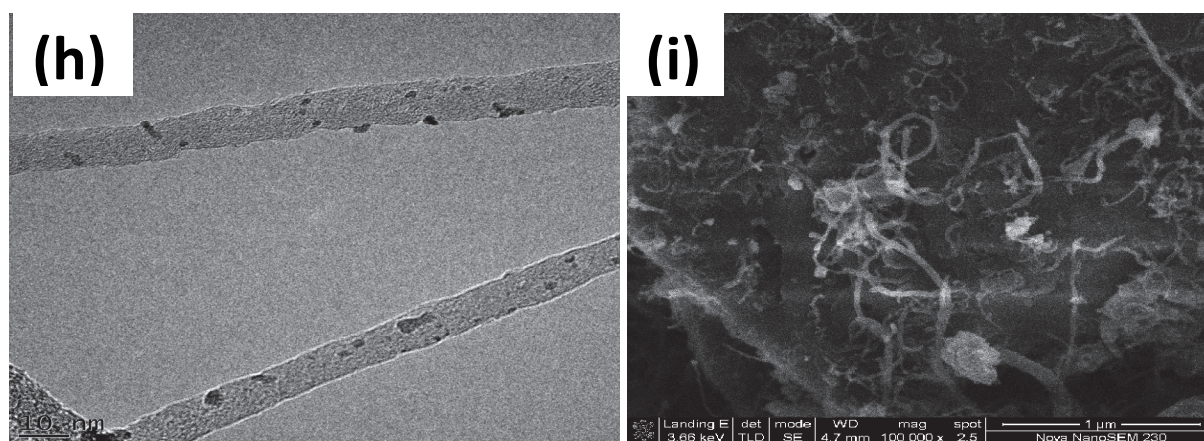
charge/discharge process, which is a requirement for supercapacitors. From the TEM image the particle size of the material was determined to be between 8 and 15nm.



**Figure 7.2.1:** TEM (d), (e) and SEM (f), (g) micrographs of Adam's method synthesized  $\text{RuO}_2/\text{Ac}$  and  $\text{RuO}_2/\text{C}$ , respectively.

Figure 7.2.1. (d) and (e) are TEM and SEM micrographs of  $\text{RuO}_2/\text{AC}$  and (f) and (g) are TEM and SEM micrographs of  $\text{RuO}_2/\text{C}$ , respectively. The dark spots on figure (7.2.1 (d)) shows the  $\text{RuO}_2$  particles adsorbed on the activated carbon. On the TEM micrograph for  $\text{RuO}_2/\text{AC}$  the particles seem to be smaller and evenly dispersed onto the activated carbon. This is encouraging because capacitance strongly depends on the amount of  $\text{RuO}_2$  particles dispersed on the support material. SEM micrograph (e) shows that  $\text{RuO}_2/\text{AC}$  has very hard surface with even distribution of  $\text{RuO}_2$  clusters which seem to be well adhered onto the support material. But these  $\text{RuO}_2$  particles though evenly distributed but they are arranged

into very big hard clusters. Since proton diffusion through Ruthenium oxide controls the redox reaction in the bulk of the oxide, the rate capability of this material may decrease with increasing particle size of the oxide. In other words, for the same discharge rate the specific capacitance of  $\text{RuO}_2$  may decrease in the case of larger particle size, since the proton will need longer time to reach the bulk of the oxide. TEM micrograph of  $\text{RuO}_2/\text{C}$  shows less  $\text{RuO}_2$  dispersion on the support with agglomerates of  $\text{RuO}_2$  particles. On SEM micrographs also clusters of bigger  $\text{RuO}_2$  particles can be observed on micrograph (g) and the material seem to be well adhered to the support.



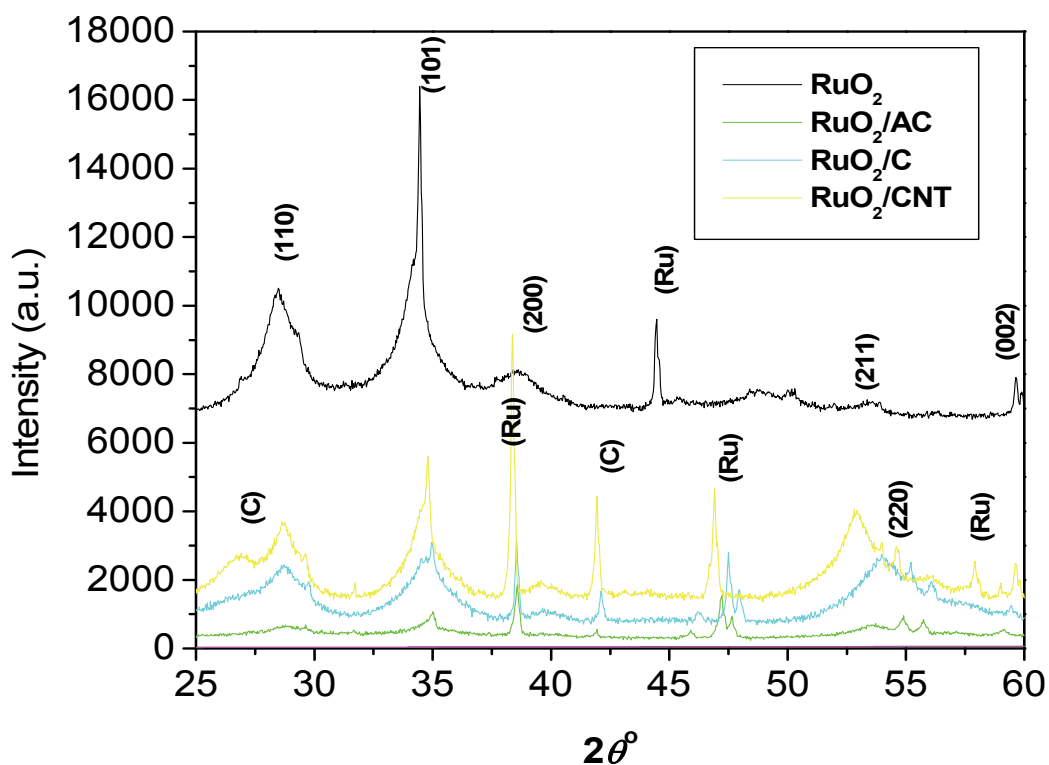
**Figure 7.2.1:** TEM (h) and SEM (i) micrographs of Adam's method synthesized  $\text{RuO}_2/\text{CNT}$ .

Figure (7.2.1) (h) and (c) are TEM and SEM micrographs of  $\text{RuO}_2/\text{CNT}$ . Micrograph (h) shows the successful decoration of  $\text{RuO}_2$  particles of different shapes and sizes on carbon nanotubes. TEM EDX also confirmed the synthesis of  $\text{RuO}_2$  carbon composites and that there were no impurities on the synthesized electrode materials.



### 7.2.2 Particle size and crystallinity study of Ruthenium Oxide and its carbon composite.

The structural analysis of the synthesized ruthenium oxide material was carried out using X-ray Diffractometer. Figure 7.2.2 below shows the XRD pattern of the Adam's method synthesized ruthenium oxide and its carbon composite electrode materials.



**Figure 7.2.2:** XRD patterns of as-prepared RuO<sub>2</sub>, RuO<sub>2</sub>/AC, RuO<sub>2</sub>/C and RuO<sub>2</sub>/CNT.

Well defined peaks (110), (101), (200) and (211) can be assigned as characteristic peaks of rutile ruthenium oxide. According to [305-307], the pseudocapacitance of ruthenium oxide is related to the degree of crystallinity, therefore the annealing process is very critical in optimizing the electrochemical performance of ruthenium oxide. From the well definition of the peaks observed, it can be concluded that the material synthesized has a polycrystalline

structure. However, a great amount of metallic ruthenium was observed (Ru). A possible explanation for this fact can be related to the preparation method. The electrodes calcination process was accomplished in air. As this process begins on the sample surface, owing to the oxygen availability, the oxygen partial pressure inside the sample could be insufficient to oxidize the organic portion to CO<sub>2</sub>. Then, the CO that is formed could react with Ru ions reducing them to the metallic state.

Peaks of the carbon support materials can be observed from the diffraction patterns. The particle size and the inter-planar spacing of the synthesized RuO<sub>2</sub> and its carbon composite were calculated using the Scherrer equation and the results are tabulated below

**Table 7.2.1:** Particle size and inter-planar spacing of the as-prepared RuO<sub>2</sub> electrode material and its carbon composites.

	Facet (110) 2θ	Facet (101) 2θ	Facet (200) 2θ	d (110) (Å)	d (101) (Å)	d (200) (Å)	D (110) (nm)	D (101) (nm)	D (200) (nm)
<b>RuO<sub>2</sub></b>	28.5	34.5	39.0	2.0	2.53	2.31	15.4	13.9	12.5
<b>RuO<sub>2</sub>/C</b>	29.4	35.5	40.5	1.9	1.64	1.5	15.1	12.2	10.7
<b>RuO<sub>2</sub>/AC</b>	29.4	35.5	40.5	1.9	1.64	1.5	14.8	12.2	10.7
<b>RuO<sub>2</sub>/CNT</b>	29.5	35.5	40.7	1.9	1.64	1.42	15.1	12.2	10.5

A decrease in particle size of the supported material is observed which resulted from the shift observed on diffraction facets to higher 2θ values and crystal lattice restructuring. The decrease in lattice spacing is due to the alloying with the carbon materials. As with TEM results the particle size for RuO<sub>2</sub>/AC is less than that of RuO<sub>2</sub>/C.

#### 7.2.4 BET surface area of as prepared RuO<sub>2</sub> and its carbon composites

The surface area and porosity of the RuO<sub>2</sub> and its carbon composite electrode material synthesized using Adam's method was determined using N<sub>2</sub> physisorption. The methodology

for the surface area and porosity determination via the N<sub>2</sub> physisorption technique is detailed in Chapter 3. The results obtained for the RuO<sub>2</sub> electrode materials are tabulated in Table 7.2.2.

**Table 7.2.2:** Surface Area and Porosity Data for RuO<sub>2</sub> and its carbon composites.

<b>Electrode Material</b>	<b>BET Surface Area (m<sup>2</sup>/g)</b>	<b>External Surface Area (m<sup>2</sup>/g)</b>	<b>Internal Pore area (m<sup>2</sup>/g)</b>	<b>Pore Volume Ads. (cm<sup>3</sup>/g)</b>	<b>Pore Volume Des. (cm<sup>3</sup>/g)</b>	<b>Av. Ads Pore Diameter (nm)</b>	<b>Av. Ads Pore Diameter (nm)</b>
<b>RuO<sub>2</sub></b>	64.87	64.90	69.83	0.150	0.158	8.59	9.60
<b>RuO<sub>2</sub>/AC</b>	41.22	32.12	43.40	0.057	0.057	5.26	4.96
<b>RuO<sub>2</sub>/C</b>	51.64	45.93	41.62	0.097	0.097	9.33	8.98
<b>RuO<sub>2</sub>/CNT</b>	42.39	38.05	48.84	0.223	0.223	18.25	17.50

The adsorption and desorption isotherms for RuO<sub>2</sub>, RuO<sub>2</sub>/AC, RuO<sub>2</sub>/C and RuO<sub>2</sub>/CNT are plotted in figure (7.2.4). All the RuO<sub>2</sub> based electrode materials displayed Type IV isotherms confirming their porous nature [330]. However the hysteresis loops are not identical implying that the porosity is different in all samples. The small slopes in the in the region of  $p/p_0$  of 0 to ~ 0.04 in the adsorption branches of the isotherms indicates the presence of a small fraction of micropores in the samples and these micropores originate from the internal space of the porous sample [330]. For all the isotherm plots, soft slopes and hysteresis loops are observed in the relative pressure ( $p/p_0$ ) region of ~0.1 to 0.9, which indicates the presence of large fractions of mesopores. The sharp increase in the uptake of N<sub>2</sub> at higher relative pressure ( $p/p_0 > 0.9$ ) demonstrates the existence of macropores in the samples which is due to the inter-particle space. Higher N<sub>2</sub> uptake shows the presence of a large fraction of macropores in RuO<sub>2</sub>/CNT compared to other RuO<sub>2</sub> based electrode materials.

The obtained BET surface area results were  $64.87\text{m}^2/\text{g}$ ,  $41.22\text{m}^2/\text{g}$ ,  $51.64\text{m}^2/\text{g}$  and  $42.39\text{m}^2/\text{g}$  for  $\text{RuO}_2$ ,  $\text{RuO}_2/\text{AC}$ ,  $\text{RuO}_2/\text{C}$  and  $\text{RuO}_2/\text{CNT}$ , respectively. The internal pore areas of the supported materials were higher when compared to the unsupported material with  $\text{RuO}_2/\text{C}$  having the highest internal pore volume. High internal pore volume is a significant property for supercapacitor materials as it is associated with high capacitive behavior.

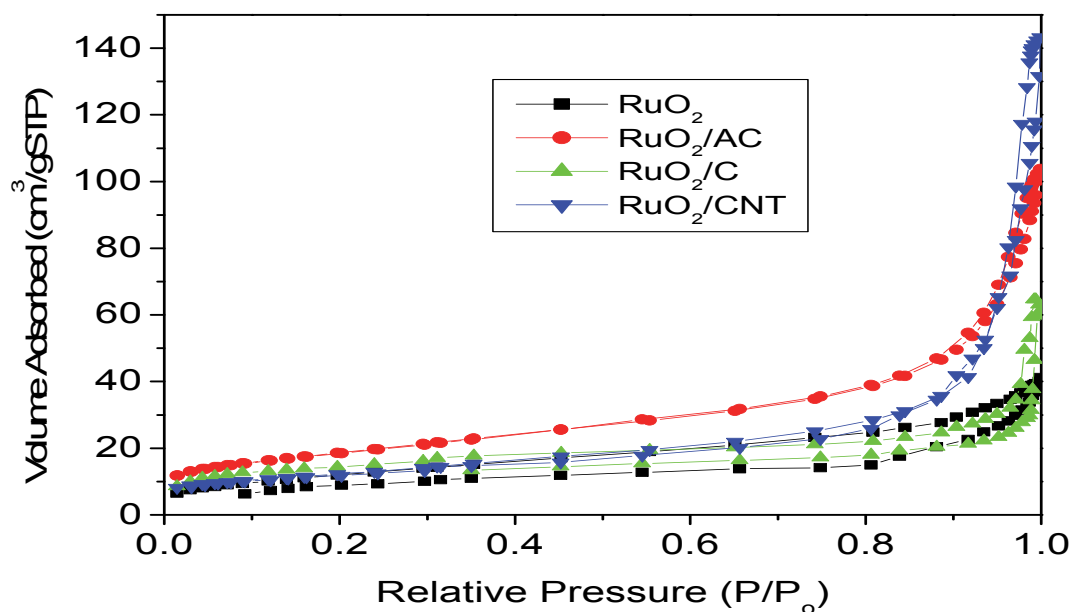


**Figure 7.2.3:** The nitrogen adsorption isotherms of  $\text{RuO}_2$  and its carbon composites at 77K.

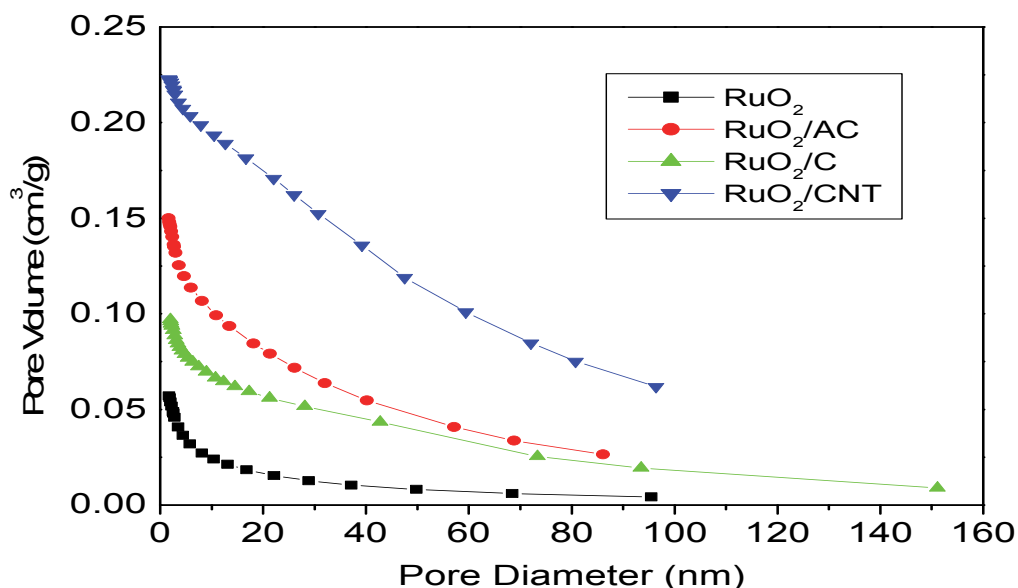


**Figure 7.2.4:** Barrett-Joyner and Halenda (BJH) pore size distribution plot of RuO<sub>2</sub> and its carbon composites.

BJH pore size distribution plot confirms the multimodal pores structures of the RuO<sub>2</sub> based electrode materials.

## 7.3 ELECTRO-CHEMICAL CHARACTERIZATION OF RUTHENIUM OXIDE AND ITS CARBON COMPOSITES

### 7.3.1 Cyclic voltammetry

Cyclic voltammetry (CV) of the ruthenium oxide and its carbon composites synthesized electrode materials were conducted. RuO<sub>2</sub> electrode materials on a carbon paper were our working electrode, Ag/AgCl used as a reference electrode, platinum gauze as a counter electrode in 0.5M H<sub>2</sub>SO<sub>4</sub> electrolyte.

Figure (7.3.1) and (7.3.2) show cyclic voltammograms of RuO<sub>2</sub>, RuO<sub>2</sub>/AC and RuO<sub>2</sub>/C, RuO<sub>2</sub>/CNT, respectively at 5, 10, 20, 25, 50 and 100mV/s scan rates.

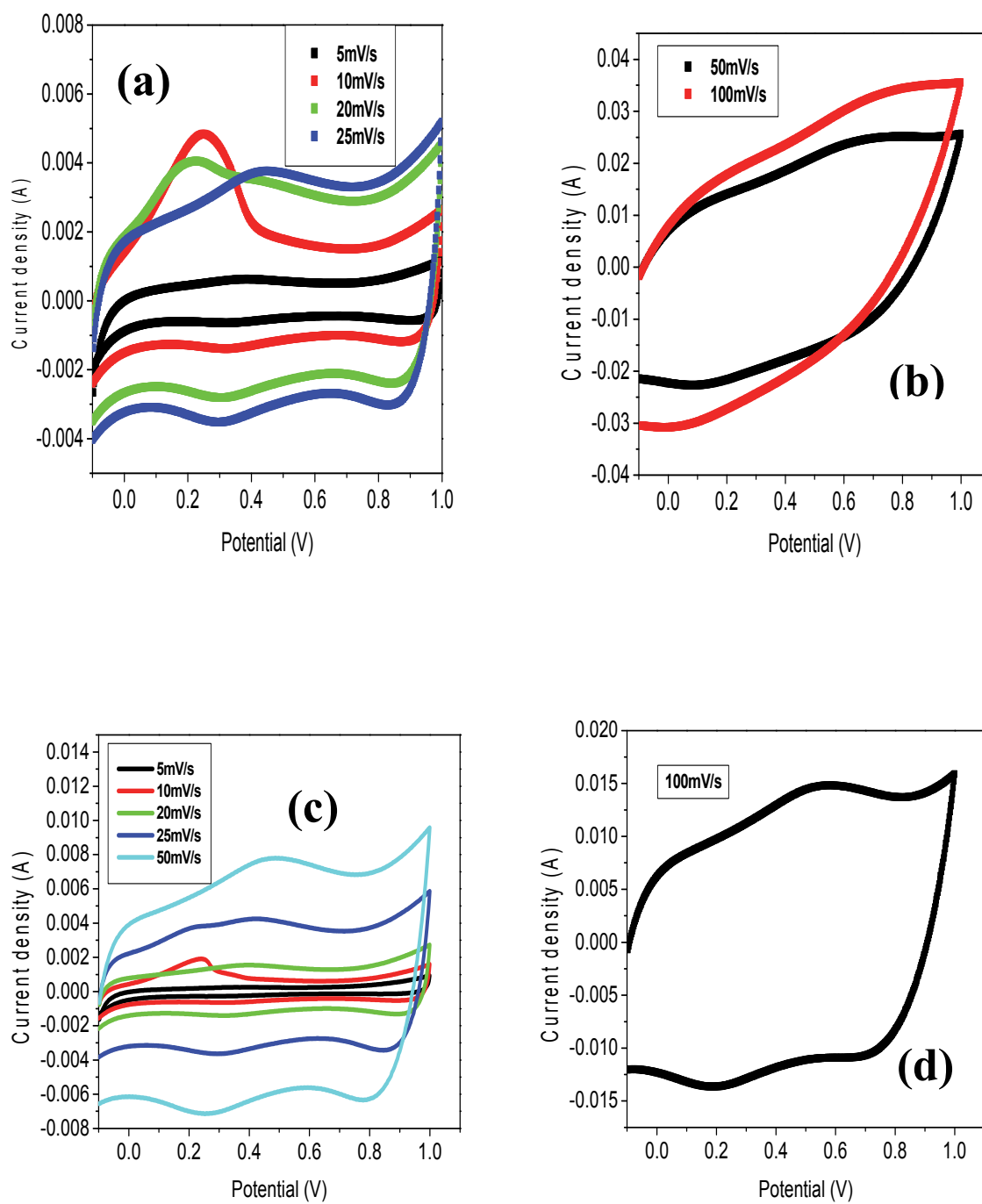


**Figure 7.3.1:** Cyclic voltammograms of RuO<sub>2</sub> (a), (b) and RuO<sub>2</sub>/AC (c), (d).

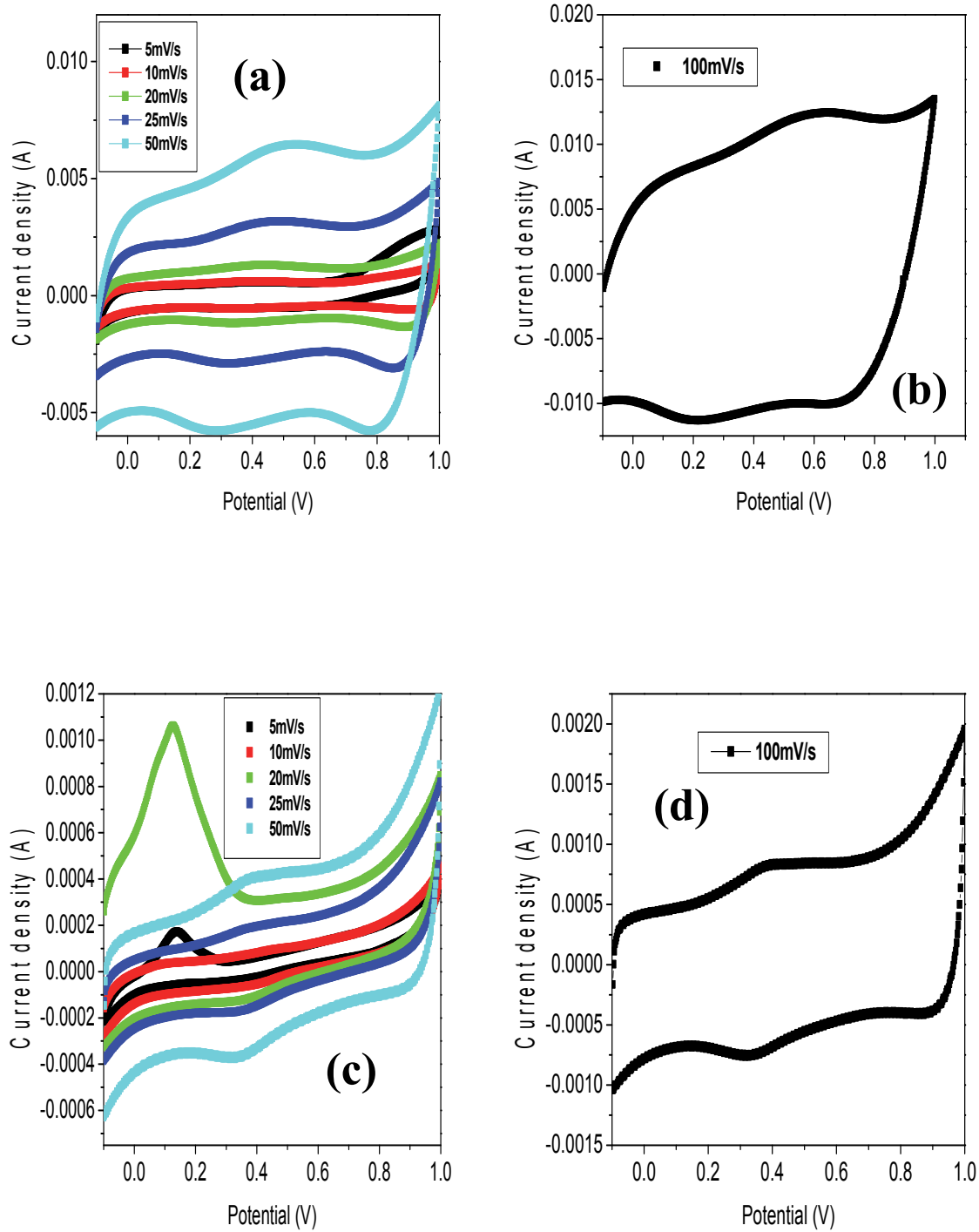


**Figure 7.3.2:** Cyclic voltammograms of RuO<sub>2</sub>/C (a), (b) and RuO<sub>2</sub>/CNT (c),(d).

The cyclic voltametric curves of the RuO<sub>2</sub> electrode materials are almost rectangular in shape even at higher scan rates which is a characteristic of good capacitive behavior and a sign of desirable fast charging and discharging property for power devices. The current under the curve is slowly increasing with scan rate, showing that the voltammetric currents are directly proportional to the scan rates of the CV, also indicating an ideal capacitive behavior [328]. Therefore, the RuO<sub>2</sub> electrode materials, especially the supported materials, because of their more distinct rectangular shape, exhibit not only stability and good capacitive behavior but also low resistance. RuO<sub>2</sub>, RuO<sub>2</sub>/AC and RuO<sub>2</sub>/CNT cyclic voltammograms had oxidation peaks around 2.5V, 2.5V and 1.0 V, respectively, which are an indication of electrochemical redox reactions taking place in the material. The specific capacitances of the materials were calculated from and are presented in table (6.3.1).

Unsupported RuO<sub>2</sub> at a scan rate of 10mV/s delivered a capacitance of 367F/g which is higher than 236.1 F /g reported in literature [329]. RuO<sub>2</sub>/AC, RuO<sub>2</sub>/C and RuO<sub>2</sub>/CNT delivered 270F/g at a scan rate of 10mV/s, 471F/g at a scan rate of 5mV/s and 303F/g at a scan rate of 5mV/s respectively. RuO<sub>2</sub>/C performed better than the other supported materials and the unsupported RuO<sub>2</sub>.

**Table 7.3.1:** Cyclic voltammetry capacitance values of RuO<sub>2</sub> and its carbon composites.

	5mV/s	10mV/s	20mV/s	25mV/s	50mV/s	100mV/s
RuO <sub>2</sub>	191F/g	367F/g	338F/g	135F/g	123F/g	78 F/g
RuO <sub>2</sub> /AC	259F/g	270F/g	192F/g	335F/g	276F/g	227F/g
RuO <sub>2</sub> /C	471F/g	114F/g	93F/g	159F/g	130F/g	106F/g
RuO <sub>2</sub> /CNT	303/g	170F/g	199F/g	124F/g	92F/g	78F/g



### 7.3.2 Charge and discharge cycling

The Charge-discharge tests of the RuO<sub>2</sub> electrode materials were done at a charge-discharge current of 1mA in a button cell using 0.5M H<sub>2</sub>SO<sub>4</sub> as an electrolyte from 0-1V. Figure 7.3.2 displays the discharge cycling behaviour of the RuO<sub>2</sub> and its carbon composites and figure 7.3.2 displays the discharge capacities and discharge capacitances versus cycle numbers.

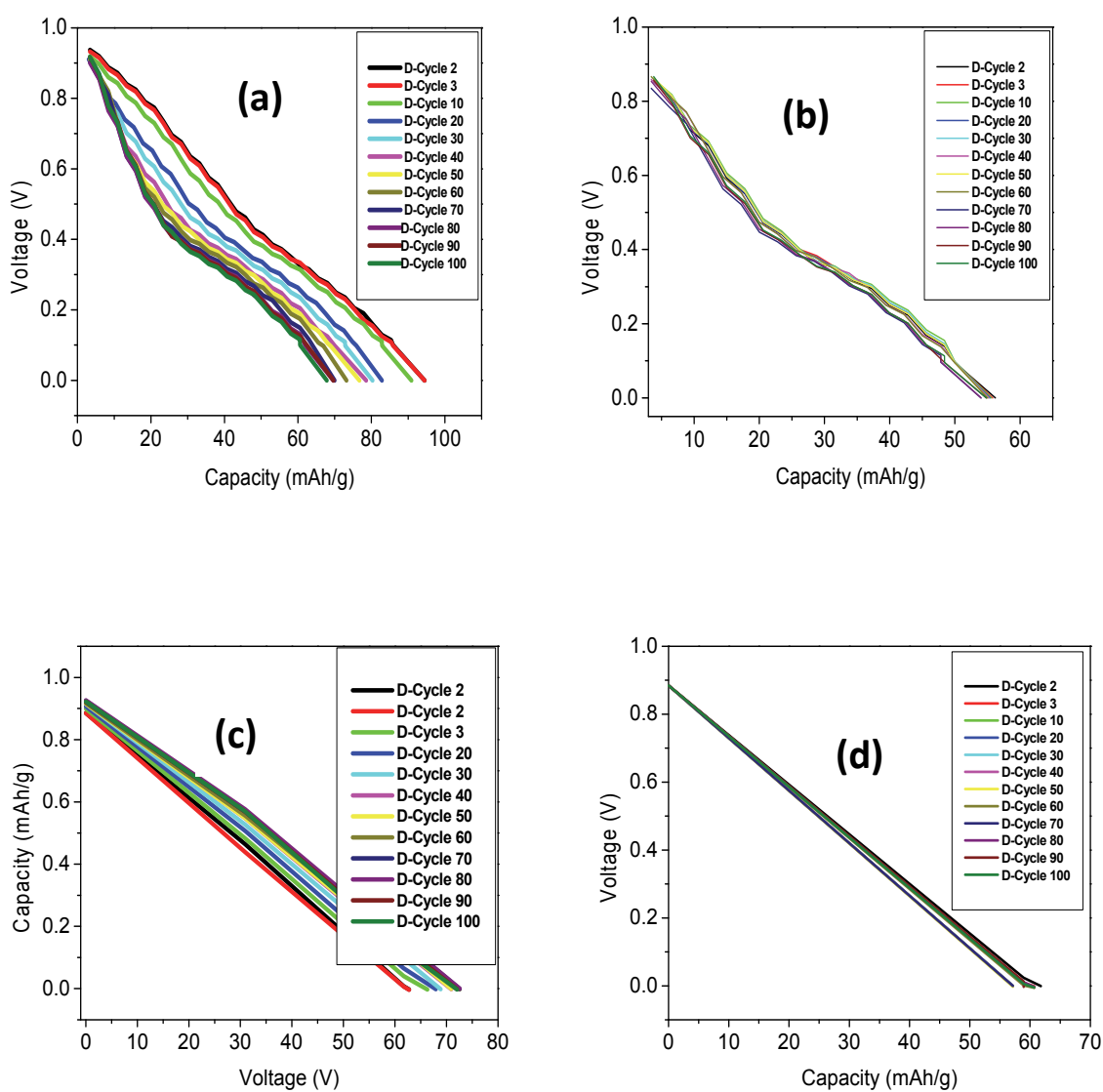


**Figure 7.3.3:** Discharge cycles of (a) RuO<sub>2</sub>, (b) RuO<sub>2</sub>/AC, (c) RuO<sub>2</sub>/C and (d) RuO<sub>2</sub>/CNT.

The shapes of charge and discharge cycling curves for RuO<sub>2</sub>/C and RuO<sub>2</sub>/CNT electrode materials reveal the characteristics of an ideal capacitor.

RuO<sub>2</sub> on the first cycle charge delivered 400.7F /g and a discharge capacitance of 340.2F/g for the same cycle with 84.9% cycle efficiency. 342.1F/g and 331.2F/g charge and discharge capacitance of the 3<sup>rd</sup> cycle with 96.8% cycle efficiency. The 100<sup>th</sup> charge cycle delivered a capacitance of 268.0F/g and a discharge capacitance of 233.3F/g with a cycle efficiency of 87.0%. The discharge capacity/capacitance of the 100<sup>th</sup> cycle is 69% of the second cycle.

RuO<sub>2</sub>/AC on the 2<sup>nd</sup> cycle delivered a charge capacitance of 258.0F /g and a discharge capacitance of 202.3F/g with 61.4% cycle efficiency. For the 3<sup>rd</sup> cycle it delivered a charge and discharge capacitance of 249.8F/g and 200.9F/g, respectively, with a cycle efficiency of 80.4%. The 100<sup>th</sup> charge cycle delivered a capacitance of 224.2F/g and a discharge capacitance of 197.3F/g with a cycle efficiency of 88.0%. The discharge capacitance of the 100<sup>th</sup> cycle is 97.5% of the 2<sup>nd</sup> cycle.

RuO<sub>2</sub>/C on the 2<sup>nd</sup> cycle delivered a charge capacitance of 278.0F /g and a discharge capacitance of 226.0F/g with 81.3% cycle efficiency. For the 3<sup>rd</sup> cycle it delivered a charge and discharge capacitance of 266.4F/g and 226.0F/g, respectively, with a cycle efficiency of 84.8%. The 100<sup>th</sup> charge cycle delivered a capacitance of 286.0F/g and a discharge capacitance of 260.0F/g with a cycle efficiency of 91.0%. The discharge capacitance of the 100<sup>th</sup> cycle is higher than that of the 2<sup>nd</sup> cycle

RuO<sub>2</sub>/CNT on the 2<sup>nd</sup> cycle delivered a charge capacitance of 302.0F /g and a discharge capacitance of 234.0F/g with 77.5% cycle efficiency. For the 3<sup>rd</sup> cycle it delivered a charge and discharge capacitance of 295.6F/g and 231.5F/g, respectively, with a cycle

efficiency of 78.3%. The 100<sup>th</sup> charge cycle delivered a capacitance of 296.0F/g and a discharge capacitance of 212.1F/g with a cycle efficiency of 72.0%. The discharge capacitance of the 100<sup>th</sup> was 91.0% of the 2<sup>nd</sup> cycle.

The discharge capacities versus cycle number and discharge capacitances versus cycle number are presented in Figure (7.3.4). The results showed a good cycling behaviour of the RuO<sub>2</sub> materials. But the specific capacitance and utilization decay rate in the pure RuO<sub>2</sub> electrode was much faster than that of the RuO<sub>2</sub> carbon composite electrodes. Meaning the carbon support materials have introduced an element of durability to the material.

The charge and discharge efficiencies for the RuO<sub>2</sub>, RuO<sub>2</sub>/C and RuO<sub>2</sub>/ AC were above 80% and that of RuO<sub>2</sub>/CNT close to 80%. This is a good indication of reversibility and high-power property of the materials which is suitable for the application of electrochemical capacitors. Among the supported materials RuO<sub>2</sub>/C performed better than other materials in terms of capacitance utilization decay see figure (7.3.4). The phenomenon called electro-activation has been observed from the RuO<sub>2</sub>/C and RuO<sub>2</sub>/AC cycles, where capacitance increases in subsequent cycles.

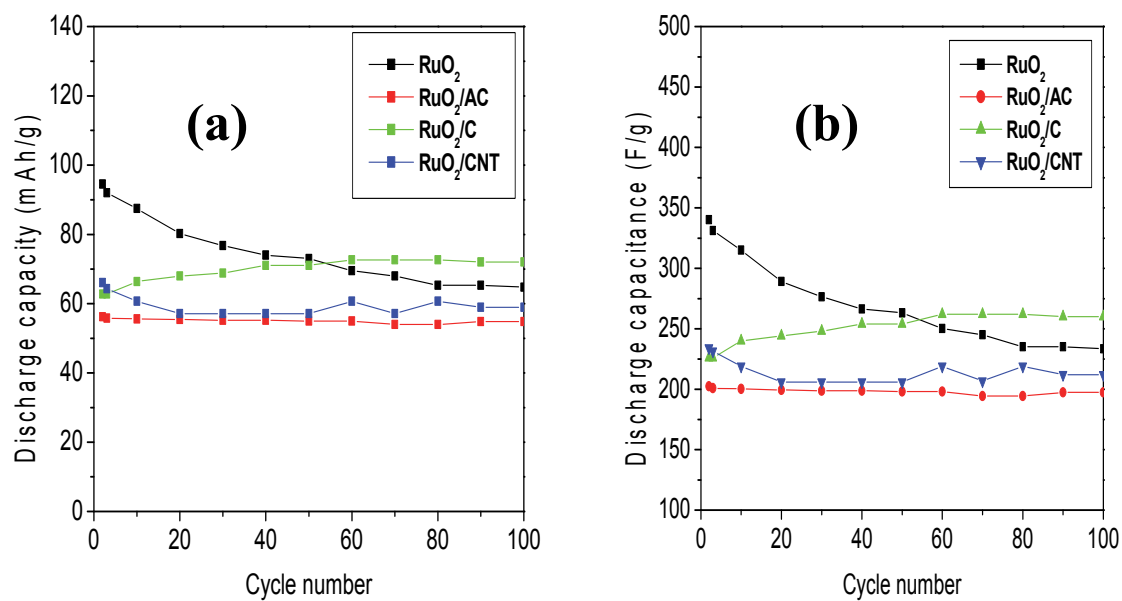


**Figure 7.3.4:** The (a) discharge capacity and (b) discharge capacitance vs. cycle number for the RuO<sub>2</sub> and its carbon composites.

## 7.4. CONCLUSION

Polycrystalline RuO<sub>2</sub> electrode material was observed from TEM and SEM analysis as the product of Adams method. Particles with an average size of 15nm which were well connected to provide a porous structure were observed on the micrographs. This material was then supported with carbon, activated carbon and carbon nanotubes and better dispersion was observed from activated carbon supported materials. The X-ray diffraction patterns of the RuO<sub>2</sub> based electrode materials showed the characteristic reflections expected for rutile RuO<sub>2</sub>. The XRD analysis also showed that the RuO<sub>2</sub> materials integrity was maintained as the polycrystalline structure array was not affected by the introduction of support materials. The porous structure of the RuO<sub>2</sub> based electrode materials was confirmed by BET analysis and the BET surface areas of the materials were determined to be 64.87m<sup>2</sup>/g, 41.22m<sup>2</sup>/g, 51.64m<sup>2</sup>/g and 42.39m<sup>2</sup>/g for RuO<sub>2</sub>, RuO<sub>2</sub>/AC, RuO<sub>2</sub>/C and RuO<sub>2</sub>/CNT, respectively. Pore areas of the materials were increased on introduction of support materials with carbon supported material pore area being the highest compared to the unsupported material, activated carbon and carbon nanotubes supported material. Cyclic voltammetric with charge and discharge cycling results confirmed the BET results when RuO<sub>2</sub>/C electrode material delivered the highest capacitance of 471F/g and highest discharge capacitance of 260F/g after 100 cycles. Also RuO<sub>2</sub>/C capacitance utilization decay when compared to other RuO<sub>2</sub> based electrode materials.

## REFERENCES

- [1]. Winter M., Brodd R. *J. Chem. Rev.* 104, (2004): 4245.
- [2]. Burke A. *J. Power Sources*, 91, (2000): 37.
- [3]. Vol'fkovich Y. M., Serdyuk T. M. *Russ. J. Electrochem.* 38, (2002): 935.
- [4]. a) *Handbook of Nanostructured Materials and Nanotechnology* (Ed: Nalwa H.S.), Academic Press, New York, (2000).
- b) *Nanostructured Materials: Clusters, Composites and Thin Films* (Eds: Shalaev V. M., Moskovits M.), American Chemical Society, Washington, DC, (1997).
- c) *Nanomaterials: Synthesis, Properties and Application* (Eds: Edelstein A.S., Cammarata R.C.), Institute of Physics, Philadelphia, PA., (1996).
- [5]. Alivisatos P., Barbara P.F., Castleman A.W., Chang J., Dixon D.A., Thompson M.L., *Adv. Mater.*, 10, (1998): 1297.
- [6]. Thiaville A., Miltat J., *Science*, 284, (1999): 1939.
- [7]. Future Trends in Microelectronics: *The Nano Millenium*, Eds: Luryi S., Xu J., Zaslavsky, Wiley- Interscience (2002), New York.
- [8]. Ross C., *Annu. Rev. Mater. Sci.* 31, (2001): 203.
- [9]. Murray C.B, Kagan C.R., Bawendi M.G., *Annu. Rev. Mater. Sci.* 30, (2000): 545.
- [10]. Wang H., Yoshio M., Thapa A.K., Nakamura H., *J Power Sources*, 169, (2007): 375–80.
- [11]. Aida T., Murayama I., Yamada K., Morita M., *J Electrochem Soc.* 154, (2007): A798–804.
- [12]. Fang B, Binder L. *Electrochim Acta*, 52, (2007): 6916–21.
- [13]. Liu X.M., Zhang R., Zhan L., Long D.H., Qiao W.M., Yang J.H., *New Carbon*

*Mater*, 22, (2007): 153–8.

[14]. Fan Z, Chen J, Cui K, Sun F, Xu Y, Kuang Y. *Electrochim Acta*, 52, (2007): 2959–65.

[15]. Wang H, Yoshio M. *Electrochem Commun.*, 8, (2006): 1481–6.

[16]. Gomibuchi E, Ichikawa T, Kimura K, Isobe S, Nabeta K, Fujii H. *Carbon*, 44, (2006): 983–8.

[17]. Xu B., Wu F., Chen S., Zhang C., Cao G., Yang Y. *Electrochim Acta* 52, (2007): 4595–8.

[18]. Kim S.U, Lee K.H., *Chem. Phys Lett.* 400, (2004): 253–7.

[19]. Sivakkumar S.R., Ko J.M., Kim D.Y., Kim B.C., Wallace G.G., *Electrochim Acta* 52, (2007): 7377–85.

[20]. Honda K., Yoshimura M., Kawakita K., Fujishima A., Sakamoto Y., Yasui K., et al. *J Electrochem Soc.* 151, (2004): A532–41.

[21]. Eikerling M., Kornyshev A.A., Lust E., *J Electrochem Soc.*, 152, (2005): E24–33.

[22]. Chun J.H., Kim N.Y., Chun J.Y., *Int J Hydrogen Energy*, 33, (2008): 762–74.

[23]. Wu M.S., Huang Y.A., Yang C.H., Jow J.J., *Int J Hydrogen Energy* 32, (2007): 4153–9.

[24]. Wahdame B., Candusso D., Francois X., Harel F., Kauffmann J.M., Coquery G., *Int J Hydrogen Energy*, 34, (2009): 967–80.

[25]. Kim I.H., Kim K.B., *J Electrochem Soc*, 153, (2006): A383–9.

[26]. Yang X.H., Wang Y.G., Xiong H.M., Xia Y.Y., *Electrochim Acta*, 53, (2007): 752–7.

- [27]. Honda Y., Haramoto T., Takeshige M., Shiozaki H., Kitamura T., Ishikawa M. *Electrochem Solid-State Lett.* 10, (2007): A106–10.
- [28]. Katakabe T., Kaneko T., Watanabe M, Fukushima T., Aida T. *J Electrochem Soc.* 152, (2005): A1913–6.
- [29]. Lao Z.J., Konstantinov K., Tournaire Y., Ng S.H., Wang G.X., Liu H.K., *J Power Sources*, 162, (2006): 1451–4.
- [30]. Zhao D.D., Bao S.J., Zhou W.J., Li H.L., *Electrochem Commun.* 9, (2007): 869–74.
- [31]. Okajima K., Ikeda A., Kamoshita K., Sudoh M., *Electrochim Acta*, 51, (2005): 972–7.
- [32]. Xing W., Qiao S.Z., Ding R.G., Li F, Lu G.Q., Yan Z.F., *Carbon* 44, (2006): 216–24.
- [33]. Choi D, Kumta P.N. *J. Electrochem Soc.*, 153, (2006): A2298–303.
- [34]. Merritt R.P. *CVD synthesis of carbon nanotubes as active materials for electrochemical capacitors*, Florida Atlantic University, (2003).
- [35]. Lewandowski A., Galinski M., *J. Power Sources*, 173, (2007): 822–8.
- [36]. Bohlen O, Kowal J, Sauer D.U., *J. Power Sources*, 172, (2007): 468–75.
- [37]. Boyea J.M., Camacho R.E, Turano S. P. and Ready W. J., *Nanotechnology Law & Business*, 4(1), (2007).
- [38]. Abruna H. D., Kiya Y. and Henderson J.C., *Physics Today*, (2008): 43.
- [39]. Mohamad R., PHD thesis, Department of Chemistry, University of the Western Cape, (2009).
- [40]. Molina M. G., *Dynamic Modelling and Control Design of Advanced Energy Storage for Power System Applications*, Alisson V. Brito (Ed.), ISBN: 978-953-7619-68-8,



InTech.

- [41]. Mitra S, Sampath S. *Electrochem Solid-State Lett.* 7, (2004): A264–8.
- [42]. Scherson D.A. and Palencsár A., *The Electrochemical Society Interface*, 22, (2006).
- [43]. Zhang Y., Feng H., Wu X., Wang L, Zhang A., Xia T., Dong H., Li X., Zhang L., *International journal of hydrogen energy*, 34, (2009): 4889-4899.
- [44]. Cuentas Gallegos AK, Rincon ME., *J Power Sources*, 162, (2006): 743–7.
- [45]. Yoshio M, Nakamura H, Wang H. *Electrochem Solid-State Lett* (2006); 9:A561–3.
- [46]. Kotz, R. & Carlen, M. *Electrochim. Acta* (2000); 45: 2483–2498.
- [47]. Miller, J. R. & Burke, A. F., *Electrochem. Soc. Interf.*, 17, (2008): 53–57.
- [48]. Jayalakshmi M., Balasubramanian K., *Int. J. Electrochem. Sci.*, 3, (2008).
- [49]. Danaee I., Jafarian M., Forouzandeh F., Gobal F., Mahjani M.G., *Int J Hydrogen Energy*, 34, (2009): 859–69.
- [50]. Wu, N.L. *Mater. Chem. Phys.*, 75, (2002): 6–11.
- [51]. Brousse, T. *J. Electrochem. Soc.*, 153, (2006): A2171–A2180.
- [52]. Rudge, A., Raistrick, I., Gottesfeld, S. & Ferraris, J. P., *J. Power Sources*, 47, (1994): 89–107.
- [53]. Conway B.E., *Electrochemical supercapacitors: scientific fundamentals and technological application*. Kluwer Academic Publishers/Plenum Press; Dordrecht/New York (1999).
- [54]. Wu M.S, Chiang P.C.J, *Electrochem Solid-State Lett.* 7. (2004): A123–6.
- [55]. Sugimoto W, Iwata H, Murakami Y, Takasu Y., *J Electrochem Soc*, 151, (2004): A1181–7.
- [56]. Dong X, Shen W, Gu J, Xiong L, Zhu Y, Li H, *J Phys Chem.*, B110, (2006) :6015–9.

- [57]. Choi D. *Synthesis, structure and electrochemical characterization of transition metal nitride supercapacitors derived by a two-step transition metal halide approach*. Pittsburgh: Carnegie Mellon University; (2005).
- [58]. Kisacikoglu MC, Uzunoglu M, Alam MS,. *Int J Hydrogen Energy*, 34, (2009): 1497-507.
- [59]. Simon P. and Gogotsi Y., *Nature Materials*, (2008):7.
- [60]. Schematic Presentation of a Pseudocapacitor, Available online 19 July 2012: [http://www.springerimages.com/Images/Chemistry/1-10.1007\\_s10008-008-0576-5-0](http://www.springerimages.com/Images/Chemistry/1-10.1007_s10008-008-0576-5-0).
- [61]. Schematic presentation of an Hybrid Capacitor, Available online 19 July 2012: <http://www.nesscap.com/product/how.jsp>.
- [62]. McEnaney B., Burchell T.D., *Carbon Materials for Advanced Technologies*, Pergamon, (1999): 1.
- [63]. Pierson H.O., *Handbook of Carbon, Graphite, Diamond and Fullerenes*, Noyes Publications, NJ, USA, (1993).
- [64]. Fitzer E., Kochling K.H., Boehm H.P., Marsh H., *Pure Appl. Chem.* 67, (1995): 473.
- [65]. Inagaki M., Radovic L.R., *Carbon*, 40, (2002): 2263.
- [66]. Image of Carbon Black, Available online 24 July 2012, <http://rubbermarketnews.net/2011/09/purchases-expansions-leave-carbon-blackproducers-vying-for-top-spot/>.
- [67]. Taylor R., Marsh H., Heintz E.A., Rodriguez Reinoso, F., *Introduction to Carbon Technologies*, Universidad de Alicante, Secretarido de Publicaciones, (1997), [167].
- [68]. Donnet J.B., Bansal R.C., Wang M.J, *Carbon Black Science and Technology*, 2nd ed., Marcel Dekker, New York, (1993)

- [69]. Osaka T., Liu X., Nojima M., *J. Power Sources*, 74, (1998): 122.
- [70]. Zheng J.P., *Electrochem. Solid-State Lett.*, 2, (1999): 359.
- [71]. Fialkov A.S., Russ. J. *Electrochem.*, 36 (2000): 389.
- [72]. Kinoshita K., *Carbon: Electrochemical and Physicochemical Properties*, Wiley-Interscience, New York, (2008).
- [73]. Beck F., Dolata M., Grivei E., Probst N., *J. Appl. Electrochem.*, 31, (2001): 845.
- [74]. Richner R., Muller S, Wokaum A., *Carbon*, 40, (2002): 307.
- [75]. *IUPAC Compendium of Chemical Terminology*, 2nd Edition, (1997).
- [76]. Amelick S., Delavignette P., *Chemistry and Physics of Carbon*, Marcel Dekker, New York (1995).
- [77]. Pierson H.O., *Handbook of Carbon, Graphite, Diamond and Fullerenes*, Noyes Publications, NJ, USA, (1993).
- [78]. Bansal R.C., Donnet J.B., Stoeckli F., Dekker M., *Active Carbon*, New York. (1998) [Chapter 2].
- [79]. Lozano-Castell'ó D., Cazorla-Amor'os D., Linares-Solano A., Shiraishi S., Kurihara H., Oya A., *Carbon*, 41, (2003): 1765.
- [80]. Pekala R.W., *J. Mater. Sci.*, 24, (1989): 3221.
- [81]. Probstle H., Wiener M., Fricke J., *J. Porous Mater.*, 10 (2003): 213.
- [82]. Tran T.D., Kinoshita K., *Electrochem. Soc.*, 98-15, (1998): 548.
- [83]. Fischer U., Saliger R., Bock V., Petricevic R., Fricke J., *J. Porous Mater.*, 4, (1997): 281.
- [84]. Escribano S., Berthon S., Ginoux J.L., Achard P., *Extended Abstracts: Eurocarbon'98*, Strasbourg, France, (1998): 841–842.

- [85]. Li W., Reichenaur G., Fricke J., *Carbon*, 40, (2002): 2955.
- [86]. Iijima S., *J. Microscopy*, 119, (1980): 99.
- [87]. Iijima S., *Nature*, 354, (1991): 56.
- [88]. Bethune D.S., Klang C., De Vries M.S, *Nature*, 363, (1993): 605.
- [89]. Iijima S, Ichihashi T., *Nature*, 363, (1993): 603.
- [90]. McEnaney B., Prace Naukowe Institutu Chemi Technologi Nafty I Wegla. Politechniki Wroclawskiej, Konferencje, 57 (2002): 10.
- [91]. An K.H., Jeon K.K., Heo J.K., Lim S.C., Bae D.J., Lee Y.H., *J. Electrochem. Soc.* 149, (2002): A1058–A1062.
- [92]. Frackowiak E., Jurewicz K., Delpeux S., B'eguine F., Liz-Marz'an L.M., Giersig M. (Eds.), *Low-dimensional Systems: Preparation, and Some Applications*, Kluwer Academic Publishers, (2003) [305].
- [93]. Frackowiak E., Jurewicz K., Szostak K., Delpeux S., B'eguine F., *Fuel Process. Technol.*, 77, 78, (2002): 213.
- [94]. Frackowiak E., Delpeux S., Jurewicz, Szostak K., Cazorla- Amoros D., B'eguine F., *Chem. Phys. Lett.*, 361, (2002): 35.
- [95]. Niu C., Sichel E.K., Hoch R., Moy D., Tennent H., *Appl. Phys. Lett.*, 70, (1997): 1480.
- [96]. An K. H., Kim W.S., Park Y.S., Choi Y.C., Lee S.M., Chung D.C, Bae D.J., Lim S., Lee Y.H., *Advanced Materials*, 13, (2003): 497.
- [97]. Du C., Pan N., *Journal of Power Sources*, 160, (2006): 1487–1494.
- [98]. Computer generated image of a multi walled carbon nanotube, Available online: 21 July 2012: <http://www.crystalsoftcorp.com/features.php>.

- [99]. Structure of single walled carbon nanotubes, Available online: 21 July 2012: <http://cnx.org/content/m22580/latest/>.
- [100]. Han G., Yuan J., Shi G., Wei F., *Thin Solid Films* 474, (2005): 64–69.
- [101]. Czardybon A., Lapkowski M., *Synth. Met.* 119, (2001): 161.
- [102]. Shirakawa H., Louis E.J, MacDiarmid A.G, Chiang C.K, Heeger A.J., *Chem Commun.*, (1977): 578.
- [103]. Chiang C.K., Fincher C.R., Park Y.W., Heeger A.J., Shirakawa H., Louis E.J. *Phys Rev Lett* 39, (1977): 1098.
- [104]. Shirakawa H., Ito T, Ikeda S., *Makromol Chem.*, 179, (1978): 1565.
- [105]. Miller J.S., *Adv Mater*, 5, (1993): 587.
- [106]. Miller J.S., *Adv Mater*, 5, (1993): 671.
- [107]. Toshima N., Hara S. *Prog. Polym. Sci.* 20, (1995): 155.
- [108]. An H., Wang Y, Wang X., Li N., Zheng L., *J Solid State Electrochem*, ( 2009), DOI 10.1007/s10008-009-0835-0.
- [109]. Laforgue A., Simon P., Sarrazin C., Fauvarque J.F., *J. Power Source* 80, (1999): 142.
- [110]. Mastragostino M., Arbizzani C., Soavi F., *J. Power Source*, 812, (2001): 97-98.
- [111]. Yu F., Tian S., Yao D., Knoll W., *Anal. Chem.*, 76, (2004): 3530.
- [112]. Baba A., Tian S., Stefani F., Xia C., Wang Z., Advincula R.C., Johannsmann D., Knoll W., *J. Electroanal. Chem.*, 562, (2004): 95.
- [113]. Tian S., Liu J., Zhu T., Knoll W., *Chem. Commun.*, (2003): 2738.
- [114]. Huang W.S., Humphrey B.D., MacDiarmid A.D., *J Chem. Soc., Faraday Trans. 1*, 82, (1986): 2385.

- [115]. Syed A.A., Dinesan M.K., *Talanta* 38, (1991):815.
- [116]. Sun Z, Geng Y., Jing J.L., Wang F., *Synth Met.* 84, (1997): 99.
- [117]. Geng Y., Li J., Sun Z., Jing X., Wang F., *Synth Met.*, 96, (1998): 1.
- [118]. Kuramoto N., Tomita A., *Synth Met.* 88, (1997): 147.
- [119]. Schematic presentation of polymerization of aniline, Available online 24 July 2012, <http://en.wikipedia.org/wiki/Polythiophene>.
- [120]. Schematic presentation of polymerization of thiophene, Available online 24 July 2012, <http://en.wikipedia.org/wiki/Polythiophene>.
- [121]. Skotheim T.A., Elsenbaumer R.L., Reynolds J.R., *Handbook of conducting polymers*. Marcel Dekker, New York, (1998) [225].
- [122]. McCullough R.D., *Adv Mater* 10, (1998): 93.
- [123]. Yamamoto T., Sanechika K., Yamamoto A., *J Polym Sci Polym Lett.*, 18, (1980): 9.
- [124]. Lin J.W.P., Dudek L.P., *J. Polym Sci Polym Chem.*, 18,(1980): 2869.
- [125]. Im S.G., Olivetti E.A., Gleason K.K., *Surface & Coatings Technology*, 201, (2007): 9406–9412.
- [126]. Pielartzik H., Reynolds J.R. *Adv Mater* 12, (2000): 481.
- [127]. Kirkchmeyer S., Reuter K. *J Mater Chem.*, 15, (2005): 2077.
- [128]. Granström M., Inganös O., *Polymer*, 36 (1995): 2867.
- [129]. Jang J., *Adv.Polym.Sci.*, 99 (2006): 189-259.
- [130]. Stejskal J, Riede A, Hlavata D, Prokes J, Helmstedt M, Holler P, *Synth Met.* 96 (1998): 55.
- [131]. Min G., 119, *Synth Met* (2001): 273.
- [132]. Golob G.M., Ehrlich P., *J. Polym. Sci. Polym. Phys.* 15 (1977): 627.

## REFERENCES

- [133]. Frommer J.E., Chance R.R., *Encyclopedia of polymer science and engineering* edited by J.I.Kroschwitz Wiley, New York (1986) [462].
- [134]. Lewis T.J., *Chem. Soc.* 88, (1989): 189.
- [135]. Hong M.S., Lee S.H., Kim S.W., *Electrochem Solid St.*,5 (2002): A227.
- [136]. Pasquier A.D., Laforgue A., Simon P., *J. Power Sources*, 125, (2004): 95.
- [137]. Pasquier A.D., Laforgue A., Simon P., Amatucci G.G., Fauvarque J.F., *J. Electrochem. Soc.* 149, (2002): A302.
- [138]. Park J.H., Park O.O., Shin K.H., Jin C.S., Kim J.H., *Electrochem. Solid St.* 5, (2002): H7.
- [139]. Amatucci G.G, Badway F., Pasquier A.D., Zheng T., *J. Electrochem.Soc.* 149, (2001): A930.
- [140]. Fabio A.D., Giorgi A., Mastragostino M., Soavi , *J. Electrochem.Soc.* 148, (2001): A845.
- [141]. Park J.H., Park O.O., *J. Power Sources*, 111, (2002): 185.
- [142]. Balducci A., Henderson W.A., Mastragostino M., Passerini S., Simon P., Soavi. F., *Electrochim. Acta*, 50, (2005): 2233.
- [143]. Yang Y., Wan M.J., *Mater Chem.* 11, (2001): 2022.
- [144]. Lewis T.W., (2000) Dissertation, University of Wollongong.
- [145]. Bates F.S., *Science* 251(1991): 898.
- [146]. Zhao D, Feng J, Huo Q, Melosh N, Fredrickson GH, Chmelka BF, Stucky GD *Science* 279, (1998): 548.
- [147]. Raez J, Barjovanu R, Massey JA, Winnik MA, Manners I, *Angew Chem Int.*39 (2000): 3862.

## REFERENCES

- [148]. Leclere P, Calderone A, Marsitzky D, Francke V, Geerts Y, Mullen K, Bredas JL, Lazoronic R, *Adv Mater* 12, (2000): 10742.
- [149]. Mannes I., *Chem Commun.*, (1999): 857.
- [150]. Wei Z, Zhang Z, Wan M, *Langmuir* 18 (2002): 917.
- [151]. Spector M.S., Price R.R., Schnur J.M., *Adv Mater* 11, (1999): 337.
- [152]. Yao T.M., Kim N.E., Xia Y., Whitesides G.M., Aksay I.A. *Nature* 390, (1997): 67.
- [153]. Lindman J, Kronberg H., *Surfactants and polymers in aqueous solution*. Wiley, Chichester, New York. (1998)
- [154]. Antonietti M, Basten R, Lohmann S, *Macromol Chem Phys.* 196, (1992): 441.
- [155]. Candau F, *Polymerization in Organized Media*. Gordon Science Publications, Philadelphia, (1992) [p 215].
- [156]. Landfester K, Bechthold N, Tiarks F, Antonietti M (1999) *Macromolecules* 32:5222.
- [157]. Landfester K, *Adv Mater*, 13, (2001): 765.
- [158]. Huczko A., *Applied Physics*, 70, (2000): 365.
- [159]. Hulteen J.C., Martin C.R., *Journal of Material Chemistry*, 7, (1997): 1075.
- [160]. Nkosi M.M., PHD thesis, Department of Chemistry, University of the Western Cape, (2005).
- [161]. Lakshmi B.B., Patrissi C.J., Martin C.R., *Chemistry of Materials*, 9, (1997): 2544.
- [162]. Han M.G., Foulger S.H., *Chem. Commun.*, (2005), 3092–3094.
- [163]. Jang J, Oh J.H., *Chem Commun.* (2004): 882.
- [164]. Demoustier-Champagne S., Legras R., *J. Chim. Phys.* 95, (1998): 1200-1203.
- [165]. Martin C.R., *Chem. Matter.* 8, (1996): 1739.



- [166]. Piraux L., Dubois S., Demoustier-Champagne S., *Nuclear Instruments and Methods in Physics Research*, B131, (1997): 357.
- [167]. Xu Y., Wang J., W. Sun, S. Wang, *Journal of Power Sources*, 159, (2006): 370–373.
- [168]. Girija T.C., Sangaranarayanan M.V., *Journal of Power Sources*, 156, (2006): 705–711.
- [169]. Li W., Chen J., Zhao J., Zhang J., Zhu J., *Materials Letters*, 59, (2005): 800–803.
- [170]. Wang J., Xu Y., Chen X., Du X., Li X., *Acta Phys. -Chim. Sin.*, 23(3), (2007): 299–304.
- [171]. Braun E., Eichen Y., Sivan U., Ben-Yoseph G., *Nature*, 391, (1998): 775.
- [172]. He Z.B., Yu S.H., Zhu J.P., *Chem. Mater.*, 17, (2005): 2785.
- [173]. Gao F., Lu Q.Y., Komarneni S., *Chem. Commun.*, (2005): 531.
- [174]. Lu Q.Y., Gao F., Komarneni S., *J. Am. Chem. Soc.*, 126, (2004): 54.
- [175]. Mao C.B., Solis D.J., Reiss B.D., Kottmann S.T., Sweeney R.S., Hayhurst A., Georgio G., Iverson B., Belcher A.M., *Science*, 303, (2004): 213.
- [176]. Shi W., Ge D.T., Wang J.X., Jiang Z.Z., Ren L., Zhang Q.Q., *Macromol. Rapid Commun.* 26, (2006): 926;
- [177]. Shi W., Liang P., Ge D., Wang J., Zhang Q. *Chem. Commun.*, (2007): 2414–2416.
- [178]. Subramanian V., Hall S.C., Smith P.H., Rambabu B., *Solid State Ionics* 175, (2004): 511.
- [179]. Liang Y.Y., Li H.L., Zhang X.G., *J. Power Sources*, 173, (2007): 599.
- [180]. Walker, R.B. King, R. Tannenbaum, *J. Solid State Chem.*, 180, (2007): 2290.
- [181]. Kim K.H., Kim G.P., Song I.K., Yang K.H., Lee B.C., Baek S.H., *Thin Solid*

- Films*, 519, (2011): 3086–3089.
- [182]. Zheng J.P., Cygan P.J., Jow T.R., *J. Electrochem. Soc.*, 142, (1995): 2699.
- [183]. Sato Y, Yomogida K, Nanaumi Y., Ohsawa M., Kawai M., *Electrochem. Solid State Lett.*, 3, (2000): 113.
- [184]. Miller J.M., Dunn B, *J. Electrochem. Soc.*, 144, (1997): L309.
- [185]. Miller J.M., Dunn B, *J. Langmuir*, (1999): 799.
- [186]. Kim H., Popov B. N., *Journal of Power Sources*, 104, (2002): 52-61.
- [187]. Arbizzani C., Gallazzi M.C., Mastragostino M., Rossi M., Soavi F., *Electrochem. Commun.*, 3, (2001): 16.
- [188]. Belanger D., Ren X., Davey J., Uribe F., Gottesfeld S., *J. Electrochem. Soc.* 147, (2000): 2923.
- [189]. Zhang S.W., Chen G.Z., *Manganese oxide based materials for supercapacitors. Review*, 3, (2008): 186-199.
- [190]. Pang S.C., Anderson M. A., Chapman T.W., *J. Electrochem. Soc.*, 147, (2000): 444–450.
- [191]. Li J., Zhitormirsky I., *J. Mater. Process. Technol.*, In press (2008).
- [192]. Chen Y.S., Hu C.C., Wu Y.T., *J. Solid State Electrochem.* 8, (2004): 467-473.
- [193]. Prasad K.R., Miura N., *Electrochem. Commun.*, 6, (2004): 1004-1008.
- [194]. Broughton J.N., Brett M.J., *Electrochem. Acta.*, 49, (2004): 4439-4446.
- [195]. Xu J.J, Kinser A.J., Owens B.B., Smyrl W.H., *Electrochem. Solid-state Lett* ,1, (1998).
- [196]. Wang L, Morishita T, Toyoda M, Inagaki M. *Electrochim Acta*, 53, (2007): 882–6.
- [197]. Chmiola J., Yushin G., Gogotsi Y., Portet C., Simon P., Taberna PL., *Science* 313,

- (2006): 1760–3.
- [198]. Zhao Y., Zheng M.B., Cao J.M., Ke X.F., Liu J.S., Chen Y.P., *Mater Lett* 62, (2008): 548–51.
- [199]. Tarascon J.M., *Mater. Technol.*, 8, (1993): 39.
- [200]. Kordesch K.V., *Batteries, Manganese Dioxide*, vol. 1, (1974), New York.
- [201]. Wang H., Lu Z., Qian D., Li Y., Zhang W. *Nanotechnology*, 18, (2007): 115616.
- [202]. Zhang L.L., Wei T., Wang W., Zhao X.S., *Microporous and Mesoporous Materials*, 123, (2009): 260–267.
- [203]. Subramanian V., Zhu H., Vajtai R., Ajayan P M., Wei B., *J. Phys. Chem. B* 109, (2005): 207.
- [204]. Sugantha M, Ramakrishnan P A, Hermann A M, Warm Singh C. Ginley D S, *Int. J. Hydrog. Energy*, 28, (2003): 597.
- [205]. Chen Y., Zhang M.L., Lin M., Shi Z.H., *J. Electrochem. Soc.*, 152, (2005): A1272.
- [206]. Liu T., Pell W.G., Conway B.E., *Electrochim. Acta*, 42, (1997): 3541.
- [207]. Gujar T.P., Shinde V.R., Lokhande C.D., Kim W.Y., Jung K.D., Joo O.S., *Electrochem. Comm.*, 9, (2007): 504.
- [208]. Galizzioli D., Tantardini F., Trasatti S., *J. Appl. Electrochem.*, 4, (1974): 57.
- [209]. Merryman S.A., *Proc. of 9th International Seminar on Double Layer Capacitors and Similar Energy Storage Devices*, Deerfiled Beach, Fl, Dec. (1999).
- [210]. Ortiz U.M., Garcia A.A., Lara V. H. C, *Sol. Energy Mater. Sol. Cells* , 90, (2006): 83.
- [211]. Tallman D.E, Vang C., Bierwagon G.P., Wallace G.G., *Electrochem Soc*, (2002); 149:173.

## REFERENCES

- [212]. Akundy G.S, Iroh J.O, *Polymer*, 42, (2001): 9665.
- [213]. Jérôme C., Demoustier-Champagne S., Legras R, Jérôme R., *Chem Eur. J*, 6, (2000): 3089.
- [214]. Choi S.J., Park S.M., *Adv Mater*, 12, (2000): 1547.
- [215]. Jiang M., Wang J., *Electroanal Chem*, 500, (2001): 584.
- [216]. Misoska V., Price W.E., Ralph S.F., Ogata N., Wallace G.G., *Synth Met.*, 123, (2001): 279.
- [217]. Yamamura M., Hagiwara T., Iwata K., *Synth. Met.* 26, (1998): 209.
- [218]. Osaka T., Naoi K., Sakai H., Ogana S., *J. Electrochem. Soc.*, 134, (1987): 205.
- [219]. Diaz A.F., Kanazawa K.K., Gardini G.P., *J. Chem. Soc.*, (1979) :635.
- [220]. Rapi S., Bocchi V., Gardini G.P., *Synth. Met.*, 24, (1998): 217.
- [221]. Ojio T., Miyata S., *Polym. J.*, 18, (1998): 95.
- [222]. Sotiropoulou S., Sierra-Sastre Y., Mark S.S., Batt C.A., *Chem. Mater.*, 20, (2008): 821.
- [223]. Cavalli S., Albericio F., Kros A., *Chem. Soc. Rev.*, 39, (2010): 241.
- [224]. Huang J.G., Ichinose I., Kunitake T., *Chem. Commun.* (2005): 1717.
- [225]. Scheibel T., Parthasarathy R., Sawicki G., Lin X.N., Jaeger H., Lindquist S.L., *Proc. Natl. Acad. Sci.*, 100, (2003): 4527.
- [226]. Ostrov N., E.G, *Angew., Chem. Int. Ed.* 49, (2010): 3018.
- [227]. Knez M., Bittner A.M., Boes F., Wege C., Jeske H., Maiss E., Kern K., *Nano Lett.* 3, (2003): 1079.

## REFERENCES

- [228]. Iroh J.O., Wood G.A., *Eur. Polym. J.*, 33 (1), (1997): 107-114.
- [229]. Li Q., Luo G., Li J., Xia X., *Journal of Materials Processing Technology*, 137,(2003): 25–29.
- [230]. Li Q., Olson J. B., Penner R. M., *Chem. Mater.*, 16, (2004): 3402.
- [231]. Wang X., Li, Y., Am. J., *Chem. Soc.*, 124, (2002): 2880.
- [232]. Gao Y., Wang Z., Wan J., Zou G., Qian Y., *Journal of Crystal Growth*, 279, (2005): 415.
- [233]. Liu Y., Zhang M., Zhang J., Qian Y., *Journal of Solid State Chemistry*, 179, (2006): 1757.
- [234]. Wang X., Li Y., *Chem. Commun.*, (2002): 764.
- [235]. Sugantha M., Ramakrishnan P. A., Hermann A. M., Warm Singh C. P., Ginley D. S., *International Journal of Hydrogen Energy*, 28, (2003): 597.
- [236]. Yang R., Wang Z., Dai L., Chen L., *Materials Chemistry and Physics*, 93, (2005): 149.
- [237]. Cherstiouk. O.V., Simonov. P.A., Savinova. E.R., *Electrochimica Acta*, 48, (2003): 3851-3860.
- [238]. Mukerjee. S. In-Situ X-ray Absorption Spectroscopy of Carbon- Supported Pt and Pt-Alloy Electrocatalysts: *Correlation of Electrocatalytic Activity with Particle Size and Alloying, Catalysis and Electrocatalysis at Nanoparticle Surfaces*, New York, Marcel Dekker Inc. (2003) [14: 501-530].
- [239]. Fultz. B, Howe J.M. *Transmission Electron Microscopy and Diffractometry of Materials*, 2nd Edition, Berlin, Springer-Verlag,(2002) [ 2: 63, 4: 203-213, 7: 339].

## REFERENCES

- [240]. Tsang. S.C, de Oliveira. P, Davis. J.J., Green. M.L.H., Hill. H.A.O., *Chemical Physics Letters*, 249, (1996): 413-422.
- [241]. Treacy. M.M.J. *Detection and Imaging of Supported Catalyst Particles, Materials Problem Solving with the Transmission Electron Microscope*, Hobbs. L.W., Westmacott. K.H., Williams. D.B., (editors), Pittsburgh, Materials Research Society, (1986) [62: 367-378].
- [242]. Ganesan. P, Kuo. H.K, Saavedra. A, De Angelis. R.J. *Journal of Catalysis*, 52, (1978): 310-320.
- [2463]. Hornyak. G.L, Peschel. S.T, Sawitowski. T.H, Schmid. G. *Micron*, 29, (1998): 183-190
- [244]. Sklad. P.S. *The Preparation of TEM Specimens form Hazardous or Difficult Materials, Specimen Preparation for Transmission Electron Microscopy of Materials*, Bravman. J.C, Anderson, R.M. McDonald. M.L.(editors), Pittsburgh, Materials Research Society, (1988) [115: 39-50].
- [245]. Rice S.B, Treacy M.J. *The Art of the Possible: An Overview of Catalyst Specimen Preparation Techniques for TEM Studies*, Bravman J.C, Anderson. R.M, McDonald M.L., (ed.), Pittsburgh, Materials Research Society, (1988) [115: 15-27].
- [246]. Han. K, Yu-Zhang. K. *Scripta Materialia* 50, (2004): 781-786.
- [247]. Chao. K.J, Wu. C. N., Chang. A.S., Hu. S.F. *Microporous and Mesoporous Materials* 27, (1999): 287-295.
- [248]. Ebbing. D.D. *General Chemistry*, 4th Edition, Boston, Houghton Mifflin Company, (1993) [14: 461-466, 606-609, 648-650].

## REFERENCES

- [249]. Jenkkins. R, de Vries. J.L, *An Introduction to X-Ray Powder Diffractometry*, Eindhoven, N.V. Phillips Gloeilampenfabrieken, [2: 8-10].
- [250]. Perego. G. *Catalysis Today*, 41, (1998): 251-259.
- [251]. Lipson. H, Steeple. H. *Interpretation of X-ray Powder Diffraction Patterns*, London, Macmillan and Company Ltd. (1970), [4: 93-94], [5: 113-114].
- [252]. Cullity. B.D. *Elements of X-ray Diffraction*, 2nd Edition, Ontario, Addison-Wesley Publishing Company Inc. (1978) [7: 188-226].
- [253]. Haber. J, *Pure and Applied Chemistry*, 63 (9), (1991): 1227-1246.
- [254]. Brunauer S., Emmett P.H., Teller E., *J. Am. Chem. Soc.*, 60, (1938): 309.
- [255]. Webb. P., A., Orr C., Camp R.W., Olivier J.P., Yunes Y.S., *Analytical Methods in Fine Particle Technology*, Georgia, Micromeritics Instrument Corporation, (1997); [1:11].
- [256]. Cattaneo. C., Sanchez de Pinto. M.I., Mishima. H., Lòpez de Mishima B.A., Lescano D., Cornaglia L., *Journal of Electroanalytical Chemistry*, 461, (1999): 32-39.
- [257]. Jarvi. T.D., Stuve. E.M.. *Fundamental Aspects of Vacuum and Electrocatalytic Reactions of Methanol and Formic Acid on Platinum Surfaces: Electrocatalysis*, Lipkowski. J, Ross Jr. P.N. (editors), New York, Wiley-VCH Inc. (1998) [3: 75-153].
- [258]. Voorhees, V., Adams, R., *J. Amer. Chem. Soc.* 44 (6), (1922): 1397.
- [259]. The Story of Adams Catalyst, *Platinum Metals Rev.*, 6 (4), (1962): 150-152.
- [260]. Krans J.M , van Rutenbeek J.M., Fisun V.V., Yanson I.K., de Jongh L.J., *Nature*, 375 (1995): 767.
- [263]. Likharev K.K., Claeson T., *Sci. Am.*, (June,1992) 80.
- [262]. Markovich G., Collier C.P., Henrichs S.E., Remacle F., Levine R.D., Heath J.R., *Acc. Chem. Res.* 32, (1999): 415.

- [263]. *Physics of Quantum Well Devices*. (Ed: B. R. Nag) Netherlands, Kluwer, Dordrecht, (2000).
- [264]. Alivisatos P. *Pure Appl. Chem.*, 72, (2000): 3.
- [265]. Notzel R., Ploog K. H., *Adv. Mater.* 5, (1993): 22.
- [266]. Nirmal M., Brus, L. *Acc. Chem. Res.*, 32, (1999): 407.
- [267]. Klimov V.I., Mikhailovsky A.A., Xu S., Malko A., Hollingsworth J.A., C.A., Leatherdale, Eisler H. J., Bawendi M. G., *Science*, 314, (2000): 290.
- [268]. Klein D.L., Roth R, Lim A. K. L., Alivisatos A.P., Mceuen P.L., *Nature*, 389, (1997): 699.
- [269]. Pettersson H., Baath L., Carlsson N., Seifert W., Samuelson L., *Appl. Phys. Lett.*, 79, (2001): 78.
- [270]. Shipway A.N., Katz E., Willner I., *Phys Chem*, 1, (2000): 18.
- [271]. Phillips J., *J. appl. Phys.*, 91, (2002): 4590.
- [272]. Coe S., Woo W. K., Bawendi M., Bulvoic V., *Nature*, 420, (2002): 800.
- [273]. Wang Z.L., *Adv.Mater.* 12, (2000): 1295.
- [274]. Sahoo N.G, Jung Y.C., So H.H., Cho J.W., *Synth. Met.* 157, (2007): 374.
- [275]. Hsieh C.C, Chao W., Horng Y.C., Lee H.M., Chin J., *Chem. Soc.* 56, (2009): 435.
- [276]. Ping Z., *J. Chem. Soc.*, Faraday Trans., 92, (1996): 3036.
- [277]. Christensen P.A., Hamnet A., *Electrochim. Acta*, 36, (1991):1263.
- [278]. Maia G., Ticianelli E.A., Nart F.C., *Zeitschrift Phys. Chem.* 186, (1994): 245.
- [279]. Kim J.W., Liu F., Choi H.J., Hong S.H., Joo J. *Polymer*, 44(1), (2003): 289–93.
- [280]. He C., Yang C., Li Y. *Synthetic Metals*, 139, (2003): 539–545.
- [281]. Wynne K.J, Bryan-Street B. *Macromolecules*; 18(12), (1985): 2361–8.



- [282]. Ou-Yang J.Y., Li Y.F., *Polymer* 38(15), (1997): 3997–9.
- [283]. Girija T.C., Sangaranarayanan M.V., *J. Power Sources*, 159, (2006): 1519.
- [284]. Li B.X., Rong G.X., Xie Y., Huang L.F., Feng C.F., *Inorg. Chem.*, 45, (2006): 6404.
- [285]. Ostwald W. Z., *Phys. Chem.*, 34 (1900): 495.
- [286]. Bao S.J., Bao O.L., Li C.M., Chen T.P., Sun C.Q., Dong Z.L., Gan Y., Zhang J., *Small* 3, (2007): 1174.
- [287]. Pelc P., *Dynamics of Curved Fronts*, Academic, San Diego, (1988).
- [288]. Chen Y., Liu C., Li F., Cheng H., *Journal of alloys and compounds*, 397 (2005): 282-285.
- [289]. Wang X., Li Y. D., *J. Am. Chem. Soc.*, 124, (2002): 2880.
- [290]. Kijima N., Yasuda H., Sato T., Yoshimura Y., *J. Solid State Chem.*, 159, (2001): 94–102.
- [291]. Patel M.N., Wang X.Q., Wilson B., Ferrer D.A., Dai S., Stevenson K.J., Johnston K.P. *J Mater Chem.*, 20, (2010): 390.
- [292]. Yuan C.Z., Gao B., Su L.H., Zhang X.G. *J Colloid Interface Sci.*, 322 (2008): 545.
- [293]. Luo J.Y., Xia Y.Y., *J Electrochem Soc.*, 154, (2007): A987.
- [294]. Lee H.Y., Goodenough J.B., *J. Solid State Chem.*, 144, (1999): 220.
- [295]. Stadniychuk H.P., Anderson M.A., Chapman T.W., *J. Electrochem. Soc.*, 143 (1996): 1629.
- [296]. Xu J.J., Kinser A.J., Owens B.B., Smyrl W.H., *Electrochem. Solid- State Lett.*, 1, (1998): 1.
- [297]. Xu M., Zhao D., Bao S., Li H., *J Solid State Electrochem* 11, (2007): 1101–1101

## REFERENCES

- [298]. Reddy R.N., Reddy R.G., *J Power Sources*, 124, (2003): 330.
- [299]. Wang Y.Q., Yin L.X., Palchik O., Hacoheh Y.R., Koitypin Y., Gedanken A. *Langmuir*, 17, (2001): 4131.
- [300]. Wen S., Lee J., Yeo I, Park J., Mho S., *Electrochimica Acta*, 50, (2004): 849–855.
- [301]. Zhang J., Chu W., Jiang J., Zhao X.S., *Nanotechnology*, 22, (2011): 125703
- [302]. Fraxkowiack E., Gautierm S., *Carbon*, 37, (1999): 61.
- [303]. Liu, C.; Cheng, H. M. *J. Phys. D: Appl Phys.* 38, (2005): R231–R252.
- [304]. Isvan, R. The 19th Int'l Seminar on Double Layer Capacitors and Hybrid Energy Storage Devices, Deerfield Beach, FL, 7–9 Dec 2009.
- [305]. McKeown D.A., Hagans P.L., Carette L.P.P., Russell A.E., Swider K.E., Rolison D.R., *J. Phys.Chem.*, B103 (1999): 4825.
- [306]. Long J. W., Swider K.E., Merzbacher C.I., Rolison D.R., *Langmuir*, 15, (1999) :780.
- [307]. Zheng J.P., Jow T.R., US Patent, 5, (1999) : 961, 887.
- [308]. Harris P. J. F., *Carbon nanotubes and related structures*, Department of Chemistry, University of Reading, (1999).
- [309]. Arbizzani C., Mastragostino M., et al. New trends in electrochemical supercapacitors, *Journal of Power Sources*, 100 (1-2), (2001): 164-170.
- [310]. Chabre Y. and Pannetier J., *Prog. Solid State Chem.*, 23 (1995): 1.
- [311]. Yamamoto S., Matsuoka O., Fukada I., Ashida Y., Honda T. and Yamamoto N., *J. Catal.* 159 (1996); 401.
- [312]. Turner S. and Buseck P.R., *Science*, 212, (1981): 1024.
- [313]. Post J. E., *Proc. Natl. Acad. Sci.; U.S.A.*; (1999); 96, 3447.

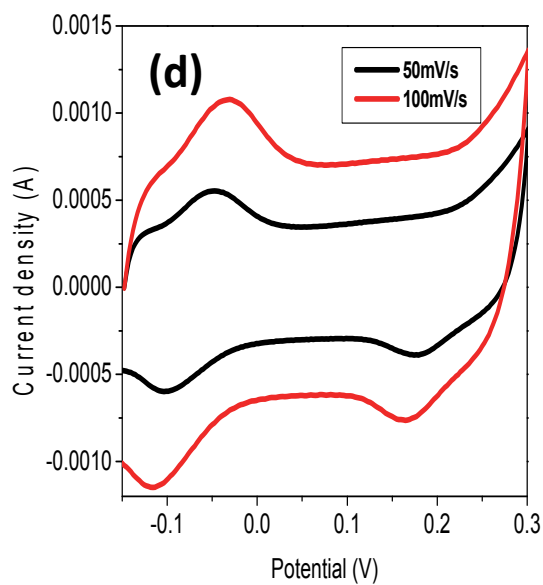
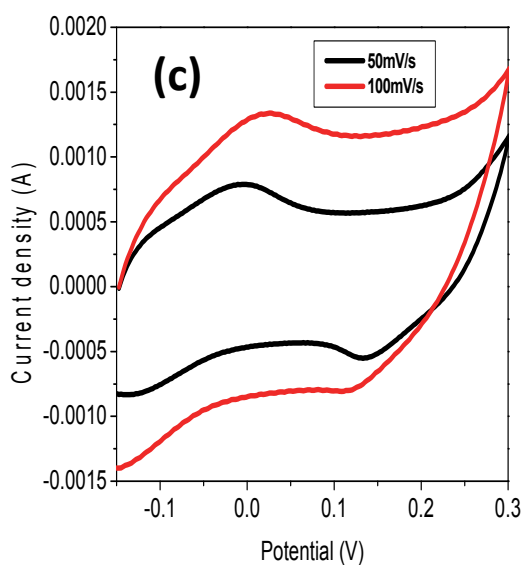
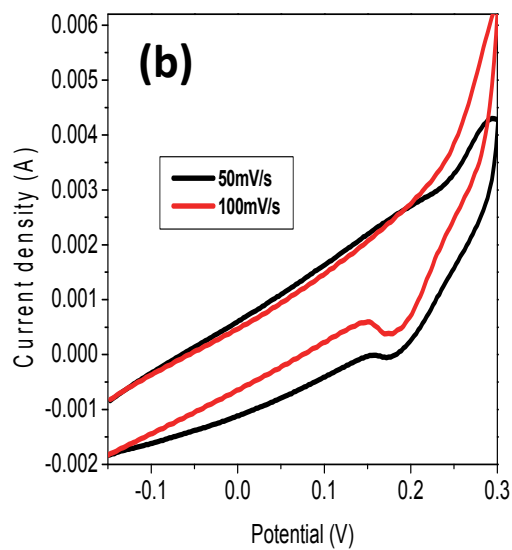
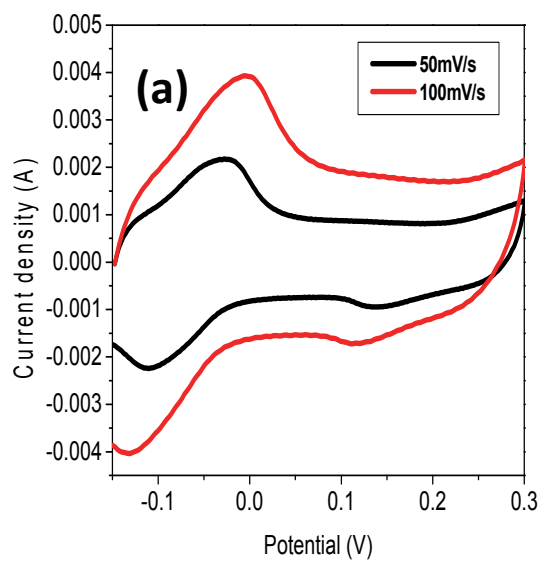
## REFERENCES

- [314]. Xiao W., Xia H., Fuh J. Y. H. and Lu L., *J. Power Sources*, 193, (2009): 935–8.
- [315]. Chatterji T., Su Y., Iles G.N., Lee Y-C., Khandhar A.P., Krishnan K.M., *Journal of Magnetism and Magnetic Materials*, 322, (2010): 3333–3336.
- [316]. Rouquerol J., Avnir D., Fairbridge C.W., Everett D.H., Haynes J.H., Pernicone N., Ramsay J. D. F., Sing K. S. W. and Unger K.K., *Pure & Appl. Chern.vol. 66*, 8, (1994): 1739-1758.
- [317]. Vinu A, Sawant D. P., Ariga K., Hartmann M., Halligudi S. B., *Micropor Mesopor Mat*, 80, (2005): 195–203.
- [318]. Qu, Q. T.; Wang, B.; Yang, L. C.; Shi, Y.; Tian, S.; Wu, Y. P. *Electrochem. Commun.*, 10, (2008): 1652–1655.
- [319]. Macheaux E., Verbaere A. and Guyomard D., *J. Phys. Chem. Solids*, 67, (2006): 1315.
- [320]. Qun P , Wenmao T., Lan D., Guomin M., *Journal of Natural Sciences*, 3,(2012): 204.
- [321]. Xia H., Lai M., Lu L. *J. Mater. Chem.* 20, (2010): 6896–6902.
- [322]. Peng C., Jin J., Chen G.Z., *Electrochimica Acta*, 53, (2007): 525–537.
- [323]. Cox P.A., *Transition Metal Oxides*, Clarendon, Oxford, (1992).
- [324]. Bartlett N., Yang X.Q., Qu D.Y., *J. Power Sources* 185, (2008): 747
- [325]. Shaijumon M.M., Ou F.S., Ci L.J., Ajayan P.M., *Chem Commun.* 20, (2008): 2373–5.
- [326]. Menon V. P., Lei J., Martin C.R., *Chem. Mater.*, 8, (1996): 2382.
- [327]. Warren. P.J, Larson. D.J, Weston. C, Cerezo. A, Petford-Long. A.K, Smith. G.D.W, Cantor. B., *Nanostructured Materials*, 12, (1999): 697-700.

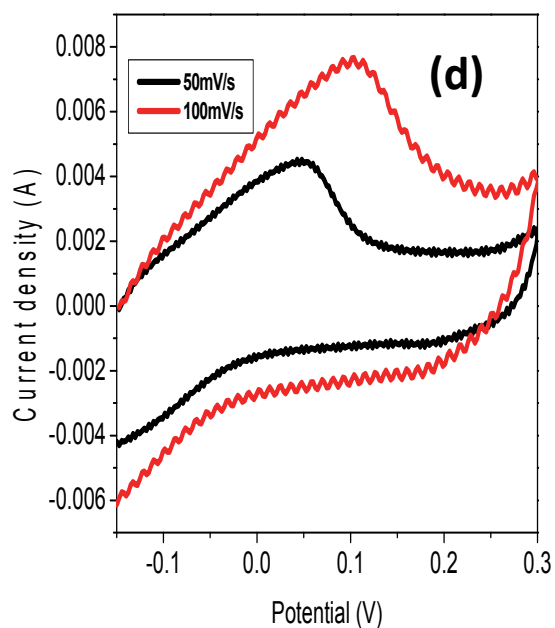
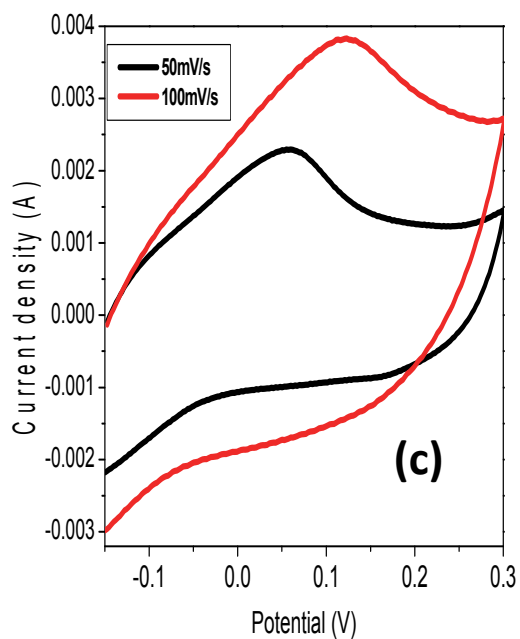
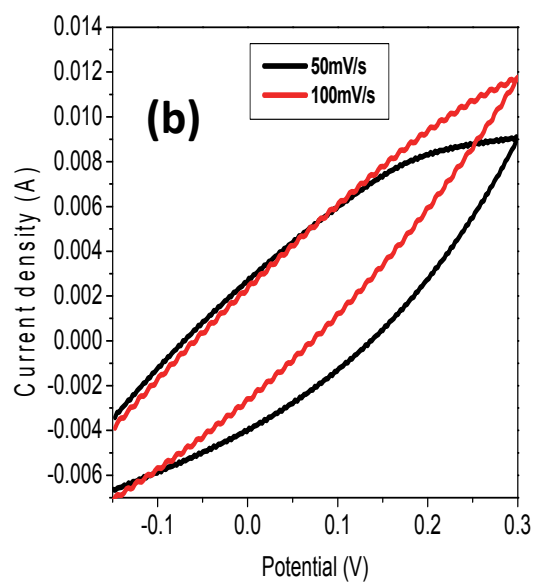
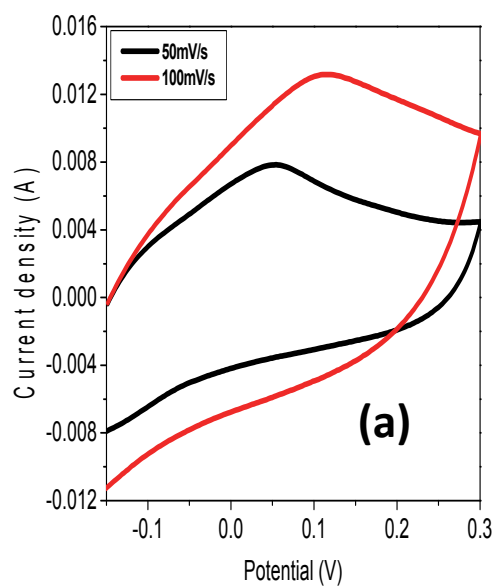
## REFERENCES

- [328]. Hu C.C. and Tsou T.W., *Electrochem. Comm.* 4, (2002): 105.
- [329]. Xia H., Meng Y.S., Yuan G., Cui C., Lu L., *Electrochemical and Solid-State Letters*, 15 (4), (2012): A60-A63
- [330]. Rouquerol F., Rouquerol J., Sing K., *Adsorption by Powders and Porous Solids*, Academic Press, London, (1999).

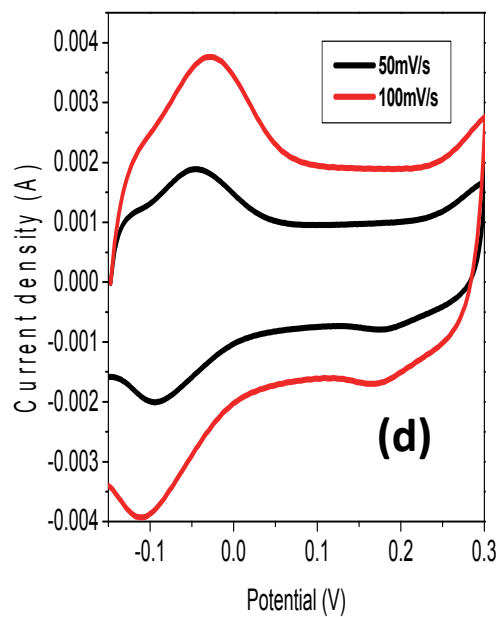
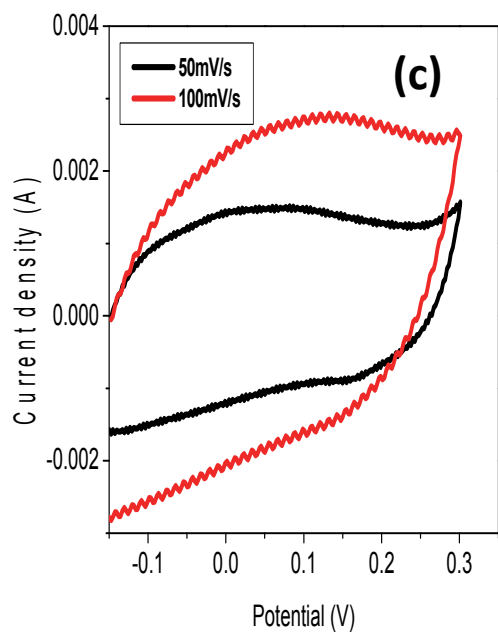
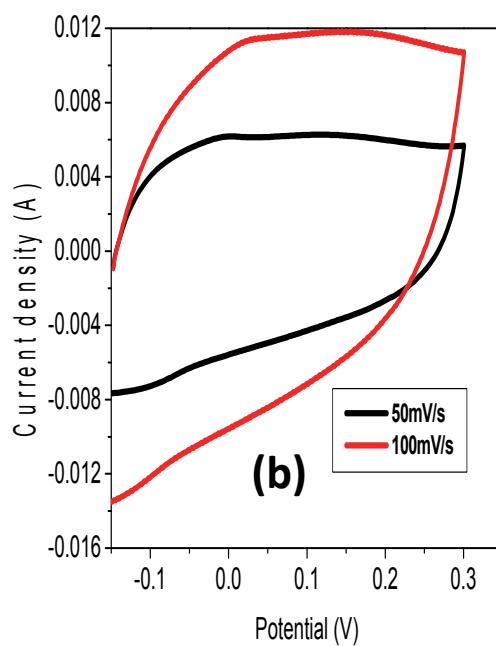
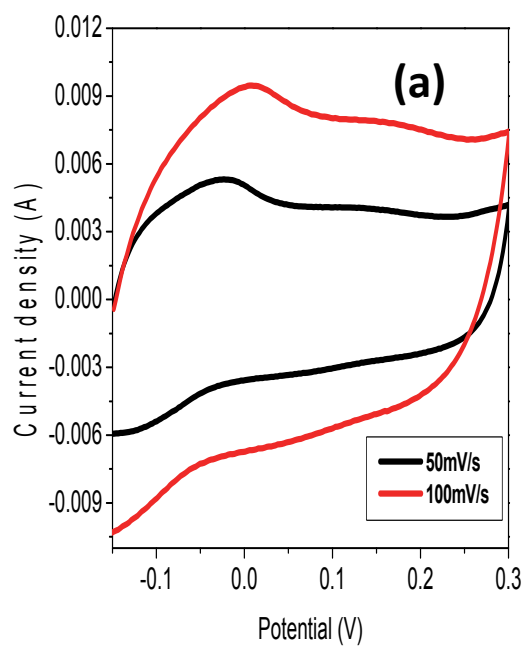
## APPENDIX A



**Appendix A1:** 50 and 100mV/s cyclic voltammograms of (a) MnO<sub>2</sub>/AC LTSS 3hrs, (b) MnO<sub>2</sub>/AC LTSS 5hrs, MnO<sub>2</sub>/AC HYDRO 5hrs, MnO<sub>2</sub>/AC HYDRO 5hrs



**Appendix A2:** 50 and 100mV/s cyclic voltammograms of (a) MnO<sub>2</sub>/C LTSS 3hrs, (b) MnO<sub>2</sub>/C LTSS 5hrs, MnO<sub>2</sub>/C HYDRO 5hrs, MnO<sub>2</sub>/C HYDRO 5hrs



**Appendix A3:** 50 and 100mV/s cyclic voltamograms of (a) MnO<sub>2</sub>/CNT LTSS 3hrs, (b) MnO<sub>2</sub>/CNT LTSS 5hrs, MnO<sub>2</sub>/CNT HYDRO 5hrs, MnO<sub>2</sub>/CNT HYDRO 5hrs

**APPENDIX B****Appendix B1 :** Capacity and capacitance values of MnO<sub>2</sub> LTSS (3hrs) in 1M Na<sub>2</sub>SO<sub>4</sub>.

<b>Cycle Number</b>	<b>Charge Capacity (mAh/g)</b>	<b>Discharge Capacity (mAh/g)</b>	<b>Charge Capacitance (F)</b>	<b>Discharge Capacitance (F)</b>	<b>Efficiency %</b>
2	40.46	28.03	161.80	112.19	69.3
3	49.27	30.02	197.08	120.08	60.9
10	31.05	26.60	124.20	106.40	85.7
20	23.82	22.71	95.28	90.84	95.3
30	18.74	18.22	74.96	72.88	97.2
40	16.24	15.96	64.96	63.84	98.3
50	15.32	14.93	61.28	59.72	97.4
60	14.81	14.53	59.24	58.12	98.1
70	16.08	15.84	64.32	63.36	98.5
80	18.98	18.62	75.92	74.48	98.1
90	21.00	20.25	84.00	81.00	96.4
100	20.85	20.41	83.40	81.64	97.9

**Appendix B2:** Capacity and capacitance values of MnO<sub>2</sub> HYDRO (3hrs) in 1M Na<sub>2</sub>SO<sub>4</sub>.

<b>Cycle Number</b>	<b>Charge Capacity (mAh/g)</b>	<b>Discharge Capacity (mAh/g)</b>	<b>Charge Capacitance (F)</b>	<b>Discharge Capacitance (F)</b>	<b>Efficiency %</b>
2	9.46	4.87	37.84	19.48	51.5
3	6.44	4.45	25.76	17.80	69.1
10	4.09	3.68	16.36	14.72	90.0
20	3.56	3.33	14.24	13.32	93.5
30	3.29	3.14	13.16	12.56	95.4
40	3.19	3.04	12.76	12.16	95.3
50	3.04	2.93	12.16	11.72	96.4
60	2.97	2.89	11.88	11.56	97.3
70	2.88	2.83	11.52	11.32	98.3
80	2.83	2.78	11.32	11.12	98.2
90	2.76	2.70	11.04	10.80	98.0
100	2.66	2.60	10.64	10.40	98.0



**Appendix B3:** Capacity and Capacitance values of MnO<sub>2</sub> LTSS (5hrs) in 1M Na<sub>2</sub>SO<sub>4</sub>.

Cycle Number	Charge Capacity (mAh/g)	Discharge Capacity (mAh/g)	Charge Capacitance (F)	Discharge Capacitance (F)	Efficiency %
2	41.95	35.10	167.80	140.40	83.7
3	38.99	33.89	155.56	135.56	86.9
10	32.50	30.65	130.00	122.60	94.3
20	26.67	25.65	106.68	102.60	96.2
30	24.45	23.98	97.80	95.92	98.1
40	21.85	21.58	87.40	86.32	98.7
50	19.82	19.45	79.28	77.80	98.1
60	17.78	17.69	71.12	70.76	99.5
70	16.85	16.85	67.40	67.40	100.0
80	15.93	15.93	63.72	63.72	100.0
90	15.65	15.37	62.60	61.48	98.2
100	14.82	14.72	59.28	58.88	99.4

**Appendix B4:** Capacity and capacitance values of MnO<sub>2</sub> (5hrs) Hydro in 1M Na<sub>2</sub>SO<sub>4</sub>.

Cycle Number	Charge Capacity (mAh/g)	Discharge Capacity (mAh/g)	Charge Capacitance (F)	Discharge Capacitance (F)	Efficiency %
2	8.99	6.66	35.96	26.64	74.1
3	8.58	6.95	34.32	27.80	81.0
10	7.60	6.90	30.40	27.60	90.9
20	6.66	6.25	26.64	25.00	93.9
30	5.84	5.64	23.36	22.56	96.5
40	8.35	5.23	33.40	20.92	97.7
50	4.70	4.58	18.80	18.32	97.4
60	4.29	4.21	17.16	16.84	98.1
70	4.04	4.04	16.16	16.16	100.0
80	3.88	3.80	15.52	15.20	97.9
90	3.76	3.68	15.04	14.72	97.8
100	3.64	3.64	14.56	14.56	100.0

**Appendix B5:** Capacity and capacitance values of MnO<sub>2</sub> (LTSS) 3hrs using 6M KOH.

Cycle Number	Charge Capacity (mAh/g)	Discharge Capacity (mAh/g)	Charge Capacitance (F)	Discharge Capacitance (F)	Efficiency %
2	108.27	37.21	433.08	148.84	34.4
3	78.54	35.06	314.16	140.24	44.6
10	43.16	30.65	172.64	122.60	71.0
20	32.76	29.03	131.04	116.12	88.6
30	31.92	28.75	127.68	115.00	90.0
40	33.43	28.99	133.72	115.96	89.2
50	32.04	28.75	128.16	115.00	89.7
60	32.32	28.83	129.28	115.32	89.2
70	35.54	29.54	142.16	118.16	83.1
80	38.24	29.66	152.96	118.64	77.6
90	40.74	29.38	162.96	117.52	72.1
100	39.75	29.15	159.00	116.60	73.3

**Appendix B6:** Capacity and capacitance values of MnO<sub>2</sub> (HYDRO) 3hrs using 6M KOH.

Cycle Number	Charge Capacity (mAh/g)	Discharge Capacity (mAh/g)	Charge Capacitance (F)	Discharge Capacitance (F)	Efficiency %
2	21.22	13.79	84.90	55.16	65.0
3	20.19	13.66	80.70	54.64	67.7
10	16.50	13.18	66.00	52.72	80.0
20	14.12	12.05	56.48	48.20	85.4
30	13.28	11.63	53.12	46.52	87.6
40	12.79	11.31	51.16	45.24	88.4
50	12.47	11.15	49.88	44.60	89.4
60	12.15	10.89	48.60	43.56	89.6
70	11.82	10.69	47.28	42.76	90.4
80	11.60	10.50	46.40	42.00	90.5
90	11.63	10.53	46.52	42.12	90.6
100	12.34	11.12	49.36	44.48	90.1

**Appendix B7:** Capacity and Capacitance values of MnO<sub>2</sub> LTSS (5hrs) using 6M KOH.

Cycle Number	Charge Capacity (mAh/g)	Discharge Capacity (mAh/g)	Charge Capacitance (F)	Discharge Capacitance (F)	Efficiency %
2	114.11	102.82	456.44	411.28	90.1
3	78.39	76.02	313.56	304.08	97.0
10	70.68	67.55	282.72	270.20	95.6
20	69.70	66.51	278.80	266.04	95.4
30	66.95	63.64	267.80	254.56	95.1
40	65.92	64.08	263.68	256.32	97.2
50	57.15	56.92	228.60	227.68	99.6
60	62.93	57.86	251.72	231.44	92.0
70	58.40	56.65	233.60	226.60	97.0
80	55.13	54.01	220.52	216.04	98.0
90	54.51	53.83	218.04	215.32	99.0
100	54.68	54.41	218.72	217.64	99.5

**Appendix B8:** Capacity and capacitance values of MnO<sub>2</sub> HYDRO (5hrs) using 6M KOH.

Cycle Number	Charge Capacity (mAh/g)	Discharge Capacity (mAh/g)	Charge Capacitance (F)	Discharge Capacitance (F)	Efficiency %
2	29.18	20.70	116.72	82.80	71.0
3	27.46	20.66	109.84	82.60	75.0
10	25.56	21.26	102.24	85.04	83.0
20	23.34	20.36	93.36	81.44	87.0
30	21.86	19.31	87.44	77.24	88.3
40	21.86	19.31	87.44	77.24	88.3
50	21.86	19.59	87.44	78.36	89.6
60	21.72	19.45	86.90	77.80	89.5
70	21.26	19.03	85.04	76.12	89.5
80	20.79	18.85	83.19	75.4	90.6
90	21.67	19.77	86.68	79.08	91.2
100	22.55	20.38	90.20	81.52	90.0

**Appendix B9:** Capacity and Capacitance values of MnO<sub>2</sub>/C LTSS (3hrs).

Cycle Number	Charge Capacity (mAh/g)	Discharge Capacity (mAh/g)	Charge Capacitance (F)	Discharge Capacitance (F)	Efficiency %
2	44.67	38.54	178.7	154.2	86.3
3	40.29	34.03	161.2	136.1	84.5
10	38.90	35.12	156.0	140.5	90.3
20	32.26	28.09	129.0	112.4	87.1
30	26.12	22.59	104.5	90.4	86.5
40	22.67	19.28	91.0	77.1	85.0
50	16.95	15.11	68.0	60.4	89.1
60	15.37	14.06	61.5	56.2	91.5
70	14.73	13.67	58.9	54.7	93.0
80	14.11	13.20	56.4	52.8	93.6
90	13.70	12.89	54.8	51.6	94.1
100	13.92	12.95	55.7	51.8	93.0

**Appendix B10:** Capacity and Capacitance values of MnO<sub>2</sub>/C HYDRO (3hrs).

Cycle Number	Charge Capacity (mAh/g)	Discharge Capacity (mAh/g)	Charge Capacitance (F)	Discharge Capacitance (F)	Efficiency %
2	34.25	33.25	137.0	133.0	97.1
3	33.50	30.50	134.0	122.0	91.0
10	29.25	27.00	117.0	108.0	92.3
20	27.00	25.25	108.0	101.0	94.0
30	26.75	24.75	107.0	99.0	93.0
40	26.25	23.50	105.0	94.0	90.0
50	25.25	23.50	101.0	94.0	93.1
60	24.75	22.75	99.0	91.0	92.0
70	24.75	22.75	99.0	91.0	92.0
80	24.75	22.75	99.0	91.0	92.0
90	24.75	22.75	99.0	91.0	92.0
100	26.75	23.50	107.0	94.0	88.0

**Appendix B11:** Capacity and Capacitance values of MnO<sub>2</sub>/C LTSS (5hrs).

Cycle Number	Charge Capacity (mAh/g)	Discharge Capacity (mAh/g)	Charge Capacitance (F)	Discharge Capacitance (F)	Efficiency %
2	60.31	58.13	241.2	233.0	96.4
3	57.19	55.94	228.8	224.0	97.8
10	49.38	48.75	197.5	195.0	98.7
20	43.13	42.18	173.0	169.0	99.3
30	38.75	38.13	155.0	153.0	98.4
40	36.56	36.56	146.2	146.2	100.0
50	35.94	35.94	144.0	144.0	100.0
60	36.25	35.94	145.0	144.0	99.1
70	33.44	33.13	134.0	133.0	99.1
80	33.13	33.13	133.0	133.0	100.0
90	32.81	32.50	129.0	130.0	99.0
100	38.44	38.13	154.0	153.0	99.2

**Appendix B12:** Capacity and Capacitance values of MnO<sub>2</sub>/C HYDRO (5hrs).

Cycle Number	Charge Capacity (mAh/g)	Discharge Capacity (mAh/g)	Charge Capacitance (F)	Discharge Capacitance (F)	Efficiency %
2	42.72	39.24	171.0	157.0	92.0
3	40.47	37.68	162.0	151.0	93.1
10	36.63	33.84	147.0	135.5	92.5
20	35.43	32.31	142.0	129.2	91.2
30	34.92	30.54	140.0	122.3	88.0
40	33.33	29.34	133.3	117.4	88.0
50	32.82	28.65	131.3	114.6	87.3
60	32.13	28.32	129.0	113.3	88.1
70	31.62	27.78	126.5	111.1	88.0
80	30.54	26.58	122.3	106.3	87.0
90	33.33	27.60	133.3	110.4	83.0
100	39.42	29.88	157.7	119.5	76.0

**Appendix B13:** Capacity and Capacitance values of MnO<sub>2</sub>/AC LTSS (3hrs).

Cycle Number	Charge Capacity (mAh/g)	Discharge Capacity (mAh/g)	Charge Capacitance (F)	Discharge Capacitance (F)	Efficiency %
2	33.97	16.83	135.88	67.32	50.0
3	30.03	16.52	120.12	66.08	55.0
10	27.87	15.59	111.48	62.36	55.9
20	24.01	14.82	96.04	59.28	61.7
30	21.46	13.82	85.84	55.28	64.4
40	19.22	13.35	76.88	53.40	69.4
50	17.52	12.35	70.08	49.40	70.5
60	16.37	11.35	65.48	45.40	69.3
70	14.51	9.65	58.04	38.60	66.5
80	12.74	7.95	50.96	28.62	56.2
90	14.74	8.41	58.96	33.64	57.1
100	15.05	8.88	60.20	35.52	59.0

**Appendix B14:** Capacity and Capacitance values of MnO<sub>2</sub>/AC HYDRO (3hrs).

Cycle Number	Charge Capacity (mAh/g)	Discharge Capacity (mAh/g)	Charge Capacitance (F)	Discharge Capacitance (F)	Efficiency %
2	32.76	14.93	131.04	59.72	46.0
3	27.70	13.89	110.80	55.56	50.1
10	16.93	11.98	67.72	47.92	70.8
20	17.71	12.50	70.84	50.00	70.6
30	21.36	13.89	85.44	55.56	65.0
40	19.97	13.02	79.88	52.08	65.2
50	21.10	13.63	84.40	54.52	64.6
60	21.62	13.63	86.48	54.52	63.0
70	21.36	13.63	85.44	54.52	63.8
80	21.10	13.28	84.40	53.12	62.9
90	18.58	12.76	74.32	51.12	68.8
100	19.45	13.02	77.80	52.08	66.9

**Appendix B15:** Capacity and Capacitance values of MnO<sub>2</sub>/AC LTSS (5hrs).

Cycle Number	Charge Capacity (mAh/g)	Discharge Capacity (mAh/g)	Charge Capacitance (F)	Discharge Capacitance (F)	Efficiency %
2	43.04	35.35	172.16	141.40	82.0
3	50.13	36.19	200.52	144.76	72.2
10	66.47	30.54	265.88	122.16	46.0
20	65.29	30.64	261.16	122.56	99.3
30	50.35	29.13	201.40	116.52	58.0
40	48.94	27.08	195.76	108.32	55.3
50	49.84	27.34	199.36	109.36	54.9
60	40.00	26.06	160.00	104.24	65.2
70	46.99	27.08	187.96	108.32	57.6
80	40.71	26.22	162.84	104.88	64.4
90	45.03	27.24	180.12	108.96	60.5
100	40.19	26.51	160.76	106.04	65.9

**Appendix B16:** Capacity and Capacitance values of MnO<sub>2</sub>/AC HYDRO (5hrs).

Cycle Number	Charge Capacity (mAh/g)	Discharge Capacity (mAh/g)	Charge Capacitance (F)	Discharge Capacitance (F)	Efficiency %
2	13.47	8.70	53.88	34.80	65.0
3	11.53	8.33	46.12	33.32	72.2
10	9.30	7.31	37.20	29.24	78.6
20	9.06	7.19	36.24	28.76	79.4
30	9.06	7.37	36.24	29.48	81.3
40	9.12	7.31	36.48	29.24	80.2
50	9.06	7.31	36.24	29.24	80.7
60	9.24	7.37	36.96	29.48	79.8
70	9.06	7.19	36.24	28.76	79.4
80	8.70	6.94	34.80	27.76	79.8
90	8.51	6.58	34.04	26.32	77.3
100	7.97	6.16	31.88	24.64	77.3

**Appendix B17:** Capacity and Capacitance values of MnO<sub>2</sub>/CNT LTSS (3hrs).

Cycle Number	Charge Capacity (mAh/g)	Discharge Capacity (mAh/g)	Charge Capacitance (F)	Discharge Capacitance (F)	Efficiency %
2	169.78	93.89	679.1	378.0	55.3
3	146.14	89.47	585.0	356.0	61.2
10	70.56	65.18	282.2	261.0	92.4
20	55.82	53.46	223.3	214.0	96.0
30	53.22	51.95	212.9	208.0	98.0
40	59.88	56.73	240.0	227.0	95.0
50	53.28	50.81	213.1	203.2	95.4
60	49.84	48.08	199.4	192.3	96.5
70	48.63	47.30	195.0	189.2	97.3
80	48.39	46.82	194.0	187.3	96.7
90	48.39	46.82	194.0	187.3	96.7
100	48.20	46.82	193.0	187.3	97.1

**Appendix B18** Capacity and Capacitance values of MnO<sub>2</sub>/CNT HYDRO (3hrs).

Cycle Number	Charge Capacity (mAh/g)	Discharge Capacity (mAh/g)	Charge Capacitance (F)	Discharge Capacitance (F)	Efficiency %
2	37.50	15.76	150.00	63.04	42.0
3	30.42	14.65	121.68	58.40	48.2
10	18.89	12.43	75.56	49.72	65.8
20	15.97	11.74	63.88	46.96	73.8
30	15.07	11.32	60.28	45.28	75.1
40	14.86	11.11	59.44	44.44	74.8
50	14.24	11.11	56.96	44.44	78.0
60	14.03	11.11	56.12	44.44	79.2
70	14.17	11.11	56.68	44.44	78.4
80	13.54	10.84	54.16	43.36	80.0
90	13.96	11.11	55.84	44.44	79.6
100	14.38	11.32	57.52	45.28	78.5



**Appendix B19:** Capacity and Capacitance values of MnO<sub>2</sub>/CNT LTSS (5hrs).

Cycle Number	Charge Capacity (mAh/g)	Discharge Capacity (mAh/g)	Charge Capacitance (F)	Discharge Capacitance (F)	Efficiency %
2	115.99	92.72	463.96	370.88	79.9
3	103.90	88.07	415.60	352.28	84.8
10	85.64	77.51	342.56	310.04	90.5
20	82.51	75.29	330.04	301.16	91.2
30	95.15	79.25	380.60	317.00	83.3
40	100.10	82.79	400.40	331.16	82.8
50	101.19	85.01	404.76	340.04	84.0
60	105.43	87.44	421.72	349.76	82.9
70	106.20	88.56	424.80	354.24	83.4
80	101.40	86.96	405.60	347.84	85.8
90	105.15	90.10	420.60	360.40	85.7
100	105.99	92.66	423.96	370.64	87.4

**Appendix B20:** Capacity and Capacitance values of MnO<sub>2</sub>/CNT HYDRO (5hrs).

Cycle Number	Charge Capacity (mAh/g)	Discharge Capacity (mAh/g)	Charge Capacitance (F)	Discharge Capacitance (F)	Efficiency %
2	43.21	31.33	172.84	125.32	72.5
3	38.62	29.52	154.48	118.08	76.4
10	30.22	24.38	120.88	97.52	80.7
20	24.38	20.01	97.52	80.04	82.1
30	20.42	17.16	81.68	68.64	84.0
40	18.20	15.56	72.80	62.24	85.5
50	16.88	14.24	67.52	56.96	84.4
60	15.77	13.27	63.08	53.08	84.1
70	14.38	12.44	57.52	49.76	86.5
80	13.76	11.53	55.04	46.12	83.8
90	12.57	10.70	50.28	42.80	85.1
100	11.32	9.31	45.28	37.24	82.2

**Appendix B21:** Capacity and Capacitance values of RuO<sub>2</sub>.

Cycle Number	Charge Capacity (mAh/g)	Discharge Capacity (mAh/g)	Charge Capacitance (F)	Discharge Capacitance (F)	Efficiency %
2	111.3	94.5	400.7	340.2	84.9
3	95.04	92.0	342.1	331.2	96.8
10	99.43	87.5	358.0	315.0	88.0
20	90.62	80.2	326.2	289.0	88.5
30	85.81	76.8	309.0	276.5	89.5
40	83.90	74.0	302.0	266.4	88.2
50	82.95	73.0	299.0	263.0	88.0
60	77.31	69.5	278.3	250.2	89.9
70	77.10	68.0	277.6	245.0	88.2
80	73.79	65.3	266.0	235.1	88.5
90	73.21	65.3	264.0	235.1	89.2
100	74.31	64.8	268.0	233.3	87.2

**Appendix B22:** Capacity and Capacitance values of RuO<sub>2</sub>/AC.

Cycle Number	Charge Capacity (mAh/g)	Discharge Capacity (mAh/g)	Charge Capacitance (F)	Discharge Capacitance (F)	Efficiency %
2	71.68	56.2	258.0	202.3	78.4
3	69.40	55.8	249.8	200.9	80.4
10	67.40	55.6	242.6	200.2	82.5
20	64.72	55.4	233.0	199.4	85.6
30	64.94	55.2	234.0	198.7	85.0
40	63.16	55.2	227.0	198.7	87.4
50	62.93	55.0	227.0	198.0	87.4
60	62.92	55.0	226.5	198.0	87.4
70	62.79	54.0	226.0	194.4	86.0
80	62.14	54.0	223.7	194.4	86.9
90	62.27	54.8	224.2	197.3	88.0
100	62.27	54.8	224.2	197.3	88.0

**Appendix B23:** Capacity and Capacitance values of RuO<sub>2</sub>/C.

Cycle Number	Charge Capacity (mAh/g)	Discharge Capacity (mAh/g)	Charge Capacitance (F)	Discharge Capacitance (F)	Efficiency %
2	77.2	62.8	278.0	226.0	81.3
3	74.0	62.8	266.4	226.0	85.0
10	72.6	66.4	262.0	240.0	91.4
20	72.6	68.0	262.0	244.0	94.0
30	76.2	68.8	274.4	248.0	90.3
40	79.2	71.0	286.0	254.0	87.0
50	79.2	71.0	286.0	254.0	90.0
60	80.2	72.6	288.8	262.0	91.0
70	82.2	72.6	296.0	262.0	88.3
80	82.2	72.6	296.0	262.0	88.3
90	80.8	72.0	291.0	260.0	89.1
100	79.2	72.0	286.0	260.0	91.0

**Appendix B24:** Capacity and Capacitance values of RuO<sub>2</sub>/CNT.

Cycle number	Charge Capacity (mAh/g)	Discharge Capacity (mAh/g)	Charge Capacitance (F)	Discharge Capacitance (F)	Efficiency %
2	83.90	66.07	302.0	234.0	78.7
3	82.10	64.30	295.6	231.5	78.3
10	78.80	60.71	284.0	219.0	77.0
20	76.79	57.14	276.4	206.0	74.4
30	76.79	57.14	276.4	206.0	74.4
40	76.79	57.14	276.4	206.0	74.4
50	76.79	57.14	276.4	206.0	74.4
60	78.57	60.71	283.0	219.0	77.3
70	78.57	57.14	283.0	206.7	73.0
80	82.14	60.71	296.0	219.0	74.0
90	83.93	58.93	302.1	212.1	70.2
100	82.14	58.93	296.0	212.1	72.0